STAR FORMATION AND ENVIRONMENT OF GALAXIES

by

SMRITI MAHAJAN

A thesis submitted to
The University of Birmingham
for the degree of
DOCTOR OF PHILOSOPHY (ASTROPHYSICS)

School of Physics and Astronomy
The University of Birmingham
December 2010

To Mummy and Papa....

Acknowledgements

"Inspiration is needed in geometry, just as much as in poetry."

-Aleksandr Sergeyevich Pushkin

Ph.D. is a journey, many a times in solitude and uncharted territories, travelled by one but never alone! As I worked through this thesis, I have grown up as a researcher and as a person. There are a number of people who have directly or indirectly contributed to my personal and academic growth and have been fellow travellers with me in this adventure. I fondly remember them all today.

During the course of Ph.D. research I have developed a fascination for the evolution of structures in the Universe, starting from the very basic element they are comprised, the galaxies, and moving further on to study one of the key drivers of this evolution– star formation. Somak, thank you for directing me towards a field I thoroughly enjoy working in. You have helped me grow as an independent thinker and taught me the art of scientific writing, qualities I will indeed cherish for ever. I am indebted to you for the never lasting support you have provided in all my academic pursuits during the course of this thesis. I have been very fortunate to have you as my guiding spirit, mentor and friend.

My special thanks are due to Ali– a senior and a friend in true spirit. I thank you for guiding me academically and personally in foreign lands whenever I felt lost, and for providing template files for this thesis. I heartily recall great times spent with fellow office mates and friends Hasnain, Paul, Tim, Vicky and Walter. My sanity during tough times over the last few

years sustained because of the companionship of fellow colleagues and very special friends Antonio, Aurelia and Ravjeet. I fondly cherish the special moments spent with all of you.

I thank the senior members of the group, Al, Chris, Graham, Habib and Louisa for discussions and feedback on my project during various formal and informal group meetings. My special regards are due to Trevor for always being very supportive in all my academic endeavours, and being a very kind mentor. Being a novice at computing, I would not have reached this destination successfully without David's help and guidance all through my tenure at Birmingham.

I also take this opportunity to thank Jane and Jo-Ann for creasing out the paper work for me and guiding me through my time at the CfA. My special thanks are due to Matt and Steve for providing me an opportunity to work on the SFRS, which has opened a lot more new avenues for my research career. I fondly cherish the fun-filled time spent at the CfA with Susmita and Dharam (and family).

My kind regards are due to Sesh for being a friend, mentor and a link between me and the very fondly missed Physics Department of the University of Delhi.

Mummy, Papa, this thesis is my tribute to you. I have never said it in so many words and I probably will never be able to say this to you in person, but I owe this thesis and all of what I am to you. I could never have achieved this without the belief you had in me all along, and I hope to make up for all the hardships and trouble you have had because of my academic pursuit in days to come. Thank you for being my guiding light and inspiration, without which I would never have fulfilled this undertaking successfully. *I gladly dedicate this thesis to you*. I warmly remember my dear sister Manisha and sweet baby brother Mohit, both of whom have always idolised me, in turn providing me with the enthusiasm to strive for the best. I give warm regards and thank my grandmothers, whose blessings and spiritual guidance showed me the light in some of the darkest moments in the last few years. And last but not the least, my heartiest thanks are due to Rahul, for standing by me during the writing-up period of this thesis, and

providing the much needed humour and moral support despite surviving my tantrums. I would not have survived the long years of academic pursuit without the faith all of you had in me.

I am very grateful to my Ph.D. examiners, Prof Bianca M. Poggianti and Prof Trevor J. Ponman for their constructive criticism that has helped in improving the content presented in this thesis.

I would also steal this opportunity to pay my tribute to two great men we lost in the past 12 months– Chris Moss and John Huchra. I feel fortunate to have interacted with them in this early phase of my career. They are irreplaceable for their contribution to the society, and in particular, the astronomical community.

The grants from ORSAS, UK, the University of Birmingham and the Endowment grant for the SAO Pre-doctoral Fellowship (2010–11) are kindly acknowledged.

I thank Dr Alexis Finoguenov and Dr Ulrich Briel for providing us the XMM-Newton EPIC/PN 0.5–2 keV mosaic image of the Coma cluster used in Chapter 4 of this thesis.

This research has made use of the SAO/NASA Astrophysics Data System, and the NASA/IPAC Extragalactic Database (NED). Funding for the SDSS and SDSS-II has been provided by the Alfred P. Sloan Foundation, the Participating Institutions, the National Science Foundation, the U.S. Department of Energy, the National Aeronautics and Space Administration, the Japanese Monbukagakusho, the Max Planck Society, and the Higher Education Funding Council for England. A list of participating institutions can be obtained from the SDSS Web Site http://www.sdss.org/.

Harvard-Smithsonian Center for Astrophysics **Smriti Mahajan**

December, 2010

Statement of originality

The work presented in this thesis involves the analysis of the publicly available spectroscopic and photometric data and data products from the Sloan Digital Sky Survey[1], taken mainly from the Garching group catalogues[2]. The mid infrared imaging data from MIPS aboard NASA's *Spitzer* space telescope are obtained from the publicly available archive. Majority of the IRAC data used in Chapter 8 of this thesis are observed as part of program PID 50128 in Cycle 5, while the rest were downloaded from the archive. The ultraviolet imaging data used in Chapter 8 are taken from the Galaxy Evolution Explorer (*GALEX*)'s public database using GalexView. The 1.4 GHz radio imaging data for all but 16 galaxies studied in Chapter 8 are taken from the NVSS public database.

Full reference is given to the original authors where derivations are presented and the origin of the work is either wholly or in part from other sources. The work has not been presented previously for any degree.

I hereby certify that the work embodied in this thesis has entirely been done by me under the supervision of Dr Somak Raychaudhury (University of Birmingham, UK), and is the result of collaboration with Dr Chris P. Haines, University of Birmingham, UK (the Coma supercluster project; Chapters 4 & 7), Dr Kevin Pimbblet, Monash University, Australia (the cluster filaments project; Chapter 5), Dr Gary A. Mamon, Institut d́Astrophysique de Paris, France (the velocity modulation project; Chapter 6), as well as Dr Matthew L. N. Ashby and Prof Steven

[1] http://www.sdss.org/

[2] http://www.mpa-garching.mpg.de/SDSS/DR4/

P. Willner from the Harvard-Smithsonian Center for Astrophysics, Cambridge, USA (The Star formation Reference Survey; Chapter 8).

The analysis of data from the dark matter simulations and theoretical modelling to fit observations presented in Chapter 6 and Appendix C are done by Dr. Gary A. Mamon (IAP, France).

The compilation and reduction of radio data used in Chapter 8 has been done by Prof Steven P. Willner (CfA, USA). Dr Matthew L. N. Ashby (CfA, USA) has compiled the FIR data from the *IRAS*, NIR data from the 2MASS catalogue, and together with other team members at the University of Western Ontario have also reduced the MIR data from *Spitzer*'s IRAC used in the same Chapter.

All the data analysis (not specifically mentioned above) as well as the UV and IR photometry (SFRS; Chapter 8) presented in this thesis are done by me.

Publications

Publications in Refereed Journals (2006–April 2011)

1. '*Red star-forming and blue passive galaxies in clusters*', **Mahajan S.**, Raychaudhury S., 2009, MNRAS, 400, 687 (This article is presented as Chapter 3)

2. '*Star formation, starburst and quenching across the Coma supercluster*', **Mahajan S.**, Haines C. P., Raychaudhury S., 2010, MNRAS, 404, 1745 (This article is presented as Chapter 4)

3. '*The evolution of dwarf galaxies across the Coma supercluster*', **Mahajan S.**, Haines C. P., Raychaudhury S., 2011, MNRAS, 412, 1098 (This article is presented as Chapter 7)

4. '*The velocity modulation of galaxy properties in and near clusters: quantifying the decrease in star formation in backsplash galaxies*', **Mahajan S.**, Mamon G. A., Raychaudhury S., submitted to MNRAS (This article is presented in Chapter 6 & Appendix C)

5. '*Photometric and spectroscopic observations of three rapidly rotating late-type stars: EY Dra, V374 Peg and GSC 02038-00293*', Korhonen H., Vida K., Husarik M., **Mahajan S.**, Szczygieł D. & Oláh K., 2010b, AN, 331, 772

Publications in Conference Proceedings

1. '*Deprojecting the quenching of star formation in and near clusters*', Mamon G. A., **Mahajan S.**, Raychaudhury S., 2010, arXiv, arXiv:1012.3114

2. '*Star Formation And Environment Of Galaxies In The Nearby Universe*', **Mahajan S.**, 2011, AAS, 43, #233.02

Manuscripts in preparation

1. '*Plunging fireworks: Why do infalling galaxies light up on the boundary of clusters?*', **Mahajan S.**, Raychaudhury S., Pimbblet K. A. (This article is presented as Chapter 5)

2. '*The Star Formation Reference Survey. I. Basic Data*', Ashby M. L. N.,... **Mahajan S.** et al. (This article contributes to Chapter 2 and 8)

3. '*The Star formation Reference Survey II: A multi-wavelength view of dust and star formation in nearby galaxies*', **Mahajan S.**, Ashby M. L. N., Willner S. P., G. G. Fazio, Raychaudhury S. (This article is presented in Chapter 8)

Abstract

Across cosmic time, stars have contributed most of the radiant energy found in the Universe and have created nearly all the chemical elements heavier than helium. Understanding the evolution of the Universe requires understanding the history of star formation. Stars form in galaxies, which are in essence huge aggregations of stars, dust and gas. Understanding star formation requires, among other things, measuring the rate at which interstellar gas is being converted into stars in a given galaxy. Star formation, a critical driver of galaxy evolution, responds both to external influences (local and global environment) and internal factors (e.g. dust).

For several decades, the properties of star formation have been studied in galaxies residing in the dense environments of galaxy clusters and compared to those in the sparsely populated field. In this thesis we aim to bridge this gap in the study of the star formation-density relation by studying the evolution of galaxy properties, particularly their star formation rate (SFR) in the critical intermediate region on the periphery of rich galaxy clusters. Using photometric and spectroscopic data from the Sloan Digital Sky survey (SDSS) we show how common observables, such as colour, SFR, and SFR/M^* are influenced when galaxies are assembled into clusters via large-scale filaments. We discover that complex galaxy populations (e.g. blue passive galaxies and [optically] red star-forming galaxies) are commonly found in and around rich clusters in the nearby ($\mathrm{z} \sim 0.1$) Universe. While the blue passive galaxies are the progenitors of passive red cluster galaxies, the (optically) red star-forming galaxies are a mix of at least two different populations. One set of red star-forming galaxies are dust obscured star-forming

galaxies, while the rest of them are normal star-forming galaxies whose colour is a result of metal-rich dominant stellar populations.

For a sample of nearby ($z \sim 0.1$) galaxy clusters from the SDSS we show that star formation in galaxies ($M_r \leq -20.5$) falling into clusters increases, in a brief interval, on the periphery of the clusters, before the cluster-related environmental mechanisms begin to dominate the evolution of galaxies therein. We argue that galaxy-galaxy interactions in the intermediate density regions such as the cluster outskirts play a critical role in galaxy evolution. We use the line-of-sight velocity information obtained from the integrated galaxy spectra together with dark matter simulations to show that statistically, a single passage through the cluster core can completely quench star formation in a galaxy.

Using the optical spectroscopic and photometric data from SDSS for the nearby ($100h_{70}^{-1}$ Mpc) Coma supercluster, we show that dwarf galaxies are star-forming everywhere except in the core of clusters and groups, while their massive counterparts mostly evolve passively irrespective of their environment. In the Coma supercluster, transitional populations (post-starburst galaxies) preferentially lie in the vicinity of clusters and occasionally in galaxy groups. These observations suggest that strong velocity fields such as those prevalent in the vicinity of rich structures are critical for quenching star formation in galaxies on a short timescale of few Myr, thus causing the post-starburst phase. By comparing mid infrared (*Spitzer*/MIPS) star formation tracers with broadband colour and optical emission lines for galaxies in the Coma and Abell 1367 clusters we find that the fraction of star-forming galaxies as a function of the cluster-centric radius may depend upon the star formation tracer used.

In order to understand the correlation between different star formation tracers we make use of the multi-band data acquired for the Star Formation Reference Survey (SFRS). Using the ultra-violet (*GALEX*), mid- (*Spitzer*/IRAC) and far-infrared (FIR; IRAS) to 1.4 GHz radio (VLA/NVSS) imaging, we compare the global SFR metric for a representative sample of star-forming galaxies in the nearby Universe. We show how the SFRs based on these canonical

indicators correlate with the ‘total’ SFR expected from a galaxy’s bolometric luminosity. We show that various individual SFR measures agree well within a factor of 1.5–4 of the ‘total’ SFR. In a multi-wavelength space spanned by the 60μm luminosity, the FIR-to-FUV flux ratio (the infrared excess ratio or IRX), F100/F60 colour temperature of dust and the $Ks-60$ colour, optically selected AGN show statistical differences with the rest of the sample for the distribution of IRX only. This suggests that, in the local Universe the AGN hosts display properties very similar to star-forming galaxies, except that they are likely to be more dusty and/or FUV faint.

Contents

List of Figures

List of Tables

Chapter 1

Galaxies: evolution and star formation history

1.1 Introduction

Clusters of galaxies are the youngest entities in the hierarchical Universe, formed by the infall of galaxies through large-scale filaments. First cosmological simulations (Springel et al. 2005), and now large sky surveys such as the Sloan Digital Sky Survey (SDSS) (York et al. 2000; Stoughton et al. 2002) and the Two-degree Field Galaxy Redshift survey (2dFGRS) (Colless et al. 2001), have shown the significant dominance of large-scale filaments in the space surrounding us. These studies reveal that matter is distributed on a filamentary 'cosmic web' structure which extends isotropically to distances we have observed so far. In this cosmic web the galaxy clusters are represented by dense nodes where filaments intersect.

Conventional wisdom suggests that cores of galaxy clusters are occupied by red, passively evolving elliptical/S0 galaxies, while their blue star-forming, spiral (or irregular) counterparts prefer the sparsely occupied regions. For several decades astronomers compared the properties of galaxies in two extreme phases of a galaxy's life, in clusters, where they evolve passively after

the end of the 'active' phase of star formation, or in the field where their evolution progresses uninhibited by the hostile influence of the intra-cluster medium and proximity to neighbouring galaxies. But the revelation of the presence of the cosmic web presents a challenge to our understanding of the processes that are involved in the evolution of a galaxy over its lifetime.

Broadband colours (e.g. Butcher & Oemler 1984; Balogh et al. 2004a; Blanton et al. 2005), surface brightness (Blanton et al. 2005), spectroscopic star formation rate (SFR)/indicators such as equivalent width (EW) of Hα and [O II] (e.g. Balogh et al. 1999; Gómez et al. 2003; Balogh et al. 2004b; Mahajan & Raychaudhury 2009) and morphology (e.g. Dressler 1980) show a gradient as a function of environment. The galactic environment is often parametrized in terms of the distance to the nth nearest neighbour (Dressler 1980; Balogh et al. 2004b), projected galaxy density (Balogh et al. 2004b; Lewis et al. 2002; Gómez et al. 2003; Haines et al. 2006b; Poggianti et al. 2008) or simply as the cluster-centric distance (e.g. Porter & Raychaudhury 2007; Porter et al. 2008). Several processes that can result in such a gradient have been proposed. All these environment related mechanisms cut off the fuel for further star formation in a galaxy, leading to the transformation of late-type galaxies into passively evolving spheroidals on different time scales.

Theories and simulations of processes like the ram-pressure stripping (Gunn & Gott 1972; McCarthy et al. 2008; Kapferer et al. 2009) or strangulation (Larson et al. 1980) suggest that the warm gas component ($\sim 10^5$ K) of the interstellar medium (ISM) may be stripped from a galaxy when it enters the galaxy cluster. Such processes are dependent on the properties of the cluster in which they operate (e.g. the depth of its potential well). Other mechanisms such as thermal evaporation of cold molecular gas from a galaxy disc via thermal conduction by the intra-cluster medium (ICM) are considered to play a key role in the evolution of dwarf galaxies (Cowie & Songaila 1977) (also see Fujita 1998 and Boselli & Gavazzi 2006 for a review of various other mechanisms). Several authors have given great importance to repeated high velocity encounters amongst galaxies or "harassment" (Moore et al. 1996) and/or galaxy-galaxy mergers for their

role in the evolution of galaxies (Lewis et al. 2002; Haines et al. 2006a; Porter & Raychaudhury 2007; Moss 2006; Porter et al. 2008; Oemler et al. 2009). The frequency and impact of such galaxy-galaxy interaction processes depends upon the local galaxy density.

The observed gradient in the observable properties of galaxies to distances surprisingly far from the centre of clusters and very low inter-galactic medium (IGM) densities implies that a combination of processes might be at play in evolving the galaxies. However, the nature of these processes is yet being debated in literature. The already complicated scenario is worsened by the discovery of starburst galaxies not far from the cores of galaxy clusters (e.g. Oemler et al. 2009), thus challenging the classical view of galaxy clusters being the breeding grounds for passively evolving galaxies only. Some of the questions that immediately come to mind are: When do specific environmental effects become important in the life of a galaxy? Do all processes influence all galaxies, or are some more important for dwarfs than giants? In what environment is a process most active? Does it matter where a galaxy resides in the global large-scale structure (LSS), or do the local surroundings dominate?

The dawn of the era of large redshift surveys (e.g. SDSS, 2dFGRS) brought with it an arsenal of data for studying not only the properties of galaxies (mainly) in the low-redshift Universe but also an opportunity to see how the variations in the LSS have profound implications on its smallest entities, the galaxies. We begin the next section by describing some mechanisms that have been proposed in literature to be of consequence to the evolution of galaxies. In effect, all the processes either force a galaxy to exhaust its fuel by providing ideal conditions for a burst of star formation or expel hot (or cold) gas from it, thereby preventing any further star formation. These mechanisms can be classified into two categories, one related to the vicinity of clusters (global environment) and those that depend upon the number density of galaxies in the surrounding space (local environment).

1.2 Large-scale structure of the Universe and the distribution of galaxies

Galaxies assemble into galaxy clusters, which together with the filaments crossing them constitute the youngest structures present today, the 'superclusters' (e.g. Shapley supercluster; Raychaudhury 1989). In *hierarchically* growing Universe, structures evolve continuously. Thus it is not surprising that the properties of the building blocks of the LSS, the galaxies, are themselves influenced by the structure they constitute.

Clusters of galaxies act as a fantastic laboratory to study the influence of the LSS on the galaxy population contained therein. The very high density of galaxies in clusters creates a deep gravitational potential well which heats up the ambient medium to few keV. This medium is detected in x-rays. So a galaxy in a cluster is not only surrounded by fellow galaxies but also by the hot x-ray emitting gas called the intra-cluster medium (ICM). In addition, the galaxy density changes rapidly with cluster-centric distance, thus providing an opportunity to study galaxy properties as a function of environment when sampled to large radii.

1.2.1 Environmental processes in clusters

Since the advent of x-ray astronomy, the effect of ICM on the cluster galaxies has been explored extensively in various studies. Pioneering amongst them is the work by Gunn & Gott (1972) where they analytically showed that the ram-pressure felt by a typical galaxy is given by $P_r \approx \rho_e v^2$, where ρ_e is the ICM density and v is the velocity of the galaxy. For a typical spiral galaxy of 10^{11} $M_\odot$ and radius 10 kpc (and for gas and star surface density of 10^{-3} g cm^{-2} and 0.06 g cm^{-2} respectively), moving through the ICM with an rms velocity of 1700 km s^{-1}, the ram-pressure exceeds the force binding the material to the disc if the ICM density is in excess of 5×10^{-4} atoms cm^{-3}. This strips out the gas from the disc of the galaxy and eventually forms a spheroid such as those found abundantly in the cores of clusters at z ~ 0 (see Fig.1.1). To this

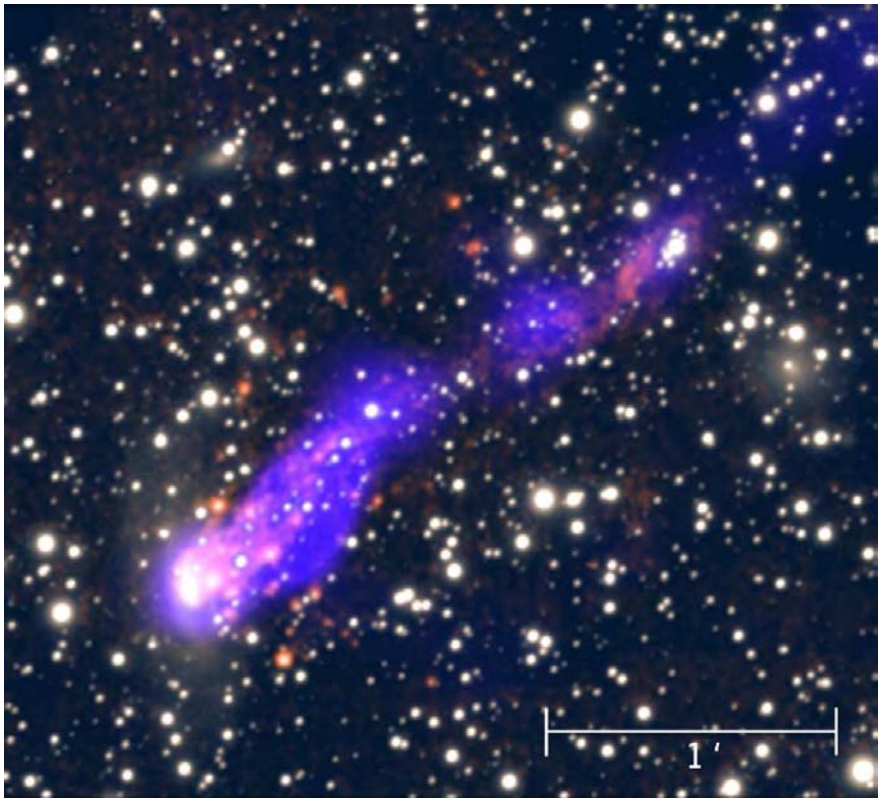

Figure 1.1: This $2.8' \times 2.8'$ composite image shows one of the rare events captured by Sun et al. (2006): ram pressure stripping of late-type galaxy ESO 137-001 orbiting in a rich cluster of galaxies Abell 3627. The long x-ray tail (blue) is overplotted with the narrow band Hα image (pink) and HST optical broad band image. At least 29 different star-forming regions have now been identified in the 10^9 $M_\odot$ tail stretching out to 70 kpc where gas has been condensing quickly to form new stars for the last $\sim 10^9$ years. (image credit: x-ray: NASA/CXC/MSU/Sun et al. 2006; optical: SOAR(MSU/NOAO/UNC/CNPq-Brazil)/Sun et al. 2006)

date, ram-pressure stripping is believed to be the best explanation for the absence of late type galaxies in galaxy clusters.

In a more recent work, McCarthy et al. (2008) have simulated the effects of ram-pressure stripping on galaxies falling into rich groups and clusters based on the above formalism except that they considered a spherical hot gas distribution unlike the face-on cold spiral disc of Gunn & Gott (1972). Their model is inspired by the idea that a disc galaxy is surrounded by a halo of hot gas which acts as a source of cold gas for star formation. Although such a hot gas halo is assumed to exist by most of the present day semi-analytic galaxy formation models, its presence

has not yet been confirmed satisfactorily despite some claims of detections (e.g. Rasmussen et al. 2006). McCarthy et al. found that stripping of the infalling galaxy is not instantaneous, and 20-40% of its reservoir of cold gas can remain intact for almost 10 Gyr. Kapferer et al. (2009) take a step further by adding spiral arms to a simple disc galaxy before exposing it to the wind. Their extensive suite of simulations shows that ram-pressure stripping is important even several Mpc away from the cluster core. Also, just as seen in the example illustrated in Fig. 1.1, simulations show that the SFR of a galaxy experiencing ram-pressure stripping can increase by a factor of up to 100, but is often not detected because it mainly occurs in discrete knots of dense gas formed in the 'wake' (Kapferer et al. 2009; Smith et al. 2010). This wake is a tail of gas and dust which trails behind the galaxy in a direction opposite to its motion through the ICM, and mainly consists of material that once formed the spiral arms.

Larson et al. (1980) suggested that since the hot gas halo would be the first to come in contact with the ICM when a galaxy falls into a cluster/group, it is stripped more easily than the disc itself. This slowly vanishing reservoir of fuel for star formation can lead to a decline in the observed SFR of a galaxy on time scales of the order of few times 10^9 years. This mechanism, often referred to as 'strangulation' or 'starvation' gives convincing results from an observational point of view (Balogh et al. 1999; Kauffmann et al. 2004), showing a slow decline in the mean SFR of galaxies as the environment becomes denser.

In a numerical simulation, Bekki, Couch & Shioya (2001) showed that the global tidal field of a cluster can efficiently remove the hot gas halo surrounding the infalling galaxy, thus quenching star formation. Bekki et al. suggested that such a tidal field may lead to a momentary burst of star formation when the galaxy first encounters the cluster's tidal field. Gnedin (2003b) suggested that the dynamical evolution of galaxies depends upon the tidal field along their trajectories in the cluster, and may not depend on the distance of their closest approach to the cluster core. They also argued that this tidal field is mostly created by the 'local' density structures such as large cluster galaxies and the unvirialized remnants of infalling galaxy groups.

In an interesting study of H I content of galaxies in three rich Abell clusters (Abell et al. 1989) and Virgo, Valluri & Jog (1991) found that the H I deficiency is stronger for larger galaxies. Given that H II gas resides in dense molecular clouds while H I is more sparsely distributed with lower densities throughout the galaxy and that bigger disc galaxies (except the low surface brightness ones) have a higher surface density, larger galaxies should protect their gaseous content more efficiently. But this is counter to the observations. After considering various possible mechanisms, Valluri & Jog (1991) suggested that the H I deficiency in their sample could only be explained by tidal interactions.

Elsewhere (Bekki 1999) it appears in a numerical simulation that when a small group (M~ 0.1M$_{clus}$) falls into a massive galaxy cluster, the *changing* gravitational field resulting from the collision can efficiently transfer cold gas to the centre of a disc galaxy belonging to the group, thus igniting a burst of star formation in it. This inflow of cold gas to the galactic nucleus is a result of the field exerted on the non-axisymmetric structure of the galaxy. A view complementary to this has been suggested by Struck (2006), who discussed the phenomenon of 'gravitational shocking'. Observations suggest that the density at the centre decreases slowly with mass in dark matter halos. So, in a hierarchical model, for comparable group and cluster halo core densities, the passage of the group through the cluster centre would substantially increase the instantaneous mass of the group. Since the typical core crossing time and the free-fall time of the group are same, the group galaxies will have enough time to be pulled together in a denser configuration. If the halo core densities of the cluster and group are comparable, the mean separation distance between galaxies would roughly be halved, increasing the galaxy density by an order of magnitude and the probability of interactions/mergers amongst them by up to a factor of 100 (density squared). The dynamical friction would dissipate relative orbital energy in these encounters, leading to galaxy-galaxy mergers. This mechanism can explain the occurrence of starburst galaxies in the infall regions of clusters or similar intermediate density environments (Moss 2006; Porter & Raychaudhury 2007; Porter et al. 2008; Oemler et al.

2009) and even in the centre of clusters (Oemler et al. 2009).

Amongst other factors, the evaporation of cold gas due to friction becomes an important influence on the evolution of galaxies falling into clusters (Cowie & Songaila 1977; Fujita 2004). This phenomenon is crucial especially for low mass galaxies (Barkana & Loeb 1999). Another important mechanism that can have profound implications on the evolution of (especially) the low mass galaxies is interactions and/or mergers with the more massive or equal mass neighbours (Haines et al. 2007).

1.2.2 Galaxy-galaxy interactions and mergers

Intuitively, galaxy-galaxy interactions/mergers seem to depend only on the local galaxy number density, but several studies (such as this work) show that the LSS may also be responsible for at least accelerating such interactions by modulating the number density of galaxies in certain regions of space. In simulations, Moore et al. (1996) have shown that the high speed encounters amongst galaxies are crucial in their course of evolution. These high speed encounters, or 'harassment', can occur at moderate galaxy densities such as those found on the outskirts of galaxy clusters. Such high speed encounters are more important for low mass galaxies, which can be easily perturbed (e.g. Larson et al. 1980).

In a classical work, Toomre & Toomre (1972) used very simple models to argue that the streaks of dust and stars seen around multiple galaxy systems such as NGC 4038/4039, NGC 4676, Arp295, etc. are tidal relics of close encounters between the parent galaxies constituting them. Based on simulations and multiple galaxy systems known at that time, Toomre & Toomre created a series of stages of mergers which is called the 'Toomre sequence'. Now the NICMOS and WFPC2 cameras aboard the Hubble Space Telescope (HST) have been used to study the systems on the Toomre sequence at optical and near infrared (NIR) wavelengths (Laine et al. 2003; Rossa et al. 2007). The optical imaging in F555W and F814W and narrow band imaging in Hα+[N II] of 11 galaxies/galaxy systems do not show much trend in nuclear properties

along the merger sequence, although the Hα emitting gas does seem to be concentrated in the central 1 kpc region in almost all the systems (Laine et al. 2003). But interestingly, the NIR imaging of these systems show a statistically significant enhancement in the brightness of nucleus with advancing merger state (Rossa et al. 2007). This result is consistent with the idea that interactions/mergers can very efficiently drive gas from the outer disc of the galaxy to its centre, thus triggering a burst of star formation (e.g. Laurikainen & Moles 1989; Bergvall et al. 2003; Jogee et al. 2005; Koulouridis et al. 2006).

Mergers are relatively rare events in the local (z$\sim$0.1) Universe. In dense environments such as groups, clusters, and their outskirts, where galaxies are under the influence of a strong potential well and/or velocity field generated by the LSS (González & Padilla 2009), the probability of mergers is reduced due to high velocities of galaxies. Hence in order to understand the evolution of galaxies, the understanding of the role played by high-speed encounters, *not* leading to mergers, is necessitated. Two key problems that inhibited the observational analysis of such galaxy-galaxy interactions for a long time are (i) the unavailability of a large homogeneous data set, and (ii) the absence of visible classic tails and bridges around such interacting galaxies.

The former is now being overcome by the data obtained by the large sky surveys. A good attempt to get rid of the latter has been recently made in a study by Reichard et al.(2008,2009). Using a sample of $>$25,000 galaxies from the SDSS, Reichard et al. have shown that the emission line signatures in the nuclear spectrum of a galaxy are well correlated with the asymmetry in its stellar light distribution between R_{50} and R_{90}, where R_x is the Petrosian radius containing x% of the galaxy's light in a particular filter. Their approach is based on the method devised by Rix et al. (1995), where a Fourier decomposition of the galaxy light is performed. The first mode of such a decomposition quantifies the overabundance of light in one side of the galaxy with a corresponding underabundance of the same in the opposite side. Reichard et al. (2009) assume this radially averaged *lopsidedness* to be the resultant of the galaxy's interactions with its neighbours. Such complementary approaches of quantifying the asymmetry in the stellar

light distribution have been attempted in some other studies (Rix et al. 1995; Abraham et al. 1996; Conselice 2003) as well, but a direct correlation between galaxy-galaxy interactions and the occurrence of nuclear starburst in such a large volume limited sample was made available for the first time by Reichard et al..

Moss (2006) employed an ensemble of 680 giant galaxies ($M_B^0 \lesssim -19$) found in eight low-redshift galaxy clusters to show that 50-70% of the galaxies falling into clusters show signs of interactions and/or mergers. Moss suggested that physical deformations in the morphology of infalling galaxies can be explained by gravitational shocking (Struck 2006), which leads to gravitational encounters amongst galaxies. Although Struck (2006) discussed this scenario for groups penetrating through the cluster core, it is undeniable that groups falling into clusters or any substructure within a cluster will also experience some degree of gravitational shocking. In fact, generalising this to the impact of the LSS, it won't be wrong to assume that *any* site within the LSS where the local galaxy density exceeds some critical value (e.g. Gómez et al. 2003) will intensify the activity of environmental mechanisms dependent on it. One of such critical sites are the building blocks of the LSS itself, the large-scale filaments of galaxies.

1.2.3 The large-scale filaments

Only in the past decade or so technology has equipped us to explore the bridge between the youth of a galaxy and its adulthood by observing the large-scale cosmic structure. Filaments of galaxies are the most recently discovered mysteries of modern day Astronomy. We know they exist but are unsure of their impact on the evolution of galaxies. High resolution simulations of a supercluster-like region by Dolag et al. (2006) show some of such difficulties. These simulations including dark matter (DM) and gas show that even though filaments host gas at temperatures $10^5 - 10^7$ K, which can be detected in the soft x-rays through Bremsstrahlung emission, or by weak lensing, will have observable signal too weak for the present day detectors.

Dynamically, the cosmic web represents preferred directions along which matter streams

into the more massive structures at the nodes. In a theoretical framework it represents the density enhancements in the primordial field, which are then sharpened by the evolution in the non-linear regime later on (Bond, Kofman & Pogosyan 1996).

Although the existence of large-scale filaments was predicted by structure formation models much before their discovery (e.g. Zeldovich, Einasto & Shandarin 1982), the identification of these large-scale structures spanning several square degrees on the sky remained a challenge. However, large sky surveys conducted in the last decade or so made it possible to create 3-d maps of the galaxy distribution in the Universe. Efforts have now been made to trace the cosmic web by using special statistical techniques (Bharadawaj & Pandey 2004; Ebeling et al. 2004; Pimbblet, Drinkwater & Hawkrigg 2004; Pandey & Bharadawaj 2006; Bond, Strauss, & Cen 2010; González & Padilla 2010; Sousbie 2010; also see Fig.1.2), and more recently indirect measures testing the impact of the filamentary environment on galaxies traversing through them (Edwards et al. 2010; Edwards, Fadda, & Frayer 2010). Filaments which have very low galaxy density may also be traced by low column density H I or warm ionized gas (McLin et al. 2002; Manning 2002; Stocke et al. 2007). In a recent work, Sato et al. (2010) studied the high temperature plasma in the Sculptor supercluster ($z = 0.108$) and constrained the O VII and O VIII intensities in the filamentary region between various clusters in it.

Accurate mapping of galaxy filaments is crucial for the baryonic mass budget of the Universe because filaments can contain up to 60% of the total cluster mass at cluster-centric distance of 4-6.5 h^{-1}Mpc (Colberg et al. 1999). While studying the properties of galaxy filaments in simulations of the ΛCDM Universe, Colberg et al. (1999) found that close pairs of galaxy clusters are almost always connected by filaments, and more than half the filaments are warped around the inter-cluster axis. Straight filaments are statistically shorter than warped filaments (Colberg et al. 1999; Pimbblet, Drinkwater & Hawkrigg 2004; Colberg et al. 2005). The more massive clusters are fed by more filaments (Colberg et al. 1999; Pimbblet, Drinkwater & Hawkrigg 2004). These results are in sync with those presented by Bond, Kofman & Pogosyan

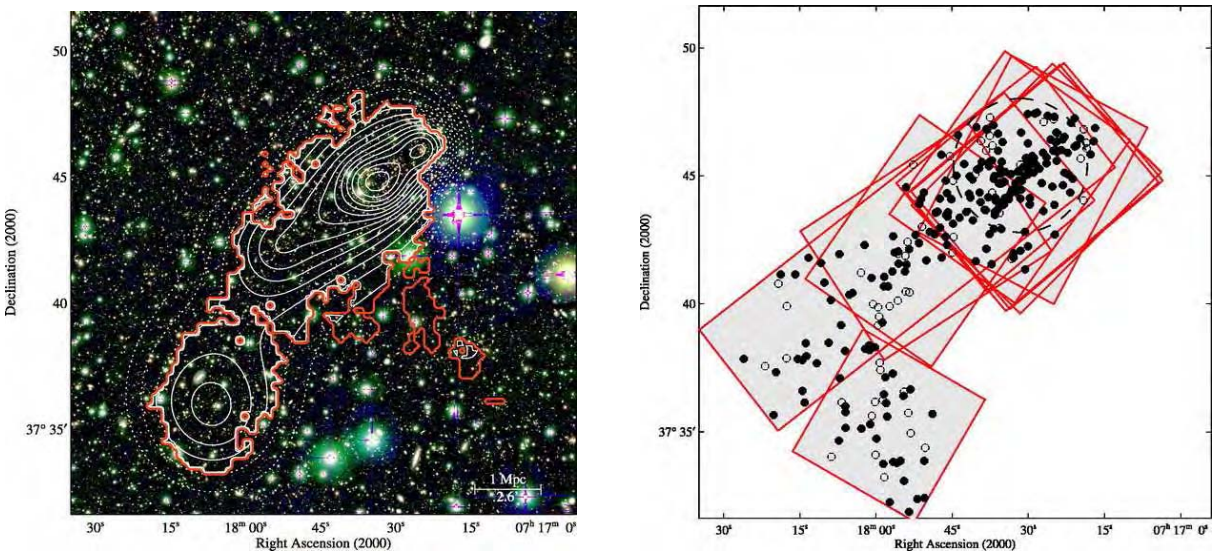

Figure 1.2: *(left)* The (VRz') image of a $20' \times 20'$ region around MACS J0717.5+3745 (z=0.551) as obtained with SuprimeCam (Subaru). The overlaid contours show the smoothed surface density distribution of galaxies with $I < 22.5$ and $V - R$ colours close to the cluster red sequence. Contours are logarithmically spaced with the lowest contour corresponding to 10 galaxies Mpc^{-2}. The levels of adjacent contours differ by 20%. Contours are shown dotted outside the region within which the adaptive-smoothing criterion (significance greater than 3σ) is met (bold red contour). The contour marking the shallow peak of the southeastern end of the filament marks a local peak galaxy surface density of 20.7 galaxies Mpc^{-2}. Since the bottom edge of the shown region is also the edge of the overall Subaru SuprimeCam image, it is conceivable that the filament extends farther south than suggested by the galaxy surface density contours shown in this image.
(right) Locations of all galaxies with spectroscopic redshifts (obtained till March 2004); filled symbols mark galaxies with redshifts between 0.52 and 0.57, i.e., the 3σ range around the systemic redshift of MACS J0717.5+3745. The shaded regions and box outlines mark the fields targeted with the individual MOS masks. The dotted line marks a circle of 1 Mpc radius around the nominal cluster center. (image credit: Ebeling et al. (2004))

(1996), who predicted that 'the more pronounced filaments will be found between clusters of galaxies that are aligned with each other and close together'.

Based on galaxy positions obtained from the 2dFGRS, Pimbblet, Drinkwater & Hawkrigg (2004) found that almost three quarters of filaments are either straight or warped with respect to the inter-cluster axis. (PDH 2004) also found that filaments become more 'curvy' with an increasing inter-cluster separation, and the curving occurs towards the more massive system in general. Despite remarkable advancements, our present day knowledge of the cosmic web still require answers to several key questions before a universal view explaining all observations of all levels of the cosmic structural hierarchy could be constructed. How do the superclusters appear in observables? How have they evolved over time? What impact do they have on the galaxies inhabiting them?

Pandey & Bharadawaj (2006) show that the distribution of red and elliptical galaxies in the SDSS is more filamentary than their bluer and 'discy' counterparts respectively. By comparing their observational results with the galaxy catalogue of the Millennium simulations, Pandey & Bharadawaj found that while the filamentarity[1] of the M* and elliptical galaxies is in good agreement between the two, simulations fail to produce the right filamentarity for the brighter and blue galaxies, implying that our current knowledge of processes involved in galaxy evolution is far from complete. In an exclusive study of large-scale inter-cluster filaments from the 2dFGRS, Porter & Raychaudhury (2007) and Porter et al. (2008) found that the SFR of galaxies is enhanced along the filaments 3-4 h_{70}^{-1} Mpc from the nearest cluster centre. By comparing the filaments of galaxies found in DEEP2 with a sample extracted from the SDSS, Choi et al. (2010) found that the filament length distribution has not significantly changed since $\mathrm{z} \sim 0.8$. However, the filament width distribution, which is sensitive to the non-linear growth of structure, broadens and shifts to smaller widths for smoothing length-scales of 5–10 h^{-1} Mpc from

[1]This shapefounder statistic is explained by Bharadawaj et al. (2000). It is defined as $F = (P^2 - 4\pi S)/(P^2 + 4\pi S)$, where P is the perimeter and S is the area. By definition $0 \leq F \leq 1$, so that an ideal filament with 0 width has $F = 1$, while a circular disc has $F = 0$.

$z \sim 0.8 - 0.1$, in accord with N-body simulations.

1.2.4 Quantifying the environment

The properties of galaxies are well correlated with their surroundings, both local and global. But the fact that our interpretation of a galaxy's neighbourhood is restricted to the plane of sky and the line of sight velocities only imply that some 'correlations' can be delusional. Hence, quantification of the environment requires not only a careful consideration of the model employed but also its limitations. We outline below some of the most commonly used methods in literature and their pros and cons where possible.

Galaxy clusters being the densest systems often serve as the origin of the richness scale. Several studies, including this one, employ the projected distance from the centre of the cluster scaled by some standard scale radius such as r_{200} (the radius at which the mean interior overdensity in a sphere of radius r is 200 times the critical density of the Universe). The obvious advantage of this method is that it does not require detailed modelling of the velocity field and/or density space around large structures. However, it works successfully only in the presence of spectroscopic data, i.e. when the contamination due to the foreground and background galaxies along the line of sight can be minimised.

Traditionally, galactic environment has been quantified in terms of the projected galaxy density. Dressler (1980) quantified the density of the surroundings of galaxies by dividing 10 by the area covered within a circle of radius equal to the distance between the galaxy under consideration and its 10th nearest neighbour, where each neighbour was constrained to be brighter that $M_V = -20.4$ ($H_0 = 50$ km s^{-1} Mpc^{-2}). Due to the ease of application this method gained immediate popularity in literature and has since been used in several varied forms. An advantage of using the nth neighbour density parameter (often designated as Σ_n) is that it quantifies the environment in units of 2-d (or 3-d if circle is replaced by a sphere) density: $h^2\,\mathrm{Mpc}^{-2}$ (or $h^3\,\mathrm{Mpc}^{-3}$).

Several authors have exploited different cluster-finding techniques to search for objects that show clustering in n-dimensional space. Although such techniques could be both parametric and non-parametric, most of those that initially found an application in Astronomy belong to the former class. The parametric algorithms often begin by giving some fiducial values to the considered parameters, for instance, local luminosity density of galaxy groups (Tully 1987) or angular coordinates (Huchra & Geller 1982). The disadvantage of this method is that it works well only when the range of values spanned by the considered parameter(s) is well known. But for galaxy cluster searching, non-parametric techniques (e.g. Pisani 1996) work better.

Haines et al. (2007) demonstrated a modification of the *adaptive kernel smoothing method* explored by several other authors (e.g. Pisani 1996). In this method, the local density $\rho(\mathbf{x}, z)$, is determined by representing each galaxy ($M_r < -18$) i by a Gaussian kernel $\kappa_i(\mathbf{x}, z)$. Unlike their predecessors, who defined the width of the Gaussian kernel iteratively as $\rho_i^{-1/2}$, Haines et al. (2007) kept the radial width fixed as 500 km s^{-1} and found the transverse width σ_i as $(8/3)^{1/2}\, D_3$, where D_3 is the distance to the third nearest neighbour within 500 km s^{-1}. It has been shown that this method robustly measures the local density of a galaxy on the scale of its DM halo, thus forming a good local density estimator for galaxies in widely different environments from poor groups to the cores of rich clusters. For each galaxy i the local density is given by:

$$\rho(\mathbf{x}, z) \propto \sum_j \eta_j \, exp\left\{ -\frac{1}{2} \left[\left(\frac{D_{ij}}{\sigma_j} \right)^2 + \left(\frac{v_i - v_j}{500 km\ s^{-1}} \right)^2 \right] \right\} \tag{1.1}$$

where, the normalisation factor η_j is $C_j^{-1}(2\pi)^{-3/2}\sigma_j^{-2}$, with C_j^{-1} being the local spectroscopic completeness for each galaxy and σ_j the width of the adaptive kernel in the transverse direction, D_{ij} is the projected distance between the galaxies i and j, v_i is the line of sight velocity of the galaxy i, and the sum is over all galaxies brighter than $M_r = -18$. The smoothing kernel approach, in its varied forms has also been adopted by many other authors (e.g. Balogh et al. 2004b).

1.3 The Spectral Energy Distribution of galaxies

Galaxies comprise stars, dust and gas. Even the star-forming regions within galaxies consist of several components- young stellar clusters, individual massive OB stars born in the cores of Giant Molecular Clouds (GMCs), older stellar populations, and a non-uniform screen of dust. At different wavelengths the observed emission is a combination of two or more of these components. We owe our current understanding of the internal structure, chemical composition, precise distance measurements, age, radial and rotational velocities, stellar evolution (in nearby galaxies), and the correlation between these and other observables in external galaxies to the knowledge gained from their spectral energy distribution (SED).

The short wavelength radiation from young stars is absorbed by dust and re-radiated at longer wavelengths. The presence and nature of the inter-stellar dust is deduced by studying the pattern in which it scatters the absorbed starlight. At optical wavelengths we see the direct starlight. Thus, the emission, for instance, in Hα or [O II] is a measure of the current and recent ($\leq$ 10 Myr) SFR of a galaxy. The OB stars are hot enough to emit ionising radiation shortward of the Lyman limit (see below), such that in the absence of large amounts of dust the corresponding radiation can be detected in narrow and/or broad-band optical imaging and spectra. Optical emission lines can also be used to trace an active nucleus by studying emission line ratios (e.g. Baldwin, Phillips & Terlevich (1981)), which can distinguish between emission from star forming galaxies and from an Active Galactic Nuclei (AGN) (also see Sec. 1.5).

In a dust free environment one can use the ultraviolet (UV) light to trace the youngest of the stars forming in a galaxy. Theoretically, the FIR and UV light together is a combination of the obscured and unobscured light from stars and hence should account for most of the galaxy's bolometric luminosity. However, the situation becomes more complicated because dust is also heated by AGN and older stellar populations. We discuss these issues in details further below. In what follows, I briefly summarise the contribution of various galaxy components at different wavelengths that help us in characterising a galaxy and its star formation history by studying

the SED.

1.3.1 Radio measures

Stars more massive than $\sim 8\,\mathrm{M}_{\odot}$ produce supernovae remnants (SNRs) from Type Ib and Type II supernovae, which accelerate most of the relativistic electrons (Condon 1992). In non-AGN galaxies the radio emission is dominated by the free-free emission originating from the H II regions. Thus radio continuum is a useful tracer of recent star formation in non-AGN galaxies because the massive stars required to produce the SNR have a lifetime of tens of Myr and the relativistic electrons live for $\lesssim 100\,\mathrm{Myr}$.

1.3.2 Infrared measures

First the Infrared Astronomical Satellite (*IRAS*) and now MIPS and IRAC aboard NASA's *Spitzer* space telescope have provided an insight into the obscured regime of dust surrounding star-forming regions. IR luminosity in extragalactic sources is mainly produced by (i) the photospheric emission from stars, (ii) synchrotron emission from relativistic electrons spiralling in the source's magnetic field, and (iii) emission by dust heated by other luminous sources (Soifer, Neugebauer, & Houck 1987). However, in most external galaxies dust heated by various radiation field dominates the mid and far IR emission.

1.3.3 Optical spectra

The optical integrated galaxy spectrum is the 'mean' energy distribution of the most dominant stellar population in the galaxy. A unique aspect of a galaxy spectrum is the presence of forbidden (also known as 'nebular') lines. These emission lines acquire their name historically from their occurrence in the spectra of planetary nebulae. At the time of their discovery in the mid-nineteenth century (Huggins & Miller 1864), they were thought to represent an undiscov-

ered light-weight element called 'Nebulium'. It was only after five decades that Bowen (1927) discovered that the 'chief nebular line' at 5007 Å ([O III]) originates from the doubly ionized atoms of normal Oxygen. Soon after, several other lines from the non-terrestrial transitions of H, He, C, N and O were also discovered (e.g. Bowen 1928). The major reason for these transitions being 'forbidden' on earth is the presence of high particle density ($\sim 10^8$ cm^{-3}) as compared to the atmosphere of (for instance) a gas nebula. Forbidden transitions are produced as a result of electron jumps from a metastable state[2].

Even in extreme cases in the high density terrestrial environments, the impact time (time gap between consecutive collisions with walls or other particles) for an electron is $\lesssim 10^{-3}$ seconds so the electron does not get time to emit a photon. But in environments such as that of a nebula, the average time between two successive collisions suffered by an electron is estimated to be of the order of $10-10^4$ seconds, and an electron excited into such a metastable state gets ample time to spontaneously return to the ground state. Hence, the forbidden transitions are actually 'delayed radiations'.

Although every line present in a spectrum tells a tale of its origin, the basic characterisation of a galaxy can broadly be made on the basis of certain major signatures. We give below a brief account of some of these features in the optical spectrum of a galaxy, and their role in probing galaxy evolution:

Hydrogen lines

Being the simplest and the most abundant species known so far, hydrogen holds a special position for our understanding of galaxy spectra. Furthermore, three of its Balmer series lines at 6563 Å (Hα), 4861 Å (Hβ) and 4300 Å (Hγ) respectively are prominent in the visible range of the spectrum. These emission lines occur when an electron excited to an energy level ≥ 3 recombines with a hydrogen ion. Electrons can be excited to such high energy levels by three

[2] A state is metastable when its mean lifetime before spontaneous emission is very long.

main processes: (i) ionising radiation from hot (mainly O and B) stars, (ii) presence of an AGN, and occasionally, (iii) shock waves emerging from interactions with neighbouring galaxies (the discussion below is concentrated on the most probable case of photoionisation).

The presence of prominent Hydrogen lines, especially Hα are indicative of massive young stars and/or an AGN in a galaxy. The Balmer lines emerge from regions of the galaxy rich in ionised hydrogen where the excited electrons in the gas are cascading to the ground state following their capture by a proton. Such regions are called H II regions. The probability of any particular transition occurring in a gas under given physical conditions is dictated by the atomic constants, and hence the relative intensities of emerging lines can be calculated. This leads to the 'Balmer decrement', the ratios of the intensities of the Balmer lines, where Hα is the strongest line, Hβ is weaker, Hγ is weaker still, and so on. Under typical conditions in nebulae, these ratios are Hα/H$\beta = 2.86$ and Hβ/H$\gamma = 0.47$ respectively at low optical depth (Osterbrock & Ferland 1989).

Observationally the Balmer decrement is found to be much higher than that predicted by theory. This discrepancy is attributed to the absorption of light by dust. Since dust absorbs blue light more than red, the fraction of Hβ photons that are absorbed is more than the relatively redder Hα photons. This conjecture can be tested by comparing the observed and predicted Hβ/Hγ ratio. Hence, Balmer decrement measure is a popular means of quantifying dust extinction.

Oxygen and other metals[3]

Despite its low abundance in the cosmos, emission-lines of oxygen (mostly forbidden) are of great importance in studying galaxy evolution because unlike H and He, the most common Oxygen ions such as [O II] and [O III] have energy levels with excitation potentials of the order of kT. Hence, Oxygen ions are one of the best candidates to serve as collisionally excited coolants for radiative cooling in order to maintain thermal equilibrium. Moreover, the [O II]

[3]The quantities mentioned in this section are taken from Osterbrock & Ferland (1989) unless stated otherwise.

lines at 3726, 3729 Å and [O III] lines at 4959, 5007 Å respectively lie in the visible region of the spectra and therefore are easily detectable in the absence of large amount of extinction. The equivalent width (EW) of [O II] line varies from 0-4 Å in E/S0s to up to 200 Å in spirals and irregular galaxies. It is commonly used to quantify the SFR, for instance, using the following relation by Kennicutt (1998a):

$$SFR(M_{\odot}yr^{-1}) = (1.4 \pm 0.4) \times 10^{-41} L[OII]\ erg\ s^{-1} \tag{1.2}$$

[O III] (also [N II] with similar atomic configuration) is one of the few ions which emit lines from different upper levels with considerably different excitation energies, making it useful for measuring the temperature of the gas in low density ($< 10^4$ cm^{-3}) gas. The [O III] line intensity ratio $(\lambda 4959 + \lambda 5007)/\lambda 4363$ is considered to be a robust measure of the nebular gas temperature. Besides this, the [S III] intensity ratio $(\lambda 9531 + \lambda 9069)/\lambda 6312$, [Ne III] $(\lambda 3869 + \lambda 3968)/\lambda 3343$, and even [O II]/[S II] are used as temperature indicators.

The closeness of the two energy levels of [O II] (3726 Å & 3729 Å) makes it useful for probing the electron density of the nebular gas. For this purpose, an ion is required to emit lines from two different levels having similar excitation potentials, so that the relative excitation rates to the two levels depend only on the ratio of the collisional strengths. Further, assuming that these levels will have different radiative transition probabilities (or different collisional deexcitation rates), the relative populations of the two states will depend upon the electron density which can then be measured from the ratio of intensities of the lines emitted by the two levels. [S II]$\lambda 6716/\lambda 6731$ is another ratio widely used for the same.

Lately, the [O III] nebular lines have been extensively employed to study the nuclear emission from the AGN host galaxies. Most of the gas in these objects seems to be photoionised by hot stars in the galactic nucleus. A small fraction of spiral galaxies have also been found to have an extremely bright nucleus with ionised gas at the centre, showing a wide range of ionisations

in its emission spectrum, the so called 'Seyfert galaxies'. According to the currently popular theory, the source of ionisation in an AGN is the accretion disc surrounding the central Supermassive Black Hole (SMBH) or the relativistic particles in the magnetic field present in the immediate vicinity of the black hole. The ionisation of neutral Oxygen to [O II] occurs at a temperature of $\sim 30,000$ K, while to [O III] might only occur around $90,000$ K. Hence [O III]/Hβ emission line ratio much larger than Hα/[N II] ratio (Baldwin, Phillips & Terlevich 1981) in a galaxy spectra is a critical optical indicator of the presence of an AGN. Some AGN, known as Seyfert I galaxies are distinguishable by characteristic broad emission lines in their spectra. The forbidden doublet of [S II] at 6716 and 6731 Å and [N II] at 6548 and 6583 Å respectively are also generally prominent in an AGN spectra.

Amongst other features significant with respect to the study of galaxy spectra are the Ca II doublet at 3935 and 3970 Å respectively (generally called the H+K following the Fraunhoffer nomenclature from the solar spectrum), and the UV emission line of Mg II at 2800 Å (mostly significant in QSOs and quasars). As mentioned before, emission lines are also helpful in interpreting the major stellar population dominating the spectrum. For instance, a typical Sc galaxy has a mean spectral type of F to G-K stars with the blue part of the spectrum being dominated by the Balmer emission lines of Hydrogen.

Lick indices

Lick/IDS indices are a set of 21 absorption-line features observed over a period of 12 years in a set of 460 stars at the Lick Observatory (Worthey et al. 1994). These indices are good indicators of metallicity for the old stellar populations. Lick indices measure six different molecular bands (CN4150, G band (centred at 4300 Å), MgH+Mg b and two TiO bands) along with 14 different blends of atomic absorption lines in the wavelength range of 4000-6000 Å. Different indices are useful for probing different stellar populations in galaxies; for instance, Ca4227 is metallicity-sensitive especially in dwarfs, while the Fe4668, also a highly sensitive metallicity indicator

gets major contributions from Mg, Cr, C_2 and Ti, along with Fe, which makes it useful to study the evolution of all types of galaxies. The G band around 4300 Å represent the population of relatively cooler sun type stars.

The 4000 Å and Balmer break

The 4000 Å-break is a characteristic feature of the old, metal rich stellar populations. It arises due to an accumulation of absorption lines mainly from the ionised metals in a narrow wavelength range. This causes a sudden 'break' in the spectral continuum around 4000 Å. As the mean temperature of stars decreases, opacity increases, and hence the 4000 Å-break becomes larger in older, more evolved stellar populations. This makes the 4000 Å-break a powerful tool to quantify the mean age of the galaxy (or of the youngest dominant stellar population therein).

The Balmer break (3646 Å), on the other hand, marks the termination of the Hydrogen Balmer series. Since Balmer lines are found to be the strongest in Hydrogen-rich A-type stars, a strong Balmer break in a galaxy spectrum implies the dominating presence of intermediate age stellar populations (0.3–1 Gyr old).

Although these two features are often treated as one while analysing galaxy spectra due to their overlapping positions, it must be taken into account that they arise from very different phenomenon, and behave differently for different compositions of stellar populations.

The Lyman break

Lyman break is denoted by the lower wavelength limit (912 Å) of the Lyman series of Hydrogen lines. This feature was first exploited by Steidel & Hamilton (1992) to discover star-forming galaxies at $z = 3.4$. The Lyman break galaxies are generally selected by doing deep imaging in at least three broadband filters (e.g. u, g, r). The star-forming galaxies at high redshifts are either very faint or invisible in the u-band but are detected in g and r because u filter is very sensitive to flux emitted from the blue side of the Lyman limit in the rest frame of the galaxy

at high redshifts. By definition of Lyman limit, the photons having wavelengths shortward of 912 Å can ionise neutral Hydrogen and hence are most likely to be absorbed. Also, not many stars in a galaxy can produce photons of such high energies, making it a rare phenomenon.

The Lyman Alpha forest

This feature visible strongly in spectra of galaxies at high redshift, arises due to the presence of gas clouds between the object and the observer. When a strong Ly_α line is emitted by (say) a quasar, it gets absorbed by the gas clouds which then re-emit it. As a result, the line gets slightly blue shifted. This procedure is repeated several times, as there would be several such clouds present, and hence what we see in the spectrum is a dense cluster of emission lines or a 'forest'. Most of the clouds contributing to this dense array of emission lines are less massive than dwarf galaxies, and hence can only be detected indirectly through spectral analysis of the Lyman Alpha forest, thus providing an insight into the density fluctuations in the Universe on the smallest observable scales.

1.3.4 Ultraviolet imaging

The infrared and radio tracers indirectly measure the recent SFR of galaxies based on the impact of the surrounding media on the UV photons emitted by massive stars. The UV light ($1200-3200$ Å) by contrast provides a direct measure of star formation in a galaxy over timescales of less than 10 Myr to ≥ 1 Gyr. Even though dust extinction is a major limitation to UV analysis of galaxy light, together with the information derived from other wavelength regimes it can well constrain the global SFR (Salim et al. 2005) and stellar-to-dust mass ratio (da Cunha et al. 2010) of the galaxies.

Buat et al. (2005) compare the dust attenuation properties of near UV ($1750-2750$ Å) and FIR (60μm) selected sources to provide new constraints for the spectral energy distribution of the star-forming galaxies. Elsewhere (Salim et al. 2005), the UV luminosity is used to estimate

the optical depth of extinction, and to derive the relationship between the galaxy mass and the probability of a recent starburst. Salim et al. (2005) found that only 5% of 10^{11} $M_\odot$ galaxies are likely to have experienced a burst of star formation in last Gyr, as compared to 20% of galaxies with mass $\sim 10^8$ $M_\odot$. The dependence of SFR on the mass of a galaxy is discussed further in §1.4.2.

1.4 Variation in star formation

The evolution of a galaxy is influenced by several internal and external processes such as feedback from nuclear activity, supernovae mass ejection, stellar winds and star formation. Amongst these, star formation, though very poorly understood, undoubtedly is one of the key drivers of galaxy evolution and the backbone of all present day galaxy formation theories. In conjunction with the knowledge of gas mass and environment, the knowledge of star formation in a galaxy not only provides an insight into its history, but can also be used to predict the evolution path adopted by the galaxy.

1.4.1 SFR and gas mass

Stars form from cold gas, which mostly inhabits the disc in late-type galaxies. Over the years technology has equipped us to measure precisely the amount of star-forming gas in a galaxy. Together with the knowledge of the current SFR, this allows us to foretell the amount of stars that will be formed by a galaxy, assuming that it will consume all the gas in the process at a steady pace. The global relation between the gas surface density and SFR surface density of galaxies was first found for our own galaxy in the pioneering study by Schmidt (1959). By studying the distribution of H I and stars normal to the galactic plane, Schmidt derived a power law of index 1.4 ± 0.15. Sanduleak (1969) and Hartwick (1971) were the first to measure the Schmidt law in external galaxies. Since then, the Schmidt like power law formalism has been

confirmed down to sub-kpc scale (e.g. Bigiel et al. 2008) for the relation between SFR density and atomic, molecular, or total gas surface density. The power law index in various studies range from 1-3. This large range suggests that either the process of star formation does not obey a universal law, or it is very sensitive to systematic methodologies involved such as the star formation tracer and variations in the considered sample.

Recently, Bigiel et al. (2008) have studied the relation between SFR, H II, and H I from pixel-to-pixel in 18 nearby galaxies. They found a Schmidt like power law with index 1.0 ± 0.2 for SFR and H II density for disc averaged values as well as in radial bins and by considering different star formation tracers. But most of their galaxies show little or no correlation between Σ_{SFR} and Σ_{HI}, resulting in large scatter in the star formation efficiency (SFE = $\Sigma_{SFR}/\Sigma_{gas}$) values across the sample, and within each galaxy. In spiral galaxies which have centres dominated by dense H II gas and H I spanning the outskirts, the SFE is found to be a function of radius (Bigiel et al. 2008; Leroy et al. 2008). It has also been suggested that the radial decline of the SFE is related to the dependence of the formation of the GMCs on environment (Leroy et al. 2008). Using a sample of 23 nearby galaxies, Leroy et al. (2008) found that the radial decline in the SFE is too steep to be produced by an increase in the free-fall time (t_{ff}) or orbital time alone. They also found that the atomic-to-molecular gas ratio is a function of radius, stellar surface density, and pressure in galaxies with H II to H I dominated ISM.

Several scenarios have been suggested in literature that may produce the Schmidt like power law with an index of 1–3. For instance, if gravitational instabilities in the ISM (H I+H II) are a key ingredient for initiating star formation, the SFR may depend upon the free fall time, t_{ff} of the total gas. Assuming that the gas scale height is constant, $t_{ff} \propto \Sigma_{gas}^{-0.5}$ or power law index, $n \sim 1.5$ (e.g. Madore 1977). Silk (1997) and Elmegreen (1997) suggested other generic scenarios where the Schmidt law of the form $\Sigma_{SFR} \propto \Sigma_{gas}^{n}$, with $n \sim 1.5$ could be produced by a scaling relation between the SFR density and the ratio of the gas density to the local dynamical

time scale.

$$\Sigma_{SFR} \propto \frac{\Sigma_{gas}}{\tau_{dyn}} \propto \Sigma_{gas}\Omega_{gas} \tag{1.3}$$

where τ is the local orbital timescale of the disc and Ω is the angular rotation speed. Kennicutt (1998b) tested this scenario using a sample of normal disc galaxies. He defined τ_{dyn} as 2πRV(R) = Rπ/Ω(R), the orbit time at the outer radius R of the star-forming region in the galaxy, and found the relation to be tighter than the Schmidt law itself.

The realisation of the fact that most of the ICM in our galaxy is in the form of GMCs revolutionised the study of the SFR and evolution of galaxies. It has been shown that the FIR luminosity (a proxy for SFR) of galaxies linearly correlates with the global HCN line (a measure of the dense molecular gas) over three orders of galaxy luminosity on a logarithmic scale (Gao & Solomon 2004). However, the $L_{IR} - L_{CO}$ relation is non-linear (Solomon et al. 1997; Gao & Solomon 2004), implying that the star formation traced by IR luminosity in a galaxy is proportional to the dense molecular gas traced by HCN, and not the total amount of molecular gas traced by CO (Gao & Solomon 2004). Recently, small number of observations have also been made in other molecular bands such as HCO^+, HCN, CN, HNC and CS (e.g. Gracià-Carpio et al. 2008), but a global SFR-molecular gas density relation from such estimates requires more work.

It yet remains to be seen whether the Schmidt law is an entirely molecular phenomenon or not. Since stars form in molecular gas, intuitively it seems obvious that the relation between the Σ_{SFR} and Σ_{HII} should be tighter than that between Σ_{SFR} and Σ_{HI} or the total amount of gas in a galaxy. For the time being literature seems divided on the issue (e.g. Kennicutt 1998b), providing motivation for future facilities such as *ALMA*[4].

[4]Atacama Large Millimeter/Submillimeter Array

1.4.2 Star formation and galaxy mass

Galaxy morphologies and SFE are known to correlate well with their mass. The passively evolving, bulge-dominated galaxies are much more massive than the star-forming, disc-dominated galaxies. There appears to be a sharp bimodality in galaxy properties that occur around a critical stellar mass of $M^* \sim 3 \times 10^{10}$ $M_\odot$ (Kauffmann et al. 2003a; Kauffmann et al. 2003b). The bimodality seems to originate from different efficiency with which gas is converted to stars in galaxies with different masses, as governed by the fundamental laws (Schmidt 1959; Kennicutt 1998a) of star formation. In the local Universe ($z \lesssim 0.1$), around 50% of the total star formation takes place in galaxies with $M^* > 2 \times 10^{10}$ $M_\odot$ and $> 90\%$ at $M^* > 10^9$ $M_\odot$ (Brinchmann et al. 2004).

Some studies suggest that the difference between the properties of giant and dwarf galaxies arises because the massive galaxies are capable of consuming all their gas in a single short (~ 2 Gyr) burst at high redshifts ($z \gtrsim 2$), while the dwarf galaxies continue to form stars on timescales comparable to a Hubble time (van Zee 2001; Brinchmann et al. 2004). For SDSS galaxies ($z \sim 0.1$) Brinchmann et al. (2004) (their fig. 22) found that the fraction of galaxies that are likely to have experienced a starburst in the recent past ($\lesssim 1$ Gyr) declines steeply with M^*. They suggested this to be a consequence of lower gas fraction in more massive galaxies and/or that the periods of intense starburst are shorter in more massive galaxies.

Recently some work has also been done to connect the atomic and molecular gas content of galaxies and the SFE to their environment. For a sample of nearby galaxies Bothwell, Kennicutt, & Lee (2009) showed that lower SFE in massive galaxies is mirrored by the lack of their H I content, suggesting that more massive galaxies ($M^* \geq 3 \times 10^{10}$ $M_\odot$) have lower SFRs due to a lack of gas supply. However, they also notice that the observed broad distribution of SFEs for dwarf galaxies is independent of their gas content. Thus, these results favour a dominance of mass dependent quenching mechanisms in galaxy evolution.

Elsewhere (Noeske et al. 2007), in a study of coevolution of SFR and M^* in field galaxies

($0 \leq \mathrm{z} \leq 1.1$), a mass-dependent gas exhaustion model has been presented. Noeske et al. found that the average specific SFR (SFR/M^* or SSFR) increase towards lower M^* at all redshifts. In the light of their findings they suggested a scenario where the redshift of major star-formation event, $SF(\mathrm{z_f})$ decreases with the mass of galaxy (also see Feulner et al. 2005). Similar trends have also been observed for galaxies at low redshift (Brinchmann et al. 2004).

Since most of the massive galaxies are passive, and most galaxies in the cores of clusters are passive, it is very difficult to isolate the effect of environment and mass on galaxy properties. But aided by the large sky surveys, some recent attempts have been made to do this. By studying $> 27,000$ galaxies from the SDSS DR4 ($0.005 \leq \mathrm{z} \leq 0.037$), Haines et al. (2007) found that the star formation histories of giant galaxies ($M^* \geq 10^{10.5}$ $\mathrm{M}_\odot$; $M_r \leq -20.5$) are driven by the initial conditions during their formation, while dwarf galaxies ($M^* \sim 10^{9.2}$ $\mathrm{M}_\odot$; $M_r \sim -18.0$) are governed by their local environment. Their most intriguing result is that none of the ~ 600 dwarf galaxies ($-18 \leq M_r \leq -16$) found in the lowest density regions were found to be passive (EW(Hα) < 2 Å). The complete absence of passive dwarfs outside twice the virial radius of the clusters may indicate that the cluster related processes (see §1.2.1) play an important role in the evolution of low-mass galaxies (Haines et al. 2007; Mahajan, Haines & Raychaudhury 2010; Mahajan, Haines, & Raychaudhury 2011a).

1.4.3 The morphology-density relation

Colour and morphology of galaxies are the fundamental physical characteristics of a galaxy. In his pioneering work, Dressler (1980) studied the morphology of galaxies in 55 rich clusters to show that while the elliptical galaxy population increases as a function of projected galaxy density (Σ_{10}), the population of spirals decreases. The population of S0 galaxies in these clusters also increased towards the higher densities but had a different distribution with respect to the ellipticals, indicating a different formation and/or evolution mechanism relative to the elliptical galaxies.

This 'Morphology-Density' relation has since been interpreted by some as a manifestation of the SFR-density relation, while others have argued in favour of different environmental mechanisms that morphologically modify an infalling galaxy and those that quench star formation in it. Also, since massive galaxies are mostly early-type galaxies residing in dense cores of galaxy clusters, it is difficult to disentangle the impact of environment and galaxy mass on the trends observed in galaxy properties. By studying galaxy clusters at z $= 0$ and 0.8 Vulcani et al. (2011) find that around 40% of M^* at both redshifts is in elliptical galaxies but $\sim$ 43% M^* is in S0 galaxies at z $= 0$ but in late-type galaxies at higher redshifts. Their analysis suggests that environment may be critical in changing the mass function of late-type galaxies through morphological transformations.

Several studies have now shown that although flatter than that observed at z $= 0$, the morphology-density relation for luminosity-selected, volume-limited samples of galaxies was in place at z ~ 1 (Postman et al. 2005; Capak et al. 2007; Tasca et al. 2009). Moreover, the morphology-density relation at all redshifts is strongest for the brightest galaxies (Tasca et al. 2009). But for a stellar-mass selected, volume-limited sample Tasca et al. found that the morphology-density relation is $\sim 3\sigma$ significant for galaxies with $M^* < 10^{10.6}$ $M_\odot$, but the morphology of massive galaxies is independent of their environment at z < 1. These results suggest that factors responsible for defining the morphology of massive galaxies are independent of environment, or, the morphological type of such galaxies is determined when they are formed. On the other hand, the morphology of dwarf galaxies just like their other properties is very much environment dependent.

1.4.4 Star formation and galaxy dynamics

The evolutionary status of a galaxy in a cluster can be defined by the velocity fields prevalent in the cluster and its vicinity. Literature suggests that galaxy properties such as luminosity (Chincarini & Rood 1977; Struble ; Bothun & Schombert 1990; Biviano et al. 1992), morphology (de

Vaucouleurs ; Sandage & Tammann 1976; Moss & Dickens ; Helou, Salpeter, & Krumm 1979; Sodre et al. 1989; Biviano et al. 1992; Girardi et al. 2003) and spectral emission lines (Biviano et al. 1997; Pimbblet, Drinkwater & Hawkrigg 2004) vary between galaxies having different velocities relative to the cluster: the early-type, massive and passive galaxies are found to have lower velocity dispersion relative to their late-type, star-forming counterparts.

An interesting case of velocity segregation in the star formation properties of galaxies arises for the *backsplash* galaxies (Gill, Knebe & Gibson 2005). These galaxies have already crossed the cluster core at least once, but are currently observed close to its periphery. Such galaxies are not expected to be found too far out from the cluster's virial radius (Mamon et al. 2004). Since these galaxies have already experienced cluster's hostile environment, they are expected to display properties similar to the virialized galaxy population in the cluster. But because they appear on the cluster's periphery with the galaxies that are currently falling into the cluster and having their star formation quenched, a clear distinction between the backsplash and infalling galaxies becomes very difficult. Nevertheless, some recent attempts have been made to segregate the two populations using observables such as luminosity in simulations (Knebe et al. 2010), and sSFR in observational data (Pimbblet 2010).

1.5 Nuclear activity and star formation

In the context of quantifying SFR, the physical interpretation of the spectroscopic data for galaxies becomes complicated in the light of the knowledge that the ionising radiation could also be emitted by an active galactic nucleus (AGN) over most of the wavelength range. At optical wavelengths the line-ratio diagnostic, more popularly known as the BPT diagram (Baldwin, Phillips & Terlevich 1981), could be used to distinguish between the 'real' star-forming galaxies and those with emission contaminated by an AGN. This diagram makes use of the Balmer lines Hα and Hβ and nebular emission lines [O III] and [N II] (see Figure3.2).

Lately it has been shown that bursts of star formation mostly occur in the circumnuclear region of a galaxy (Popescu et al. 2005; Prescott et al. 2007). An interesting question then is whether AGN support star formation or quench it. Reichard et al. (2009) found a relatively strong correlation between the youth of stellar population and the growth rate of the black hole[5] but a weak correlation of either of these with the morphological asymmetry of the galaxy. Based on these results derived from the SDSS data, Reichard et al. suggested that the presence of cold gas in the central kpc region of the galaxy is a necessary but insufficient condition for continuous fuelling of the black hole, and therefore processes other than those responsible for driving the cold gas to the centre of the galaxy (such as interactions with neighbouring galaxies) must be required to deliver that gas to the black hole.

Chen et al. (2009) showed that the SFR/M^* in the central $\sim 1-2$ kpc region of local ($0.03 \leq \mathrm{z} \leq 0.08$) AGN correlate well with the Eddington ratio[6] of their supermassive black hole. Studies of this genre are exploring the role of supernovae driven winds originating from the starburst in the circumnuclear region in driving the gas to the central engine for the growth of black hole (Davies et al. 2007; Chen et al. 2009). Schawinski et al. (2009) found that optical colour $(g-r)$ of x-ray selected AGN galaxies is in the intermediate range between the red sequence and the blue galaxies, implying that the episode of active star formation in these galaxies ended ~ 100 Myr ago. This can be explained by two scenarios, either the AGN are very long-lived, continuing accretion for around a Gyr, or there is a time delay of ~ 100 Myr between the end of the starburst and detectable accretion by the central black hole. For the present day estimates of the AGN lifetimes, the former seems unlikely, leading Schawinski et al. to suggest that the low-luminosity ($\sim 10^{44}$ erg s^{-1}) AGN may be responsible for shutting off star formation in these galaxies (also see Chen et al. 2009; Rogers et al. 2009). The mass ejecta from the winds generated by OB associations have very high velocities and hence low accretion

[5]The studies mentioned in this section measure the black hole growth rate from the extinction corrected [O III] luminosity, unless stated otherwise.

[6]Eddington ratio quantifies the strength of an AGN. It is measured as the bolometric luminosity in units of the Eddington luminosity, i.e. $\lambda = L_{\odot}/L_{Edd}$; where, $L_{Edd} = 1.38 \times 10^{38}$ erg s^{-1}.

efficiency onto the black hole, but AGB stars can drive winds with low velocities, and hence have high accretion efficiency (Davies et al. 2007). This scenario is also in agreement with the observed delay of 10–300 Myr between the onset of AGN and termination of the circumnuclear starburst (Koulouridis et al. 2006; Davies et al. 2007; Schawinski et al. 2009).

Intuitively it seems plausible that if interactions/mergers lead to the inflow of gas to the centre of the galaxy igniting a nuclear starburst, this gas may then also fuel the black hole. But to test such ideas high quality, spatially well resolved imaging and/or spectroscopic data are required. From very deep NIR observations of the central 100–300 pc regions of a sample of nine galaxies, Davies et al. (2005) found no evidence to support a difference between the dominant mechanism leading to the excitation of gas in the nuclear and circumnuclear regions.

Li et al. (2008) attempted to distinguish between the star formation in the nuclear region of AGN host galaxies caused due to gas accretion on the black hole from that due to the inflow of gas because of tidal interactions with a companion galaxy. They found that star formation in AGN with a close companion is enhanced in similar way as in their non-AGN counterparts, suggesting that the accretion of gas onto the central black hole and nuclear star formation triggered due to other mechanisms (such as galaxy-galaxy interactions) are distinct events. By studying close pairs (< 30 kpc apart and within 500 kms^{-1} of each other) of early-type galaxies from the SDSS, Rogers et al. (2009) found that with respect to a control sample of early-type galaxies, the recent star formation in close pairs is increased. They also found that the AGN luminosity increased with decreasing pair separation, thus supporting the scenario whereby the first stage of galaxy-galaxy interaction triggers star formation, followed by a more efficient inflow towards the centre, which feeds the black hole and eventually turn on the AGN thereby quenching star formation in the host galaxy.

So, the issue is currently debatable in literature and it yet needs to be seen whether the triggering of AGN activity in a galaxy depends on its environment, and what impact does it have on the interplay between environment and the process of star formation in it.

1.6 Evolution of star formation rate

All observables of galaxies evolve over time and are influenced by the immediate and global environment of the galaxy. Galaxies in the past were more star-forming (e.g. Madau et al. 1996; Bouwens et al. 2010), bluer (Butcher & Oemler 1984), and statistically, smaller (e.g. Bouwens et al. 2004) and less regular. These observational inferences have been drawn by studies conducted over decades, but some aspects of the trends seen in the evolution of galaxies are still being debated. In this section we discuss some such trends and their contradictory aspects.

1.6.1 Cosmic evolution of the SFR density

It is inevitable that the galaxies in the past were more actively forming stars than their present day counterparts. The reason could be the high SFE of galaxies in the past (see §1.4.2), or, if the monolithic collapse scenario as suggested by some is true, the present day cluster galaxies formed in a single major star formation event at high redshift ($z \gtrsim 2$). But whatever the cause, literature seems to agree that the SFR density of the galaxies in the Universe has been progressively declining since $z \sim 2$ (Fig. 1.3; also see for instance Bouwens et al. 2010 and references therein). The first insight into this evolutionary trend in the star formation history of the Universe was provided by the pioneering work of Madau et al. (1996). Since then, several attempts have been made to interpret and improve this well known redshift vs SFR density relation (assuming a particular cosmological model), often called the 'Madau plot' or the 'Madau-Lilly plot', following the additional efforts put in by Lilly et al. (1996) in correcting the SFR density values for extinction. The Madau plot (Madau et al. 1996) shows that the star formation history of the Universe peaked at $1 \leq z \lesssim 2$ and has been declining since (Madau et al. 1996; Lilly et al. 1996; Steidel et al. 1999; Trentham et al. 1999; Hopkins 2004; Bouwens et al. 2010).

A key issue of concern with such an interpretation that remains is that the evolutionary trend

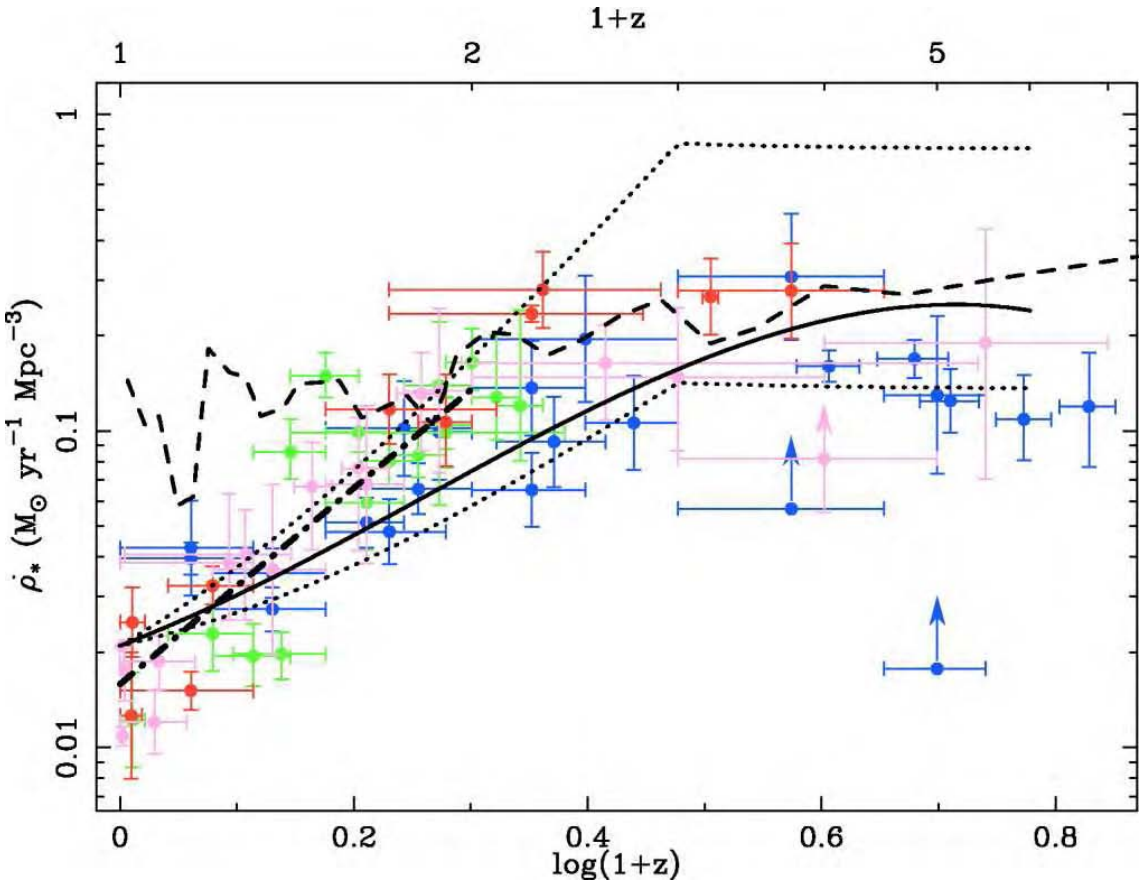

Figure 1.3: This figure shows the evolution of SFR density with redshift, using a common obscuration correction where necessary. The points are color-coded by rest-frame wavelength as follows: Blue: UV; green: [O II]; red: Hα and H$_\beta$; pink: x-ray, FIR, submillimeter, and radio. The solid line shows the evolving 1.4 GHz luminosity function (LF) derived by Haarsma et al. (2000). The dot-dashed line shows the least-squares fit to all the z < 1 data points, $\log(*) = 3.10\log(1+z) - 1.80$. The dotted lines show pure luminosity evolution for the Condon (1989) 1.4 GHz LF, at rates of Q $= 2.5$ (lower dotted line) and Q $= 4.1$ (upper dotted line). The dashed line shows the "fossil" record from Local Group galaxies (Hopkins, Irwin, & Connolly 2001). (image credit: Hopkins 2004)

has at least two distinct aspects to it, one, determined by the optical observations (as done by Madau et al. 1996) and the other that is being explored by the recent IR and UV observations (e.g. Steidel et al. 1999; Trentham et al. 1999; Bouwens et al. 2010). In other words, the consistency of large-scale flux-limited surveys to determine the SFR density at all redshifts must be taken into account while interpreting a Madau like plot of evolution in the SFR of galaxies.

In order to understand the general picture of SFR density evolution, several cautions are necessitated. For instance, it is possible that at the present epoch a major contribution to the SFR density from a non-negligible fraction of galaxies are ignored because they are insignificant in optical light but very bright in the IR (e.g. Arp 220), although some studies (Trentham et al. 1999) report otherwise. Another caution that should be considered when interpreting this result is that we observe only the brightest starburst galaxies at the farthest distances conceivable. Such a generalisation of a special class of objects at any epoch thus require very precise modelling and careful statistical corrections. Presently these are mostly sourced from simulations and/or by extrapolating the local empirical relations.

Hopkins (2004) (also see Bouwens et al. 2010) presented an extensive compilation of SFR density measurements as a function of redshift from literature (Fig. 1.3). These data have been converted to a consistent set of SFR calibrations, common cosmology, and consistent dust obscuration corrections where necessary. Hopkins (2004) show that by combining the constraints from the global SFR density evolution with those from the 1.4 GHz radio source counts at sub-millijansky levels, the well known degeneracy between the luminosity evolution [$L \propto (1+\mathrm{z})^{\mathrm{Q}}$] and density evolution [$\phi \propto (1+\mathrm{z})^{\mathrm{P}}$] of star-forming galaxies can be broken. For a concordance cosmology from these combined constraints, Hopkins (2004) found a preferred evolution model with $Q = 2.70 \pm 0.60, P = 0.15 \pm 0.60$.

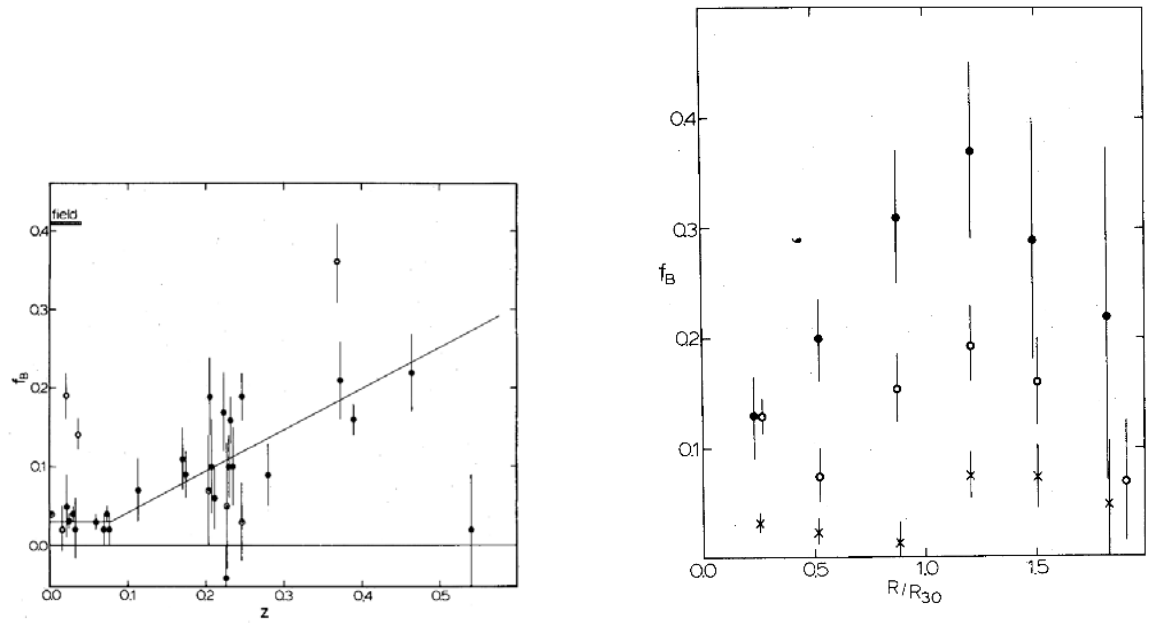

Figure 1.4: *(left)* The fraction of blue galaxies (f_B) for galaxy clusters at different redshifts. This evolutionary trend, i.e. clusters in the past had a higher fraction of blue galaxies as compared to their low redshift counterparts, first seen in the legendary work of Butcher & Oemler (1984) came to be known as the 'Butcher-Oemler effect'.
(right) Butcher & Oemler (1984) further showed the radial dependence of the blue-fraction in nearby clusters (*crosses*), and those at intermediate (*open circles*) and high redshift (*filled circle*). Within $2R_{30}$ ($\sim 1.5\,h_{70}^{-1}$ Mpc for Abell clusters), they found that f_B increases outward from the cluster core at all redshifts. (image credit: Butcher & Oemler 1984)

1.6.2 The Butcher-Oemler effect

Amongst trends of galaxy evolution, the one discovered by Butcher & Oemler (1984) (Fig. 1.4; also see Butcher & Oemler 1978) is the most intriguing and still controversial in literature. Butcher & Oemler found that the galaxy clusters at $\mathrm{z} \sim 0.2$ have an excess of blue galaxies as compared to their low redshift counterparts. Butcher & Oemler estimated the blue fraction within a cluster-centric radius of R_{30}, i.e. the radius containing 30% of the cluster's red sequence galaxies ($M_V < -20$; $\mathrm{H}_0 = 50$ km s^{-1} Mpc^{-1}). This so called 'Butcher-Oemler effect' has since been explored for various samples of galaxies and using other galaxy properties such as morphology (Goto et al. 2003b), stellar mass (De Propris et al. 2003) and IR emission (Haines et al. 2009).

Ellingson et al. (2001) and De Propris et al. (2004) use various multiples of cluster-centric radius, scaled with r_{200} to show the effect of chosen aperture size on the blue fraction (also see Fig. 1.4). Ellingson et al. (2001) suggest that the origin of the Butcher-Oemler effect lies in the fact that the relative fraction of 'blue' galaxies on the outskirts of clusters at higher redshifts is higher than in their local counterparts. Even though most of the above mentioned studies use optical spectra for most or all of their sample (except for Butcher & Oemler 1984), the spectroscopic information is used only for assigning cluster membership.

By studying MIR properties of galaxies in 30 massive galaxy clusters at $0.02 \leq \mathrm{z} \leq 0.40$, using *Spitzer*/MIPS 24μm and near-infrared data, Haines et al. (2009) found the best-fit redshift evolution model of the form $f_{SF} \propto (1+\mathrm{z})^{\mathrm{n}}$, where $n = 5.7^{+2.1}_{-1.8}$. They remarked that, statistically, this excess is associated with galaxies found at large cluster-centric radius, specifically $r_{500} < \mathrm{r} < \mathrm{r}_{200}$, implying that the MIR Butcher-Oemler effect can be attributed to a combination of the global decline in star formation in the Universe since $\mathrm{z} \sim 1$, and enhanced star formation in the infall regions of clusters at intermediate redshifts.

We discuss several other aspects of the Butcher-Oemler effect in context of the results derived in this thesis and their implications in the following chapters.

Chapter 2

Data used in this work

In this thesis we make use of data from UV to radio wavelengths sourced from various publicly available catalogues and archives. We give below a brief account of various datasets and data characteristics in increasing order of wavelength. In particular, I have sourced the optical SDSS data, and performed photometry on IRAC and *GALEX* UV data. The radio data for the Star Formation Reference Survey (SFRS) galaxies (Chapter 8) has been reduced by Prof. S.P. Willner (CfA), while Dr. M.L.N. Ashby (CfA) has compiled all other ancillary data for this dataset (see below). The IRAC data for SFRS galaxies has been reduced by Dr. M.L.N. Ashby (CfA) and other SFRS team members at the University of Western Ontario.

2.1 The ultraviolet data

The ultraviolet (UV) data used for SFRS (Chapter 8) are taken from data releases 4/5 and 6 of the *Galaxy Evolution EXplorer* (*GALEX*; Martin et al. 2005; Morrissey et al. 2005). *GALEX* is conducting an all-sky imaging survey along with targeted programs at two photometric bands: 1520 Å in far ultraviolet (FUV) and 2310 Å in the near ultraviolet (NUV). In Chapter 8 (SFRS) we studied the global star formation properties of a representative sample of FIR selected galaxies. the aim of this project was to understand the correlation between SFR measured at different

wavelengths. To do so we employed 1.4 GHz radio continuum, UV, FIR and MIR imaging data to measure global SFR for a representative sample of nearby star-forming galaxies. We cross-correlated the SFRS catalogue with the UV database, requiring to observe the galaxy in at least one band. Almost three quarters of the UV imaging data used in this paper were taken as a part of *GALEX*'s primary all sky survey (AIS) having an effective exposure time of ~ 0.1 ks, and the nearby galaxies survey (NGS) with an effective exposure time of ~ 1.5 ks. The remainder were observed as a part of other *GALEX* surveys as well as individual guest investigator programs. Since bulk of the SFRS sample is comprises nearby bright and big galaxies, we did not impose any exposure time or brightness limit for the matches. For the same reason, we did not impose any constraint on the location of galaxy in the 1.2 degree *GALEX* field of view even though the point spread function (PSF) varies across *GALEX* images, thus requiring non-negligible aperture corrections for faint sources detected away from the image centre. However, where possible, we chose to analyse images where the galaxy was closer to the centre of the field of view than towards its edges. Whenever a galaxy was observed as a part of more than one program we chose the deepest observations. These criteria resulted in a match for 332/369 (90%) galaxies. Three galaxies– NGC 2500, IRAS10120+1653 and IRAS10565+2448W were observed in NUV only. Q10120+1653, IRAS11102+3026 and IRAS16053+1836 are observed as a part of the AIS, and the low exposure times ($\lesssim 200$ s) have resulted in no detection in FUV.

Photometry and aperture correction

We derive the photometry using SEXTRACTOR (Bertin & Arnouts 1996). To do so, we first registered the two *GALEX* images and the four IRAC images using SWARP (Bertin et al. 2002). SWARP brings all six images to a common pixel size of $0\farcs867$ SEXTRACTOR is then run in dual mode, such that the apertures are selected on the 3.6μm IRAC image (see Sec. 2.3.1). The 3.6μm image is chosen for reference because this band is most sensitive to the star light of the galaxy. All images are visually inspected to check if tidal features visible in UV and/or IR were

included in estimating the total magnitudes, else the relevant processes as mentioned above were repeated.

Next we apply the extended-source correction to the obtained fluxes. Fig. 4 of Morrissey et al. (2007) shows that the aperture correction for apertures of radius $< 3.8''$ and $> 6''$ are approximately linear. Hence, following Fig. 4 of Morrissey et al. (2007) we bin our data into three sets with $r < 3.8'', 3.8'' - 6''$ and $> 6''$, where r is the half-light radius from the *2MASS* catalogue (§2.3.1). To the first set we apply a linear correction of the form $Ar + B$, where $A = -0.5608\,(-0.6521)$ and $B = 2.4912\,(3.0682)$ respectively in *FUV*(*NUV*). To the second set we apply the corrections suggested by Morrissey et al. (2007) for the $6''$ radius aperture. To the third set we apply the linear correction by approximating the curve of growth from $6''$ onwards such that $A = -0.0016\,(-0.0028)$ and $B = 0.14\,(0.2128)$ respectively for *FUV*(*NUV*). We compare the fluxes hence obtained with those presented in Dale et al. (2007) for six of our galaxies which overlap with the SINGS sample (Kennicutt et al. 2003) and find a perfect agreement within errors.

Galactic extinction

The dust in the Milky way attenuates the light from external galaxies. Amongst others, the amount of this extinction depends upon the galactic latitude of the external source. This foreground extinction becomes even more important in the UV wavebands. In order to take this into account we apply a correction of $A_{FUV} = 8.29E(B-V)$ and $A_{NUV} = 8.18E(B-V)$ (Seibert et al. 2005), where the colour excess $E(B-V)$ calculated using the dust reddening maps of Schlegel et al. (1998) is taken from the NASA Extra-galactic Database (NED)[1].

[1]http://nedwww.ipac.caltech.edu/

Internal extinction

The UV light emitted by young hot stars is absorbed by the dust enshrouding the star forming regions. The amount of this extinction not only varies from galaxy to galaxy, but also from one star forming region to another within the same galaxy. Recently, Boquien et al. (2009) analysed H II regions in eight nearby galaxies to show that the observed dispersion in dust attenuation of normal star-forming galaxies is likely due to a range of dust geometries and extinction curves. Some of it is also caused by potential dilution of the youngest stellar population by the relatively older populations formed in earlier unrelated bursts of star formation.

In this work we employ the IRX based empirical prescription provided by Buat et al. (2005) to correct for intrinsic dust extinction.

$$A_{FUV} = -0.0333p^3 + 0.3522p^2 + 1.1960p + 0.4967, \text{ and} \tag{2.1}$$

where, $p = Log(L_{FIR}/L_{FUV})$ (§2.3.1).

$$A_{NUV} = -0.0495q^3 + 0.4718q^2 + 0.8998q + 0.2269 \tag{2.2}$$

where, $q = Log(L_{FIR}/L_{NUV})$ (Sec. 2.3.1). This correction is based on the idea that the amount of UV light lost due to the absorption by dust can be known exactly by assuming that all the FIR light from the galaxy is the re-emission of the absorbed short wavelength light. However, as mentioned before this is not always the case because some FIR light also comes from the dust due to heating by older stars. In §8.4 we compare the IRX and IRXn[2] with extinction indicators at other wavelengths, as well as the classical spectroscopic extinction tracer, the balmer decrement.

[2]Throughout this work we use IRX to represent the ratio of fluxes FIR/FUV and IRXn for FIR/NUV

2.2 The Sloan Digital Sky Survey

The Sloan digital sky survey (SDSS) (York et al. 2000; Stoughton et al. 2002) is the largest photometric and spectroscopic survey covering π steradians (mainly) of the northern sky. The survey is done using a 120-megapixel CCD camera on the 2.5-m telescope at the Apache point observatory. This set-up maps 1.5 square degrees of sky at a time, in the drift-scan mode. We briefly describe some basic characteristics of the data below.

2.2.1 Photometric measurements

The photometry is done in five bands, u, g, r, i, z, with a pixel scale of $0\farcs396$ pixel^{-1}. The SDSS images have an exposure time of 53.9 s and the median PSF $= 1.4''$ in the $r-\mathrm{band}$. The astrometry is done with $< 0.1''$ rms absolute per coordinate. The faint limit of SDSS for photometry of a point source in the r-band is 22.2 mag.

We use the SDSS Petrosian magnitudes as a measure of the optical flux in the five bands (Blanton et al. 2001). In all bands the Petrosian magnitudes are calculated using the aperture set by the 'Petrosian radius'[3] in the r-band, thus providing consistent measurements. Theoretically, SDSS Petrosian magnitudes should recover all the flux for an exponential galaxy profile and about 80% of the flux for a de Vaucouleurs profile. Blanton et al. (2001) have shown that this fraction is fairly consistent with the axis ratio, but shows variations when galaxies become smaller. These magnitudes are k-corrected to $\mathrm{z}=0.1$ (median redshift of the sample, Yang et al. 2007). Unless stated otherwise, we only consider galaxies with absolute magnitude $M_r \leq -20.5$ (this corresponds to the apparent magnitude limit of $r \leq 17.77$ for the SDSS spectroscopic catalogue at the median redshift of our sample, $\mathrm{z}=0.1$).

[3]The 'Petrosian ratio' at a radius r from the centre of an object is defined to be the ratio of the local surface brightness in an annulus at r to the mean surface brightness within r (Blanton et al. 2001).

2.2.2 The spectroscopic catalogue

In the SDSS, spectroscopy is performed by employing 3″ fibres, and covers a wide wavelength range of 3800-9200 Å with a spectral resolution, R = $\lambda/\delta\lambda$ of 1850–2200. The spectroscopic targets for SDSS are automatically picked from the imaging catalogue using the algorithm described in Strauss et al. (2002). The main galaxy sample comprises galaxies brighter than 17.77 mag in the Petrosian r-band, and having Petrosian half-light surface brightness radius $\mu_r \leq 24.5$ mag arcsec^{-2}. At a median redshift of 0.104, these selection criterion select ~ 90 galaxy targets per square degree of the sky (Strauss et al. 2002). Around 6% of the selected targets could not be observed because they have a companion closer than $55''$, which is the minimum separation between the spectroscopic fibres (Strauss et al. 2002). The high signal-to-noise ratio (S/N ≥ 4 per pixel at $g = 20.2$) of the SDSS spectra ensures that redshifts for most of the sample are measured precisely, with a statistical error less than 30 km s^{-1} (Strauss et al. 2002).

For the spectral reduction, the spectrum fitting algorithm locates the emission lines to measure a redshift, and then all the possible emission lines are again compared to a list of emission lines. For latter, the line list is divided into three categories: lines that should be found in (i) QSOs, (ii) galaxies, and (iii) both, based on which the spectrum is then classified.

The derived data products from this spectroscopic catalogue are described in Appendix B.

2.3 *Spitzer*: Mid infrared data

2.3.1 IRAC data for SFRS

The Infrared Array Camera (IRAC) observations of most SFRS sources (Chapter 8) were carried out during Cycle 5 (PID 50128, PI G. Fazio) using standard observing parameters. Each of the 273 galaxies targeted by this project was observed with at least 6×12 s full-array exposures using a cycling dither and a medium dither scale factor. All sources were observed in both IRAC

fields of view, yielding a total exposure time of at least 72 s in each of the four IRAC bands at 3.6, 4.5, 5.8, and 8.0μm. All sources not included in PID 50128 had already been observed by other programs and the corresponding data were downloaded from the archive; these and the PID 50128 were reduced together in as homogeneous a manner as possible.

The basic IRAC data reduction was carried out by the SFRS team members at the University of Western Ontario and at the Harvard-Smithsonian Center for Astrophysics. In both instances it was based on the Basic Calibrated Data (BCD). The BCD frames were object-masked and median-stacked on a per-AOR basis; the resulting stacked images were visually inspected and subtracted from individual BCDs within each AOR. This was done to eliminate long-term residual images arising from prior observations of bright sources from the 3.6, 5.8, and 8.0μm BCD frames (the 4.5μm detector array did not suffer from residual images during *Spitzer*'s cryogenic mission); it also served to minimise gradients in the celestial background around each source.

After these preliminaries, the data for each galaxy were mosaiced into four spatially-registered mosaics using IRACproc (Schuster, Marengo & Patten 2006). IRACproc augments the capabilities of the standard IRAC reduction software (MOPEX). Photometry was carried out with SExtractor (ver. 2.5.0; Bertin & Arnouts 1996). Since our interest lies in global photometry and in particular in ensuring accurate global SEDs, we first registered all IRAC and *GALEX* mosaics (for which *GALEX* data were available, see below) to a common spatial scale using SWarp (version 2.17.1) and then applied SExtractor in two-image mode to photometer our galaxies. This was done because the IR and UV mosaics were found in many instances to have significant morphological differences; two-image mode prevents this fact from biasing the global colour measurements. In two-image mode, SExtractor performs detection and characterisation of the surface brightness distribution in one image, and applies that surface brightness distribution to a second image. We used the IRAC 3.6μm mosaic – the best tracer of the stellar light distribution, as the detection image and photometered the *GALEX* and IRAC mosaics using the surface brightness distribution at 3.6μm to define the apertures. In a few cases, where UV-bright fea-

tures dominate, it was necessary to use the *GALEX* NUV image as the detection image in order to ensure that the SExtractor captures all the light in all six *GALEX* and IRAC bands.

2.3.2 MIPS data for the Coma supercluster

For the mid-infrared study of Coma and Abell 1367 (Chapters 4 & 7), we use archival 24μm *Spitzer* MIPS data covering $2\times2\,\mathrm{deg}^2$ in the case of Coma (PID: 83, PI G. Rieke) and $30'\times30'$ for Abell 1367 (PID: 25, PI G. Fazio). The Coma 24μm dataset consists of four contiguous mosaics (see Fig. 7.2) obtained in medium scan mode, with scan leg spacing equal to the half array width, producing homogeneous coverage over the mosaic, with an effective exposure time per pixel of 88 s. Bai et al. (2006), who used these data to determine the 24μm luminosity function of Coma, estimate the 80% completeness limit to be 0.33 mJy, corresponding to a SFR of $0.02\,\mathrm{M}_\odot\,\mathrm{yr}^{-1}$ at the redshift of Coma. The Abell 1367 24μm dataset consists of a single mosaic obtained in medium scan mode, with scan leg spacing equal to the full array width, producing an effective exposure time per pixel of 40 s.

The SExtractor package (Bertin & Arnouts 1996) was used to automatically detect sources, and obtain photometric parameters. The images were first background-subtracted, and then filtered with Gaussian functions, with full width half maximum (FWHM) matching the 24μm point-spread function (PSF). Aperture photometry was obtained for all objects having eight contiguous pixels above the 1σ rms background noise level. Following SWIRE, we measured the fluxes within circular apertures of diameter 21, 30, 60, 90 and 120″. For the vast majority of sources, the 6″ FWHM PSF of MIPS leaves the object unresolved at 24μm, and hence we estimate the total 24μm flux of these objects from the flux contained within the 21″ aperture, corrected by a factor 1.29.

However, at the redshift of the Coma and Abell 1367 clusters, many of the brighter galaxies (spirals in particular) are larger than our nominal 21″ diameter aperture, such that a significant fraction of their 24μm flux is missed. For these galaxies, we use instead one of the larger

apertures, matched to contain the optical flux as parametrised by R_{90z} (the radius which contains 90% of the z-band flux) as measured from the SDSS image (see Sec. 2.2). Finally, for some of the bright cluster galaxies (9 in total), the value of R_{90z} is underestimated. To correct for this, SM eyeballed the 24μm images of these objects, and estimated an appropriate radius, in each case, for extracting the 'total' 24μm flux. In the case of the brighter spiral galaxies in Coma and Abell 1367, the 24μm emission often shows significant structure due to spiral arms and star-forming regions, necessitating a high value of the deblending parameter, to prevent the galaxy being shredded by SExtractor. Particular care was required to correctly deblend the face-on spiral NGC 3861 from NGC 3861B, while keeping NGC 3861 intact. We note that for $\sim$50% of our sample the typical measurement error in the 24μm flux is < 0.1 mJy (which is $\lesssim 10\%$ of the measured flux), and for $> 95\%$ the error is < 0.35 mJy. In total, $\sim$90% of our galaxies have 24μm flux measured with $< 30\%$ uncertainty.

2.4 2MASS: Near infrared data

The near infrared (NIR) data for all the 369 galaxies belonging to SFRS used in Chapter 8 are sourced from the public database of the Two Micron All Sky Survey (2MASS)[4]. 2MASS provided the all-sky photometric census of galaxies brighter than $Ks = 13.5$ mag. The final catalogue of $> 1,500,000$ galaxies include photometric measurements in three NIR bands, J, H and Ks which are sensitive to the stellar populations dominating the luminous mass.

2.5 *IRAS*: FIR data

For the selection of the SFRS sample (Chapter 8), we used the *IRAS* 60μm luminosity as an unbiased star formation tracer by virtue of the breadth and uniformity of its coverage and because of the proximity of the 60μm band to the SED peak associated with star formation for selecting

[4] http://www.ipac.caltech.edu/2mass/

the SFRS galaxies (Chapter 8). The parent sample is the PSCz catalogue (Saunders et al. 2000), a full-sky database of 15,000 nearby star-forming galaxies brighter than 0.6 Jy at 60μm. Most PSCz objects are closer than $\mathrm{z}=0.2$. The PSCz galaxy luminosities range from $\mathrm{L}(60\mu\mathrm{m})=10^7$ to $10^{12}L_{\odot}$.

2.6 1.4 GHz Radio data

Most of the radio observations come from the NRAO VLA Sky Survey (NVSS; Condon et al. 1998), a snapshot survey of 82% of the celestial sphere at 1.4 GHz. The angular resolution of NVSS is 45″, while the typical rms brightness fluctuations in the survey are 0.45 mJy beam^{-1}. The survey catalogue reaches the 50% completeness level at $S = 2.5$ mJy. In practise, the Star Formation Reference Survey (SFRS henceforth; Ashby et al. 2011) sources studied in Chapter 8 were retrieved from the online catalogue [5] with a 30″ search radius. Such queries returned results for 342/369 of the SFRS galaxies, all with unique matches. Fig. 6 of Condon et al. (1998) shows a 1% chance of finding a spurious match within this distance of an arbitrary position. For 192 galaxies the flux densities based on the NVSS data were taken from Condon et al. (2002), while for the others the NVSS images were examined and blends were deconvolved to retrieve flux corresponding to the desired object, which were almost always separable in the IRAC or NED[6] image.

16 SFRS sources which either were not detected in the NVSS or had very low signal to noise were observed with the VLA in D configuration in 2008 July (program AA 319). The observations used the same observing frequencies and bandwidth as those of the NVSS but were $\geq$7 minutes longer in comparison to 30 s for the NVSS in the relevant declination bands. The data were reduced as consistently as possible with the NVSS data.

[5] http://www.cv.nrao.edu/nvss/NVSSlist.shtml, lookup done in 2010 in catalogue dated 2004
[6] The NASA/IPAC Extragalactic Database; http://ned.ipac.caltech.edu/

Chapter 3

Red star-forming and blue passive galaxies in clusters

3.1 Introduction

If, as is widely believed, large-scale structures form in the Universe by means of the hierarchical assembly of dark haloes, one would expect the most massive galaxies to be the youngest, as they would be formed from mergers over time. However, the brightest galaxies, elliptical in morphology, typically found at the centres of rich clusters, appear to be dominated by old stellar populations. Galaxies with current star formation, on the other hand, have been shown to be disc-dominated, mostly occurring in regions of lower density. Such relations between the properties of galaxies and their environment were first pointed out using morphology to characterise galaxies (Oemler 1974; Melnick & Sargent 1977; Dressler 1980), but, in later studies, other photometric properties such as colour (e.g. Kauffmann et al. 2003a; Balogh et al. 2004b; Weinmann et al. 2006; Cooper et al. 2007) have been shown to correlate with environment as well.

In addition to understanding the formation of dark matter haloes, the study of galaxy for-

mation and evolution clearly requires detailed knowledge of the various physical processes that affect baryons, such as mergers, tidal interactions, stripping, cooling and feedback. Observations of the relevant galaxy features and their dependence on environment are very important in our comprehension of the relative importance of these processes, a subject that remains an issue of considerable disagreement (see, e.g., Oemler et al. 2009).

The availability of large-scale spectroscopic surveys, such as the Sloan Digital Sky survey (henceforth SDSS), has resulted in structural parameters of galaxies being largely replaced by spectroscopic properties, in the exploration of the impact of the global and local environment on the nature of a galaxy (Balogh et al. 2004b; Porter & Raychaudhury 2005; Haines et al. 2006a; Haines et al. 2006b; Pimbblet, Drinkwater & Hawkrigg 2004; Weinmann et al. 2006; Porter & Raychaudhury 2007; Porter et al. 2008; Mahajan, Raychaudhury & Pimbblet 2011c, among others). Compared to broad-band colours, spectroscopic parameters such as integrated star formation rate (SFR), specific star formation rate (SSFR or SFR/M^*), Hδ equivalent width (EW) and the 4000 Å break (D_n4000), in principle, give more detailed information about the underlying stellar populations in galaxies, but one cannot expect these parameters to behave in the same way with environment as the global photometric properties.

Various factors, including the presence of dust, and the well-known degeneracy between the effect of age and metallicity, prevent a straight-forward correspondence between the star formation history of a galaxy and its broad-band colours (e.g. Faber 1973; Calzetti 1997). As a result, the use of broad-band colours and of spectroscopic indicators might yield different classification for a galaxy on an evolutionary sequence. In order to compare observational studies where different photometric or spectroscopic parameters have been used to define sub-samples, one would like to ask, for instance, for what fraction of galaxies the correspondence between morphology, colour and star formation properties fails to hold, and whether such galaxies could be identified from other observable properties. Are these unusual galaxies more likely to occur in certain kinds of environment?

In order to address some of these questions, we choose, for this study, galaxies in and around rich clusters in the low redshift Universe. Galaxy clusters are well suited for such an analysis, since from their cores to their infall regions, they provide a wide range of environments, with varying space density and velocity dispersion. The aim of this work is to examine how well galaxy properties obtained from two mutually independent techniques, namely photometry and spectroscopy, correlate with each other, and to explore the possible causes of discrepancy.

The outline of this paper is as follows: in the next section we define the galaxy sample, and the galaxy properties to be used here. We plot the specific star formation rate of these galaxies against colour, and identify the four classes of galaxies that we will deal with: red sequence, red star-forming, blue star-forming and blue passive. In §3.3, we examine the various galaxy properties, derived from photometry and spectra, that we use in this analysis. The insight these properties provide into the nature of blue passive and red star-forming galaxies are discussed in §3.4, and the main conclusions are summarised in §3.5. Throughout this chapter we adopt a cosmology with $\Omega_m = 1$ & $\Omega_\Lambda = 0$ and $h = 70$ km s^{-1} Mpc^{-1} for calculating distances and absolute magnitudes. We note that in the redshift range chosen for this work ($0.02 \leq z \leq 0.12$), the results are insensitive to the choice of cosmology.

3.2 The observational data

The galaxy data used in this Chapter are discussed in §2.2 and the methodology for deriving SFR and SSFR are described in Appendix B.

3.2.1 Cluster membership

We take all Abell clusters (Abell et al. 1989), in the redshift range 0.02$<$ z $\leq$0.12, that lie sufficiently away from the survey boundary so as to be sampled out to $\leq 6\,h_{70}^{-1}$ Mpc from the cluster centre. We constrain our sample to moderately rich clusters by considering only those

that have at least 20 galaxies (brighter than the magnitude limit, $M_r \leq -20.5$) with SDSS spectra within $3\,h_{70}^{-1}$ Mpc of the cluster centre. This leaves us with a sample of 119 clusters.

We aim to study the effect of present and recent star formation on the observed properties of galaxies over a wide range of environment, and so we seek to examine galaxies not just in the cores of the clusters, but also on the outskirts. Detailed studies of the velocity structure in the infall regions of clusters show that the turnaround radius of clusters extends out to almost twice the virial radius (Diaferio & Geller 1997; Rines & Diaferio 2006; Dünner et al. 2007), so we chose to examine radial trends of the properties of galaxies out to a projected radius of $R=6\,h_{70}^{-1}$ Mpc of each cluster centre. Within this radius, we pick galaxies within the following velocity ranges about the mean redshift of the cluster:

$$\Delta \mathrm{z} = \left\{ \begin{array}{ll} 3000 \text{ km s}^{-1} & \text{if } R \leq 1 \text{ Mpc} \\ 2100 \text{ km s}^{-1} & \text{if } 1 < R \leq 3 \text{ Mpc} \\ 1500 \text{ km s}^{-1} & \text{if } 3 < R \leq 6 \text{ Mpc} \end{array} \right\}. \tag{3.1}$$

In Fig. 3.1 we show the phase-space distribution of galaxies selected for two clusters, Abell 85 and 1024, representative of our sample. Fig. 3.1 shows that by adopting the differential velocity slices helps in reducing interlopers, in the absence of a rigorous procedure for assigning cluster membership, and hence is well suited for a statistical study like this. Note that other popular methods, such as the $3\sigma_v$ velocity dispersion cut, are prone to include galaxies at large projected radius from the cluster centre. Our velocity cuts are also consistent with the caustics in velocity space used by the CAIRNS survey (e.g. Rines et al. 2003; Rines & Diaferio 2006).

3.2.2 Cluster parameters

We find the velocity dispersion (σ_v) of each cluster, from the identified members, using the bi-weight statistics (ROSTAT, Beers, Flynn & Gebhardt 1990). The characteristic size of the

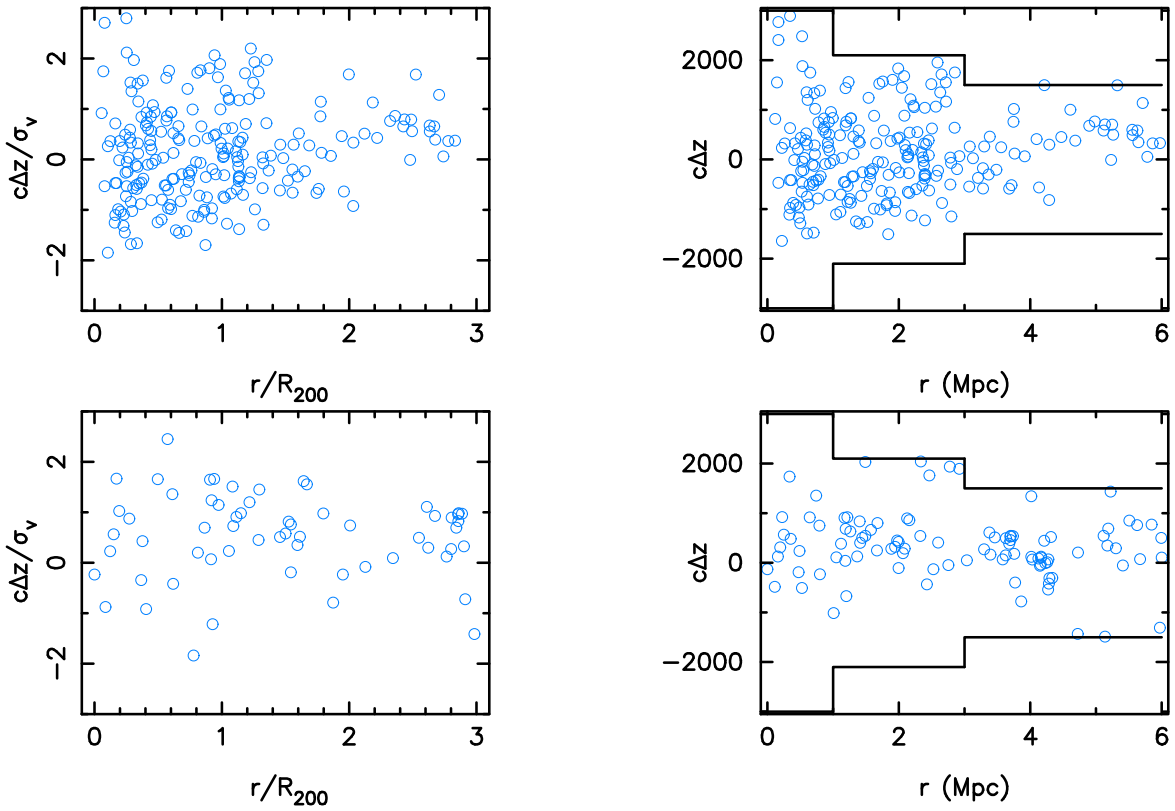

Figure 3.1: This figure shows the cluster galaxies ($M_r \leq -20.5$) selected by our velocity cut for two typical clusters in our sample: (*top*) Abell 85 & (*bottom*) Abell 1024, in a scaled velocity-scaled radius space (*left*), and the same in linear phase-space (*right*). The l.o.s. velocity of galaxies is scaled by the velocity dispersion (σ_v) of the cluster, while the cluster-centric radius is scaled by the cluster's R_{200}. The bounding lines in the right-hand plots correspond to the redshift slices mentioned in Eqn. 3.1. In order to keep the results based on stacking all cluster galaxies together, independent of cluster to cluster variations, we select galaxies in linear space but perform the analysis using scaled quantities.

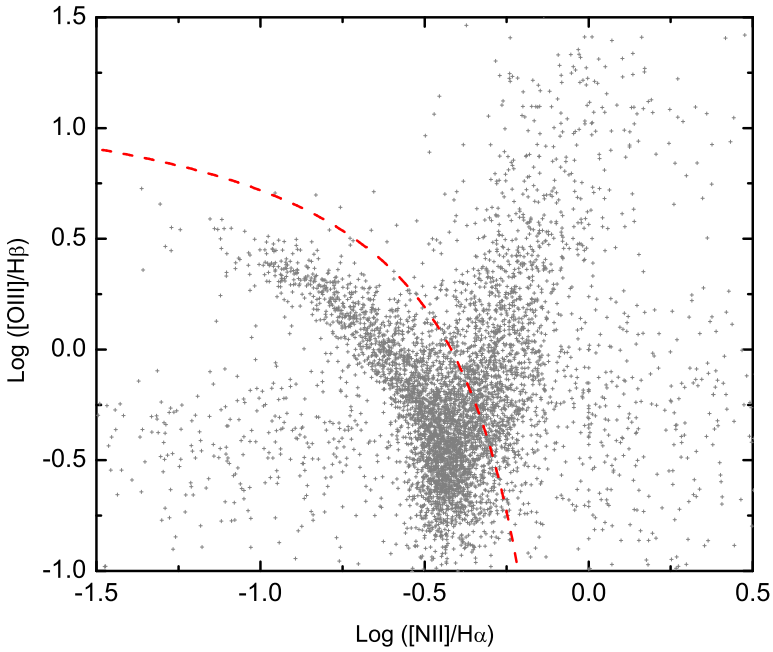

Figure 3.2: The distribution of the galaxies used in this work in the plot of the two line-ratios, recommended by (Baldwin, Phillips & Terlevich 1981; BPT), that are often used to discriminate between star-forming (and composite) galaxies (below the *red* line; Kauffmann et al. 2003c) and the AGN-dominated galaxies (above). All galaxies in our sample, except the 'unclassified', are plotted here.

cluster (the radius at which the mean interior over-density in a sphere of radius r is 200 times the critical density of the Universe) is calculated using the relation given by Carlberg, Yee & Ellingson (1997): $r_{200} = \sqrt{3}\sigma_v/10H(\mathrm{z})$. Our final sample comprises of 119 Abell clusters ($\mathrm{z} < 0.12$) in which there are 6,010 galaxies within $3\,r_{200}$ of the cluster centres.

3.2.3 Four categories of galaxies

Galaxy properties measurable from photometry or spectra, such as colour, SFR or SSFR ($\equiv$ SFR/M^*) have been extensively used in studies of their dependence on the environment of the galaxy (e.g. Balogh et al. 2004b; Haines et al. 2006a; Haines et al. 2006b; Pimbblet, Drinkwater

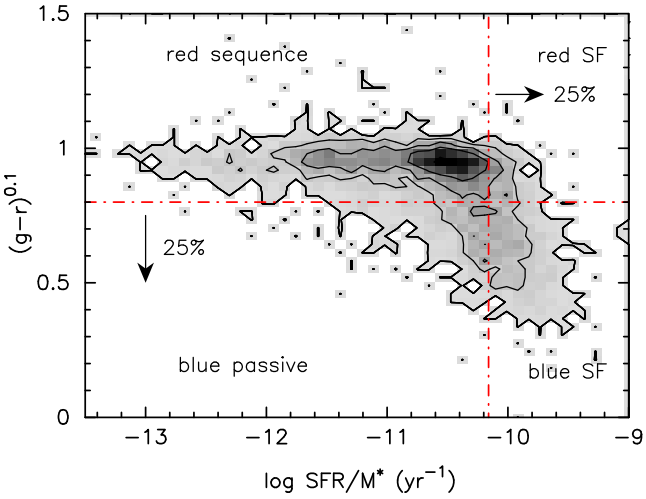

Figure 3.3: The relation between specific star formation rate (SSFR or SFR/M_*) for all galaxies found within $3\,r_{200}$ of the centre of each galaxy cluster in our sample. The contours represent 150, 100, 50 and 25 galaxies respectively. The horizontal line marks the colour cut adopted by most Butcher-Oemler effect studies, i.e. 0.2 mag bluer than the red sequence: this labels $\sim 25\%$ of all galaxies as blue. To match this cut, we adopt a SSFR threshold, SFR/$M^* = -10.16$ yr^{-1} such that 25% of all the galaxies are classified as star-forming. We thus categorise our galaxy ensemble into four classes: (*clockwise from right*) red star-forming, blue star-forming, blue passive and red sequence galaxies respectively.

& Hawkrigg 2004; Weinmann et al. 2006; Porter & Raychaudhury 2007; Porter et al. 2008; Mahajan, Raychaudhury & Pimbblet 2011c), or on other variables representing mass, such as the stellar mass of the galaxy (Kauffmann et al. 2003b) or its circular velocity (Graves et al. 2007).

In this work, we study the colour and SSFR as indicators of the evolutionary stage of a galaxy. In Fig. 3.3 we plot the colours of all galaxies found within $3\,r_{200}$ of the centres of all the clusters in our sample against their specific star formation rates. In a pioneering study of evolution of galaxies in clusters, Butcher & Oemler (1984) had adopted a colour cut to define blue galaxies as $B-V=0.2$ mag lower than the cluster's red sequence. Here we stack all the cluster galaxies together, and fit a red sequence to galaxies which has a slope of -0.034 with an absolute deviation of 0.080. Since this slope is negligible, we adopt a null slope red sequence at $(g-r)^{0.1}=1$. We note that using the actual red sequence fit does not change our results at all.

	red SF	red sequence	blue passive	blue SF
Clusters	539	3998	538	935
Entire SDSS	24039	163904	44877	113909

Table 3.1: Number of galaxies in the four categories

The blue galaxies are thus defined to have $(g-r)^{0.1} \leq 0.8$. This classifies $\sim 25\%$ of all galaxies as blue.

Correspondingly, we choose the SSFR threshold at SFR/M^*= -10.16 yr^{-1}, defining the 25% of all galaxies with a higher value of SSFR as star-forming. We note that our results do not qualitatively change even if the SSFR threshold is changed to the 50-percentile value (SFR/M^*= -10.45 yr^{-1}). We thus classify the galaxies in the 4 quadrants of Fig. 3.3 as red star-forming, red sequence, blue passive and blue star-forming, anti-clockwise from top right. Table 3.1 gives the number of galaxies in our cluster sample in each category, and also the corresponding numbers in the whole of SDSS DR4 spectroscopic catalogue in the same redshift and magnitude range as our cluster galaxy sample.

3.2.4 Spatial distribution of galaxies in clusters

Having divided the galaxies into four classes, we consider their radial distribution within the clusters to examine the possible influence of local environment. Fig. 3.4 shows the distribution of galaxies in all four categories as a function of distance from the corresponding cluster, scaled by r_{200}. For each category, the curve has been normalised by the total number of galaxies in that category.

As expected, the fraction of the passive red sequence galaxies increase towards the cluster centre. The red star-forming galaxies closely follow the distribution, but their fraction inside r_{200} does not increase as steeply as that of the red sequence galaxies, suggesting a different evolutionary path. Here it would have been very interesting to examine the detailed difference between these two distributions as a function of halo mass, since in both clusters and groups the

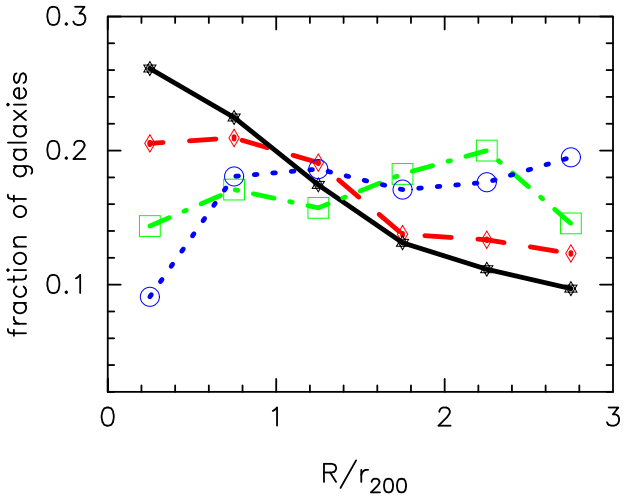

Figure 3.4: The radial distribution of galaxies in the four categories defined in §3.2.3 is plotted as a function of cluster-centric radius, scaled by r_{200}. Each distribution is normalised to unity. The Poisson error on each point is smaller than the size of symbols. The fraction of red sequence galaxies *(solid black)*, as expected, increases toward the cluster centre, and the red star-forming galaxies *(red dashed)* follow them closely. The blue star-forming galaxies *(blue dotted)* show a decline within r_{200}, while their passive counterparts *(green dot-dashed)* show a constant fraction out to $3\,r_{200}$, except for a mild increase $\sim 2\,r_{200}$.

morphology and star formation properties seem to vary between dwarfs and giants (Khosroshahi et al. 2004; Miles, Raychaudhury & Russell 2006), and/or central and satellite galaxies (Ann, Park, & Choi 2008), indicating different evolutionary histories. But in this work, over the redshift range of our sample, we have to be confined mostly to M_* and brighter galaxies ($M_r \leq -20.5$).

At the other extreme, the blue star-forming galaxies show a constant distribution beyond r_{200}, dropping steeply in the cluster core. This is the consequence of the observed lack of neutral gas in galaxies in the cores of rich clusters (e.g. Giovanelli & Haynes 1985; Raychaudhury et al. 1997).

However, the blue passive galaxies, which also have a more or less constant radial distribution over the entire range, do not show this rapid drop in the cores. This is consistent with the observation, discussed below in some detail, of nuclear star formation in a substantial fraction of brightest cluster galaxies (Bildfell et al. 2008; Reichard et al. 2009), which will cause the

innermost bin to be significantly higher for this distribution than that for the blue star-forming galaxies. It is interesting to note that the fraction of blue passive galaxies also show a minor increment around $2\,r_{200}$. Other studies have shown that in clusters, particularly those that are fed by filaments, there is an enhancement of nuclear star formation in the infalling galaxies beyond r_{200} (e.g. Porter & Raychaudhury 2007; Porter et al. 2008; Mahajan, Raychaudhury & Pimbblet 2011c).

3.3 Do the Galaxy properties derived from photometry and spectroscopy agree with each other?

One of the objectives in this paper will be to examine the hypothesis that the galaxy populations can indeed be divided, on the basis of a single parameter, into two classes: passive and star-forming, and that the incidence of red star-forming or blue passive galaxies is merely due to the scatter in the measured parameters within reasonable errors. As we show below, this hypothesis fails to hold.

3.3.1 The effect of extinction and abundance

Star-forming regions in a galaxy are often surrounded by dust, which can significantly affect quantitative analyses based on optical light. Conversely, the presence of dust in a galaxy would imply the presence of star-forming regions therein. In the absence of infrared observations, which are often used to quantify the effect of dust in star-forming systems (e.g. Calzetti 1997), optical photometry can also be used to constrain the internal extinction in a galaxy (also see Fig. 3.10).

In one such attempt, Kauffmann et al. (2003b) have estimated the degree of dust attenuation (A_z) in the SDSS z-band, by comparing model colours to the measured colours to estimate the reddening for each galaxy. The shape of the attenuation curve from observations is found to

resemble a power law with slope ~ -0.7 over a wavelength range from 1250-8000 Å (Calzetti et al. 1994). A standard attenuation curve, of the form $\tau_\lambda \propto \lambda^{-0.7}$, is then extrapolated to obtain the extinction in the SDSS z-band. We use the A_z values from Kauffmann et al. (2003b), expressed in magnitudes, in this section. The typical 1σ error on the estimated A_z is ~ 0.12 mag. They also note that comparison of $g-r$ and $r-i$ colours yield similar extinction values for most galaxies if the colours are corrected for nebular emission.

The red colour of a galaxy can result from a combination of several factors, involving the presence of dust and/or metals in the interstellar medium and old stars. In our attempt to interpret the apparent evidence of star formation in the fibre spectra of some red galaxies ('red SF'), and the low values of SFR in the spectra of some blue galaxies ('blue passive'), we plot, in Fig. 3.5, the distribution of internal extinction A_z of the galaxies in the four populations as classified in Fig. 3.3.

As expected, the 'red sequence' galaxies, most of which are passively evolving massive galaxies in the cores of clusters, show very little extinction (negative values of A_z being interpreted as zero here). However, even among passive galaxies, there is a small fraction that constitutes a tail extending to non-negligible extinction values. The blue star-forming galaxies, on the other hand, show a clear sign of attenuation going upto 1.9 mag in the z-band, with most galaxies having extinction values around 0.6 mag for the blue star-forming galaxies and 0.35 mag for the blue passive galaxies respectively.

In contrast, the red star-forming galaxies show a mix of at least two different populations: about half of them are unattenuated (similar to the red sequence galaxies), and the other half contributing to the skewed high extinction end of the distribution. We employ the KMM algorithm (Ashman, Bird & Zepf 1994) to quantify the existence of bimodality in our data. The KMM algorithm fits a user specified number of Gaussian distributions to the dataset, calculates the maximum likelihood estimate of their means and variances, and assesses the improvement of the fit over that provided by a single Gaussian. The KMM likelihood ratio test statistics

(LRTS) used here is a measure of improvement in using two Gaussian distributions (since we are testing bimodality) over a 1-mode fit.

For the distribution of extinction, in the red star-forming galaxies the KMM test gives the value of likelihood ratio (LRTS) to be 75, when using a bimodal fit to the data than using a unimodal fit, with nil probability of the null hypothesis being satisfied. The 2-modes of the internal extinction distribution are found to be centred around A_z=-0.06 (read zero extinction) and 0.72 mag respectively for the sample of cluster galaxies. We further note that the improvement in fit to an asymmetric data by double Gaussians relative to a single in itself is inconclusive to how many such modes would best describe the data. However, in this case the physical significance of this bimodality in the distribution of A_z becomes clearer in the context of other galaxy properties that are discussed below. Interestingly, we find that even by changing the selection criteria for defining the red star-forming galaxies to a higher value of log SFR/M^* = -10 yr^{-1}, the KMM test still yields statistically significant result in favour of a bimodal fit to the data (LRTS=21 at a significance level 5×10^{-5}).

Along with the distribution of extinction values for the cluster galaxies, we also show the corresponding distributions for $>$300,000 galaxies, with the same magnitude and redshift range as our cluster sample, drawn from the entire SDSS DR4 spectroscopic catalogue (grey thin lines). For this much larger sample, the histograms of extinction values are not significantly different from those for the cluster sample, except for the red star-forming galaxies, where cluster galaxies seem to have relatively fewer galaxies with high extinction values than similar galaxies in the larger all-SDSS sample.

3.3.2 Hδ and the 4000Å break

In order to probe the presence of young (< 1 Gyr old) stellar populations among galaxies with an unusual combination of SFR/M^* and colour, we plot the distributions of the EW of the Hδ absorption line, and of the D_n4000 values in Figs. 3.6 and 3.7 respectively. The D_n4000 is the

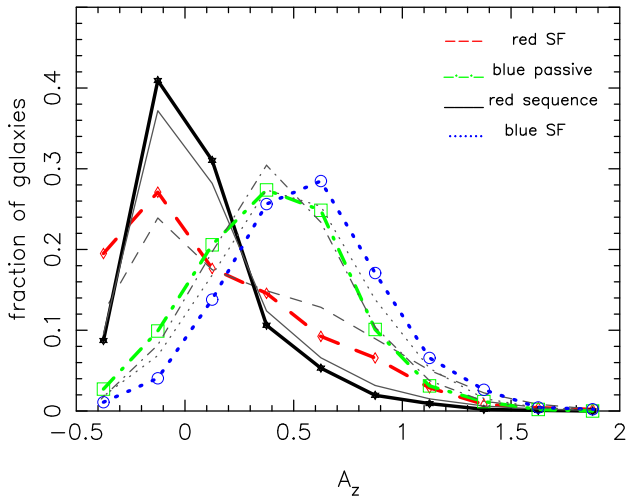

Figure 3.5: The distribution of internal extinction among our cluster galaxies in the four quadrants as specified in Fig. 3.3. Each histogram is normalised to unity. It is clear that in general more 'blue' galaxies are prone to internal reddening than the 'red' ones, with star-forming (*blue dotted*) and passive blue galaxies (*green dot-dashed*) showing slight offsets. Interestingly, while $< 45\%$ of the red sequence galaxies (*black solid*) show signs of some extinction, the red star-forming galaxies (*red dashed*) have a bimodal distribution in extinction values (see text). The *grey lines* represent the same distributions as above, but for $> 300,000$ galaxies found in the entire SDSS DR4, divided in the four quadrants in the same way as described for the sample of cluster galaxies studied here. Here, negative values of A_z indicate the absence of extinction.

strongest discontinuity occurring in the optical spectrum of a galaxy, mainly due to the presence of ionised metals. On the other hand, Hδ absorption is detected after most of the massive hot stars have finished evolving on the main sequence, i.e. at least 0.1–1 Gyr after a starburst is truncated. Thus the Hδ EW is a measure of the age of the youngest stellar population in a galaxy, and has been extensively used to estimate the mean stellar ages as well (Worthey & Ottaviani 1997). Even though several studies have shown that the Balmer emission due to HII regions, AGN and/or planetary nebulae can fill in the underlying Balmer absorption lines, causing age estimates to be spuriously high (Trager et al. 2000; Prochaska et al. 2007), the Hδ EW remains a popular stellar age indicator because it is less affected than the lower order Balmer lines, due to the steep Balmer decrement in emission (Osterbrock & Ferland 1989; Worthey & Ottaviani 1997).

Here we use the measured values of the (emission corrected) Hδ EW, and the (Ne III con-

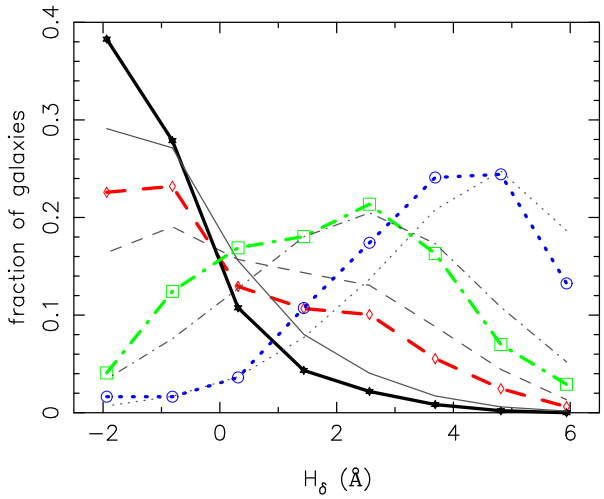

Figure 3.6: The distribution of the (emission corrected) Hδ equivalent width (EW) for galaxies in our cluster sample, with line styles the same as in Fig. 3.5. As expected, the blue star-forming galaxies have the highest absorption, showing the presence of < 1 Gyr old stellar population/s, while the red sequence galaxies show little evidence for absorption in Hδ. The blue passive galaxies have a broad distribution with equal probability of finding Hδ in emission (negative EW) or absorption. The distribution for red star-forming galaxies is bimodal, which, in conjunction with the distribution of their internal extinction (Fig. 3.5), indicates the presence of two distinct galaxy populations.

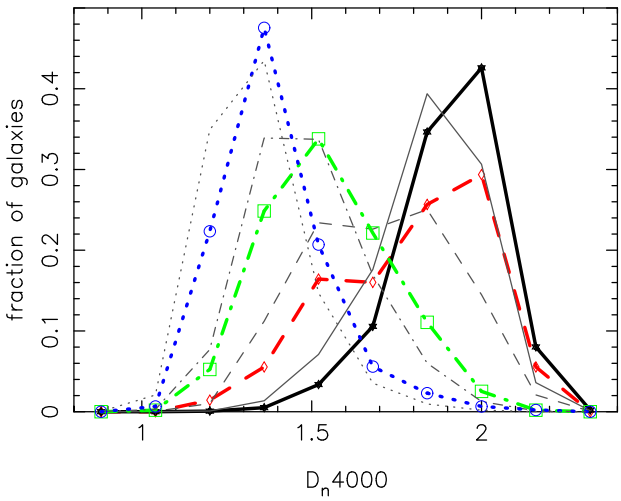

Figure 3.7: The distribution of the (NeIII continuum corrected) D$_n$4000 values, with line styles the same as in Fig. 3.5. As expected, the red sequence galaxies have the largest values, while the blue star-forming galaxies the smallest values for D_n4000 respectively. The blue passive galaxies have a small offset (~ 0.2) from their star-forming counterparts, revealing the presence of slightly older stellar populations. The histogram for red star-forming galaxies has a statistically significant bimodality (see text), similar to that seen in Figs. 3.5 & 6.5.

tinuum corrected) D_n4000 from Kauffmann et al. (2003b), who, for the latter, have adopted a modified version of the original definition (Bruzual 1983) of the D_n4000 introduced by Balogh et al. (1999). A stronger D_n4000 is an indicator of a metal-rich inter-stellar medium, which, together with the Hδ EW, indicates whether the galaxy has been forming stars continuously (intermediate/high D_n4000 plus low Hδ EW) or in bursts (low D_n4000 plus high Hδ EW) over the past 1-2 Gyr (Kauffmann et al. 2003b). We note that the observational error in D_n4000 index is very small, typically $\sim$0.02, but the same is not true for the Hδ EW, which has an uncertainty of 1-2 Å in measurement (Kauffmann et al. 2003b). Kauffmann et al. (2003b) discuss the physical constraints leading to these uncertainties, and show that the Hδ index can assume only a selected range of values for all possible star formation histories. The large observational errors on the Hδ EW imply that the estimated value of this index is constrained by the parameter space spanned by the acceptable models.

The red sequence galaxies in our sample do not show Hδ in emission[1], and yield large values for the D_n4000, confirming the fact that their main ingredient is a population of old, passively evolving stars, which determines the overall galaxy colours and dominates the spectra. The high observational uncertainty in the EW(Hδ) implies that it is hard to determine whether Hδ is actually occurring in emission, or the negative EWs are a result of a high correction factor in individual galaxies. This is a common problem with the use of Hδ index in individual systems, but this might not be an important issue for this statistical study. The blue star-forming galaxies, in sharp contrast, yield small values for the D_n4000 and strong Hδ in absorption. The blue passive galaxies follow the blue star-forming galaxies, with the mean value for the D_n4000 systematically higher by ~ 0.2, but with a very broad distribution of Hδ EW, revealing a mix of galaxies with a large scatter in the ages of their youngest stellar populations. In red star-forming galaxies, the distributions of Hδ EW as well as the D_n4000 are bimodal. The KMM test prefers

[1]Note that since the EW(Hδ) used here are corrected for emission, galaxies for which the spectra have been overcorrected due to the lack of any absorption, appear to show Hδ in emission (private communication, Kauffmann, G.)

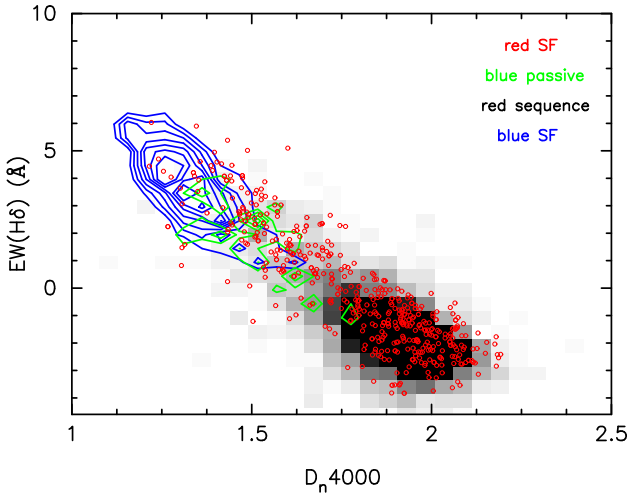

Figure 3.8: The relation between the equivalent width of the Hδ line EW(Hδ) and the 4000Å break index D$_n$4000, for all galaxies in our sample. These two indices together form a robust diagnostic of the star formation history of a galaxy, irrespective of the stellar ages and metallicity (Kauffmann et al. 2003a), also see text). The red sequence galaxies *(grey scale)* form a core in the passive region of the plane, while the blue star-forming galaxies *(blue contours)* occupy the region indicating recent and ongoing star formation. The blue passive galaxies *(green contours)* closely follow the blue star forming galaxies, but with somewhat higher D$_n$4000 and low EW(Hδ), indicating recent truncation of star formation. The innermost contours represent 24 galaxies in both cases, and the number decreases by 3 at every successive level of contour. The red star-forming galaxies seem to span the entire range in both indices defining this space, a relatively large fraction of them being passively evolving just like the red sequence galaxies, but a non-negligible fraction intruding the space dominated by the blue star-forming galaxies.

a 2-mode fit over a 1-mode fit with likelihood ratios of 78 and 84, for Hδ EW and D$_n$4000 respectively, with zero probability for the null hypothesis in both cases.

We also check whether this bimodality is a result of the threshold chosen to define whether a galaxy is star-forming or not. As for the internal extinction, the KMM test results remain statistically significant, for both Hδ EW and the D$_n$4000, when the red star-forming galaxies are selected with an even higher SSFR threshold (log SFR/M^* = –10 yr^{-1}), showing that these results are not sensitive to how the four categories are chosen, within reasonable limits. The above results become even more convincing when we plot the four different galaxy populations on the plane defined by the two indices D$_n$4000 and EW(Hδ) (Fig. 3.8). Kauffmann et al. (2003a) have shown that these two indices taken together can very effectively determine the

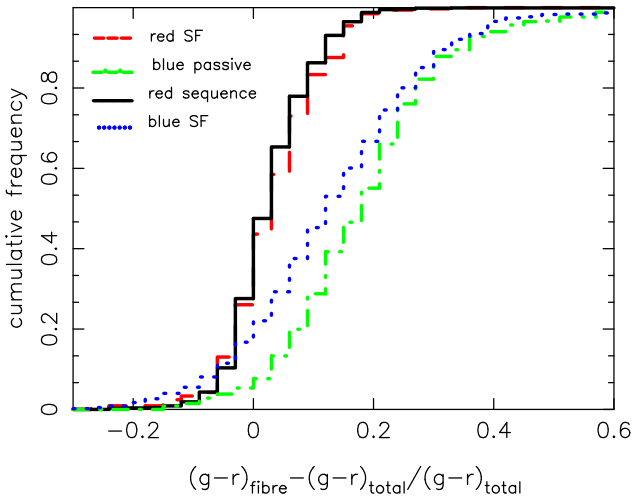

Figure 3.9: The cumulative distributions of $g-r$ aperture colour, measured within the 3″ SDSS fibre, relative to the overall colour of the entire galaxy. At $z \sim 0.1$, $> 60\%$ of the light in the fibre comes from the bulge and hence the fibre colour can be assumed to be a proxy for the colour of the bulge. The slope of the distributions for blue galaxies is much steeper than that of the red ones, showing the large spread in the relative colour, irrespective of the SSFR. Although the red galaxies have a relatively small spread in colour, a significant number of red star-forming galaxies have bluer bulges. This could be the signature of the presence of active nuclei supporting star-formation activity in the core of the galaxies, while the overall galaxy colour remains dominated by the older stellar population elsewhere in the galaxy.

star formation history of a galaxy. As shown in Fig. 3.8, this indeed seem to be the case. The blue star-forming and the passive, red sequence galaxies occupy the opposite ends of the space. But whilst the blue passive galaxies seem to follow the blue star-forming galaxies, although with somewhat lower EW(Hδ) and higher D$_n$4000, the red star-forming galaxies span the entire range of values in both indices, as would be expected given their bimodal distribution.

3.3.3 AGN and star formation

Figs. 3.5, 3.6, 3.7 and 3.8 clearly show that while most of the cluster galaxies follow the classical picture, blue colours correlating with higher SSFR, and redder colours with negligible star formation activity, there is a non-negligible fraction of galaxies in either class which deviate from the norm. It is thus crucial to understand the properties of these galaxies and identify the cause of their occurrence. In order to do so, we make use of the classification of galaxies,

based on the BPT diagram, as star-forming, composite, AGN and those without emission lines (unclassified; see Appendix B).

Ignoring, for the time being, the unclassified galaxies for which the nature of star formation activity cannot be conclusively determined from the spectroscopic data, we find that $>$30% of the red star-forming galaxies and $\sim$50% of the red sequence galaxies are classified as AGN. This agrees with the well-known observation that AGN are predominantly hosted by the massive elliptical galaxies. In Fig. 3.10, we plot 1.4GHz radio sources (from NVSS, Best et al. 2005) and IRAS 60μm sources found in the SDSS DR2 (Cao et al. 2006), along with all the galaxies found in the same redshift range ($\mathrm{z} \leq 0.12$) and magnitude limit ($\mathrm{M}_r \leq -20.5$) in our galaxy sample. The radio-loud AGN are clearly seen to be hosted mostly in the red sequence galaxies. Interestingly, not many of the red star-forming galaxies are found in the IRAS 60μm source catalogues, disagreeing with the usual expectation that the colour of the red star-forming galaxies is a result of the presence of dust around star-forming gas clouds. We further explore this issue in §3.4.2.

3.3.4 Aperture vs global colours

An SDSS spectrum comes from a fixed aperture, which is equal to the diameter of the fibres ($3''$) used in the spectrograph. Since this aperture would encompass a varying fraction of the light of a galaxy depending upon its size and distance, going up to $\sim$40-60% at $\mathrm{z} = 0.1$, the spectrum might not, in most cases, be a true representation of the galaxy's mean overall star formation activity. In this work, we compare photometric colours and spectroscopically derived specific star formation rates, which come from independent observations of the same galaxies. It would be interesting to see how the colour derived from the fibre aperture, as opposed to the value averaged over the entire galaxy, relates to SSFR. For instance, if an early-type galaxy has significant star formation in the core, we would expect to see a bluer core, while the overall photometric colour would be dominated by the older stellar populations elsewhere in the galaxy.

In Fig 3.9, we plot the difference between the colour measured within the fibre and the overall colour of the galaxy, normalised by the overall colour, separately for galaxies belonging to the four categories. A noticeable characteristic of this plot is that irrespective of their star formation properties, the blue and red galaxies have very different slopes for this cumulative distribution. The steeper slope for the blue galaxies is a consequence of their wider range in colour. While most of the galaxies have fibre colours that are redder than the overall galaxy colours, $\sim$15% of the blue star-forming and $\sim$15% of the red star-forming and red sequence galaxies have bluer cores. This suggests the presence of centrally concentrated star formation in these galaxies. It must be noted that although relative fibre colour is a good first approximation to the colour of the bulge of a galaxy, in this work where we stack galaxies over a range of redshift, the ratio of central and overall colour is not derived on the same physical scale for all galaxies. This result should therefore be considered to be a qualitative one.

3.4 Discussion

Numerous studies of the evolution of galaxies have made use of either global photometric properties such as colour (e.g. Butcher & Oemler 1984), morphology (Dressler 1980) or luminosity of a galaxy, or spectroscopic properties such as circular velocity (e.g. Graves et al. 2007), the D_n4000, EW of Hδ absorption line (e.g. Balogh et al. 1999), emission lines of Hα or OII (e.g. Lewis et al. 2002; Gómez et al. 2003; Balogh et al. 2004b; Haines et al. 2007) or integrated SFR and/or SSFR (B04). Often samples are chosen based on colour or star formation properties. Are the properties derived from photometry and from spectra correlated enough to yield similar results?

Blue galaxies are thought to be of late-type morphology and and have significant star formation activity, while red galaxies are early-type and show little or no evidence of current star formation. However, with the recent availability of extensive multi-wavelength photomet-

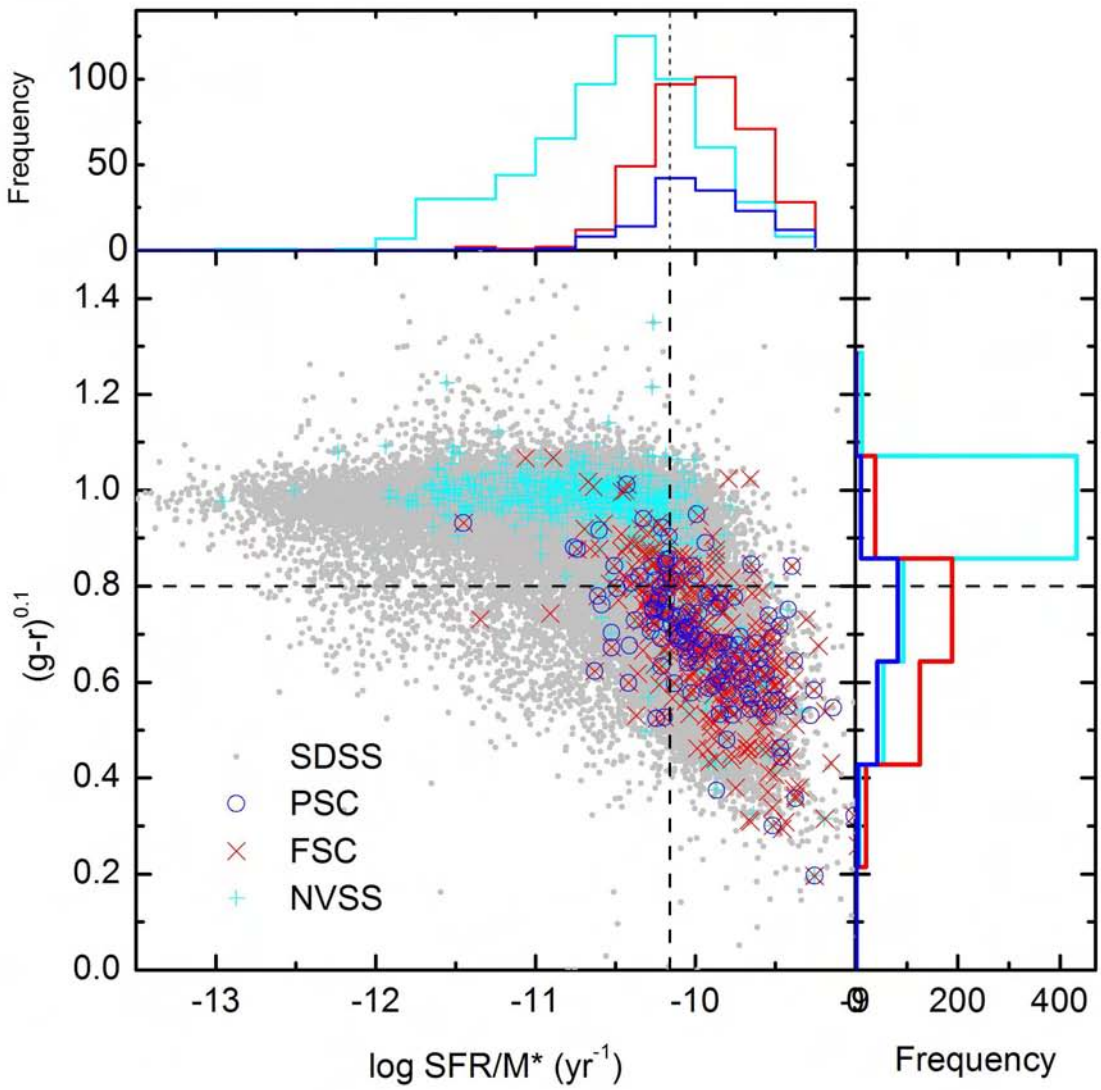

Figure 3.10: The central panel of this plot shows the $(g-r)^{0.1}$ colour of all the spectroscopically covered SDSS DR4 galaxies (*grey dots*) in the colour-SSFR space (same as Fig. 3.3), found in the same redshift range and magnitude limit as our cluster galaxy sample. Over-plotted are 1.4 GHz radio sources from the NVSS (*cyan*), *IRAS* point sources (PSC, *blue*) and IRAS faint sources (FSC, *red*) respectively. The top and the right panel show the histograms of these quantities along the two axes. As expected, most of the radio-loud AGN concentrated along the red sequence, and IR bright sources in the blue star-forming galaxies. It is interesting to note that the red star-forming galaxies (top right quadrant, central panel), a large fraction of which are expected to be dust-reddened, do not seem to have many IRAS sources. This supports our conclusion here that a non-negligible fraction of the red star-forming galaxies obtain their colour from the presence of excessive metals.

ric databases, and of large optical spectroscopic surveys, several authors (e.g. Wolf, Gray & Meisenheimer 2005; Bildfell et al. 2008; Haines et al. 2008; Koyama et al. 2008; Saintonge, Tran & Holden 2008; Graves, Faber, & Schiavon 2009; Wolf et al. 2009) have suggested that optical colour may not necessarily be a good representation of a galaxy's evolutionary state. In this paper, we have explored both photometric colours and spectroscopic specific star formation rate from optical observations of galaxies, in a wide range of environments, in and near rich clusters in the local Universe, to examine cases where the usual correlation between the two fails to hold.

We find that >80% of the red galaxies ($(g-r)^{0.1} \geq 0.8$) that are classified to be part of the red sequence of clusters, on the basis of photometric colours, also have very little or no star formation (SFR/$M^*\leq$-10.16 yr^{-1}, see Fig. 3.3). Similarly, 65% of the blue galaxies found within $3\,r_{200}$ of rich clusters also have high SSFR. However, in addition to these 'normal' galaxies in which the colour and spectroscopic SFR/M^* correspond well with each other, a significant fraction of galaxies deviate from the norm, and would be classified differently, if treated solely on the basis of one of their spectroscopic and photometric properties.

3.4.1 Blue passive galaxies

The blue passive galaxies in our cluster sample (Fig. 3.3) have spectroscopic properties quite similar to their star-forming counterparts. The colour of a galaxy cannot be expected to, and indeed does not, correlate in the same way with environmental properties, as the star formation properties do (e.g. Kauffmann et al. 2003b). Our analysis shows that the values for the D_n4000 (Fig. 3.7) and internal extinction (A_z; Fig. 3.5) for blue passive galaxies are similar to those of blue star-forming galaxies, but the Hδ EW distribution (Fig. 3.6) is very different for the two populations. Since our sample is chosen to be in or near rich clusters, the discrepancy between their mean photometric colour, and their SSFR derived from spectra, suggests two possible scenarios: (i) these are galaxies in which star formation has been recently ($\sim$1-2 Gyr) shut off

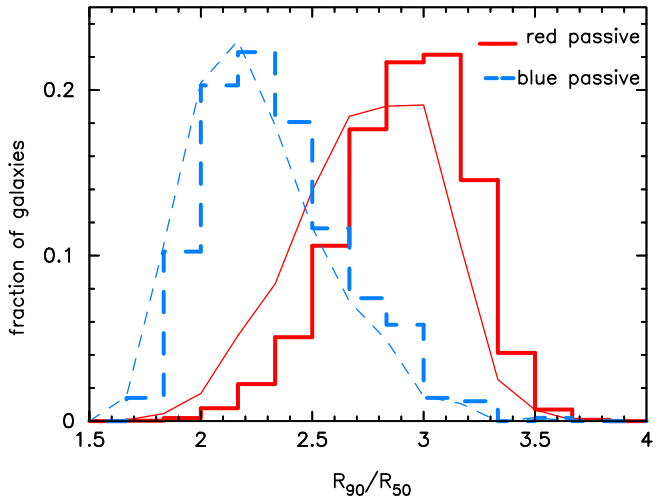

Figure 3.11: The distribution of the concentration parameter, $C \equiv R_{90}/R_{50}$ for the red sequence (*red solid*) and blue passive (*blue dashed*) galaxies respectively. The thick and thin lines represent the distributions with and without unclassified galaxies in each case respectively. The blue passive galaxies clearly have late-type morphologies along with bluer colours. The fact that these galaxies have very low SSFR thus make them candidates for progenitors of the red sequence galaxies, in which star formation has been recently (< 1 Gyr) truncated, eventually leading to red colour and early-type spheroidal structure typical of the present day cluster red-sequence galaxies.

due to the impact of local and/or global environment (e.g. Porter & Raychaudhury 2005; Porter & Raychaudhury 2007; Porter et al. 2008; Mahajan, Raychaudhury & Pimbblet 2011c), or (ii) these are bulge dominated galaxies where the mean colour is dominated by the young stellar populations distributed in the disc but the spectrum sourced from an almost dead centre shows little sign of star formation activity.

A galaxy that has experienced a major burst of star formation 1-2 Gyr ago will show significant absorption in Hδ, which is found in a non-negligible fraction of the blue passive galaxies here (Figs. 3.6 and 3.8). This is because the A stars which significantly contribute to the Hδ absorption, have a lifetime of $\sim$1.5 Gyr, but the burst of star formation produces enough ionising radiation to fill in the Hδ absorption line. But the absorption line shows up in the galaxy spectrum once the starburst has been truncated/ended.

Fig. 3.11 provides statistically significant evidence in favour of (ii). As a morphological

Distributions	D	p
Red & blue star-forming galaxies (including unclassified galaxies)	0.67	0.0000
Red & blue star-forming galaxies (excluding unclassified galaxies)	0.60	0.0000
Red star-forming galaxies (including & excluding unclassified galaxies)	0.08	0.1870
Blue star-forming galaxies (including & excluding unclassified galaxies)	0.02	0.9999
Red & blue passive galaxies (including unclassified galaxies)	0.35	0.0000
Red & blue passive galaxies (excluding unclassified galaxies)	0.29	0.0000
Red passive galaxies (including & excluding unclassified galaxies)	0.08	0.1772
Blue passive galaxies (including & excluding unclassified galaxies)	0.01	0.9999

Table 3.2: K-S test results for distributions in Fig. 3.11 & 3.12 respectively

index, here we use the concentration parameter $C \equiv R_{90}/R_{50}$, where R_x is the Petrosian radius encompassing x% of the galaxy's light in the r-band from SDSS images. In Fig. 3.11, we plot the distribution of C for the red and blue passive galaxies respectively. The blue passive galaxies clearly show late-type morphologies ($C < 2.6$; Strateva et al. 2001), while their red counterparts mostly have values of concentration typical of spheroidals. The galaxies in the former category are similar to the passive blue spirals that have been studied by other authors (e.g. Goto et al. 2003a; Wild et al. 2009).

By analysing the spatially resolved long-slit spectroscopy of a few passive spiral galaxies selected from the SDSS, Ishigaki et al. (2007) find that the Hδ absorption lines are more prominent in the outer regions of the disc, while the nuclear regions show strongest values for D_n4000. Their findings are consistent with the idea that the star formation in passive late-type galaxies ceased a few Gyr ago. Kannappan et al. (2009) have recently identified, characterised and studied the evolution of galaxies which, though morphologically classified as E/S0s, lie on the blue sequence in the colour-stellar mass space, and suggest that these systems almost always have a

bluer outer disk, and that they are a population in transition, potentially evolving on to the red sequence, or have (re)formed a disk and are about to fall back in the class of late-types. Hence, the blue passive galaxies can be considered to be the progenitors of their red counterparts, in which star formation has been recently shut-off: these galaxies will eventually acquire redder colours and early-type morphologies, over a period that depends upon their environment (Goto et al. 2003c).

3.4.2 Red star-forming galaxies

Even more interesting are red galaxies with signs of active star formation in their fibre spectra. We find that 53.4% of the 539 galaxies in this class have significant emission lines on the basis of which their SSFR has been evaluated. These red star-forming galaxies are made up of at least two kinds of galaxies (chosen from simple limits in colour and SSFR). One kind appears to be very similar in photometric properties to the red sequence galaxies but with spectroscopically derived properties consistent with their late-type counterparts, while the other class has both photometric *and* spectroscopic properties similar to the red sequence galaxies, yet has a high SSFR.

The origin of the latter class is not clear. It is likely that these galaxies are currently experiencing a starburst, which has started very recently ($\lesssim$0.5 Gyr). Stellar populations resulting from such a starburst would be detected in spectral indices such as Hα EW (leading to high values of SFR/M^*), but will not dominate the D$_n$4000 and the Hδ EW for another $\sim$0.5–1 Gyr. The former sub-population is most likely to be bright cluster galaxies (BCGs), with nuclear star-formation linked with the AGN (see Goto 2006; Bildfell et al. 2008; Reichard et al. 2009). In the following we turn our attention to this sub-population.

Star formation at the core of giant ellipticals

The hypothesis that AGN and star formation activity in the core of a galaxy may be linked is supported by the fact that $\sim$30% of the red star-forming galaxies with emission lines are classified as AGN on the BPT diagram (e.g. Fig. 4.8). The fact that 50% of the emission-line red sequence galaxies (defined according to Fig. 3.3) are also classified as AGN does not contradict this scenario because either (i) the red sequence AGN galaxies in general have high stellar mass, and so can have low SSFR even though they have significantly high SFR, or (ii) they do not have enough cold gas to form stars, because of the presence of an active nuclei.

A significant fraction of giant ellipticals show evidence of ongoing star formation or signs of recent ($<$2 Gyr) star formation in their cores, particularly in environments where the likelihood of recent mergers is high (e.g. McDermid et al. 2006; Nolan et al. 2007). For a sample of BCGs in 48 X-ray luminous clusters, Bildfell et al. (2008) find that 25% of the BCGs have colour profiles $(g-r)$ that turn bluer toward the centre. Our radial distribution of galaxies in this category (Fig. 3.4), compared to the distribution of blue star-forming galaxies, is consistent with this (see §3.2.4).

Elsewhere, Gallazzi et al. (2009) analyse an extensive dataset, covering UV to IR SEDs for galaxies in the Abell 901/902 cluster pair, to show that $\sim$40% of the star-forming galaxies residing in intermediate to high density environments have optically red colours. They show that these galaxies are not starbursts, and have SFRs similar to or lower than that of their blue counterparts. Whether the occurrence of blue cores in red sequence galaxies is linked to their nuclear activity, and whether the nuclear activity itself is modulated by the immediate environment of a galaxy (such as the presence of close neighbours), remains a debatable issue. We intend to return to this in future work involving a more detailed study of nuclear starbursts (also see Li et al. 2008; Reichard et al. 2009).

The scenario discussed in (ii) above complements the blue passive galaxy population discussed in §3.4.1– massive galaxies without much cold gas could be formed in dry major mergers

of the passive blue progenitors, while high speed encounters amongst them in moderately dense environments, such as in the infall regions of clusters (e.g. Porter et al. 2008; Mahajan, Raychaudhury & Pimbblet 2011c), could lead to excessive loss of cold gas, leaving the galaxy to evolve passively thereafter.

In a spatially resolved spectroscopic study of 48 early-type galaxies, the SAURON team (de Zeeuw et al. 2002) simultaneously observed the CO(1-0) and CO(2-1) lines with 28% detection rate (12/43) (Combes et al. 2007). In this sample they find that the CO-rich galaxies show strongest evidence of star formation in the central ($\sim$4x4 arcsec^2) regions and also tend to have higher Hβ and lower Fe5015 and Mgb indices. The results presented in this work also support various studies based on the UV data obtained by the Galaxy Evolution Explorer (*GALEX*) which suggests that a significant fraction ($\sim$15%) of bright ($M_r < -22$) early-type galaxies show signature of recent ($\lesssim$1 Gyr old) star formation (e.g. Yi et al. 2005; also see Crocker et al. ; Gallazzi et al. 2009).

Stellar and gas phase metallicities

Since star formation in a galaxy is often associated with the presence of dust, one would naively expect these red star-forming galaxies to be the dusty starburst galaxies widely discussed in the literature (Wolf, Gray & Meisenheimer 2005; Bildfell et al. 2008; Koyama et al. 2008; Saintonge, Tran & Holden 2008; Gallazzi et al. 2009; Wolf et al. 2009). However, we find that only ~ 50% of the galaxies in this class show presence of any optical extinction (Figs. 3.5 & 3.10). So why are the rest of the galaxies red?

To address this question, we explore two other factors affecting galaxy colours, namely age and metallicity. We use stellar metallicities and mean luminosity-weighted stellar ages from the work of Gallazzi et al. (2005), which are estimated from 150,000 Monte Carlo simulations of a full range of physically plausible star formation histories. These models are logarithmically distributed in a metallicity range of 0.2–2.5 $Z_\odot$. In a given model, all stars have the same metal-

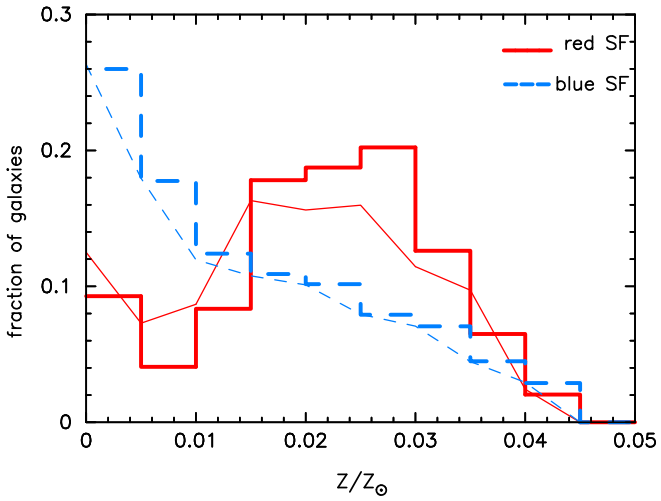

Figure 3.12: The distribution of stellar metallicities (from Gallazzi et al. (2005) for the red star-forming (*red solid*) and blue star-forming (*blue dashed*) cluster galaxies in our sample. The thick and thin curves are distributions including and excluding the unclassified galaxies respectively in each case. The distributions evidently show that the stars in the red star-forming galaxies are much more metal-rich with respect to their bluer counterparts. Given that the internal extinction in galaxies belonging to the two categories does not show a significant difference (Fig. 3.5), presence of metal-rich stellar populations in the red star-forming galaxies seems to be a likely cause of their redder colours.

licity, interpreted as the 'luminosity-weighted stellar metallicity'. For each model in the library, Gallazzi et al. (2005) measure the strength of the D_n4000, and the $H\beta$, $H_{\delta A}$+$H_{\gamma A}$, [Mg_2Fe] and [MgFe]′ spectral indices in the same way as they are measured in the SDSS spectrum of a galaxy. By comparing the strengths of these indices in the observed spectrum to the model spectra in their library, the probability density functions (PDFs) of several physical parameters, such as age and metallicity of a galaxy, are constructed.

We use the r-band luminosity weighted ages (hereafter referred to as 'mean galaxy ages') and stellar metallicities derived from these PDFs[2]. For galaxies in our cluster sample, we find that the red star-forming galaxies are systematically older than their blue counterparts by 5-7 Gyr. In Fig. 3.12, we compare the distributions of stellar metallicities of the red and blue star-forming galaxies. We confirm that the two distributions are statistically different by using the Kolmogorov-Smirnoff (K-S) statistics, which finds the probability of two datasets being

[2]http://www.mpa-garching.mpg.de/SDSS/DR4/Data/stellarmet.html

drawn from the same parent population. The K-S test finds the maximum difference between the cumulative frequency distributions of the red and blue star-forming galaxies to be $D = 0.35$, with the probability of the null hypothesis being satisfied to be essentially zero.

Further support for the presence of excessive metals in the red star-forming galaxies is provided by a comparison between the gas-phase metallicities (log[O/H]+12) estimated by Tremonti et al. (2004)[3], who have compiled a sample of ∼53,000 star-forming galaxies from the entire SDSS DR4 (selected to have H_α, $H\beta$ & [NII] emission lines at $> 5\sigma$ detection). We find that the cumulative distributions of the gas-phase metallicities of the red and blue populations are statistically different. The K-S test yields $D = 0.18$ at a significance level of 0.043. Though the two samples compared here have widely different numbers of galaxies, our conclusion is consistent with that of Ellison et al. (2008), who show that for a sample of 43,690 galaxies selected from the SDSS DR4, the gas-phase metallicities of galaxies with high SSFR are lower by 0.2 dex, compared to those with low SSFR at fixed stellar mass. The fact that their metallicities are estimated by a comparable but independent method (see Kewley & Dopita 2002 for details), further strengthens our result.

Around 35% of all red star-forming galaxies are classified as star-forming or composite galaxies from their spectra. This is in agreement with the results of Graves, Faber, & Schiavon (2009) who also find ∼30% of nearby red sequence galaxies from SDSS show presence of emission lines in their spectrum. They analyse LINER like emission in these galaxies to show that they are systematically younger by 2.5-3 Gyr than their quiescent counterparts without emission at fixed rotational velocity. At $z \sim 0.1$, Tremonti et al. (2004) have shown that the metallicity is well correlated with the stellar mass of the galaxy. These quantities correlate well for 8.5≤log M^* ≤10.5 $M_\odot$, but the relation flattens thereafter. The fact that ≥60% of our red galaxies have log M^* in the range 10.6-10.9 $M_\odot$ supports the hypothesis that a significant fraction of the red star-forming galaxies obtain their red colours from the residual older generations of stars.

[3]http://www.mpa-garching.mpg.de/SDSS/DR4/Data/oh_catalogue.html

We have also shown that ∼50% of all the red star-forming galaxies are likely to be attenuated by >0.2 mag in the SDSS z-band (Fig. 3.5), and have bimodal Hδ EW and D$_n$4000 distributions (Figs. 3.6, 3.7 and 3.8) which are very different from that of the typical red sequence galaxies. As discussed in §3.3.1 and §3.3.2, the red star-forming class of galaxies remain bimodal in the distributions of A$_z$, Hδ and D$_n$4000, even if the selection criterion based on SFR/M^* is changed to a significantly different value (e.g. ∼15-percentile, corresponding to log SFR/M^* = -10 yr^{-1}). This clearly indicates that the component of red star-forming galaxies that are similar in properties to the red sequence galaxies are not merely a result of scatter from the red sequence (quadrant 1; Fig. 3.3).

3.4.3 Implications for the Butcher-Oemler effect

Butcher & Oemler (1984) found that clusters at moderate to high redshift contain an excess of blue galaxies, compared to their low-redshift counterparts. For the redshift regime of our sample ($z \sim 0.1$), they found a uniform blue fraction f$_b$ of ∼0.03 in all clusters within R$_{30}$, the radius containing 30% of the cluster's red sequence population. This exercise has been repeated several times in recent years for many samples of clusters (Butcher & Oemler 1984; Margoniner & Carvalho 2000; Ellingson et al. 2001; De Propris et al. 2004). Most studies of this kind define 'blue' galaxies in terms of a broadband colour that is bluer by 0.2 mag than that of the cluster's red sequence galaxies. From the above discussion, it is clear that this cut leaves out a significant fraction of star-forming galaxies that have redder broadband colours, and classifies some passively evolving galaxies as 'star-forming'.

Margoniner & Carvalho (2000) found the blue fraction of galaxies to be f$_b$=0.03±0.09, similar to Butcher & Oemler (1984), for 44 Abell clusters at 0.03≤z≤0.38 within a fixed cluster-centric distance of 0.7 Mpc, which translates into the mean R$_{30}$ for most Abell clusters below $z \lesssim 0.1$. However, Margoniner et al. (2001) measured the fraction to be $(1.24 \pm 0.07)z - 0.01$ for clusters at $z \leq 0.25$, again for galaxies within a fixed cluster-centric aperture of 0.7 Mpc.

Elsewhere (Ellingson et al. 2001; De Propris et al. 2004), various multiples of cluster-centric radius, scaled with r_{200}, have been used to show the effect of chosen aperture size on the blue fraction. Ellingson et al. (2001) suggest that the origin of the Butcher-Oemler effect lies in the fact that the relative fraction of 'blue' galaxies on the outskirts of the clusters at higher redshifts is higher than in their local counterparts. If confirmed, this result can have a critical impact on the study of evolution of galaxy properties. It is worth mentioning here that even though most of these studies use optical spectra for most or all of their sample (except for Butcher & Oemler (1984)), the spectroscopic information is used only for assigning cluster membership.

Recently, with the increasing availability of large multi-wavelength datasets, the possibility of the Butcher-Oemler effect being observed in other fundamental galaxy properties (e.g. morphology, Goto et al. 2003b), or in non-optical data e.g. mid-IR, Saintonge, Tran & Holden 2008; Haines et al. 2009), are being explored. The study of Wolf, Gray & Meisenheimer (2005) unraveled the presence of young stars and dust in the red sequence galaxies in a cluster pair at z$\sim$0.17, while Bildfell et al. (2008) found that the colour profile of 25% of the brightest cluster galaxies (BCGs) turn bluer by 0.5–1.0 mag towards their centres, compared to the average colours seen in the cluster's red sequence. All of this has serious implications for Butcher-Oemler like effects based on global photometric properties.

Our sample provides some additional insight to this discussion. The presence of metals, and of colour gradients related to SFR in a galaxy, will affect the estimated fraction of 'star-forming' galaxies in low redshift clusters. The fact that nearby cluster galaxies are more metal-rich than those in high-redshift clusters, will artificially enhance the fraction of passive galaxies that are selected solely on the basis of their colour. Such an effect is usually not accounted for while comparing the blue/star-forming galaxy fraction in clusters at different redshifts. A quantitative analysis of this effect requires a consistent study of an unbiased sample of mutually comparable galaxy clusters spanning a wide redshift range, for which both photometric and spectroscopic multi-wavelength data are available. We leave this for a later consideration.

3.5 Summary and Conclusion

We divide a sample of >6,000 galaxies found in or near rich Abell clusters (z≤0.12) in the SDSS spectroscopic catalogue, into four populations, defined by placing simple limits in $(g-r)^{0.1}$ colour (derived from photometry) and specific star formation rate (derived from the detailed modelling of optical spectra). While most blue galaxies have evidence of star formation, and red galaxies do not, this identifies two significant populations of blue passive galaxies and red star-forming galaxies.

We trace the spectroscopic and photometric properties of galaxies in these four sub-samples in detail, using data available from SDSS DR4. The main results of our analysis can be summarised as follows:

- For the blue passive galaxies, the dust content and values for the D_n4000 are similar to those of the blue star-forming galaxies, indicating similar metal content, mean ages and internal extinction.

- Since the blue passive galaxies have a broad distribution of Hδ EW, along with late-type morphologies, they appear to be similar to the passive blue spirals studied by other authors. Our results support the hypothesis that these galaxies could be the progenitors of the red sequence galaxies in which star formation has been recently shut off due to the impact of local/global environment.

- An intriguing find of this study is that only ∼50% of the red star-forming galaxies have significant values of extinction, indicative of the presence of dust.

- By comparing the stellar metallicities, gas-phase metallicities and mean ages of the red and blue star-forming galaxies, we find statistically significant evidence in support of the fact that, for at least half of the red star-forming galaxies, the red colours result from a relatively metal-rich stellar population. Our argument remains valid even if the criterion

for classification as star-forming based on SSFR is changed within reasonable limits (15-50 percentile, instead of the 25-percentile used in this work).

- A significant (around 15%) fraction of the red star-forming galaxies have blue cores, indicating recent star formation which might be linked to the AGN activity in these galaxies.

- More than 30% of red star-forming galaxies are classified as AGN from their spectral emission lines.

- The population of passive red sequence galaxies increase toward the cluster centre, closely followed by the red star-forming galaxies, except that the latter does not rise steeply in the cluster core.

- The blue star-forming galaxies are distributed uniformly at 1-3r_{200} from the cluster centre, but decline steeply within r_{200}. The blue passive galaxies on the other hand show a constant distribution, except for a small increase around $2r_{200}$.

- Galaxy evolution studies which base their sample selection criterion only on broadband colours to test Butcher-Oemler like effects, may be significantly affected by the presence of 'complex' galaxy populations such as the red star-forming and blue passive galaxies discussed here.

Chapter 4

Star formation, starbursts and quenching across the Coma supercluster

4.1 Introduction

The Coma supercluster is the nearest rich supercluster of galaxies (Chincarini & Rood 1976; Gregory & Thompson 1978), consisting of two rich Abell clusters, separated by $30\,h_{70}^{-1}$ Mpc, but connected by a prominent filament of galaxies and poorer groups (e.g. Fontanelli 1984), which is part of the supercluster identified as the "Great Wall" in the first major redshift survey of galaxies in the nearby Universe (Geller & Huchra 1989). At a distance of $\sim 100\,h_{70}^{-1}$ Mpc, it affords a closer look at the properties of individual galaxies (1 kpc $\simeq$ 2.1 arcsec), but its large angular scale on the sky presents observational challenges for the narrow fields of view of most instruments.

It is interesting to note that even though they are the two most significant structures in the supercluster, the two Abell clusters are remarkably different in every respect. The optical luminosity function of galaxies in the Coma cluster, for instance, has a much steeper faint-end slope than that of its neighbour Abell 1367 (Iglesias-Páramo et al. 2003). Early studies (e.g. Dressler

1980) revealed that the fraction of spiral galaxies in the Coma cluster is anomalously low compared to Abell 1367. In addition, galaxies in the core of the Coma cluster were identified to be unusually deficient in neutral hydrogen (e.g. Sullivan & Johnson 1978; Giovanelli & Haynes 1985; Bernstein et al. 1994), ionised hydrogen (Raychaudhury et al. 1997) and molecular gas (H_2/CO) (Boselli et al. 1997a). Bothun, Schommer, & Sullivan (1984) found a strong H I gradient in Coma galaxies- many of the inner, H I poor spirals being quite blue, suggesting that some gas removal process has acted quite recently, while Abell 1367 was found to be a mixture of H I poor and rich galaxies.

The availability of more detailed analyses of star formation, based on multi-wavelength data, and of spectral indices sensitive to stellar ages, has made this field more interesting. Estimates of star formation activity from mid-infrared (IR) (Boselli et al. 1997b) and Galaxy Evolution Explorer (*GALEX*) ultraviolet (Cortese, Gavazzi, & Boselli 2008) photometry show that star formation in Coma on the whole is substantially suppressed compared to that in the field, while Abell 1367 has an abundance of bright star-forming galaxies (Cortese, Gavazzi, & Boselli 2008).

In a hierarchical model of the formation of structures in the Universe, it is not surprising that a rich cluster, with a relaxed appearance in its x-ray image, such as Coma, would represent the end product of the gradual assimilation of several galaxy groups over time. In spite of the claim of Dressler & Shectman (1988) that the Coma cluster does not have significant substructure, it has subsequently been shown to have at least three major subclusters in the optical (e.g. West 1998) and x-ray maps (e.g. Davis & Mushotzky 1993; Adami et al. 2005). At the other end of the supercluster, Abell 1367 is also found to be elongated with three major subclusters, along the axis of the filament, with a population of star-forming galaxies infalling into the SE cloud and possibly the other two as well (Cortese et al. 2004). This has prompted a multitude of studies attempting to link the dynamical history of the supercluster with the properties of individual galaxies to investigate both the process of building clusters, as well as the effect of large-scale

structure on the star formation history of galaxies (e.g. Haines et al. 2006b).

By employing the spectral analysis of galaxies in Coma, together with the x-ray map of Neumann et al. (2003), Poggianti et al. (2004) found that the post-starburst (k+A) galaxies, in which star formation has been quenched within the last 1-1.5 Gyr, are associated with the x-ray excess attributed to the substructure in Coma. However, this work was limited to 3 fields in the $\sim$2 Mpc region surrounding the centre of Coma.

In addition to star formation indices measured from optical spectra, the availability of *Spitzer* MIPS mid-IR observations has been recently utilised by several authors to characterise the star formation properties of the obscured component in galaxies in clusters and groups (e.g. Saintonge, Tran & Holden 2008; Haines et al. 2009; Wolf et al. 2009; Bai et al. 2010), since the 24μm flux can be used as a representation of the dust-reprocessed overall IR flux.

Hereafter, we will refer to the pair of clusters Coma and Abell 1367, along with the associated filament of galaxies as the Coma Supercluster. In this paper, we use the *Spitzer* MIPS 24μm observations, wherever available, along with the broadband colours and spectral star formation indicators from the SDSS. We adopt the distance modulus of the Coma Supercluster to be $m-M=35.0$, and use cosmological parameters $\Omega_\Lambda=0.70, \Omega_M=0.30$, and $H_0=70$ km s^{-1} Mpc^{-1} for calculating the magnitudes and distances. We note that at the redshift of Coma (z$=0.023$), our results are independent of the choice of cosmology. In the next section, we present our data and reduction methodology, and summarise our main results in §4.3 and §4.4. We discuss their implications, and compare the properties of galaxies in various parts of the supercluster in §4.5, summarising in §4.6.

4.2 Observational Data

The optical spectroscopic and photometric data used in this chapter are defined in §2.2. The 24μm MIR data are described in §2.3.2. In the following section we describe how the two

datasets are matched in position against each other.

4.2.1 Matching the SDSS spectroscopic catalogue with the 24μm sources

To match the SDSS spectroscopic catalogue for the Coma supercluster with the MIR 24μm data, we choose the nearest optical counterpart within 5″ of each 24μm source. This accounts for a displacement of no more than 2.5 h_{70}^{-1} kpc between the centres. We note that $\gtrsim$80% of the matches are found to have centres within 2″ of each other. None of our sources above the detection threshold were found to have multiple matches.

Our final dataset comprises of 3,787 galaxies ($r \leq 17.77$) with spectroscopic redshifts from SDSS, and radial velocity within $\pm$2,000 km s^{-1} of Coma or Abell 1367, in around 500 square degree region of the sky covered by the Coma supercluster. Out of these, 197 within $\sim$2 h_{70}^{-1} Mpc of the centre of Coma and 24 within $\sim$0.65 h_{70}^{-1} Mpc of the centre of Abell 1367 are found to have a 24μm counterpart. The catalogue of data for these 24μm detected galaxies is presented as Table A.1.

4.3 Star formation and AGN across the Coma supercluster

Located $\sim$100 Mpc from us, the Coma supercluster offers a unique opportunity for investigating the effect on individual galaxies of the hierarchical formation of structures in the Universe, as galaxies progress through various environments towards the cores of the clusters.

In order to give a general overview of the optical star formation properties of galaxies along the entire supercluster, in Fig. 4.1 we plot the positions of all the galaxies from the SDSS spectroscopic catalogue found in our redshift range, and the major galaxy groups obtained from the NED. In order to avoid multiple detections, we consider the groups only from the NGS, WBL, USGC and HCG catalogues, and even amongst these, we identify duplication by merging groups closer than 1′ and within $\pm$100 km s^{-1} of each other.

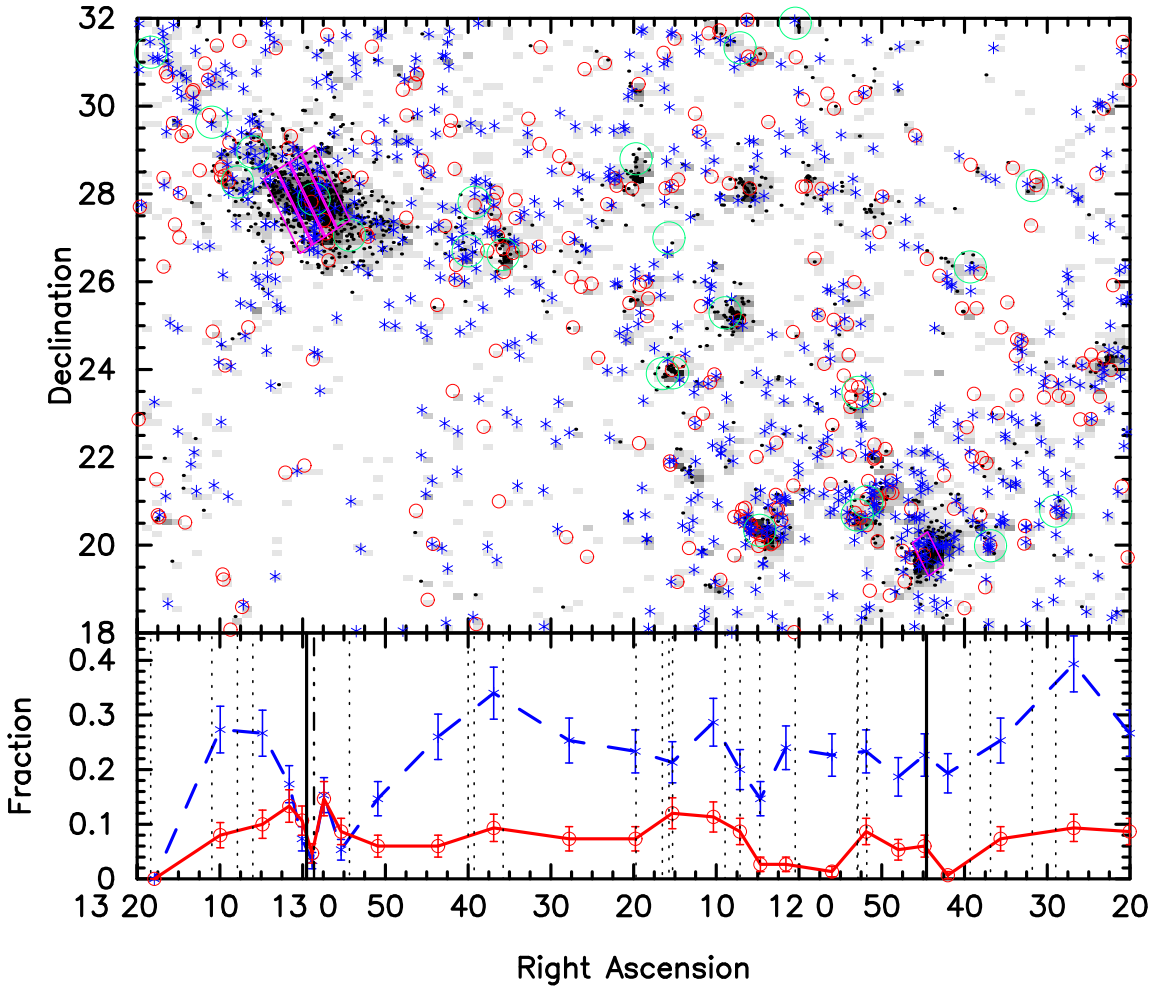

Figure 4.1: **Top panel:** The surface density of galaxies in the Coma supercluster is shown in *grey*. The positions of passive galaxies (*black dots*), AGN host galaxies (*open red circles*) and starburst galaxies *(blue stars)*; EW(Hα) $\geq$ 25Å$\sim$ log SSFR$\sim$ -10yr^{-1}) are indicated. The *big green circles* are the groups in the region, from the NASA Extragalactic Database. The rectangular pink regions show the *Spitzer* MIPS fields of view for the two clusters. **Bottom panel:** The *solid red* line and the *dashed blue* line show the fraction of AGN and of the starburst galaxies, among all the galaxies shown in the upper panel. The bins are chosen to have 150 galaxies in each of them. The solid vertical lines represent the centres of the Coma cluster and Abell 1367 respectively, while the *dot-dashed line* shows the RA position of the NGC 4839 group (see text). All the dotted lines represent the positions of groups, shown in the upper panel.

The positions of AGN host galaxies, identified using the BPT diagram (e.g. Baldwin, Phillips & Terlevich 1981; also see §4.4.2), and non-AGN starburst galaxies (star-forming on the BPT diagram, and having EW(Hα)$\geq$25Å), are indicated in Fig. 4.1. We also show the limited regions at the cores of the Coma and Abell 1367 clusters, over which the 24μm data are available, and utilised in this paper. Plotted in the bottom panel of the same figure is the distribution of the AGN and starburst galaxies, as fractions of the 150 galaxies contributing to each bin. It is worth mentioning that although these distributions are a fair representation of the data, the binning has resulted in a spurious feature at the position of Abell 1367. As is already well known in the literature, the central region of Abell 1367 is sparsely populated, the majority of galaxies in the core being late-type. In this figure, it appears that the fraction of starburst galaxies does not decline in the core of Abell 1367, but if the data is re-binned so as to have equally-spaced bins, this would not be the case. Having said that, the decline in the fraction of starburst galaxies at the centre of Abell 1367 is much shallower than that seen in Coma.

In general, the optically-identified AGN seem to be more or less uniformly distributed throughout the supercluster (Figs. 4.1 and 4.2), except for a sharp decline in the cores of both the clusters. This latter result is counter-intuitive, because AGN hosts are known to be early-type massive galaxies which mostly reside in dense environments. Hence, this may indicate that the optical emission from the AGN present in this region is obscured and/or detectable at other wavelengths (radio/x-ray). The latter is beyond the scope of this work, but our MIPS 24μm data supports the former possibility. As seen in Fig. 4.11, not only does the relative fraction of the red 24μm galaxies marginally increase towards the centre, around 50% of them are found within 0.5 h_{70}^{-1} Mpc of the centre of the Coma cluster, indicating that optical emission from several AGN hosts may be obscured. Further evidence in support of this argument may be drawn from Fig. 4.8 where a large fraction of galaxies detected at 24μm do not show [O III] and/or Hβ in emission, but their Hα/[N II] flux ratios are consistent with the presence of an AGN (Miller et al. 2003) on the BPT diagram (Baldwin, Phillips & Terlevich 1981).

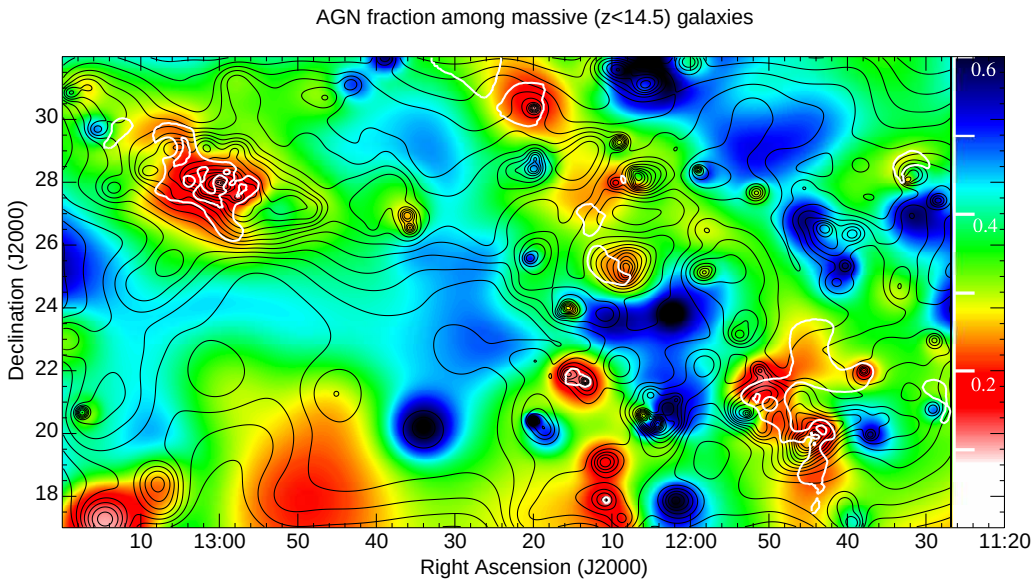

Figure 4.2: The local AGN fraction (f_{AGN}) among massive galaxies ($z<14.5$), as a function of spatial position across the Coma supercluster. The map is colour-coded with f_{AGN}. The *black contours* indicate the local luminosity-weighted (z-band) galaxy density across the supercluster. The *white contours* indicate regions with AGN fraction $f_{AGN}=1$ and 2-σ below the mean value over the supercluster.

We further investigate the environmental trends for AGN and star formation activity within the Coma supercluster, by estimating the local fraction of star-forming galaxies (f_{SF}) and AGN (f_{AGN}) over the entire supercluster, both for massive galaxies (e.g. $z<14.5$; $M_z<M^*+1.8$, assuming $M_z^*=-22.32$ from Blanton et al. 2001) and the dwarf galaxy population ($z>15$; $M_z>M^*+2.3$). Following Haines et al. (2007), we define the local projected density of galaxies ($\rho(\mathbf{x})$) using a variant of the adaptive kernel estimator (Silverman 1986; Pisani 1993), where each galaxy i is represented by an adaptive Gaussian kernel $\kappa_i(\mathbf{x})$. This is different from the algorithm of Silverman (1986), which, in its previous applications to astronomical data, requires the kernel width σ_i to be iteratively set to be proportional to $\rho_i^{-1/2}$. In this work, we fix the transverse width σ_i to be proportional to D_3, where D_3 is the distance to the third nearest neighbour within 500 km s^{-1}.

The dominant factors governing the star formation properties of a galaxy are the mass of its

DM halo, and whether it is the central or a satellite galaxy in a halo (Kauffmann et al. 2004; Yang et al. 2005; Blanton et al. 2006). We adopt the above method, and choose the dimensions of the kernel, keeping this in mind. In the case of galaxies within groups or clusters, the local environment is measured on the scale of their host halo (0.1–1 Mpc), while for galaxies in field regions the local density is estimated by smoothing over their 5–10 nearest neighbours or on scales of 1–5 Mpc (e.g. for details, see Haines et al. 2007).

We can then map the local galaxy density (ρ) and z-band luminosity density (j_z) as $\rho(\mathbf{x}) = \sum_i \kappa_i(\mathbf{x}-\mathbf{x}_i)$ and $j_z(\mathbf{x}) = \sum_i L_{z,i}\,\kappa_i(\mathbf{x}-\mathbf{x}_i)$, where $L_{z,i}$ is the z-band luminosity of galaxy i (see Fig. 4.3). Following Yang et al. (2005), we identify local maxima in the z-band luminosity density as galaxy groups and clusters, whose masses correlate with the total z-band luminosity associated with the peak. By comparison with the Millennium simulation, we expect all groups with 4 or more members to be associated with a local maximum in $j_z(\mathbf{x})$ (Haines et al. 2007). The local z-band luminosity density is shown as black contours in Figs. 4.2–4.4.

In Fig. 4.2 we show the spatial variation of f_{AGN} among massive galaxies ($z<14.5$) across the supercluster, where we calculate f_{AGN} as $\sum_{i\subset AGN} \kappa(\mathbf{x}-\mathbf{x}_i)/\rho(\mathbf{x})$, where $i\subset AGN$ is the subset of galaxies classified as optical AGN, based on the ratios of thermally excited and recombination lines used in the BPT diagram. We do not consider the lower mass galaxies, as the fraction of AGN declines rapidly to zero below $M_z > M^*+2$.

For comparison, Fig. 4.3 shows the distribution of $f_{SF}(\mathbf{x})$ as $\sum_{i\subset SF} \kappa(\mathbf{x}-\mathbf{x}_i)/\rho(\mathbf{x})$, where $i\subset SF$ is the subset of galaxies classified as star-forming according to the line-ratios used in the BPT diagram. Fig. 4.4 shows a map of the local mean equivalent width (EW) of Hα of star-forming dwarf galaxies as $\langle EW(H\alpha)(\mathbf{x})\rangle = \sum_{i\subset SF} \mathrm{EW(H}\alpha)\,\kappa(\mathbf{x}-\mathbf{x}_i)/\sum_{i\subset SF}\kappa(\mathbf{x}-\mathbf{x}_i)$, plotted in a manner analogous to that used by Haines et al. (2006b) for galaxy colours in the Shapley supercluster.

In Fig. 4.2 we see that the AGN fraction f_{AGN}, among massive galaxies ($z<14.5$) declines at the centre of the Coma and Abell 1367 clusters, while elsewhere, it is uniformly distributed.

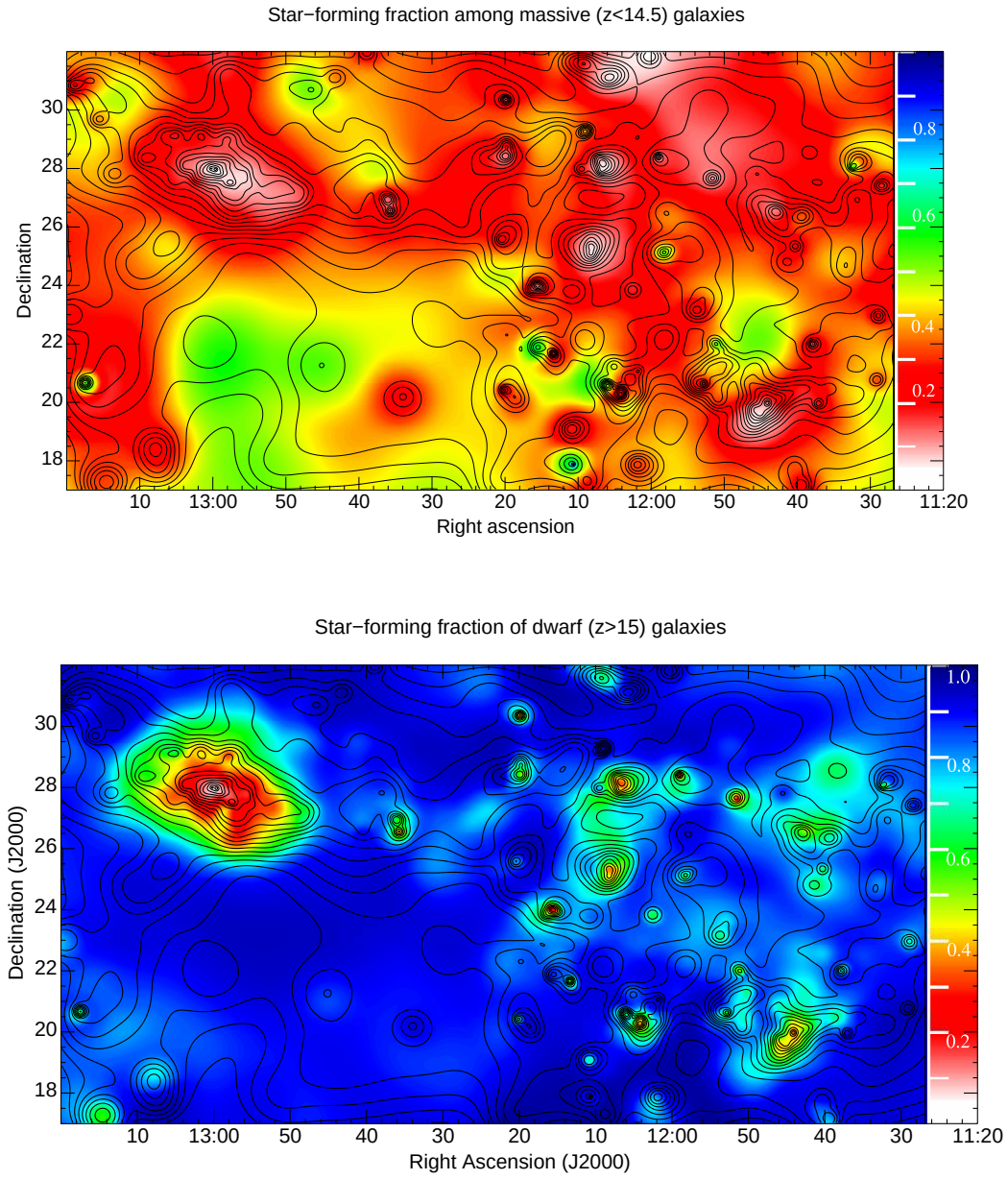

Figure 4.3: The local fraction of star-forming galaxies (f_{SF}) as a function of spatial position across the Coma supercluster, for massive galaxies ($z < 14.5$; *top panel*) and dwarf galaxies ($z > 15$; *lower panel*). The colours indicate f_{SF}, and the same colour scale is used in both the panels. Overlaid are black contours indicating the z-band luminosity-weighted galaxy density across the supercluster. This figure shows that in the Coma supercluster, star formation in the massive galaxies ($z < 14.5$) seems to be suppressed independent of their local environment, while the dwarf galaxies ($z > 15$) are star-forming everywhere except in the dense environment in the vicinity of rich clusters and galaxy groups.

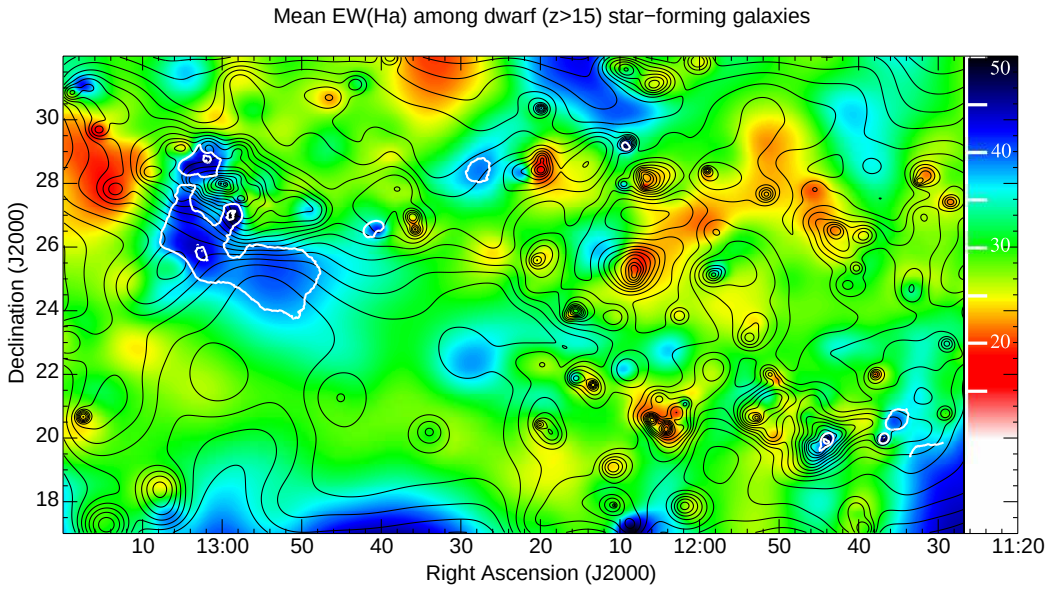

Figure 4.4: The local mean Hα equivalent width of star-forming (EW(Hα) > 2Å) dwarf ($z > 15$) galaxies across the Coma supercluster, indicated by colour. Overlaid are *black contours* indicating the z-band luminosity-weighted galaxy density across the supercluster, and *white contours* showing regions where the local observed mean value of the EW(Hα) is 2 and 3-σ above that averaged over the whole supercluster.

This appears to contradict the results of Haines et al. (2007), who found the AGN fraction to be independent of environment, and to be a monotonically increasing function of stellar mass. However, the volume studied by Haines et al. (2007) within SDSS DR4 did not cover clusters as rich as Coma or Abell 1367. This may indicate that only the very dense environments affect the optical AGN activity of galaxies. The relation between f_{AGN} and local environment is unclear in the intermediate density group environment. While the f_{AGN} values decline in the centre of some groups, in others they exceed the mean value for the field. Although there is a slight indication that the groups in which the f_{AGN} appears to be declining, mostly lie on the filament connecting the Coma and Abell 1367, or in the vicinity of the clusters themselves, while the groups with higher values of f_{AGN} lie in underdense regions. However, it is not possible to draw any firm statistical inferences from this observation.

Whether the AGN fraction f_{AGN} varies with environment or not depends on how the activity of the galactic nuclei is defined. Miller et al. (2003) do not find any correlation between galaxy

density and f_{AGN} in a large sample of galaxies ($M_r = -20; 0.05 < z < 0.095$), where the AGN are defined in terms of optical emission line ratios characterised by the BPT diagram. Other studies find higher incidence of optical AGN in groups and clusters (Arnold et al. 2009). If the AGN were selected according to their radio, mid-IR or x-ray properties, they would be found in different hosts: radio AGN in early-type galaxies, IR AGN in bluer galaxies, and x-ray AGN in galaxies of intermediate colour (Hickox et al. 2009). The environment dependence of AGN activity is thus largely linked to the distribution of the hosts. The incidence of x-ray AGN is higher in galaxy groups than in galaxy clusters (Martini et al. 2006; Shen et al. 2007). The fraction of radio-loud AGN is the same in the brightest galaxies of groups and clusters and in the field, but higher in non-central galaxies (Best et al. 2005). Del Pozzo et al. (2011) showed that the mass function of black holes is independent of environment, and the variation in the distribution of optical, radio and x-ray AGN can be understood in terms of the accretion processes that lead to the manifestation of the AGN in the various ranges of electromagnetic radiation.

We measured the significance of the spatial variations seen in f_{AGN} across the supercluster by performing Monte Carlo simulations, in which we made repeated maps of f_{AGN} after randomly assigning the positions of the AGN to the bright galaxies (i.e. testing the null hypothesis that f_{AGN} is constant across the supercluster), and measuring the fraction of maps in which a given local value of f_{AGN} was obtained within one of the Monte Carlo simulations. The results of these simulations are represented by the white contours, which indicate regions that have $f_{AGN} = 1$ and 2-σ below the mean value across the supercluster. This confirms that the decline in f_{AGN} seen towards the core of the Coma cluster is significant at the 3σ level, while that seen in Abell 1367 is significant at the 2σ level.

In Fig. 4.3 we show the general correlation between the fraction of star-forming galaxies (f_{SF}) and environment for massive galaxies ($z < 14.5$; top panel) and the dwarf galaxies ($z > 15$; bottom panel). For the massive galaxies we find an almost uniform $f_{SF} < 0.5$ in all the

environments. For dwarf galaxies, we see a much stronger SF-density relation, with f_{SF} rising rapidly from the $f_{SF} < 0.1$–0.4 seen in the cluster cores, to $f_{SF} > 0.95$ in the field. This result is in agreement with literature, where, using colour or SFR indicators, it has been shown that dwarf galaxies exhibit much stronger radial trends with environment than their massive counterparts (e.g. Gray et al. 2004; Tanaka et al. 2004; Smith et al. 2006; Haines et al. 2007 among others). The origin of the SF-density relation for the dwarf galaxies can be attributed to the fact that (i) the star formation in dwarf galaxies can easily be quenched by the tidal impact of a massive neighbour and/or the ICM of the cluster (e.g. Larson et al. 1980), and (ii) unlike their massive counterparts, dwarfs (of the luminosities considered here) do not become passive by internal mechanisms such as gas consumption through star formation, merging etc.. However, the effects of supernovae wind blowouts and feedback become significant for relatively faint ($M^* \lesssim 10^7$ M$_\odot$) dwarfs (e.g. Mac Low & Ferrara 1999; Marcolini et al. 2006). In this work we do not find any evidence for the quenching of star formation in galaxies on the filament(s), but only in the cores of the embedded galaxy groups.

The Hα emission traces the current SFR of a galaxy, while the continuum flux under this line can be used as an indicator of its past SFR, making the globally averaged EW(Hα) from a galaxy an effective indicator of the birthrate parameter ($b \equiv$ current SFR normalised by the SFR averaged over the lifetime of a galaxy). Recently, Lee et al. (2009) have shown that EW(Hα) ~ 40Å corresponds to $b = 1$. In Fig. 4.4 we show the variation in the mean EW(Hα) as a function of environment for the star-forming dwarf galaxies. This is potentially a very powerful technique for dissociating the intrinsically active star formation history (SFH) of low-mass galaxies from a starburst caused by the impact of local environment (see Haines et al. 2007 for instance).

If galaxies are slowly quenched by interactions with their environment (Balogh et al. 2004b), a decline in the mean EW(Hα) is expected in the regions of denser environment. On the other hand, if star formation is triggered due to the impact of environment, the mean EW(Hα) should

increase. Unlike the slow quenching of dwarfs in dense environments (Tanaka et al. 2004; Haines et al. 2007), here in the Coma supercluster, we find that the dwarf galaxies follow different evolutionary paths in galaxy groups and in the denser cluster environment. In galaxy groups, a dwarf galaxy is slowly quenched via interactions with the other group members and/or the tidal field of the group, while in the clusters, an infalling dwarf experiences a starburst in the intermediate density environment at the cluster periphery (Porter et al. 2008; Mahajan, Raychaudhury & Pimbblet 2011c), and is then rapidly quenched via cluster-related environmental mechanisms, such as ram-pressure stripping.

In analogy to Fig. 4.2, we measure the significance of the spatial variations seen in the mean EW(Hα) via Monte Carlo simulations, this time by making repeated maps after randomly swapping the values of EW(Hα) among the dwarf star-forming galaxies. In doing this, we seek to test the null hypothesis that the EW(Hα) is independent of spatial position among star-forming galaxies. In Fig. 4.4, we show, as overlaid white contours, the regions in which the local observed mean value of the EW(Hα) is 2 and 3σ above that averaged over the whole supercluster. This confirms that the excess star formation seen in the infall regions of Coma, and towards the core of Abell 1367, is indeed significant at $> 3\sigma$ level. In quantitative terms, this excess in the infall regions of the Coma cluster is due to a population of ~ 30 dwarf starburst galaxies ($z > 15$, EW(Hα) > 40Å) located within or along the white 2-σ contours in Fig. 4.4. The analogous excess in the core of Abell 1367 can be ascribed to ~ 10 starburst dwarf galaxies.

4.4 Optical and mid-IR analysis of Coma and Abell 1367 galaxies

The IR emission from normal galaxies around λ=24μm is dominated by hot dust in the H II regions of massive stars, in addition to (usually) minor contribution from asymptotic giant branch (AGB) stars and the general interstellar medium (ISM). This recycled emission, together with

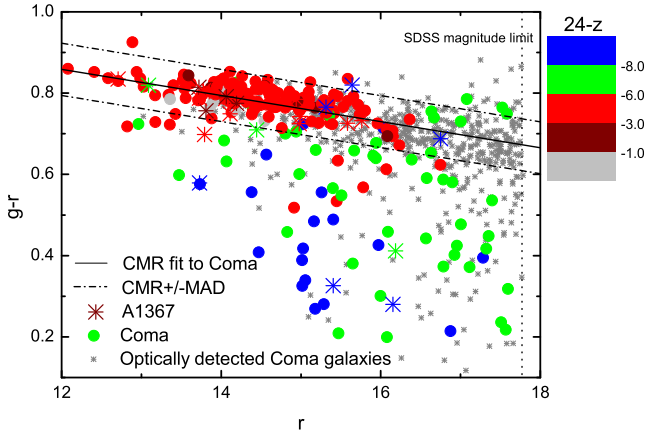

Figure 4.5: The $(g-r)$ vs r colour-magnitude relation for the 24μm bright galaxies detected in the Coma cluster (*circles*) and Abell 1367 (*big stars*). The solid line shows the colour-magnitude relation (CMR) fitted to the Coma data points, while the dot-dashed lines mark the mean absolute deviation (MAD) boundaries on either side. We adopt the lower MAD boundary in $(g-r)$ for segregating the red sequence from the blue cloud. Note that we do not use any upper bound for the red sequence because fitting is done using spectroscopically confirmed cluster members only. The symbols are colour-coded according to the $(24-z)$ colour of the MIR bright sources (Fig. 4.6). All the other Coma galaxies are shown as *grey stars*. Note that $(24-z)$ = -6 mag separates the red sequence galaxies from the blue ones in a $z-(24-z)$ plane (Fig. 4.6).

the optical emission, can thus provide a good estimate of the total starlight of a galaxy and be used to better constrain the current and past SFR of a galaxy (e.g. Calzetti et al. 2007; Kennicutt et al. 2009; Rieke et al. 2009 among others). While IR astronomers usually study late-type galaxies, early-type galaxies have received sporadic attention only in the context of the warm dust component detected in a few of them (e.g. Knapp et al. 1989).

In this chapter, we combine the optical photometric and spectroscopic data taken by the SDSS DR7, with the 24μm *Spitzer*/MIPS data, which is sensitive to processed optical emission from stars, to study the star formation activity of galaxies residing in the denser regions of the Coma supercluster.

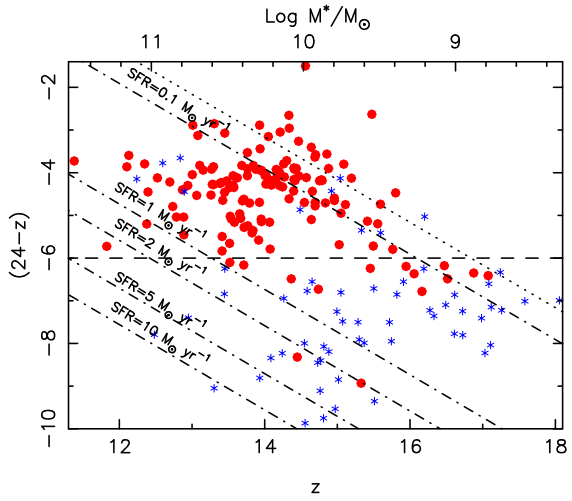

Figure 4.6: The $(24-z)$ colour of all galaxies in the Coma supercluster sample, divided into blue cloud (*blue stars*) and red sequence (*red*) (Fig. 4.5) galaxies, are plotted against their z-band magnitudes. The dotted line shows the 80% completeness limit of the 24μm data. The constant SFR lines are drawn using the conversion factor given by Calzetti et al. (2007). The horizontal dashed line at $(24-z) = -6$ mag is our empirically chosen criterion for selecting star-forming galaxies. The top axis shows the stellar mass of galaxies estimated using a relation from Bell et al. (2003).

4.4.1 Optical and MIR colours

In Fig. 4.5, we show the colour magnitude relation (CMR) for all the spectroscopic galaxy members ($r \leq 17.77$) found in this region in the SDSS DR7, and those that are also detected at 24μm in the *Spitzer*/MIPS observations. For comparison, the 24μm galaxies found in Abell 1367 are also shown. We only use galaxies brighter than $r = 15.5$. The CMR is of the form $g-r = 1.244-0.032\,r$ for all the Coma galaxies, where the mean absolute deviation from the relation is ± 0.064 mag.

We repeat this analysis in Fig. 4.6 for the near-infrared (NIR) band of SDSS (z-band), and the 24μm MIPS band. The galaxies classified as red and blue on the optical colour-magnitude diagram, split into two separate classes around $(24-z) = -6$ mag on the plot of the near/mid IR colour and magnitude as well. Although we overplot the lines of constant SFR in Fig. 4.6, according to the empirical relation given by Calzetti et al. (2007), it is important for the reader to consider that the 24μm flux alone is an accurate SFR indicator only for the late-type, dusty

star-forming galaxies (we return to this issue below). The SDSS z-band, centred at ~ 9000Å, is a good measure of the light from evolved stars, and hence the stellar mass of a galaxy. The top axis shows the stellar mass of galaxies estimated using the relation $\log M^* = -0.306 + 1.097(g-r) - 0.1 - 0.4(M_r - 5\log\ h - 4.64)$, from Bell et al. (2003). On the other hand, the 24μm MIPS band in the MIR is a good proxy for the dust-processed light. This makes the $(24-z)$ colour an excellent approximation for the value of the specific star formation (SSFR or SFR/M*) of galaxies.

Figs. 4.5 and 4.6 together show that the 24μm detected red sequence galaxies in Coma have consistent optical and MIR colours. We note that the optical-MIR colours of the red sequence galaxies are not consistent with those expected from photospheric emission from old stellar populations, with an excess emission always apparent at 24μm. The *Spitzer* Infrared Spectrograph observations of early-type galaxies in Virgo and Coma clusters show that the diffuse, excess emission, apparent at 10–30μm in these galaxies, is due to silicate emission from the dusty circumstellar envelopes of mass-losing evolved AGB stars (Bressan et al. 2006; Clemens et al. 2009). The strength of this silicate emission is a slowly declining function of stellar age (Piovan, Tantalo & Chiosi 2003), and persists even for very evolved stellar populations (> 10 Gyr). The optical-MIR colours of Virgo and Coma galaxies have been found to be consistent with such old stellar populations (Clemens et al. 2009).

The blue galaxies in Fig. 4.5 have a wide spread in both colour and magnitude. The inhomogeneity of this class of galaxies becomes even more clear in Fig. 4.7, where we plot the optical $(g-r)$ colour against the near/mid-IR $(24-z)$ colour. Just as in Fig. 4.5, the passive red galaxies cluster in a small region of the colour-colour space, but the blue galaxies and (optical) AGN span a wide range along both the axes. We note the clear separation of star-forming (blue stars) and passive (red points) galaxies in $(24-z)$ colour. The horizontal dashed line in Fig. 4.7 indicates our empirically chosen criterion to separate the two populations about $(24-z) = -6$. Interestingly, although the AGN and star-forming galaxies (green and blue symbols respec-

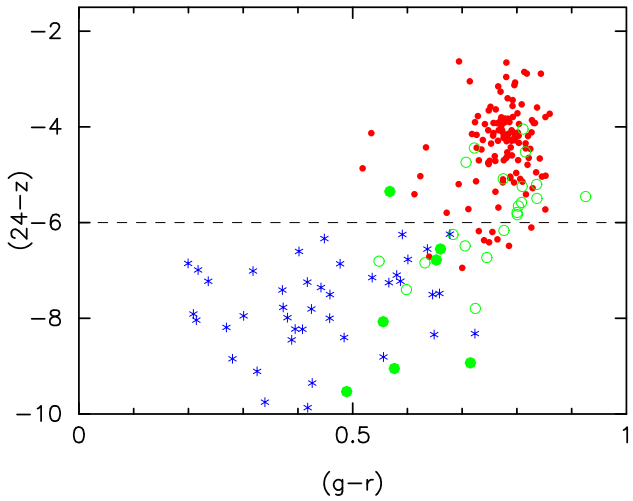

Figure 4.7: This colour-colour diagram shows that the galaxies identified as AGN (*green circles*) and star-forming (*blue stars*), on the basis of the BPT diagram according to their optical spectra (see Fig. 4.8), occupy different regions on the near/mid IR magnitude-colour diagram. The *solid* and *open green circles* represent AGN classified on the BPT diagram and by the Miller et al. (2003) criterion respectively (see text). The passive galaxies (*red points*) detected at 24μm are concentrated in a small region on the top right of the diagram. The horizontal line at $(24-z) = -6$ mag marks the boundary between these two classes in the z-$(24-z)$ IR colour magnitude space (Fig. 4.6).

tively) are classified on the basis of their optical spectra on the BPT diagram (e.g. Baldwin, Phillips & Terlevich 1981; also see §4.4.2), they occupy distinct regions in this plot of optical vs optical-IR colour, as well.

4.4.2 Optical and 24μm star formation indicators

The understanding of the formation of stars in galaxies requires, among other things, the measurement of the rate at which the interstellar gas is converted into stars. With the development of appropriate technology, radio, IR and UV photometry and spectroscopy are increasingly being employed, in addition to the traditional optical observations, for the purpose of measuring the rate of star formation. The dust clouds surrounding the young stellar concentrations absorb starlight and re-radiate it at IR wavelengths. Thus, the SFR measured by IR measurements is accurate only in the optically thick limit. The observed UV radiation escaped from the molecu-

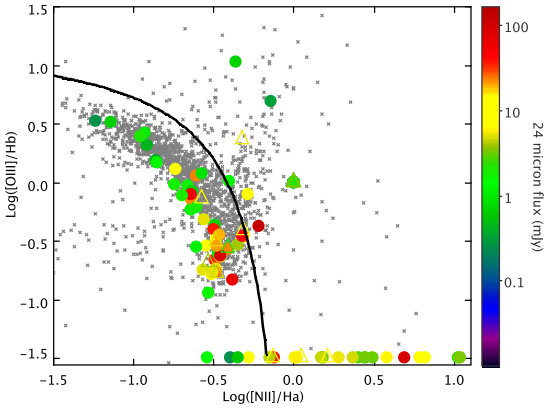

Figure 4.8: The BPT diagram (Baldwin, Phillips & Terlevich 1981) for the 24μm detected galaxies in the Coma cluster (*filled circles*) and in Abell 1367 (*open triangles*), colour coded by their 24μm flux. We also plot all the galaxies within $\pm$ 2,000 km s^{-1} of Coma or Abell 1367, in the 500 square degree supercluster region, but not detected at 24μm, as *grey crosses* . The points plotted in a line at log[O III]5007/H$_\beta = -1.5$ are the galaxies which have no detected [O III] and/or H$_\beta$ emission. It is interesting to observe that a large fraction of the Coma galaxies without [O III] and/or Hβ have their [N II]/Hα flux ratios as expected for AGN, suggesting that these galaxies may have their nuclear emission obscured. We classify such galaxies as AGN if they have Log([N II]/Hα)>-0.2 (Miller et al. 2003).

lar clouds which block the UV light at earlier ages, comes mostly from stars with ages 10^7 - 10^8 yrs (Calzetti et al. 2005). Hα emission is produced only in the first few million years from the most massive stars (Leitherer et al. 1999). Indeed, a combination of UV, Hα and IR observations is required to give a full measure of the obscured and unobscured star formation (see chapter 8). In this section, we attempt to combine the direct (optical) and the obscured (IR) radiation from the Coma and Abell 1367 galaxies to understand the process of star formation across this supercluster.

The 24μm IR emission in galaxies can result from dust heated by young massive star clusters as well as the AGN. Since our MIPS data comes from the densest regions at the core of the Coma cluster (Fig. 4.1), which is a favourable environment for AGN hosts, it is important to investigate the origin of the 24μm emission in these galaxies. To do so, in Fig. 4.8 we plot the usual ratios of optical emission linewidths ([O III], Hβ, [N II] and Hα), known to distinguish star forming galaxies from those dominated by AGN, in what is popularly known as the BPT

diagram (Baldwin, Phillips & Terlevich 1981).

In Fig. 4.8, we show all the emission-line galaxies found in the $\pm$2,000 km s^{-1} redshift slice around Coma and/or Abell 1367, in the $\sim$500 square degrees Coma supercluster region (see Fig. 4.1), along with the galaxies detected at 24μm (MIPS) in Coma (circles) and Abell 1367 (open triangles). Although we find a significant number of 24μm detected galaxies with [N II]/Hα ratios suggestive of AGN, this does not mean that the 24μm emission is predominantly due to AGN. Goulding & Alexander (2009) have tried to estimate the contribution of the AGN component to the IR emission from galaxies using *Spitzer*/IRS spectroscopy. Although only a few galaxies in their sample have IR fluxes produced predominantly by AGN, they also find that a substantial fraction of AGN are optically obscured, consistent with the results presented here.

We find that most of the galaxies which have measured values of all four emission lines are dusty star forming galaxies. However, interestingly, a large number of galaxies detected at 24μm in Coma that do not show emission in [O III] and/or Hβ, do have a [N II]/Hα flux ratio consistent with the presence of an AGN. Such galaxies can be classified as AGN if $\log$ ([N II]/Hα)$>$-0.2 (Miller et al. 2003).

The EW of the balmer lines, especially that of the Hα emission line, has been extensively used to estimate the current optical SFR of galaxies. It has been shown in the literature that the 24μm flux is a good measure of dust-processed star light (e.g. Calzetti et al. 2007). But, the 24μm observations used in this work cover the very central regions of the Coma cluster, and Abell 1367, which comprises mostly of early-type galaxies. In order to test the correspondence between the direct and dust-processed SFR tracers, in Fig. 4.9 we plot the $(24-z)$ colour as a function of spectroscopically measured EW(Hα). We also colour-code the symbols according to the concentration parameter of the galaxies (ratio of the Petrosian radii R_{90r}/R_{50r} from the SDSS photometric catalogue, which is an indicator of morphology), to show that the early and late-type galaxies are uniformly distributed along both the axes. Passive spirals often have

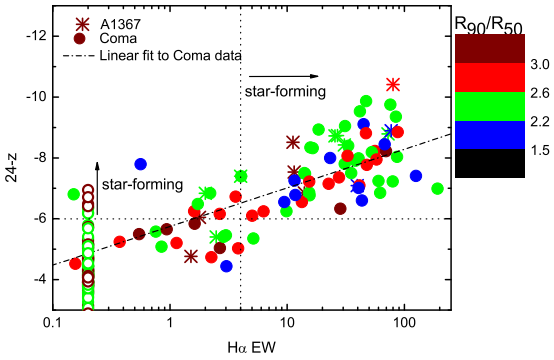

Figure 4.9: The $24-z$ colour as a function of Hα EW for Coma (filled circles) and Abell 1367 (stars) galaxies respectively. The straight line represents the linear fit to galaxies in the Coma cluster. Though there is a considerable scatter, the correlation between the two quantities is significant. The dotted lines represent the lower limits adopted to select star-forming galaxies using (Hα EW=4Å) and $24-z$ colour$= -6.0$ (see Fig.4.6). For completeness, we also show the 24μm detected galaxies that do not have Hα emission in SDSS spectra at EW(Hα)$=0.2$Å (*open circles*). The 24μm emission in these galaxies is likely to come from the evolved AGB stars.

concentration indices consistent with early-types (e.g. $R_{90r}/R_{50r} > 2.6$; also see Mahajan & Raychaudhury 2009). But Fig. 4.9 implies that the emission-line galaxies detected at 24μm at the core of Coma and Abell 1367 are not dominated by galaxies of any particular morphological type (as quantified by the concentration index).

Due to the dominance of early-type galaxies in our 24μm sample, it is not surprising that only a small fraction of galaxies classified as star-forming on the basis of their $(24-z)$ colour (Fig. 4.6), show no signs of current star formation in their optical spectra. For completeness, at EW(Hα)$=0.2$Å we plot all the 24μm detected galaxies that do not show optical emission in Hα. As expected, most of these galaxies have $(24-z)$ colours and concentration parameters consistent with those of quiescent early-type galaxies. This suggests that their 24μm emission is primarily due to the contribution from AGB stars, which (unlike young stars) do not produce Hα emission. The good overall correspondence between the photometric $(24-z)$ colour and spectroscopic EW(Hα) makes the $(24-z)$ colour a good candidate for comparing the star formation activity in nearby galaxies, in the absence of optical spectra.

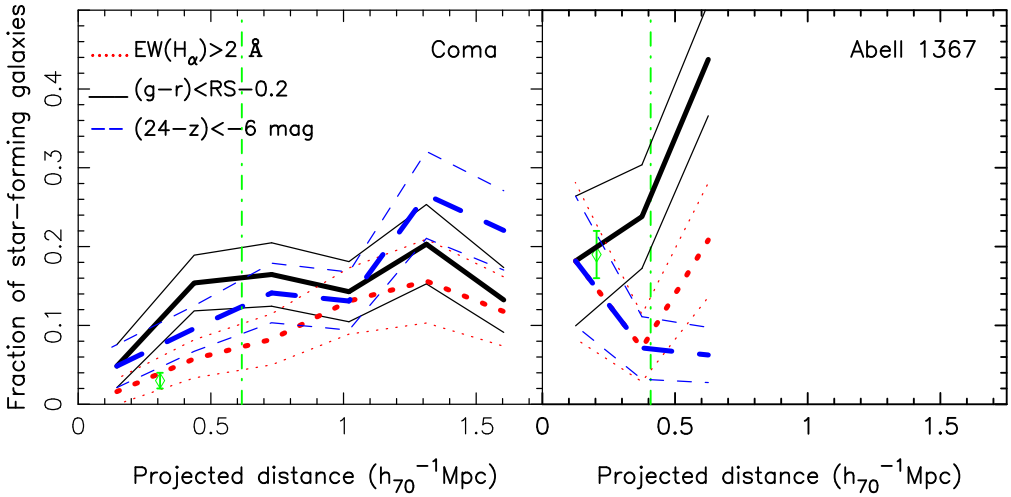

Figure 4.10: The fraction of star-forming galaxies as a function of (projected) cluster-centric radius for Coma in the *left* panel and Abell 1367 on the *right*. In both panels, the *solid black line* shows the radial variation in the fraction of star-forming galaxies, selected using the $(g-r)$ colour threshold, the *dotted red line* makes use of the Hα EW ($\geq$2Å) and the *dashed blue line* represents the same, for star-forming galaxies chosen by the $(24-z) < -6$ criterion. The corresponding *thin curves* show the $\pm 1-\sigma$ Poisson scatter. In all cases, all the spectroscopically identified galaxy members with $M_z < -20.82$ ($M_z^* + 1.5$; see text), and l.o.s. velocity $\pm$ 3,000 km s^{-1} of Coma and/or Abell 1367, are used to estimate the fractions. For Abell 1367, we show galaxies only within the region, of scale $\sim$0.75 h_{70}^{-1} Mpc, for which the 24μm data is available. This diagram shows the importance of taking account of the star formation activity used to quantify and understand evolutionary trends, such as the Butcher-Oemler effect. For comparison, the R_{30} radius adopted by Butcher & Oemler 1984, and the fraction of blue galaxies found in Coma and Abell 1367, are also shown by the vertical *dot-dashed lines* and *open green diamonds* respectively.

4.4.3 Varying fractions of star-forming galaxies with SFR tracer: implications for the Butcher-Oemler effect

Photometric colours and EWs of emission lines like O II and Hα have been extensively used for studying the evolution of galaxies in time and across the sky. In one such pioneering work, Butcher & Oemler (1984) found that clusters at moderate to high redshifts contain an 'excess' of blue galaxies, relative to their local counterparts. They estimated the blue fraction by considering galaxies found within R_{30} (radius containing 30% of all red sequence galaxies), for which the optical broadband colours are bluer by at least 0.2 mag than that of the red sequence

galaxies. For the redshift regime of Coma (≤ 0.1), BO84 found a uniform blue fraction within R_{30}. Since then, several such studies have sought to quantify and validate the Butcher-Oemler effect for different samples of clusters. Some of these define their samples in a way similar to that of BO84, and obtain similar results (e.g. Margoniner & Carvalho 2000).

Using panoramic MIR data for 30 clusters (including both Coma and Abell 1367) over $0 < z < 0.4$, Haines et al. (2009) are able to reproduce the Butcher-Oemler effect using a fixed limit in L_{IR} ($5{\times}10^{10} L_{\odot}$) (equivalent to a fixed SFR of $8\,M_{\odot}yr^{-1}$), but show that the Butcher-Oemler effect can be largely explained as a consequence of the *cosmic* decline in star formation (Le Floc'h et al. 2005; Zheng et al. 2007). In this case, the blue galaxies in clusters are those that are recently accreted from the field (e.g. accretion has occurred at a relatively constant rate since $z \sim 0.5$; Berrier et al. 2009), but since the global level in star formation among these galaxies has declined, a smaller fraction of the infalling population is classed as blue (which assumes a non-evolving level of star formation), resulting in the observed Butcher-Oemler effect.

Elsewhere, studies (Balogh, Navarro & Morris 2000; Ellingson et al. 2001; De Propris et al. 2004) going out to several multiples of the cluster-centric radius, scaled by R_{200}, show the effect of the chosen aperture size on the blue fraction. It has been shown that the observed gradual radial trend of f_{SF} is consistent with a simple infall scenario, whereby the star-forming galaxies are infalling field galaxies, which are then quenched rapidly upon their first passage through the cluster core (Balogh et al. 2000; Ellingson et al. 2001; Haines et al. 2009). By comparing the photometric colour with the spectroscopically determined SSFR, Mahajan & Raychaudhury (2009) show that the presence of metal-rich stellar populations in low redshift cluster galaxies can also influence the evolutionary trends such as the Butcher-Oemler effect, if they are studied only using galaxy colours. Several recent studies indicate that a non-negligible fraction of red sequence galaxies show signs of ongoing star formation from their optical spectra and/or broad-band colour, and that a robust separation of passive and star-forming galaxies requires mutually independent data (e.g. Bildfell et al. 2008). In this work, we show that in the

Coma Supercluster, the value of f_{SF} not only varies with the cluster-centric aperture used for measuring the blue fraction, but can also be severely effected by the SFR tracer employed.

In Fig. 4.10 we plot the fraction of non-AGN, star-forming galaxies found using three different criteria: (i) IR colour [$(24-z) \leq -6$ mag; Fig. 4.6], (ii) EW(Hα)$\geq$ 2Å and, (iii) the photometric colour $(g-r)$ is bluer than that of the fitted red sequence (Fig. 4.5, by more than the mean absolute deviation, for all the Coma and Abell 1367 galaxies. BO84 had included galaxies brighter than $M_V = -20$ ($H_0 = 50$ km s^{-1}Mpc^{-1}) in their sample. To make a fair comparison with the work of Butcher & Oemler (1984), without adding uncertainties by using empirical relations to convert magnitudes from one passband to the other, in Fig. 4.10 we choose to only include galaxies brighter than $M_z^* + 1.5$ (e.g. $M_z^* = -22.32$; Blanton et al. 2001) for calculating the fractions. Also, note that *all* the spectroscopic galaxy members are used to calculate the fractions in each radial bin.

These distributions show that, by taking into account the obscured star formation estimated from the 24μm flux, the fraction of star-forming galaxies can dramatically vary at any given radius from the centre of the cluster. In both clusters, the 'blue' fraction (f_b) is higher, and flattens at lower cluster-centric radii, than the f_{SF} estimated using the EW(Hα), evidently showing a significant contribution of the post-starburst galaxies to the fraction f_b (also see Section 4.5.2). We note that this trend may vary if the dusty red galaxies have a non-negligible contribution in building the red sequence (also see Chapter 8). But as seen in Fig. 4.5, in the Coma cluster, this does not seem to be the case.

It is interesting to note that unlike Coma, Abell 1367 has an increasing fraction of blue galaxies with cluster-centric radius (black lines), but an inverse trend emerges when the fractions are measured using the $(24-z)$ colour (blue lines) or the Hα EW (red lines). This implies that some of the blue galaxies outside the core of Abell 1367 are post-starburst galaxies (see Fig. 4.12). This result supports the results obtained in our general work by Mahajan & Raychaudhury (2009) (chapter 3), where we showed that using a single galaxy property, such as

the broadband colour, is not an appropriate way of quantifying evolutionary trends like the Butcher-Oemler effect.

4.5 Discussion

In this chapter we set out to understand the relationship between the star formation activity in galaxies, as depicted by an assortment of indicators encompassing the optical and 24μm mid-IR wavebands, and their immediate and global environment, in the Coma supercluster. A wide range of local and global environments of galaxies, and a uniform optical coverage across the entire ~ 500 square degrees of sky, make this supercluster an ideal laboratory for examining the environmental dependence of galaxy properties. We discuss below the implications of the results from our analysis presented in §4.3 and §4.4.

4.5.1 The spatial and velocity distribution of galaxies detected at 24μm

The 24μm data for the Coma cluster extend out to a few times its core radius (Fig. 4.10), allowing us to analyse the spatial (sky and velocity) distribution of the galaxies detected at 24μm, relative to all the spectroscopic members found in the SDSS. In order to do so, in Fig. 4.11, we plot the distribution of all the spectroscopic galaxies, and the (optically) red and blue galaxies detected at 24μm respectively. As discussed above (Figs. 4.5 and 4.6), in Coma both the 24μm and optical colours mostly segregate the same galaxies into 'red' and 'blue' ones. Fig. 4.11 (top panel) shows that, of the 24μm detected galaxies, the distribution of the (optically) red ones is similar to that of all the galaxies, but the (optically) blue ones tend to peak $\gtrsim$1.0 h_{70}^{-1}Mpc from the centre of Coma.

In Fig. 4.11 (bottom panel), we plot the distribution of the line of sight (l.o.s.) velocities of galaxies, with respect to the mean velocity of the Coma cluster (called the 'relative velocity' hereafter), for the same three sets of galaxies. The distribution of the relative velocity of 'all'

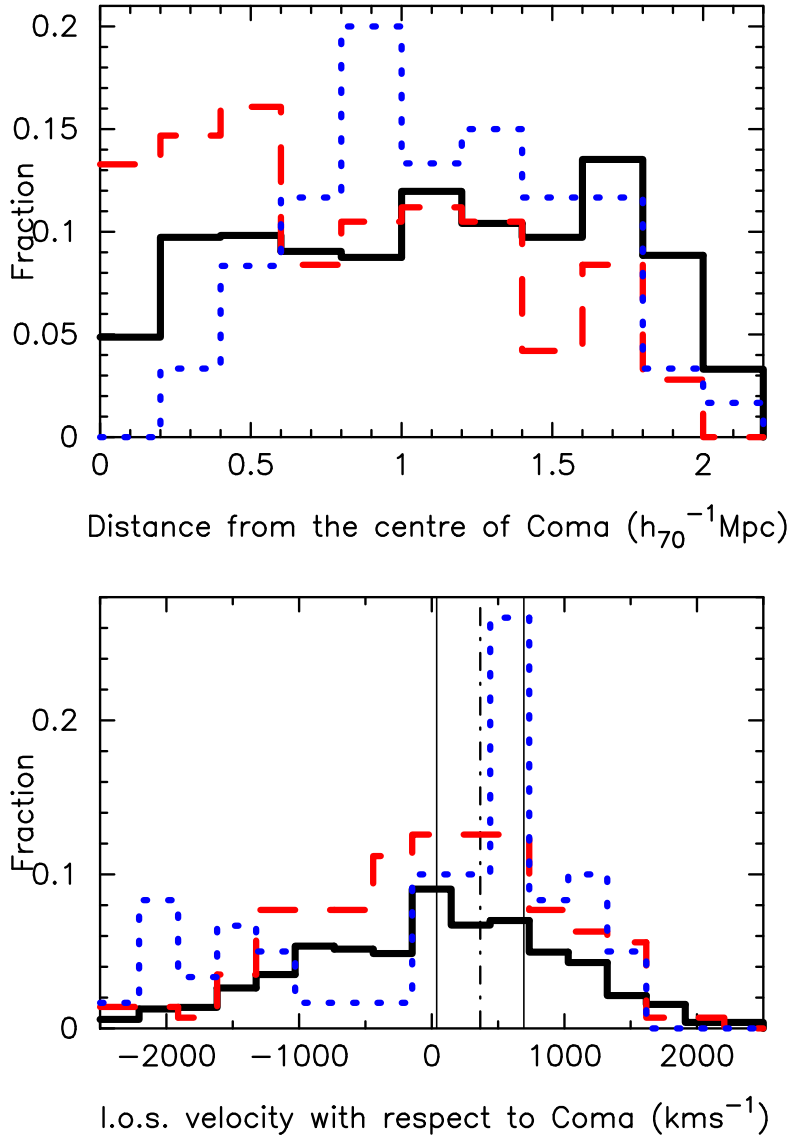

Figure 4.11: *(top panel):* The distribution of cluster-centric distance for all the spectroscopically identified galaxies in a $\pm$3000 km s^{-1} slice in the Coma cluster (*thick black* histogram). The *solid red* and *open blue* histograms show the same for the 24μm MIPS galaxies, divided into red and blue galaxies on the basis of the $(g-r)-r$ colour-magnitude plot (Figs. 4.5 & 4.6). The horizontal axis is limited by the coverage of the MIPS field. Interestingly, even though the red 24μm galaxies are uniformly distributed within a $\sim$2 Mpc radius, the blue galaxy population seems to peak away from the cluster core at 1–1.5 Mpc from the centre. *(bottom panel):* These histograms represent the the same galaxies as in the upper panel, but for the l.o.s. velocity of galaxies, relative to the mean redshift of the Coma cluster. Intriguingly, while the red galaxies follow the distribution of *all* the spectroscopic galaxy members of the Coma cluster, the blue 24μm galaxies show a remarkable peak around the velocity of the galaxy group NGC 4839, shown here as the *dot-dashed* line, with $\pm\sigma_v = 329$ km s^{-1} (Colless & Dunn 1996).

and (optically) red galaxies are statistically similar. But the (optically) blue 24μm galaxies show a bimodal distribution, with a large fraction of one mode concentrated around relative velocity $\sim$ 600 km s^{-1}. A Kolmogorov-Smirnoff (K-S) test suggests that the probability of the parent distribution of the relative velocities of red and blue galaxies being sampled from the same population is $p = 8.023 \times 10^{-5}$. The same comparison between the relative velocity distribution of 'all' and blue galaxies gives $p = 0.005$, suggesting that it is highly unlikely that the blue and red (or 'all') galaxies are drawn from the same parent distribution (Fig. 4.11). This leads us to conclude that a non-negligible fraction of the (optically) blue 24μm galaxies within $2\,h_{70}^{-1}$ Mpc of the centre of the Coma cluster are star-forming galaxies which may belong to the substructure associated with NGC 4839 (see §4.5.3 for further discussion).

The l.o.s. velocity distribution of the (optically) blue 24μm galaxies is highly non-Gaussian, with an excess at $\sim$600 km s^{-1}, suggesting that many of them have recently entered the cluster. If these blue 24μm galaxies were virialized, a Gaussian distribution centred on 0, like that seen for the red (red dashed histogram) and 'all' (solid black histogram) galaxies would be expected.

The current episode of star formation in these galaxies can be attributed to the environmental impact of the cluster's ICM (e.g. Poggianti et al. 2004), or the enhanced galaxy density in the infall region (e.g. Mahajan, Raychaudhury & Pimbblet 2011c). This result is consistent with the findings of Caldwell & Rose (1997), who analysed the spectra of early-type galaxies in 5 nearby clusters, including Coma, and found that in 4 of the 5 clusters, the early-type galaxies show signatures of recent star formation in their spectra (also see §4.5.2).

4.5.2 The distribution of k+A galaxies

The post-starburst, or k+A galaxies, as they are popularly known in the literature, are passive galaxies that have recently (1-1.5 Gyr) experienced a strong burst of star formation. These galaxies are very crucial in understanding the impact of environment on various galaxy properties, especially their SFR. The spectrum of a k+A galaxy shows strong absorption in Hδ, but

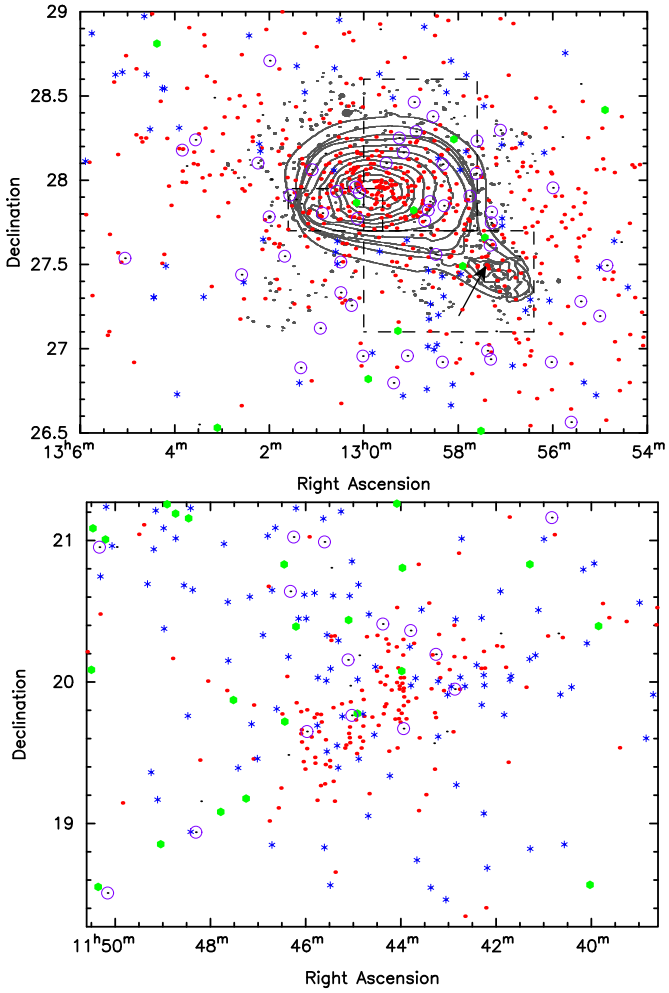

Figure 4.12: **(Top):** The distribution of the passive *(red dots)*, AGN host *(green points)*, star-forming *(blue stars)* and the post-starburst (k+A) *(purple circles)* galaxies in $\sim 5.0 \times 4.2\, h_{70}^{-1}$Mpc region surrounding the centre of Coma. The contours show x-ray emission from a *XMM-Newton* EPIC/PN observation. As can be noticed, not only the star-forming, but also the k+A galaxies seem to avoid the dense cluster centre. Also, the presence of k+A galaxies out to almost twice the virial radius from the centre shows how strong the impact of the 'global' cluster environment is on the evolution of galaxies in the vicinity of massive structures. **(Bottom):** Same as above, but for the $5.0 \times 5.0\, h_{70}^{-1}$Mpc region surrounding the centre of Abell 1367. It is interesting to see that in contrast with Coma, most of the k+A galaxies in Abell 1367 seem to be aligned along the direction of the filament feeding it from the direction of Coma. We also note that the (optical) AGN in both the clusters are mostly found in the direction of the filament connecting Coma and Abell 1367.

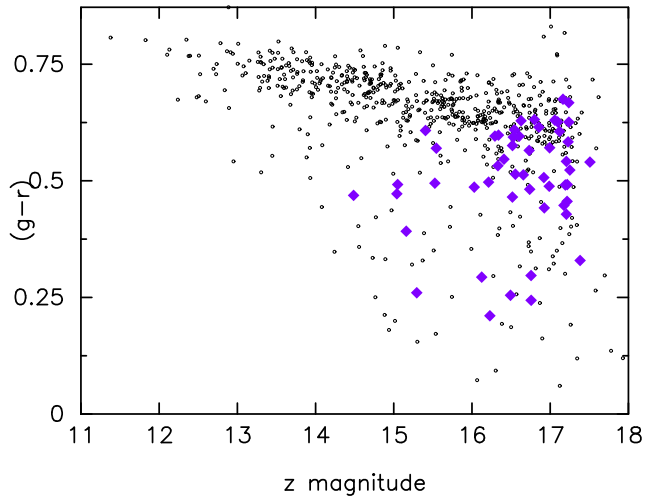

Figure 4.13: The $(g-r)-z$ colour-magnitude diagram of all the spectroscopically identified galaxies *(black points)* in the $\sim 5.0 \times 4.2\, h_{70}^{-1}$Mpc region surrounding the centre of the Coma cluster (shown in Fig. 4.12). The k+A galaxies *(purple diamonds)* are mostly blue dwarfs. These observations confirm that the low-mass galaxies are the first ones to experience and reflect the impact of rapid change in their local environment.

little or no emission in Hα.

In this work we make use of the SDSS DR7 spectroscopic galaxy catalogue ($r \leq 17.77$) for identifying the k+A galaxies (EW(Hδ) < -3Å & EW(Hα) < 2Å) in the Coma supercluster (Please note that throughout this work, negative values of EW indicate absorption). In Fig. 4.12 we show these k+A galaxies together with the passive, star-forming and AGN galaxies in and around the Coma and Abell 1367 cluster respectively. As can be easily seen, the k+A galaxies preferentially avoid the dense region in the cluster core but inhabit the surrounding infall regions out to $\sim 5\, h_{70}^{-1}$Mpc (almost twice the virial radius). In Fig. 4.12 we have also over-plotted the contours of intensity from the mosaiced 0.5–2 keV image of the core of Coma cluster from XMM-Newton EPIC/PN observations (Finoguenov, Briel & Henry 2003), kindly supplied to us by A. Finoguenov. We note that there are almost no star-forming galaxies in the x-ray emitting region of the core. This observation further strengthens the argument that the changes in environment experienced by a galaxy on the outskirts of clusters play a key role in modulating the properties of galaxies, especially the dwarfs (e.g. Porter & Raychaudhury 2007; Porter et

al. 2008).

By analysing deep ($M_B \lesssim -14$) photometric and spectroscopic optical data for 3 regions in Coma (two near the centre and one near NGC 4839, each $\sim 1 \times 1.5$ Mpc in size), Poggianti et al. (2004) found that $\sim$10% of the cluster's dwarf ($M_V > -18.5$) galaxies have post-starburst spectra. They also used the results from the x-ray analysis of Neumann et al. (2003) to show that the k+A galaxies in the Coma cluster are likely to be a result of the interaction between the Coma cluster and the adjoining NGC 4839 galaxy group (see §4.5.3). In Fig. 4.12, we overplot as dashed rectangles, the approximate location of the substructures found by Neumann et al. (2003) in the temperature map. As has been shown by (Poggianti et al. 2004; their Fig. 6), on the western side of the Coma cluster, the k+A galaxies seem to lie along the x-ray temperature substructure (e.g. also see Fig. 2 of Neumann et al. 2003). We demonstrate this by overplotting contours of x-ray intensity in Fig. 4.12.

However, it is also interesting to note that the southern substructure, apparent from the x-ray surface brightness contours, is almost devoid of k+A galaxies, but has a stream of star-forming dwarf galaxies flowing towards the cluster core (Fig. 4.4; also see §4.5.4). Contrary to Poggianti et al. (2004), by taking into account the extended region surrounding the Coma cluster, we find that the k+A galaxies preferentially avoid the cluster core but their spatial distribution does not show any correlation with the substructure evident in the x-ray temperature map of the gas (Fig. 4.12).

In Fig. 4.13 (also see Fig. 4.1) we examine the position of the k+A galaxies in the Coma cluster in the plot of $(g-r)$ colour vs z magnitude. Fig. 4.13 show that almost all the k+A galaxies in Coma are dwarfs ($z \lesssim 15$), suggesting that either only the infalling dwarf galaxies are rapidly quenched, or the SFR-M^* relation (e.g. Feulner et al. 2005) dilutes the post-starburst signature in massive galaxies. Since dwarf k+A galaxies in the Coma supercluster are found on the outskirts of Coma and Abell 1367 clusters, and occasionally in galaxy groups embedded elsewhere in the large-scale structure (LSS), this might suggest that dwarf galaxies falling into

Table 4.1: Dwarf ($z > 15$ mag) galaxies in the Coma supercluster

	Total	Star-forming	k+A
Coma ($\sim 5 \times 4.2$ Mpc^2; Fig. 4.12)	438	55	50
Abell 1367 ($\sim 5 \times 5$ Mpc^2; Fig. 4.12)	391	203	19
Supercluster (excluding regions mentioned above)	1106	667	23

deeper potentials are more likely to show k+A features, while those being assimilated into galaxy groups may be quenched on a longer time-scale. We discuss this in greater detail in chapter 7.

The handful of galaxies with very blue colours ($(g-r) < 0.5$; Fig. 4.13) are the k+A dwarfs in which the episode of starburst could have ended ~ 300 Myr ago, unlike the more evolved red post-starburst dwarfs (Poggianti et al. 2004) (Fig. 7.1). By studying spectra of early-type galaxies ($M_b < 16.7$) in Coma, Caldwell & Rose (1997) also found that $\sim 15\%$ of these galaxies show signatures of recent or ongoing star formation. Based on this result, Caldwell & Rose (1997) suggested that the present day clusters act as a catalyst for galaxy evolution, though at a reduced level as compared to their high redshift counterparts.

Given the vulnerable nature of dwarf galaxies, it is not surprising that a large fraction of them are the first ones to reflect the impact of rapid changes in their environment during the transition from filament to cluster. This contributes to dwarf galaxies having a better-defined SF-density relation, relative to their more massive counterparts (Fig. 4.4). Table 4.1 shows that 11.4% of dwarfs in Coma, 4.8% in Abell 1367 and 2.1% in the neighbouring supercluster region have spectra with k+A features. This evidently shows that the mechanisms responsible for quenching star formation in dwarf galaxies and rapidly transforming them to passive galaxies via the post-starburst phase, are strongly dependent on the cluster potential. This result is also in agreement with the observation of excessive red, dwarf ellipticals (dEs) in the Coma cluster (Jenkins et al. 2007). In Table A.2 we provide a list of all the 110 k+A dwarf ($z > 15$) galaxies found in the

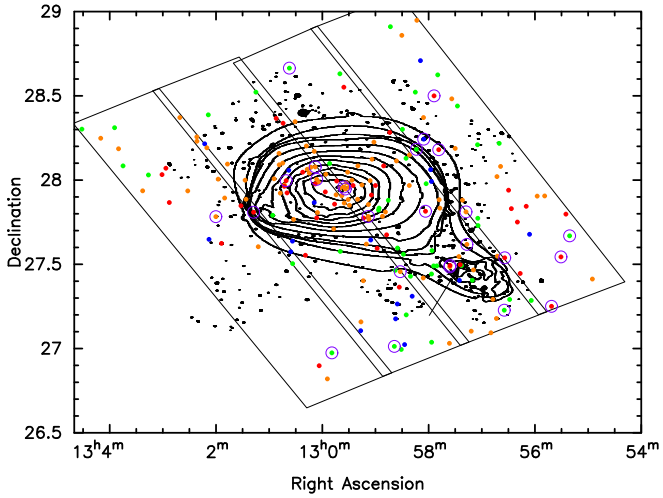

Figure 4.14: The spatial distribution of galaxies detected at 24μm in the Coma Supercluster region. The galaxies are coded by their $(24-z)$ colour as following: red:>-4, orange: $-4 \leq (24-z) < -6$, green:$-6 \leq (24-z) < -8$ and blue: ≤ -8. The *purple circles* are the blue 24μm galaxies moving at velocities similar to that of the NGC 4839 galaxy group (i.e. having l.o.s. velocity $= 7339 \pm 329$ km s^{-1}; Colless & Dunn 1996). We note that 19 of these 26 galaxies have $(24-z)$ colour corresponding to that of the passive galaxies (i.e. $(24-z) \leq -6$; Fig. 4.6). The contours are from a 0.5–2 keV XMM-Newton EPIC/PN x-ray mosaic image of the extended Coma cluster.

entire Coma supercluster. We continue the discussion on the properties of Coma supercluster dwarfs, particularly the evolutionary link between the dEs found at the centre of clusters and the k+As residing in the less dense regions closer to their outskirts in Chapter 7.

4.5.3 Coma and NGC 4839

As noted above, the Coma cluster is known to have significant substructure in the optical and x-ray maps. The most prominent x-ray emitting substructure is associated with a galaxy group, of which NGC 4839 is the most prominent galaxy. By combining N-body hydrodynamical simulations with *ROSAT* x-ray and VLA radio observations, Burns et al. (1994) remarked that the NGC 4839 group has already passed through the core of Coma ~ 2 Gyr ago, and is now on its second infall (also see Caldwell & Rose 1997). However, several other studies based on optical spectroscopy and imaging, and x-ray observations conclude otherwise (Colless & Dunn

1996; Neumann et al. 2003; Adami et al. 2005). No consensus seems to have been reached on the dynamical state of NGC 4839. Studies supporting the first infall argument suggest that the NGC 4839 galaxy group has a velocity dispersion (σ_{cz}) of 329 km s^{-1} (e.g. Colless & Dunn 1996), while others claim it to be as high as 963 km s^{-1} (e.g. Caldwell et al. 1993), the latter being consistent with the scenario where the galaxies belonging to the group have dispersed during their first passage through the cluster.

Located ~ 1.1 Mpc from the centre of the Coma cluster, the NGC 4839 galaxy group was first detected as an asymmetric extension to the otherwise relaxed x-ray morphology of Coma (Briel, Henry and Böhringer 1992). Several authors have discovered post-starburst (k+A) galaxies associated with this group (Caldwell et al. 1993; Caldwell & Rose 1997; Poggianti et al. 2004). In this work, we find that most of the known post-starburst galaxies in Coma, such as those found by Poggianti et al. (2004), are either not detected at 24μm, or show little MIR emission. We hence confirm that almost none of these post-starburst galaxies have a significant amount of obscured star formation going on in them.

Struck (2006) suggests that when a galaxy group passes through the core of a cluster, as suggested by Burns et al. (1994) for Coma and NGC 4839, the group galaxies are gravitationally shocked. In this scenario, enhancement in star formation activity is a natural consequence of an increase in galaxy-galaxy interactions among group galaxies. Such a scenario has been suggested for Coma and NGC 4839 by Neumann et al. (2003). Fig. 4.14 may provide circumstantial evidence to support this argument.

In Fig. 4.14 we show the spatial distribution of the 24μm detected Coma galaxies colour-coded by their $(24-z)$ colour. The blue 24μm galaxies constituting the peak, which also corresponds to the mean velocity of the NGC 4839 group (Fig. 4.11), are explicitly shown. We note that 19 of the 26 galaxies belonging to this peak have colours consistent with that of passive 24μm detected galaxies ($(24-z) \leq -6$; Fig. 4.6). The probability of picking 19 red galaxies out of the 197 24μm detected galaxies (of which 143 are red) is $\sim 8.77 \times 10^{-4}$, suggesting that

the occurrence of these galaxies in a narrow velocity range (Fig. 4.11) may not be an event of random chance. The fact that these galaxies are not concentrated close to NGC 4839, and a large fraction of them are passively evolving, may indicate that the NGC 4839 galaxy group has already passed through the centre of Coma and is now on its second infall towards the Coma centre (e.g. also see Burns et al. 1994; Caldwell & Rose 1997). However, our data does not allow us to draw firm conclusions on either of the two scenarios associated with the NGC 4839 galaxy group and the Coma cluster, namely, (i) whether the group is on it's first infall, or (ii) it has already passed through the core and is on it's second passage.

4.5.4 Coma, Abell 1367 and the filament

In the hierarchical model, galaxy clusters grow by accretion and/or mergers with other clusters and groups. In simulations, galaxies are seen to be accreted along the network of filaments of galaxies, feeding these clusters, along preferred directions (e.g. Bond, Kofman & Pogosyan 1996). Although several observational techniques are now being implemented to detect and quantify such large-scale structures (LSS), the low surface density of matter, enormous spatial scale, and projection effects make it difficult to observe the extent of these filaments of galaxies (Colberg 2007).

One way of exploring the evolution of the LSS is to probe its impact on the galaxies traversing them. The spectacular filament crossing the Coma and Abell 1367 clusters is an exclusive object in the low redshift Universe, because it is not only traced by the spatial distribution of galaxies (Fig. 4.1), but has also been detected at radio wavelengths (Kim et al. 1989). One of the aims of this chapter is to understand and interpret the difference in the evolutionary paths adopted by galaxies in the vicinity of the clusters, the filament and the groups embedded in the filament. In agreement with the scenario emerging in the literature (e.g. Gray et al. 2004; Tanaka et al. 2004; Smith et al. 2006; Haines et al. 2007 among others), we find that the SFR-density relation across the Coma supercluster is much weaker for the massive galaxies

($z<14.5$; Fig. 4.3), relative to the dwarfs ($z>15$; Figs. 4.3 & 4.4).

Empirical studies of galaxies infalling into clusters along filaments suggest that an enhanced galaxy density at the cluster periphery may lead to a burst of star formation in them, consuming a large fraction of cold gas (e.g. Porter et al. 2008; Mahajan, Raychaudhury & Pimbblet 2011c). This effect would be more efficient for the dwarf galaxies. In a study based on the SDSS data, Haines et al. (2007) find that the dwarf galaxies ($-19 < M_r < -18$) residing in high density regions show a systematic reduction of $\sim 30\%$ in their Hα emission relative to the mean of the sample, leading the authors to favour slow quenching of star formation in these galaxies (also see Balogh et al. 2004b; Tanaka et al. 2004). On the contrary, in Coma it is likely that the infalling star-forming dwarf galaxies undergo a burst of star formation, followed by rapid quenching leading to the k+A population (Fig. 4.4, also see §4.5.2).

In contrast, star formation in dwarf galaxies infalling into galaxy groups, seems to be slowly quenched without an intermediate starburst phase, resulting in the observed reduction in the mean EW(Hα) values seen in the vicinity of groups in Fig. 4.4. This observation could be attributed to the relatively inefficient ram-pressure stripping in galaxy groups (Tanaka et al. 2004), transforming infalling galaxies slowly over several Gyr via a process involving progressive starvation (Larson et al. 1980).

Another notable fact in Fig. 4.4 is the orientation of the stream of blue star-forming galaxies southward of Coma, almost orthogonal to the direction of elongation of the galaxy density (Figs 4.3 & 4.4). This may be significant given the observations presented in the previous section (also see Burns et al. 1994). Consistent with the results presented in literature, we find that the instantaneous SFR of a galaxy depends upon the stellar mass of the galaxy, as well as on the local galaxy density, and on whether the galaxy is in a group or cluster. The cosmic web does play a crucial role in defining the evolutionary path of the galaxy, as is seen by different rate of quenching of dwarf galaxies in groups and clusters (Fig. 4.4). The different fractions of dwarf k+A galaxies in the three major components of this supercluster further strengthens this

argument (Table 4.1). It is indeed remarkable that the Coma and Abell 1367 clusters, that are well known to have very different galaxy properties, influence the star formation histories of the infalling galaxies very differently. While the fraction of star-forming and k+A dwarf galaxies in Abell 1367 vary by a factor of 10 ($\sim$ 52% & 4.8% respectively; Table 4.1), in the Coma cluster neither dominate (12.5% & 11.4% respectively; Table 4.1).

4.6 Conclusions

This work is a step ahead in understanding the star formation properties of galaxies in one of the richest nearby superclusters. We analyse the spectroscopic and photometric data obtained by the SDSS and archival 24μm data obtained by the MIPS instrument on board *Spitzer*. Our major results are:

- The fraction of (optical) AGN drops significantly ($f_{AGN} < 0.25$) in the dense cluster environment. But the relation between AGN activity and environment is unclear in the intermediate density environments of groups.

- Star formation in the massive galaxies ($z < 14.5$) seems to be low everywhere in the supercluster region studied here, almost independent of the local environment. In sharp contrast, the dwarf galaxies ($z > 15$) can be seen to be rapidly forming stars everywhere, except in the dense cluster and group environments.

- The passive, AGN host and star-forming galaxies as classified from their optical spectra, occupy different regions on the $(24-z)-(g-r)$ colour-colour diagram.

- The fraction of star-forming galaxies in Coma is determined to within ± 10%, irrespectively of the definition of star-forming in terms of optical $(g-r)$ colour, optical-mid-IR $(24-z)$ colour or EW(Hα). Many of the blue galaxies in Coma are found to be post-starburst galaxies, whose blue colours are due to a recent burst of star formation which

has now terminated, as revealed by their lack of Hα emission and excess Hδ absorption. However, in Abell 1367, the f_{SF} obtained using the 3 different indicators show different trends. While the fraction of blue galaxies increases outward from the centre, the f_{SF} obtained by employing the $(24-z)$ near/mid IR colour decreases away from the centre of Abell 1367.

- Most of the (optically) blue 24μm galaxies detected in Coma are on their first infall towards the cluster. The current episode of star formation in such galaxies is possibly a result of a rapidly changing local environment.

- 11.4% of all dwarf ($z > 15$) galaxies within $5 \times 4.2\ h_{70}^{-1}$ Mpc^2 of the centre of Coma, and 4.8% within the same area around Abell 1367 have post-starburst (k+A) type spectra. In the surrounding supercluster region this fraction drops to 2.1% only, suggesting that the mechanism(s) responsible for quenching star formation in dwarfs depends upon the cluster's potential. The starburst, rapid quenching and subsequent k+A phase requires the dense ICM and high infall velocities attainable in rich clusters, as opposed to galaxy groups where star formation in infalling dwarf galaxies appears to be quenched gradually. The k+A galaxies preferentially avoid the dense centre of the cluster.

- There is no correlation between the spatial distribution of k+A galaxies and the substructure seen in the x-ray emitting gas in the Coma cluster, suggesting that the merger with NGC 4839 group could be one, but not the only origin of k+A dwarf galaxies in Coma.

Chapter 5

Evolution of galaxies in the cosmic suburbs

5.1 Introduction

Several spectacular starburst galaxies have recently been discovered in galaxy clusters. Most of these galaxies are found at high redshifts ($z \geq 0.2$; Keel 2005; Moran et al. 2005; Sato & Martin 2006; Marcillac et al. 2007; Fadda, Biviano & Durret 2008; Oemler et al. 2009), but some have also been found in the low redshift Universe (Sun & Murray 2002; Gavazzi et al. 2003; Cortese et al. 2007; Reverte et al. 2007). These serendipitous discoveries challenge the conventional picture where galaxy clusters are always populated by passively evolving quiescent galaxies, which progressively assume bluer colours and higher SFRs with increasing clustercentric radius (e.g. Dressler 1980; Gómez et al. 2003; Balogh et al. 2004b; Pimbblet et al. 2006).

It has long been established that environment of a galaxy profoundly effect its properties-both intrinsic and physical. Colours (Butcher & Oemler 1984; Balogh et al. 2004a; Blanton et al. 2005; Mahajan & Raychaudhury 2009), surface brightness (Blanton et al. 2005), spectroscopic SFR/indicators such as EW of Hα and O II (e.g. Balogh et al. 1999; Gómez et al. 2003; Balogh et al. 2004b; Mahajan & Raychaudhury 2009) and morphology (Dressler 1980)

show a gradient as a function of environment. The galactic environment is often parametrised in terms of the distance to the nth nearest neighbour (e.g. Dressler 1980; Balogh et al. 2004b), projected galaxy density (e.g. Balogh et al. 2004b; Lewis et al. 2002; Gómez et al. 2003; Haines et al. 2006b; Poggianti et al. 2008) or simply as the cluster-centric distance (e.g. Porter & Raychaudhury 2007; Porter et al. 2008). Several processes that can result in such a gradient have been proposed.

Essentially, all environment related mechanisms cut-off the fuel for further star formation in a galaxy, leading to the transformation of star-forming late-type galaxies into passively evolving S0 or ellipticals. Theories and simulations of processes like the ram-pressure stripping (Gunn & Gott 1972; McCarthy et al. 2008) or strangulation (Larson et al. 1980), suggest that the warm (and cold) gas component ($\sim 10^5$K) of the inter-stellar medium (ISM) may be stripped from a galaxy when it enters a galaxy cluster. Such processes are thus dependent on the properties of the cluster in which they operate (e.g. the depth of cluster potential well).

Other mechanisms such as thermal evaporation of cold molecular gas from a galaxy disk via thermal conduction by the intra-cluster medium (ICM), are considered to play a key role in the evolution of dwarf galaxies (Cowie & Songaila 1977) (also see Fujita 2004 and Boselli & Gavazzi 2006 for a review of various other mechanisms). Several authors have given great importance to repeated high velocity encounters amongst galaxies or "harassment" (Moore et al. 1996), and/or galaxy-galaxy mergers, for their role in the evolution of galaxies (Lewis et al. 2002; Haines et al. 2006a; Porter & Raychaudhury 2007; Moss 2006; Porter et al. 2008; Oemler et al. 2009, among others). The frequency and impact of such galaxy-galaxy interaction processes depends upon the local galaxy density and the velocity field generated by the cluster's potential.

So, in principle any site within the large-scale structure (LSS), with galaxy density above the 'critical' value (see Gómez et al. 2003 for instance), should encourage interactions amongst galaxies, capable of initiating a burst of star formation. The LSS in the form of filaments and

sheets of matter exert tidal field on objects embedded in it (Colberg et al. 1999). Recent studies suggest that filaments of galaxies (Porter & Raychaudhury 2007; Boúe et al. 2008; Fadda, Biviano & Durret 2008; Porter et al. 2008) and infall regions of clusters (Rines et al. 2005) are some of such favourable sites, which provide intermediate galaxy densities *and* favourable velocity fields.

The study of photometric properties of galaxies belonging to the Shapley supercluster (Raychaudhury 1989) reveal that the supercluster environment might be solely responsible for the evolution of faint ($\gtrsim M^*+2$) galaxies (Haines et al. 2006b). Elsewhere (Struck 2006), the effect of gravitational shocking by LSS on galaxies falling as small groups into clusters, is discussed (also see Moss 2006; Oemler et al. 2009). In a 2dFGRS based study of inter-cluster filaments it has been found that the SFR of galaxies falling into clusters through filaments is enhanced at 3–4 h_{70}^{-1} Mpc from the cluster centre (Porter & Raychaudhury 2007; Porter et al. 2008). Porter et al. employed the statistical η–parameter (Madgwick et al. 2002) from the 2dFGRS database as a proxy for SFR, to find that the enhancement in SFR occurs exclusively in dwarf galaxies ($M_B \geq -20$). They proposed this to be a consequence of galaxy-galaxy harassment (Moore et al. 1996), due to enhanced galaxy density and a coherent velocity field (González & Padilla 2009) on the outskirts of galaxy clusters.

In this chapter we re-address the issue of enhancement in star formation activity in galaxies found on the outskirts of nearby galaxy clusters. We employ integrated SFR and specific star formation rate (SFR/M^*) to quantify the star formation activity of galaxies in our sample, and emission line ratios to separate out the emission due to AGN from that of 'true' star formation. We also use a catalogue of large-scale filaments of galaxies sourced from the SDSS DR 4 to evaluate the impact of the position of a galaxy in the cosmic web, on its star formation properties. The data and sample properties used in this chapter are described in §2.2. The outline of this chapter is as follows: in the following section we discuss the properties of clusters, and different galaxy populations (unclassified, starburst etc.) therein. We present the star formation

properties of our cluster galaxies in §5.3, briefly discussing the behaviour of galaxies falling in clusters for the first time. The impact of the immediate and the LSS environment on the star formation properties of galaxies is discussed in §5.4, and the main results are summarised in §5.5. Throughout this work we adopt a cosmology with $\Omega_m = 1$ & $\Omega_\Lambda = 0$ and $h = 70$ kms^{-1} Mpc^{-1} for calculating distances and magnitudes. We note that in the redshift range chosen for this work ($0.02 \leq z \leq 0.15$), our results are insensitive to the choice of cosmology.

5.2 Clusters and galaxies

5.2.1 Cluster membership

The galaxy members for the Abell clusters (Abell et al. 1989) in the redshift range $0.02 < z \leq 0.15$ studied in this chapter are chosen using the methodology described in §3.2.1.

5.2.2 Cluster parameters

Once the galaxy members of the clusters are known we find the velocity dispersion (σ_v) using the bi-weight statistics (ROSTAT, Beers, Flynn & Gebhardt 1990). Then assuming the cluster mass $M(r) \propto r$, r_{200} (the radius at which the mean interior over-density in a sphere of radius r is 200 times the critical density of the Universe) is calculated using the relation given by Carlberg, Yee & Ellingson (1997): $r_{200} = \sqrt{3}\sigma_v / 10H(z)$.

We exclude any comparison clusters (described below) which are not fully covered by the SDSS DR 4 footprint. We also exclude any clusters for which reliable velocity dispersion information is neither available in literature nor obtainable from our data. This gives us a final sample of 107 Abell clusters ($0.02 < z < 0.15$; Abell et al. 1989), lying in those regions of the sky where SDSS DR 4 has $\geq 70\%$ spectroscopic coverage.

5.2.3 The Unclassified galaxies

Any galaxy which can not be classified using the BPT diagram (Butcher & Oemler 1984) because of low S/N ratio or absence of all the required emission lines (N II, [O III], Hα and Hβ) in the BPT diagram, is termed as 'unclassified', which makes this class of galaxies highly amorphous. But a more careful analysis shows that these are bulge dominated systems, in fact even more concentrated (concentration parameter $\equiv$ R_{90}/R_{50}, where R_x is the radius emitting x% of the galaxy's light in the Petrosian r-band; Strateva et al. 2001) than the AGN or composite galaxies (private communication with Brinchmann, J.). The spectra sampled from the 3″ fibre, which encompasses $\sim$ 40-60% of the galaxy's light (at z ~ 0.1) may only represent the dead centre of the galaxy, lacking any emission. An investigation of whether all of these galaxies are indeed passively evolving or comprise a sub-population of dust obscured galaxies with an AGN supported star formation in the galactic nucleus, is beyond the scope of this work (see Mahajan & Raychaudhury 2009 or Chapter 3 where we briefly address this issue).

In Fig. 5.1 we plot the distribution of absolute SFR and log SFR/M^* of all galaxies ($-23 \leq M_r \leq -18$) in SDSS DR 4 as a function of their luminosity for the three different classes: star-forming (& composite), AGN and the unclassified (Brinchmann et al. 2004). As previously speculated, the unclassified galaxy class seems to be dominated by quiescent galaxies (also see §B.1 in Appendix B for a discussion on the methodology and reliability of SFR estimate for the unclassified and AGN galaxies). It is also not surprising that the galaxies hosting AGN which are known to be bulge-dominated systems, follow the same distribution as that of the unclassified galaxies.

In agreement with previous findings, Fig. 5.1 shows that most low-luminosity galaxies are efficiently forming stars (Kauffmann et al. 2004; Haines et al. 2006a; Haines et al. 2007; Damen et al. 2009; Mahajan & Raychaudhury 2009; Mahajan, Haines & Raychaudhury 2010). Interestingly, the observed bimodality in SFR, such as Hα EW (e.g. Brinchmann et al. 2004, Haines et al. 2007; also see Mahajan & Raychaudhury 2009) is seen exclusively in the un-

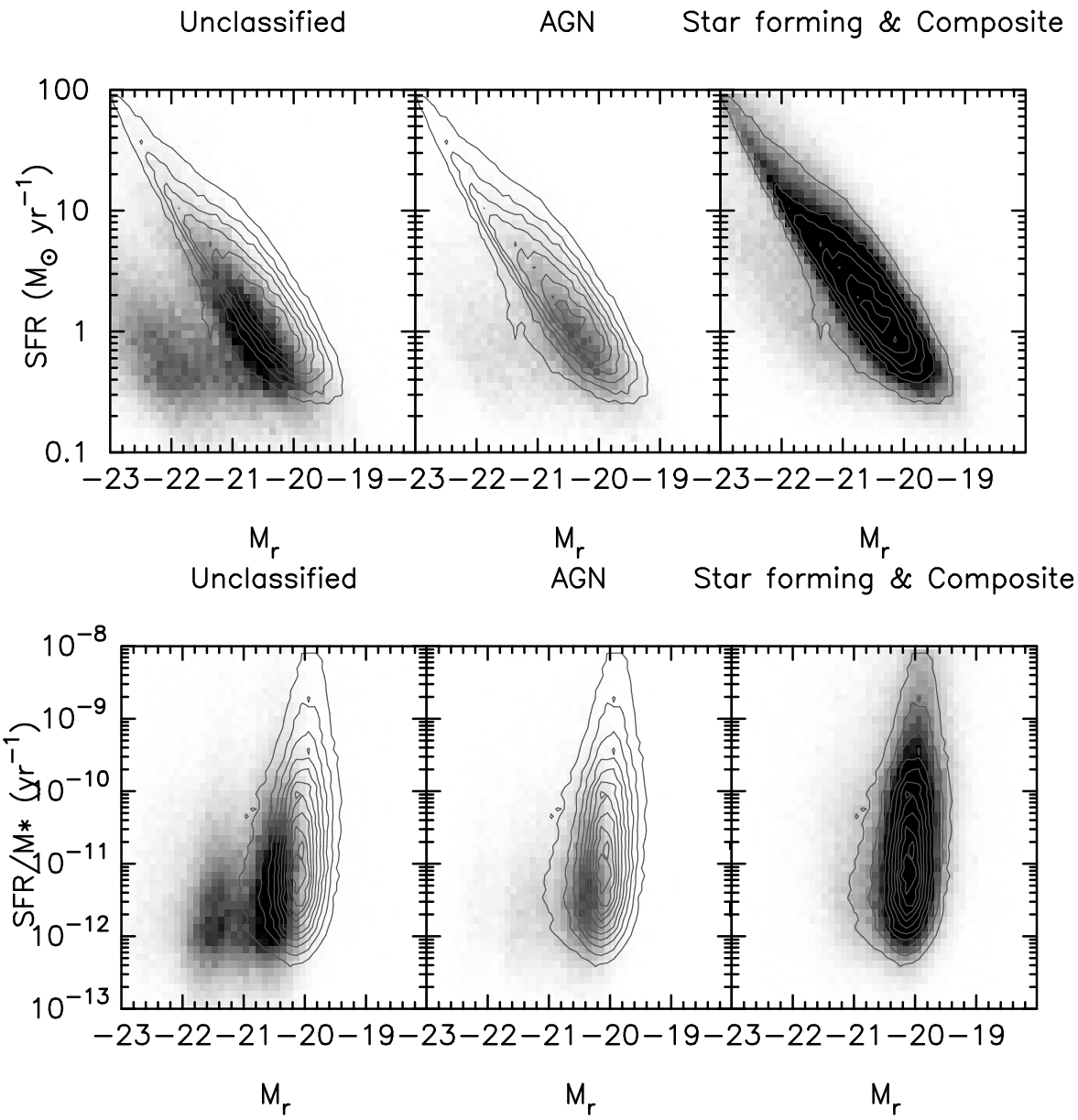

Figure 5.1: *(top)* SFR and *(bottom)* SFR/M^* as a function of r-band magnitude for all the galaxies in SDSS DR4, divided according to their position in the BPT diagram (e.g. Fig. 4.8). The contours for star-forming+Composite class (right panel) are repeated in other panels to compare the relative distributions. The outermost contour in each case represents 100 galaxies per bin, increasing by 100 for every consecutive contour inwards. As expected, the AGN seem to follow the passive galaxy distribution. It is also interesting that the difference between various classes become more distinct for SFR/M^* (bottom panel). These plots show that absolute SFR follows the galaxy luminosity, but the trend reverses when specific SFR is considered. Another interesting feature that emerges here is that the observed bimodality in SFR seems to be largely contributed by the 'non-emission line' galaxies only. This plot gives no indication of enhanced star formation in AGN, although it would be wiser to consider that this might be due to the obscuration of emission lines by dust around the active nuclei.

classified galaxies. If the SFR of the star-forming galaxies is a function of environment, one should expect the distribution of their SFR to show a bimodal distribution in a dataset which samples a wide range of environments, such as that employed here. We also note that in our present analysis no conclusive remarks can be made on the issue of starburst-AGN connection, because at visible wavelengths the circumnuclear star formation (which largely contributes to the $3''$ SDSS fibre spectra) may be entirely obscured by dust enshrouding the active nucleus (also see Mahajan & Raychaudhury 2009 for a relevant discussion on this issue).

5.2.4 Starburst galaxies

'Starburst galaxy' is an ambiguously used term in literature. In general, a galaxy with current SFR much higher than that averaged over its past lifetime, may be regarded as a starburst. In agreement with several other studies (e.g. Feulner et al. 2005; Noeske et al. 2007), we note that by choosing starburst galaxies according to absolute SFR or SFR/M^* alone, biased the selected galaxies to giant or dwarf galaxies respectively (also see Damen et al. 2009). Hence, in context of this paper, we adopt a dual criterion to define a starburst galaxy: log SFR/$M^* \geq -10$ yr^{-1} *and* SFR ≥ 10 M$_\odot$yr^{-1}. These limits are purely empirical, driven by the idea of selecting galaxies having current SFR much higher than that averaged over the past star formation history of galaxies. These limits thus encompass the galaxies contributing to the high end tail of the SFR and SFR/M^* distributions only. In particular, they label $\sim 3\%$ of all cluster members and $\sim 13\%$ of all star-forming galaxies in our sample as a starburst. These starburst galaxies cover a wide range of structural properties; some typical examples found on the cluster outskirts (1-2R$_{200}$) are shown in Fig. 5.2.

Please note that the above definition of starburst galaxies is used only to sub-classify galaxy clusters in our sample, and qualitatively our results remain unaffected by the specific choice of SFR and SFR/M^* thresholds for defining starburst galaxies (see §5.3 for a detailed discussion).

Figure 5.2: True colour SDSS images of some of the typical starburst galaxies found on the outskirts (1-2r_{200}) of SB clusters in g', r' and we' filters (represented by red, $green$ and $blue$ colours respectively). These galaxies cover a wide range in morphologies, and some show structural deformities and presence of close neighbours. Overlaid on the 2 galaxies ($magenta$; far right) are the unsmoothed contours representing the UV light distribution in the UW1 ($top; \lambda_{\rm mean} \sim 2500$Å) and UM2 filter ($second\ row; \lambda_{\rm mean} \sim 2250$Å) from the SWIFT archival data respectively.

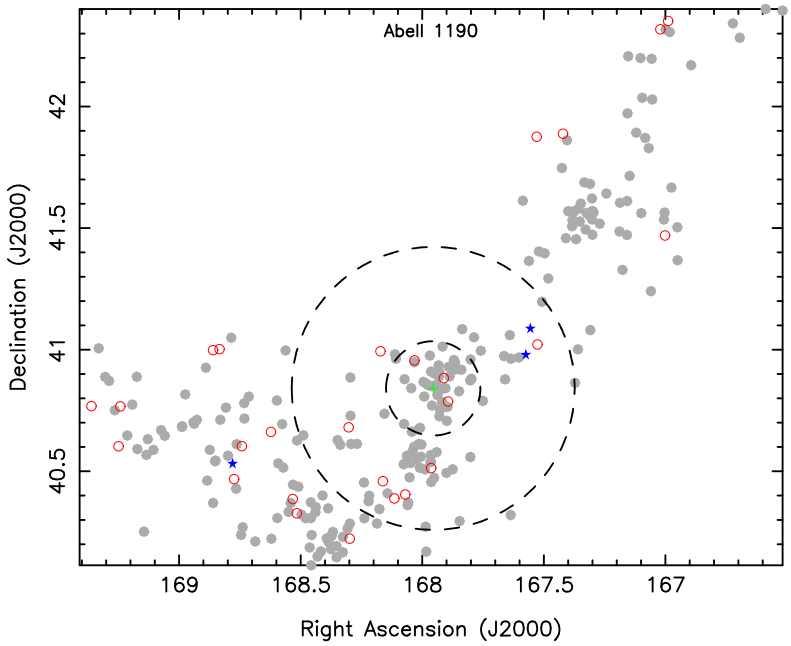

Figure 5.3: Galaxies ($M_r \leq -20.5$) in the cluster and the filaments feeding Abell 1190. The star-forming and starburst galaxies (see §5.2.4) are shown as *red circles* and *blue stars* respectively. The dotted circles show the r_{200} and $3\,r_{200}$ boundaries.

5.3 Star formation & environment

From our sample of 107 clusters we select those which have a non-AGN starburst galaxy ($M_r \leq -20.5$; as defined in §5.2.4) *anywhere* within 3 h_{70}^{-1} Mpc of the cluster centre (see for instance Fig. 5.3). This distance is chosen empirically, based on the fact that the R_{200} of most of the galaxy clusters in our sample is $\sim 1.5\ h_{70}^{-1}$ Mpc. So, the starburst galaxies chosen to sub-classify the cluster sample either lie in the cluster or its infall region. The choice of this distance in linear units ensures that our analysis done with respect to the scaled radius remains independent of this classification criteria (Fig. 3.1). In order to make the selection procedure independent of the uncertainties in the SFR estimates (§B.1), we ignore the unclassified galaxies with high SFR ($\geq 10\ M_\odot\ yr^{-1}$; also see Fig. B.1). This yields 46 clusters which are termed 'SB clusters' (clusters with starburst galaxies) henceforth. The rest of the 61 clusters which do not have any starburst galaxy within 3 h_{70}^{-1} Mpc of the cluster centre form our comparison sample ('CN clusters' henceforth). The fundamental properties of our cluster samples are listed in tables

A.3 and A.4 respectively. In total 3,966 galaxies ($M_r \leq -20.5$) are found within $3R_{200}$ of the cluster centres, of which 3,903 are non-AGN and are used for all further analysis unless stated otherwise. In the absence of any other underlying difference between the properties of the clusters with a starburst galaxy in or around them (SB clusters), and those without it (CN clusters), the occurrence of starburst galaxies in some of them is purely coincidental. So, it can be hypothesised that the CN and SB clusters will display similar properties. We show below that this hypothesis fails to hold.

5.3.1 The 'burst' of star formation

The 4000 Å break (D_n4000) is one of the strongest discontinuity that occurs in the optical spectrum of a galaxy. It arises because a large number of absorption lines, mainly from ionised metals accumulate in a small wavelength range. In hot massive stars, the metals are multiply ionised and hence the opacity is low, and D_n4000 has a smaller value, relative to old, metal rich stars. We use the same definition of D_n4000 as adopted by Brinchmann et al. (2004), which is the ratio of average flux density in the narrow continuum bands (3850-3950 and 4000-4100 Å). This definition was initially introduced by Balogh et al. (1999) and is an improvement over the original definition of Bruzual (1983) in the sense that the narrow bands make the index considerably less sensitive to reddening effects.

The Hδ absorption line occurs when the optical light from the galaxies is mainly contributed by the late-B and early-F stars. A large absorption in Hδ implies that the galaxy has experienced a major burst of star formation $\sim 0.1 - 1$ Gyr ago. A stronger D_n4000 is an indicator of metal-rich ISM, and hence together with the Hδ EW indicate whether a galaxy has been forming stars continuously (intermediate/high D_n4000 and low Hδ EW) or in bursts (low D_n4000 and high Hδ EW) over the past 1–2 Gyr (Kauffmann et al. 2003a). In Fig. 5.4 we show the distribution of the spectacular starburst galaxies (SFR≥ 10 $M_\odot yr^{-1}$ & log SFR/$M^* \geq -10.5$ yr^{-1}), relative to all other galaxies in the SB cluster sample, in the D_n4000-Hδ plane. Fig. 5.4 clearly shows

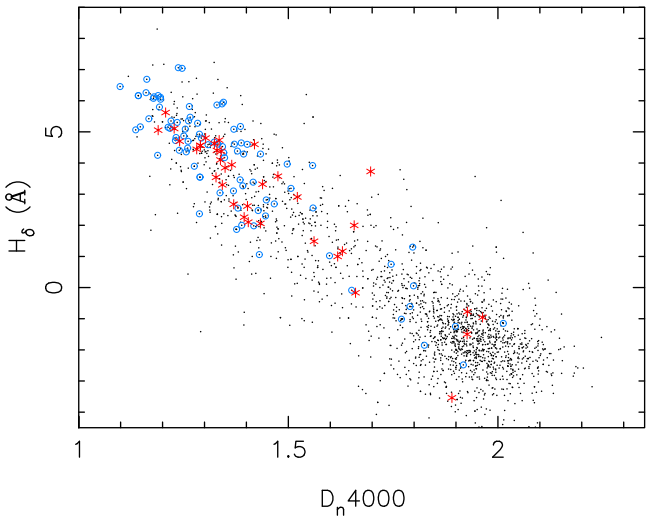

Figure 5.4: All galaxies in the SB clusters are plotted as *black* dots in the D_n4000-Hδ space. Overplotted as *red* stars are starburst galaxies found at $1 \leq r/r_{200} \leq 2$. The *blue* circles are galaxies at same distance from the cluster, but having absolute SFR ≥ 1 M$\odot$ yr^{-1}. Most of these infalling galaxies with high SFR (and SFR/M^*) occupy positions in the D_n4000-Hδ space where galaxies with currently ongoing or recent starbursts are expected to lie.

that our adopted criteria for defining starburst galaxies (red stars) on the basis of integrated SFR and SFR/M^* well segregate these galaxies in the space defined by spectral indices sensitive to recent star formation (also see Mahajan & Raychaudhury 2009). For a comparison, we also show galaxies which have the same SFR/M^* but absolute SFR which is upto 10 times lower than our starburst galaxies (blue points).

5.3.2 Starburst galaxies on cluster outskirts

We began this section by sub-classifying the clusters on the basis of the presence of a starburst galaxy anywhere within 3 h_{70}^{-1} Mpc of their cluster centre (e.g. Fig. 5.3). We now want to test the hypothesis that these starburst galaxies occur randomly within a cluster. To do so, in Fig. 5.5 we plot the first, square root of the second and the third moment (mean, standard deviation & skewness) of SFR respectively, as a function of the (scaled) cluster-centric radius. We extend our analysis upto $3\,R_{200}$ because it encompasses the core of the galaxy cluster and the infalling region surrounding it (Diaferio & Geller 1997; Lewis et al. 2002; Gómez et al. 2003; Rines et

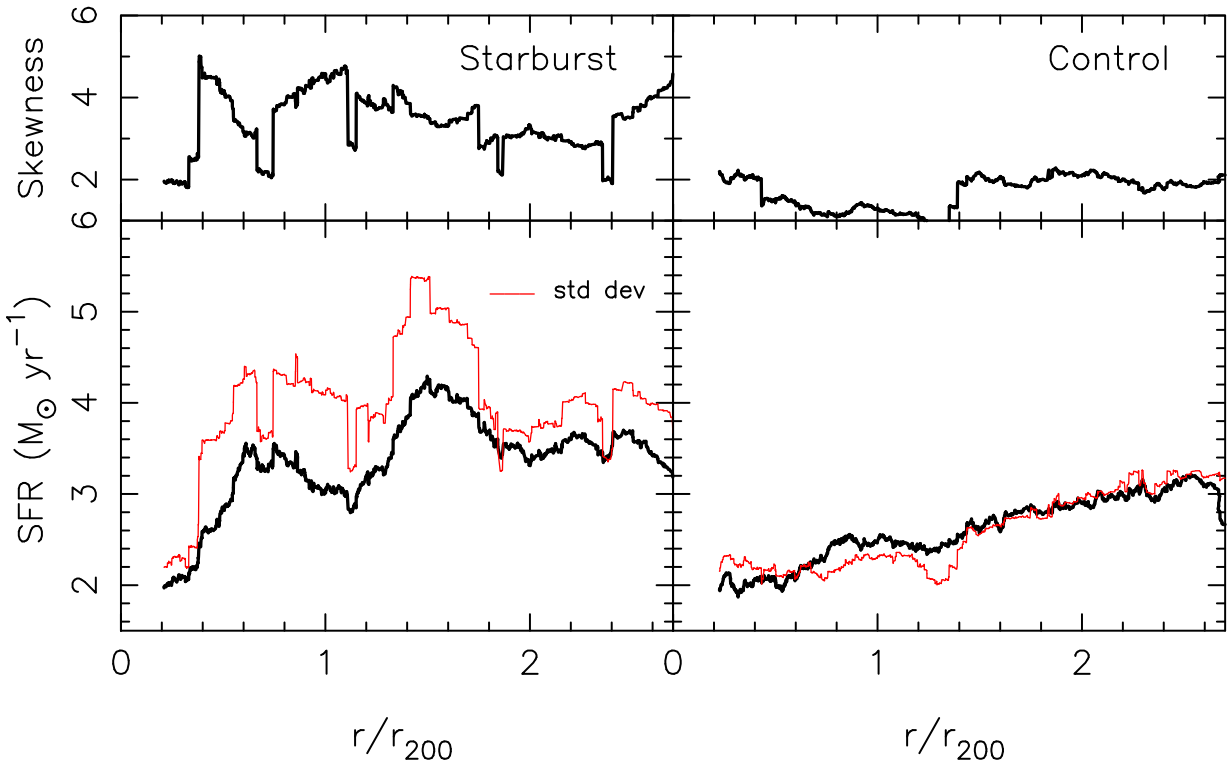

Figure 5.5: The mean (*solid line, bottom panel*), skewness (*upper panel*) and standard deviation (*red*) in SFR of galaxies in SB (*left*) and CN (*right*) clusters in running bins (250 galaxies per bin) of (scaled) cluster-centric radius. AGN and unclassified galaxies with SFR> 10 $M_\odot$ yr^{-1} are excluded. As expected the SFR falls toward the cluster centre. But the difference in the SFR profiles of the two samples is striking. The high standard deviation at the cluster boundary ($r/r_{200} \sim 1$) indicates the presence of galaxies with extreme SFRs. It is also noticeable that the mean SFR of CN clusters is lower than that of SB clusters in general.

al. 2003; Rines et al. 2005), providing us with a range of galactic environments.

The SFR profiles of the two samples are strikingly different, with CN clusters showing a lower mean SFR at almost all radius. The most striking feature of this plot is the sudden increase in the standard deviation (red curve) in SFR, accompanied by positive skewness (top panel) in the SB clusters. This shows that several star-forming galaxies with very high SFR are present just outside the boundary ($\sim 1.5R_{200}$) of these clusters. Given that our selection criteria demanded that the starburst galaxies could occur anywhere within the given threshold (3 h_{70}^{-1}Mpc), it seems highly unlikely that occurrence of such a 'blip' is a random chance. There seems to be another region of increase in the mean SFR of galaxies in the SB clusters

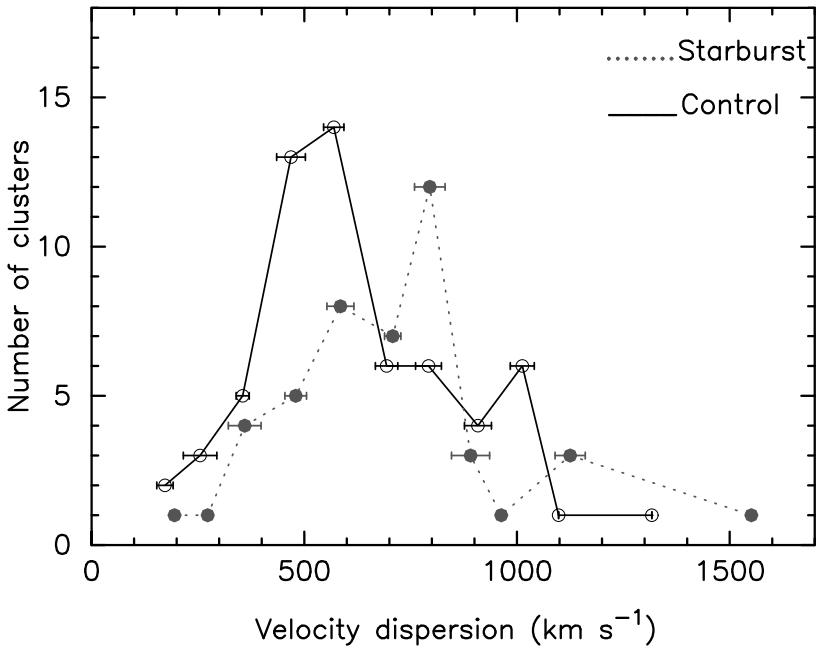

Figure 5.6: The velocity dispersion distribution of SB (*dotted*) and CN (*solid*) clusters respectively. The error bars show the 2σ scatter in each bin. There is a clear indication that the SB clusters are systematically more massive than the CN clusters.

at $\sim 0.5\mathrm{R}_{200}$. We note that this second feature is neither due to the presence of group-like structures ($\leq$ 300 km s^{-1}) nor due to the nearby interacting cluster pair Abell 2197 and 2199 present in our sample. Both these features in the SFR profile of SB clusters are thus considered real. We discuss them in detail in the following sections.

5.3.3 Clusters & Filaments

In order to explore whether the enhancement in SFR of galaxies found on cluster outskirts (as discussed in §5.3.2), is related to the properties of clusters themselves, we plot the velocity dispersion (σ_v) distribution of the two cluster samples in Fig. 5.6. Since the velocity dispersion values are derived from spectroscopic redshifts using an iterative procedure (ROSTAT; Beers, Flynn & Gebhardt 1990), the error in individual σ_v values are very small. The massive galaxy clusters have a deeper potential well, so they are expected to show higher σ_v than their low mass counterparts. Fig. 5.6 clearly shows that despite the wide range of objects covered by

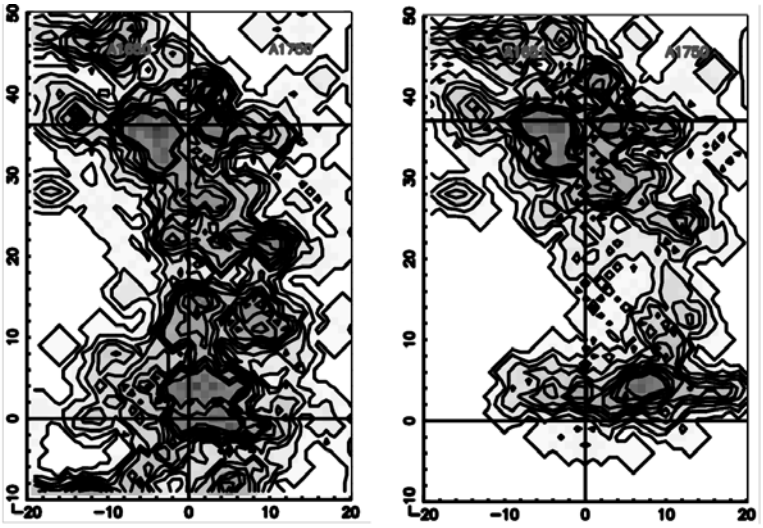

Figure 5.7: Contours and gray-scale showing galaxy density on the two projected planes in a warped filament detected in our SB cluster sample. The two horizontal lines mark the positions of the two Abell clusters, while the vertical line is the inter-cluster axis. Both axis are in units of Mpc with the centre of frame of reference set at the lower cluster.

both the cluster samples (group-like structures to massive clusters), their σ_v distributions are significantly different.

Statistically, the SB clusters have higher σ_v than the comparison cluster sample. The Kolmogorov-Smirnoff (K-S) test finds the maximum difference between the cumulative distributions of σ_v of the two cluster sample to be $D = 0.2858$, at a significance level of 0.022. The observed difference is definitely not due to different redshifts of clusters because both the samples are uniformly spread over a small redshift range (0.02–0.15) spanning only ~ 1.5 Gyr in lookback time. This implies that either SB clusters are (i) more massive, or (ii) less relaxed than the CN clusters. Unfortunately, since x-ray data for majority of our cluster sample are unavailable we could not pursue any argument in favour of (ii) above.

Recently, several authors have shown that the global environment, the LSS in which the galaxies are embedded, may also play a significant role in their evolution (e.g. Haines et al. 2006b; Porter & Raychaudhury 2007; Fadda, Biviano & Durret 2008; Porter et al. 2008). We evaluate the impact of the LSS on the star formation properties of galaxies, by studying their

position in the cosmic web. We employ the catalogue of galaxy filaments sourced from SDSS DR4 by using the algorithm described in (Pimbblet, Drinkwater & Hawkrigg 2004; PDH 2004 hereafter). The morphological classification of filaments in this chapter is the same as described in PDH (2004), where types I to V refer to straight, warped, sheet-like, uniform and irregular distribution of galaxies respectively, projected on two orthogonal planes with respect to the inter-cluster axis (e.g. Fig. 5.7). Simulations show that the properties such as matter density of filaments, are closely related to their morphology (Colberg et al. 2005; Dolag et al. 2006). So, by studying the morphology of filaments through which a galaxy approaches the cluster, we intend to explore how, if at all, is the LSS effecting the evolution of galaxies.

The algorithm for identifying filaments is well described in PDH (2004), but for the benefit of reader we briefly describe it here: to identify galaxy filaments in a large-scale survey such as the SDSS involves setting up orthogonal planar pair projections of the filaments viewed along the inter-cluster axis. The planes correspond to ± 20 Mpc from the inter-cluster axis and have a depth of ± 5 Mpc around it. This choice of depth and width ensures that we retain an ability to see highly curved and complex filaments (Fig. 5.7; also see fig. 1 of PDH 2004). Finally, those filaments for which both Mahajan and Pimbblet agreed on the same morphological type, are chosen to be a part of the 'clean' sample, and are used for all further analysis.

In Fig. 5.8 we plot the distribution of type of filaments belonging to both the cluster samples. The errors are calculated using binomial statistics, where, if n out of N clusters in the given sample have a particular morphological type for a filament, then the likelihood of a cluster to have that class of filaments is given by: $L \propto f^n(1-f^n)^{N-n}$ (De Propris et al. 2003). The scatter on the fraction of clusters is given by the standard deviation

$$\Delta f_x = \sqrt{\frac{n(N-n)}{N^3}}. \tag{5.1}$$

Each distribution is independently normalised to unity. The number of filaments classified for

Table 5.1: Type of filaments

Sample	I	II	III	IV	V	undetermined
SB	18	10	2	1	7	47
CN	25	35	6	3	9	68

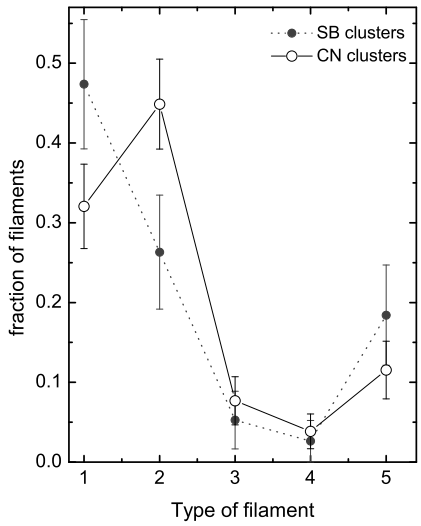

Figure 5.8: The distribution of filament type for the 'clean' filaments in the SB (*dotted*) and CN (*solid*) cluster samples respectively. The errors are calculated using Eqn.5.1. The SB and CN clusters show significantly different preferences for type we and type II filaments respectively.

each cluster sample are listed in Table 5.1. Note that a large fraction of our filaments remain unclassified mainly because our choice of magnitude cut, $M_r \leq -20.5$, excludes low-mass galaxies from the analysis, thus significantly underestimating the density of galaxy filaments. On the other hand, this also implies that the uncertainty in determining the morphological class of the classified filaments is very small.

Although the number of filaments associated with individual clusters do not show any particular trend, Fig. 5.8 do suggests that the CN clusters are more likely to be fed by Type II (warped) filaments. We return to this observation in §5.4.2.

5.4 Discussion

Superclusters (e.g. Shapley; Raychaudhury 1989) are the most massive and youngest structures in the Universe, within which groups and clusters of galaxies are evolving through interactions and mergers. In this hierarchical model, clusters assemble by accreting surrounding matter in the form of galaxies and galaxy groups (e.g. Bekki 1999; Struck 2006; Oemler et al. 2009) through large-scale filaments (Zeldovich, Einasto & Shandarin 1982; Colberg et al. 2000; Porter & Raychaudhury 2007; Fadda, Biviano & Durret 2008; Porter et al. 2008; González & Padilla 2009; Gay et al. 2009). The galaxies under the influence of varying environment evolve not only by *exhausting* all the fuel for star formation, but also by *loosing* it to their surroundings.

The cluster cores contain passively evolving red galaxies which have lost all their cold gas to the hostile ICM of the cluster either due to the processes like ram-pressure stripping (Gunn & Gott 1972; McCarthy et al. 2008), or a burst of star formation resulting from the first encounter with the ICM and/or galaxy-galaxy interactions (e.g. Moss 2006; Porter & Raychaudhury 2007; Porter et al. 2008; Gay et al. 2009; Oemler et al. 2009). The low density environments outside the clusters mostly host young late-type galaxies, which account for over 50% of the SFR density of the Universe (e.g. Brinchmann et al. 2004). But a crucial missing link required to fully understand the process of galaxy evolution is to find how does galaxies in cluster cores become passive while those in the field remain star-forming? How does the hierarchy of structure formation influence the properties of individual galaxies? Does the physical process of star formation in a galaxy dependent on its local environment only, or does it matter where the galaxy resides in the cosmic web?

5.4.1 Excessive star formation on the outskirts of clusters

In the past few years extensive studies have been undertaken to understand the evolution of galaxies in various environments. Some of these studies are generalised (e.g. Kauffmann et al.

2004; Tanaka et al. 2004), while others target particular environments (Gavazzi et al. 2003; Balogh et al. 2004b; Mercurio et al. 2004; Rines et al. 2005; Marcillac et al. 2007; Porter & Raychaudhury 2007; Porter et al. 2008; Verdugo et al. 2008, among others). Recently, several starburst galaxies are serendipitously discovered in and around rich clusters, most of which are at high redshifts. In this chapter we attempt to understand the nature and origin of such starburst cluster galaxies.

To do so, we take all Abell clusters ($0.02 < \mathrm{z} \leq 0.15$) in SDSS DR4, and classify the galaxies ($M_r \leq -20.5$) found within $3\mathrm{R}_{200}$ of their centres, into SB and CN samples as described in §5.3. We find that the mean SFR distribution of the galaxies in the two samples, as a function of the (scaled) cluster-centric radius are very different (Fig. 5.5). It is worth noting that despite selecting SB clusters such that they have at least one starburst galaxy (§5.2.4) *anywhere* within $3\ h_{70}^{-1}$ Mpc of the cluster centre, the major 'blip' in the SFR of SB clusters occur close to the cluster boundary.

The ICM density on the outskirts of a cluster is very low, hence any cluster related environmental process that could directly influence the infalling galaxies, such as ram-pressure stripping, can be ruled out as a cause of enhancement in the SFR of galaxies (but see Kapferer et al. 2009 for an alternative view). The local conditions on the outskirts of clusters: small relative velocities amongst galaxies, a coherent velocity field (González & Padilla 2009) and higher galaxy density with respect to the field, seems to favour interactions amongst galaxies as a possible explanation for the observed enhancement in SFR of galaxies in these regions. Fig. 5.9 provide further evidence in support of this argument by showing that the starburst galaxies at $0.5\text{–}2\,\mathrm{R}_{200}$ are more likely to have at least one neighbouring galaxy ($M_r \leq -20.5$) relative to other cluster galaxies at similar distance from the cluster centre.

Several other observational studies (Lewis et al. 2002; Balogh et al. 2004b; Moran et al. 2005; Sol Alonso et al. 2006; Porter & Raychaudhury 2007; Porter et al. 2008; Oemler et al. 2009) and simulations (Fujita 1998; Gnedin 2003b) have also considered galaxy-galaxy inter-

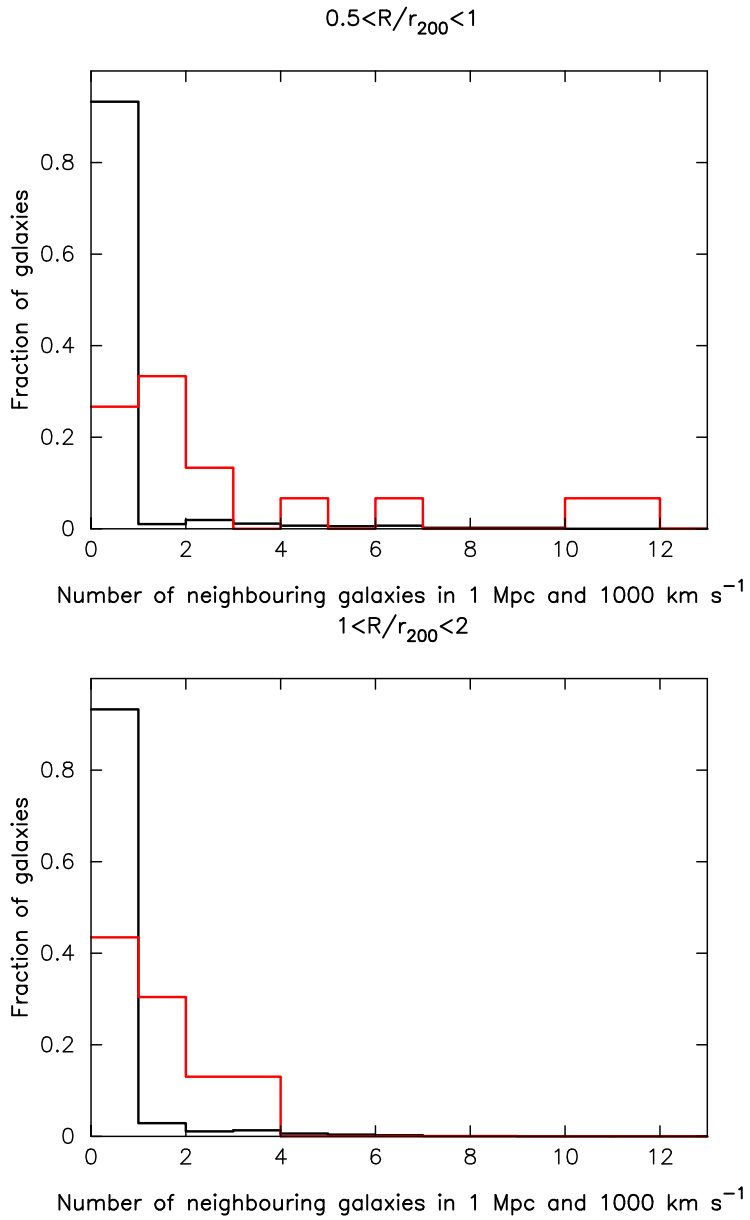

Figure 5.9: Distribution of number of neighbouring ($M_r \leq -20.5$) galaxies around starburst galaxies (*red*) and other cluster galaxies (*black*) in the scaled radial range of $0.5 \leq \mathrm{R}/\mathrm{r}_{200} \leq 1$ (*top*) and $1 \leq \mathrm{R}/\mathrm{r}_{200} \leq 2$ (*bottom*). This shows that the starburst galaxies are more likely to have at least one (or more) neighbouring galaxies than other cluster galaxies residing in similar environments.

actions as the most suitable candidate for explaining the observed differences among galaxies in clusters and field.

Study of close galaxy pairs in the 2dFGRS and SDSS suggests that interactions amongst galaxies are most efficient in triggering a burst of star formation when the projected distance between galaxies is $< 100\ h^{-1}$ kpc and their relative velocity is < 350 km s^{-1} in low/moderate density environments (Sol Alonso et al. 2006). At the cluster periphery, the local projected density (Σ_5) is $\sim 2 - 3\ h^2$ Mpc^{-2} (Rines et al. 2005), which is similar to the critical density mentioned elsewhere (Balogh et al. 2004b). The conditions just outside the cluster boundary are thus well suited for galaxies to tidally influence each other. But given the complicated kinematics involved, galaxies do not have enough time to merge completely while they are progressively drifted towards the cluster core with an additional effective infall velocity of $\sim$ 220–900 km s^{-1} (for clusters having mass $10^{12} \leq M_{\rm clus} \leq 10^{15}$ M$_\odot$; Pivato, Padilla, & Lambas 2006). Pivato, Padilla, & Lambas (2006) also found that even when considering the broad cluster mass range as above, the maximum infall velocity always occurred in the narrow clustercentric radial range of $2h^{-1} < r_{max} < 6h^{-1}$ Mpc.

The blips in the mean SFR profile of SB clusters (Fig. 5.5) could be a result of these short-time interactions. As the galaxy approaches the core of the cluster into which it is falling in, it begins to experience the tidal influence of the residual substructure in the cluster (Gnedin 2003b). We stress that such a trend has yet not been widely noticed in literature because it is very difficult to detect *and* quantify the meek signal for an enhancement in the star formation activity, occurring on small timescales and confined to very narrow regions on the sky. Hence it is not surprising that despite stacking a fairly significant sample of clusters together, we detect a subdued signal. Also, studies where radial distribution of SFR/indicator is analysed as a function of cluster-centric radius, or projected galaxy density (e.g. Lewis et al. 2002; Balogh et al. 2004a; von der Linden et al. 2010), the small signal of enhancement in SFR of galaxies falling into massive clusters can be wiped out by stacking them with their less massive

counterparts.

Kauffmann et al. (2004) (their fig. 12) show that D_n4000 in star-forming galaxies is well correlated with internal extinction (measured in SDSS z-band). For $D_n4000 \sim 1$ (for reference note that most of our cluster galaxies have $D_n4000 \gtrsim 1$; Fig. 5.4), the internal extinction can be as high as 1.5 magnitudes (in z-band). Hence it is very likely that the number of observed starburst galaxies at visible wavelengths may be severely underestimated, making observations of this phenomenon even more difficult with visible data alone (Fadda, Biviano & Durret 2008, also see Wolf, Gray & Meisenheimer 2005; Koyama et al. 2008; Mahajan & Raychaudhury 2009; Wolf et al. 2009).

A radially infalling galaxy will experience decrease in star formation time scale, but increase in star formation efficiency (Elmegreen & Efremov 1997; Fujita & Nagashima 1999) due to the rapidly changing tidal field of the cluster and residual substructure in it (Bekki 1999), and/or ram-pressure stripping (Kapferer et al. 2009). The star formation efficiency of a cloud of cold molecular gas with mass $\sim 10^5$ $M_\odot$ is enhanced when it experiences a pressure of about $10^3 P_\odot$, where $P_\odot = 3 \times 10^4$ cm^{-3}, is the total pressure in the solar neighbourhood (the star formation time scale of such a cloud in the solar neighbourhood will be ~ 10 Myr with an efficiency of ~ 0.1; Elmegreen & Efremov 1997). Hence, the interactions of a galaxy with the ICM near the cluster core ($\sim 0.5 R_{200}$) would then result in a more devastating tidal stripping scenario, where not only the H I gas and stars, but also the H II gas residing in the dense molecular clouds (mostly) in the circumnuclear regions of the galaxy are removed from it (e.g. Weinmann et al. 2006; Dolag et al. 2009). The first impact of this encounter has both the ingredients required to trigger a burst of star formation: cold gas in galaxies, and an external influence (Fig. 5.5). The SFR that is boosted at the first encounter with the cluster on its periphery, will thereafter decline as the galaxy approaches its burial grounds at the core of the cluster.

A cluster with deeper potential will attract relatively more galaxies. The increased galaxy density on the outskirts of galaxy clusters imply higher probability for galaxy-galaxy inter-

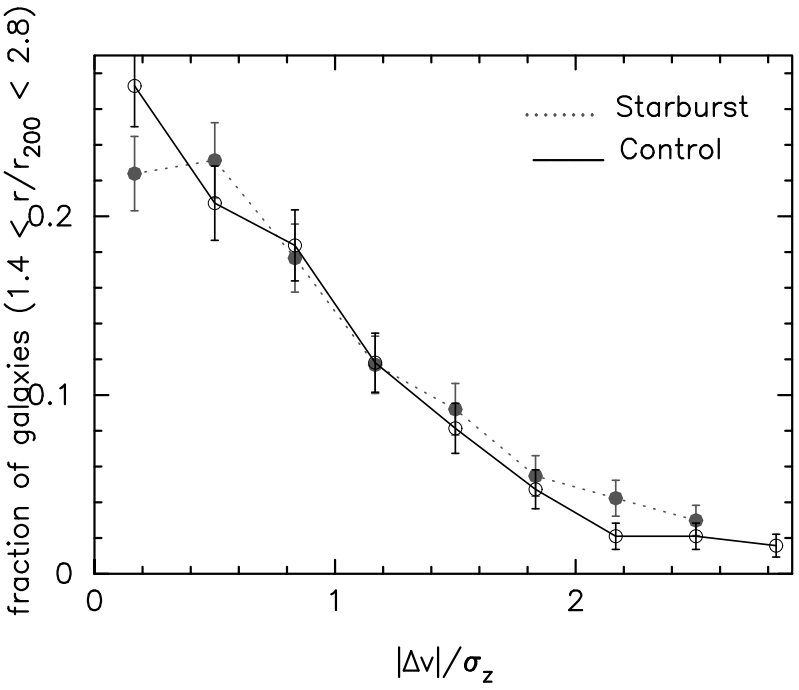

Figure 5.10: Fraction of galaxies ($1.4 \leq$ r/r$_{200} \leq 2.8$) in the SB (*dotted*) and CN (*solid*) cluster samples as a function of scaled relative velocity. No significant peak at 0 or above implies that these galaxies are a mix of infalling and backsplash galaxies.

actions. It is therefore not surprising that SB clusters seems to be relatively more massive (Fig. 5.6), though in literature there seem to be an ambiguity in the observational results. By analysing 25 clusters, Poggianti et al. (2006) find that although the fraction of emission-line galaxies is anti-correlated with cluster's σ_v at high redshifts ($0.04 < \mathrm{z} \leq 0.8$), the intermediate mass ($\sigma_v \sim 500 - 600$ km s^{-1}) z $= 0$ clusters do not show any systematic trend. At $\mathrm{z} = 0$ Biviano et al. (1997) showed that the fraction of emission-line galaxies is higher by $\sim$ 33% in clusters with $\sigma_v > 900$ km s^{-1} as compared to those with $\sigma_v < 600$ km s^{-1}. But in a study of 17 clusters from the 2dFGRS, Lewis et al. (2002) find no difference between the mean luminosity normalised SFR (proxy for specific star formation rate) profile of their cluster sample ($0 < \mathrm{z} \leq 0.8$) separated around $\sigma_v = 800$ km s^{-1}.

It might be argued that the observed enhancement in the SFR of galaxies on the periphery of clusters is due to the mixing of 'backsplash' galaxies with those infalling in the cluster for the

first time. These 'backsplash' galaxies are supposed to have crossed the cluster's core at least once (Balogh et al. 2000; Mamon et al. 2004; Rines et al. 2005; Gill, Knebe & Gibson 2005; Mahajan, Mamon & Raychaudhury 2011b). Gill, Knebe & Gibson (2005) used hydrodynamical DM simulations to show that the population of backsplash galaxies can be detected by a distinct centrally peaked σ_v in the radial interval 1.4-2.8R_{200}; while a non-zero velocity distribution peak shows that the galaxies are falling into the cluster for the first time (see Chapter 6; Mahajan, Mamon & Raychaudhury 2011b).

We test this hypothesis by plotting the distribution of the relative line-of-sight (l.o.s.) velocities of galaxies in the interval 1.4-2.8R_{200}. The distribution for SB (and CN) clusters' sample as shown in Fig. 5.10 show no prominent peak at $|\Delta z|/\sigma_v = 0$, suggesting that the galaxies on the outskirts of our cluster samples are a mix of infalling and backsplash populations. This is in agreement with literature (Rines et al. 2005; Pimbblet et al. 2006), confirming that some emission line galaxies in and around clusters are backsplash, but a pure backsplash model can not explain all their properties.

Earlier studies have shown that the starburst galaxies in distant ($z \sim 0.5$) clusters are likely to be dwarf galaxies (Poggianti et al. 1999). Moran et al. (2005) observe an enhanced O II emission at 1.8 h_{70}^{-1} Mpc from the centre of the cluster CL0024 ($z = 0.4$). All the high emission line galaxies in CL0024 are dwarfs ($M_B > -20$). Haines et al. (2006b) find an excess of blue dwarf galaxies ($M_r > -18$) around 1.5 h_{70}^{-1} Mpc from the centre of the Shapley supercluster. In Mahajan et al. (2010a, 2011a) we analysed the star formation properties of galaxies in the Coma supercluster region. Our analysis suggested that unlike giant galaxies, star formation in dwarf galaxies is independent of their environment, except in very dense environments.

Although, due to the flux limitations of the SDSS data used in this work, we have not included the low luminosity ($M_r \geq -20.5$) galaxies in our analysis, it is worth noting that the picture portrayed above will hold for them too. The only exception in case of dwarf galaxies might be the absence of the second burst seen near the cluster centre ($\sim 0.5 R_{200}$; Fig. 5.5). This

is because amongst others, evaporation of cold gas becomes very important for dwarf galaxies (Fujita 2004; Boselli & Gavazzi 2006). Hence even a relatively softer encounter with a more massive galaxy may lead to loss of all gas via tidal stripping and/or evaporation. Porter & Raychaudhury (2007) and Porter et al. (2008) also find that the enhancement in star formation (quantified using the η-parameter) seen in filament galaxies is exclusive to dwarf galaxies. Studies of dwarf galaxies in the nearby Coma supercluster show that the dwarf population is more vulnerable to the impact of the changing environment on cluster outskirts, as a result of which they experience a burst of star formation on first encounter, and are quenched soon thereafter (Smith et al. 2008; Mahajan, Haines, & Raychaudhury 2011a).

5.4.2 The LSS connection

High resolution simulations suggest that intermediate-density regions like inter-cluster filaments can host a significant fraction of gas with temperature of 10^5-10^7 K (Cen & Ostriker 1999; Croft et al. 2001; Phillips, Ostriker & Cen 2001; Dolag et al. 2006). It thus becomes crucial to understand the properties of galaxies on these filaments in order to evaluate their role in the evolution of galaxies. This gas may be detected as radio emission (e.g. Kim et al. 1989), or through its bremsstrahlung emission in soft x-rays. But not only is the signal too weak for the present day detectors, the former can be employed only for very nearby cluster pairs. However, in literature there are a few claims of detections of such warm intergalactic medium (e.g. Kaastra et al. 2003; Markevitch et al. 2003).

Recently, Dolag et al. (2006) have attempted a hydrodynamical dark matter (+ gas) simulation to understand the global properties of these large-scale structures. They show that due to very low gas density (10^{-28} g cm^{-3} in 3-d and 10^{-3} g cm^{-2} in projected space respectively) and temperature $< 10^7$ K, it is very difficult to observe these filaments directly. In order to understand the role of filaments in the evolution of galaxies indirectly, some studies have specifically targeted the galaxies traversing through filaments (e.g. Porter & Raychaudhury 2007; Boúe et

al. 2008; Fadda, Biviano & Durret 2008; Porter et al. 2008; Mahajan, Haines & Raychaudhury 2010).

Semi-analytic modelling shows that galaxies with similar local density, but different 'global' environment (i.e. different position in the LSS), show subtle but non-negligible differences in their SFR and colours (González & Padilla 2009). González & Padilla attribute their result to the coherent motion of galaxies approaching clusters through large-scale filaments (Porter & Raychaudhury 2007; Fadda, Biviano & Durret 2008; Porter et al. 2008; Mahajan, Haines & Raychaudhury 2010). Struck (2006) discuss an interesting scenario whereby the galaxies in a galaxy group crossing a cluster may be pulled towards each other, thus increasing the local galaxy density by an order of magnitude, and the probability of galaxy-galaxy interactions by about a factor of 100 (density squared). Even though we do not find any statistically significant evidence to support that the enhancement in SFR is seen in galaxies falling in as groups, some other observational studies seem to favour this scenario (Gavazzi et al. 2003; Moss 2006; Oemler et al. 2009).

Type I (straight) filaments mostly occur between close ($\lesssim 5-10$ Mpc) pairs of clusters (Colberg et al. 2005; Dolag et al. 2006; Pimbblet, Drinkwater & Hawkrigg 2004). But majority ($\geq 50\%$) of filaments in the cosmic web are of type II (warped). Relatively shorter length (Colberg et al. 2005; Dolag et al. 2006; Pimbblet, Drinkwater & Hawkrigg 2004) and higher matter density may imply that the probability of galaxy-galaxy interactions occurring amongst galaxies on these filaments is higher than their warped counterparts. Fig. 5.8 favours this scenario. We find that $\sim 32\%$ of the (classifiable) filaments feeding the comparison (CN) clusters are of type I (straight), as compared to $\sim 47\%$ in the SB clusters. This is in agreement with the results from simulations, where it is shown that in a CDM Universe more massive structures are more strongly clustered than their less massive counterparts (Colberg et al. 2005). Hence, the relatively massive ($\sigma_v \gtrsim 500$ km s^{-1}) clusters are more likely to have a straight filament connecting them to a nearby companion cluster. It is worth noting that the morphology of a significant

fraction of our filaments remain uncertain because of low galaxy ($M_r \leq -20.5$) densities, so the quantities mentioned in this section may only be considered representative, not precise.

On a final note, we suggest that our SB clusters are most likely to be relatively massive clusters connected to a neighbouring cluster through a straight filament. The occurrence of starburst galaxies at their periphery is a direct consequence of the way local conditions (i.e. galaxy density and relative velocity) are affected by the global LSS layout.

5.4.3 Future implications

As compared to the galaxies at z ~ 0, galaxies in the past were more gas-rich. Hence it would not be an exaggeration to say that such events of spectacular starbursts would be more commonly seen at higher redshift; although a confirmation of this can only be made by studying an unbiased sample of high redshift clusters, sampled upto their infall regions (e.g. Kartaltepe et al. 2008; Verdugo et al. 2008).

Once such data are available, one can ask the question whether the excess of blue galaxies observed in clusters at higher redshift, the well known 'Butcher-Oemler effect' (Butcher & Oemler 1984) is linked to the occurrence of starburst galaxies in infalling galaxies, which appear to be nearer the cluster centre in projection (see Oemler et al. 2009 for instance). For a sample of x-ray luminous clusters at $0.18 <$ z < 0.55, Ellingson et al. (2001) showed that the galaxy populations in the cluster cores are same at all epochs, but higher redshift clusters show a steeper gradient in the fraction of blue galaxies when region outside the core ($> 0.5\mathrm{R}_{200}$) are considered. But such colour-based studies may have inherent bias due to the non-negligible fraction of galaxies that deviate from the normal correspondence between photometric colours and spectroscopically derived SFR/indicators (see Mahajan & Raychaudhury 2009 for instance).

Another interesting idea to explore, though relatively more plausible in simulations, is to find what is the likelihood of seeing a starburst galaxy on the filament feeding a cluster along the line of sight. Such a galaxy will appear to be at the centre of cluster, yet showing physical

and intrinsic properties as that of its counterparts far away from the cluster core (for instance see Oemler et al. 2009).

It would also be very interesting to study the intermediate/dwarf ($M_r \leq -20.5$) galaxies in the infalling regions of the SB clusters. Since they can be harassed more easily relative to their massive counterparts, a detailed morphological analysis of the dwarf starburst galaxies can provide useful clues to understanding the impact of environment on galaxy evolution (e.g. Moss 2006). Considering galaxy-galaxy harassment to be the process dominating the current star formation properties of galaxies on cluster outskirts, these galaxies may show signatures of tidal interactions with their neighbouring galaxies. But unfortunately, the SDSS data used in this work limits us from doing either of the above mentioned, and we leave this for future communication.

5.5 Summary and Conclusion

Using the integrated SFR (and SFR/M^*) derived by Brinchmann et al. (2004) for galaxies in the SDSS DR4, we have analysed the star formation properties of galaxies ($M_r \leq -20.5$) in nearby ($0.02 \leq z \leq 0.15$) Abell clusters. The main results obtained in this chapter are:

- Star formation activity in galaxies on the outskirts of some clusters is enhanced near their boundary (R_{200}), and less prominently but significantly, further into the clusters at $\sim 0.5 R_{200}$.

- In agreement with several other observational studies and simulations, we find that this enhancement in the SFR of galaxies on cluster outskirts is most likely to be due to enhanced galaxy-galaxy interactions.

- The galaxy-galaxy interactions seems to be more efficient in the infall regions of relatively massive clusters (Fig. 5.6), which are likely to be fed by high-density straight filament.

The clusters which do not show any starburst galaxy on their outskirts (CN), are more likely to be fed by type-II (warped) filaments.

- The galaxies on the cluster outskirts ($1.4 \leq \mathrm{r}/\mathrm{R}_{200} \leq 2.8$), showing high SFR are a mix of galaxies that have passed through the cluster core at least once (the 'backsplash' population), and those which are falling in it for the first time.

Chapter 6

Velocity modulation of galaxies in and near clusters

6.1 Introduction

The wide variety in star formation properties of galaxies is an inevitable consequence of the varied environments they inhabit. Physical properties of galaxies such as morphology (Dressler 1980), colour (e.g. Balogh et al. 2004a), luminosity (e.g. Adami, Biviano, & Mazure 1998), individual spectral indices used as star formation rate (SFR) tracers, such as the EW of O II or Hα (e.g. Balogh et al. 2004b; Haines et al. 2006a), are known to vary systematically with environment. As they leave their sparsely populated base in the *field* for the high density regions of galaxy clusters, galaxies see their dominant stellar population become older, emission lines disappear from their spectra, complex spirals transform into more uniform spheroids, and the SFR decreases by 1-2 orders of magnitude.

It is thus generally believed that the cluster environment is hostile to star formation. For example, the denser the environment, the stronger will be the stripping of interstellar gas either by the ram pressure of the intra-cluster gas (Gunn & Gott 1972) or by the tidal field of the

cluster (Merritt 1983), leading to starvation for subsequent star formation (Larson et al. 1980). So a galaxy that entered the cluster virial radius ~ 1 Gyr ago, and has since crossed the core of the cluster, should have lost its gas via either of these two effects during its passage through the cluster core (see for instance Vollmer 2009 for the impact of ram-pressure stripping in the Virgo cluster). Moreover, in the intermediate density environments on the cluster outskirts, mechanisms like galaxy-galaxy interactions (e.g. Moore et al. 1996) seem to dominate the process of galaxy evolution (e.g. Porter & Raychaudhury 2007; Porter et al. 2008; Mahajan & Raychaudhury 2009). Thus star-forming *infalling* galaxies are expected to have distinctive properties compared to the passively evolving *virialized* population inside the cluster.

However, one can define an intermediate population of galaxies that have travelled through the cluster core (perhaps more than once) and have not yet had time to mix with the virialized population. These *backsplash*[1] galaxies would have felt the first effects of the cluster environment, but may not have evolved all the way to attain the passive properties of the virialized population. In their simulations of six clusters, Balogh et al. (2000) found that $54\% \pm 20\%$ of dark matter (DM) particles at $1-2\,R_{200}$ from the cluster centre had been inside the virial radius (R_{200}) at some earlier time. Gill, Knebe & Gibson (2005) estimated similar fractions, considering a virial radius equivalent to R_{100}, and further added that 90% of such particles went as close to the cluster centre as 50% of the virial radius. Mamon et al. (2004) used both analytical methods and cosmological simulations to conclude that DM particles travel through the core of the cluster out to 1–2.5 R_{100} on the other side.

The backsplash galaxies may contribute to the observation that the radial trends of star formation diagnostics extend to at least twice the virial radius (Balogh et al. 2000) from cluster centres. Hence, the intermediate environments found in inter-cluster filaments and on the outskirts of galaxy clusters play a key role in defining the evolutionary history of galaxies (Rines et al. 2003; Gill, Knebe & Gibson 2005; Porter & Raychaudhury 2007; Porter et al. 2008;

[1]The term *backsplash galaxies* was first coined by Gill, Knebe & Gibson (2005).

Mahajan & Raychaudhury 2009).

Most results indicate that the properties of galaxies evolve as they encounter denser environments, i.e. progress from the field towards the cluster. This could be due to the prevalence of smaller clusters (galaxy groups) as one approaches rich clusters, as the tidal field and possibly some mild form of ram pressure stripping might play a similar role, as they do in more massive clusters, to deplete the gas reservoirs of galaxies. Alternatively, it is possible that the gas reserves of galaxies may be protected by the pressure of the surrounding intra-group medium (IGM) from being tidally perturbed, preventing the star formation in the galaxy from being quenched, even after spending > 1 Gyr in crossing the cluster. In such a case, an increase in tides generated during the group–cluster merger may instead result in an enhancement of SFR in group galaxies (Bekki 1999). Although such a group pre-processing scenario is yet to be confirmed, some evidence in its favour is found in recent observational studies (e.g. Oemler et al. 2009).

The main difference between infalling and backsplash galaxies is that the former have larger apocentres, hence larger radial (3D) velocities. Therefore one expects that backsplash galaxies will have lower absolute line-of-sight (hereafter, LOS) velocities[2] than the infalling galaxies. One is therefore motivated to study the modulation of the radial trends of galaxy properties with absolute LOS velocity.

In the central regions of clusters, the relative velocities of galaxies have been found to be correlated with their luminosity (e.g. Chincarini & Rood 1977; Struble ; Bothun & Schombert 1990; Biviano et al. 1992 among others), morphology (de Vaucouleurs ; Sandage & Tammann 1976; Moss & Dickens ; Helou, Salpeter, & Krumm 1979; Sodre et al. 1989; Biviano et al. 1992; Girardi et al. 2003, and more recently spectral type (Biviano et al. 1997; Pimbblet et al. 2006). The early-type, massive and passive galaxies are found to have lower velocity dispersion relative to their late-type, star-forming counterparts. It has been shown that this velocity

[2]Our absolute LOS velocities are in the cluster frame.

segregation of mass (or luminosity) in cluster galaxies is neither induced by morphological segregation nor limited to cD galaxies (Biviano et al. 1992).

There has been some efforts to study the velocity segregation in galaxy properties on the outskirts of galaxy clusters (e.g. Mohr et al. 1996; Rines et al. 2005; Pimbblet et al. 2006). In particular, Rines et al. 2005 find no significant difference in the velocity distribution of the emission-line and absorption-line galaxies with projected radii between 1 and $2\,R_{200}$ in a sample of eight nearby x-ray bright clusters. However, emission-line galaxies outside the virial radius appear to have a significantly larger velocity dispersion than their absorption-line counterparts (but Rines et al. 2005 do not provide any quantitative estimate of the significance). Moreover, from Fig. 6 of Rines et al. (2005), the mean velocity dispersion profile of emission-line galaxies appears significantly steeper than that of non-emission-line galaxies (this trend was not noted by the authors). Rines et al. (2005) concluded that star-forming galaxies in the infall regions are not field interlopers, which leads them to reject a simple model where the truncation of star formation at low projected radius is solely caused by the efficient quenching of star formation in (backsplash) galaxies that have crossed through the cluster.

In this chapter, using the very large Sloan Digital Sky Survey (SDSS), we have collected sufficient data around hundreds of clusters to analyse the differences in the distribution in *projected phase space* (projected radius R and absolute LOS velocity $|v_{\rm LOS}|$) of star-forming and passive galaxies at much finer resolution than previously performed. We look for and find a significant velocity modulation of the variations of stellar mass and star-formation properties with projected radius. We also build simple dynamical models involving the virial, infalling and backsplash populations of galaxies to explain our results, calibrating our models and the projection effects using a cosmological simulation (Appendix C).

6.2 Data

The observational dataset and star formation diagnostics used in this chapter are described in §2.2 and Appendix B respectively.

We selected our galaxy clusters from the 'group' catalogue compiled by Yang et al. (2007) from DR4 of the SDSS. The selection criterion and cluster properties are described in Appendix B.

From the spectroscopic galaxy catalogue of SDSS DR 4 (§2.2) we select galaxies that meet the following criteria:

1. redshift range $0.02 \leq z \leq 0.15$;
2. absolute magnitude: $M_r \leq -20.5$;
3. half-light angular radius: $\theta_{\rm eff} \leq 5''$;
4. projected separation with cluster: $R < 2\,R_{\rm v}$;
5. velocity relative to cluster: $\left|v_{\rm LOS} - v_{\rm LOS}^{\rm cluster}\right| \leq 3\,\sigma_v^{\rm cluster}$.

Our luminosity limit roughly corresponds to $L \geq 0.5\,L*$ (given that $M_{r,*}^{0.1} = -20.44\ +5\ \log\ h$ Blanton et al. 2003), which corresponds to the apparent magnitude limit ($r \leq 17.77$) for the SDSS spectroscopic catalogue at $z = 0.1$. The galaxy redshifts are chosen in an interval that is slightly larger than for the clusters, so as to avoid missing galaxies lying behind (or in front) of the most (least) distant clusters. The angular size criterion ensures that the spectrum obtained from the $3''$ SDSS fibre is a fair representation of the light from the galaxy, and does not just correspond to the passive central bulge of the galaxy, although it may also imply that the sample is limited to compact galaxies only. However, we find that excluding this condition from the sample selection procedure adds only a few more galaxies to the sample, and thus statistically the results discussed in this chapter are not affected by any potential biases arising due to this criteria.

This gives us a sample of 19,904 galaxies in or near 268 clusters covered out to 2 virial radii in projection and 3 times the cluster velocity dispersions along the LOS.

The cluster galaxies are compared with a sample of 21,100 field galaxies, randomly chosen to have the same redshift and luminosity distributions as those of the cluster galaxies. We required the field galaxies to lie at least 10 Mpc away from the centres of all groups with $N \geq 5$ and halo mass $\geq 10^{12.5}\,\mathrm{M}_{\odot}$ in the Yang et al. (2007) catalogue (this includes clusters). Since the galaxy properties depend on their distance from the nearest large structure (e.g. Mahajan, Raychaudhury & Pimbblet 2011c) out to $\sim 3R_{200}$ ($\lesssim 6\,h_{70}^{-1}$ Mpc; e.g. Rines et al. 2003; Mahajan & Raychaudhury 2009), a linear distance of 10 Mpc (corresponding to typically $6.7\,R_{\rm v}$) from all groups and clusters ensures that our field sample is not contaminated by the effect of any groups or clusters.

6.3 Star formation diagnostics

In this chapter, as our principal diagnostic we use the specific star formation rate (SFR/M^{*}) of a galaxy as estimated, from the optical spectrum by Brinchmann et al. (2004) for all the galaxies belonging in the spectroscopic catalogue of SDSS DR4. From this and a few other spectral indices, namely the emission-corrected Hδ_A (hereafter, Hδ) EW and the 4000 Å break, estimated in a related work (Kauffmann et al. 2003a), we compare the trends seen in the current star formation activity and star formation histories (SFHs) of different types of galaxies (Appendix B).

The spectrum of a galaxy that has experienced a burst of star formation in the recent past (1–3 Gyr ago) is expected to show a strong absorption of Hδ in the optical spectrum. This is because A type stars, which significantly contribute to the Hδ absorption have a lifetime of $\lesssim 1.5$ Gyr, but the starburst can produce enough ionising radiation to fill in the Hδ absorption. However, as the episode of star formation ends, the Hδ absorption line becomes more transparent. The

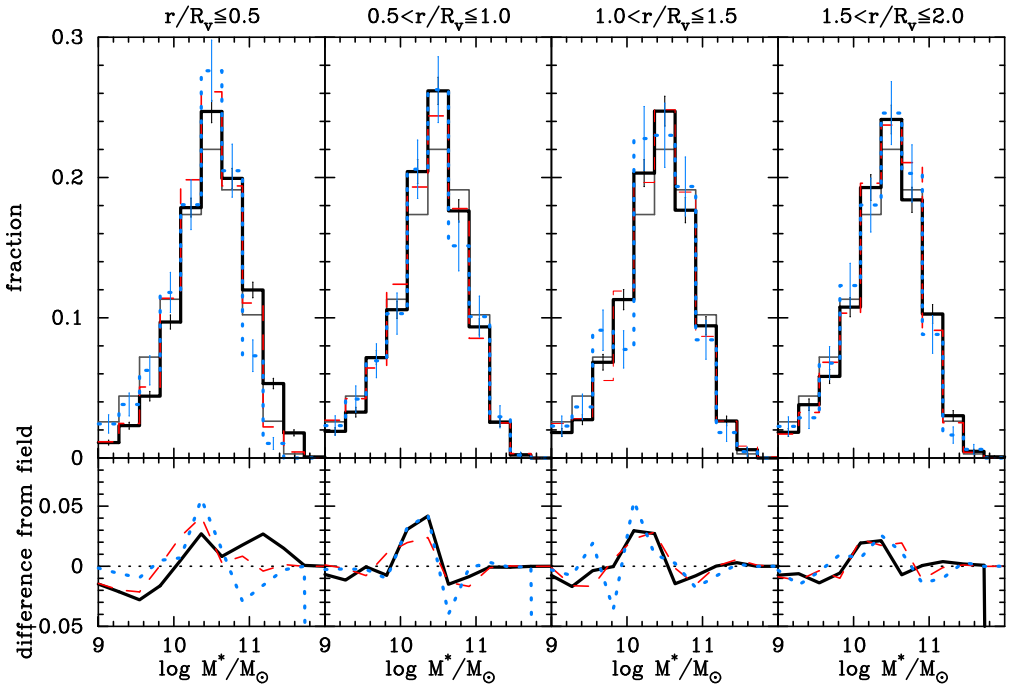

Figure 6.1: The distribution of stellar masses for our galaxy samples, in four bins of projected radius in the four panels from left to right. The *solid black*, *dashed red* and *dotted blue* distributions represent absolute LOS velocity bins $|v_{\rm LOS}|/\sigma_v = 0$–1, 1–2 and 2–3 respectively. The *thin grey distribution* denotes the field. The *bottom panels* show the difference between the binned cluster distributions and that of the field. The *error bars* are Poisson. In the flux limited SDSS, galaxies in the local Universe have their M^* distribution centred around $M^* = 3 \times 10^{10}$ $\rm M_\odot$ (Kauffmann et al. 2003a). A significant fraction of galaxies with $M^* \geq 10^{11}$ $\rm M_\odot$ are found only in the core of galaxy clusters. Interestingly, the low absolute LOS velocity galaxies in the cores are the ones which are more massive, while the high velocity galaxies mostly inhabit the low mass end.

EW of Hδ has been extensively used in literature to measure the mean stellar age of galaxies, and the elapsed time since the last major burst (e.g. Worthey & Ottaviani 1997, Kauffmann et al. 2003a). On the other extreme is the 4000 Å break (D$_n$4000), which is the strongest discontinuity occurring in the optical spectrum of a galaxy from the accumulation of absorption lines of mainly ionised metals. As the opacity increases with decreasing stellar temperature, the value of D$_n$4000 is largest for old and metal-rich stellar populations. Stellar population synthesis models indicate that D$_n$4000 is mostly sensitive to age, except for sub-solar metallicity populations older than 1 Gyr, where it is also strongly dependent on metallicity (Kauffmann et al. 2003a).

Interestingly, the variation of Hδ with D$_n$4000 is not sensitive to metallicity or dust extinction, thus providing a good measure of SFH, such that for a given D$_n$4000, stronger Hδ implies that the galaxy has experienced a recent burst in star formation (Kauffmann et al. 2003a). In particular, the right panel of Kauffmann et al. (2003a)'s fig. 2 indicates that the combination of $\mathrm{H}\delta > 2$ Å and $\mathrm{D}_n4000 < 1.5$ leads to stellar populations younger than 1 to 3 Gyr for solar and 0.2 solar metallicity populations, respectively.

6.4 Velocity modulation of galaxy properties

The key issue that we are trying to address in this chapter is whether it is possible to distinguish the galaxies that have passed through the cluster core from those that are falling into it for the first time, based on observable parameters. DM simulations show that the backsplash population is most likely to be seen between $1-1.5R_{\rm v}$ and with velocity lower than the mean velocity of the cluster (for instance Mamon et al. 2004; Gill, Knebe & Gibson 2005). So, we stack together all the galaxies found in clusters within $2R_{\rm v}$ and $|\Delta v_{\rm LOS}| < 3\,\sigma_v$, into four bins of projected radius of width $0.5R_{\rm v}$, and into three bins of absolute LOS velocity: $|\Delta v_{\rm LOS}|/\sigma_v$ <1, 1–2 and 2–3 respectively. Below we describe the features of these distributions for various galaxy properties

with respect to one another and the field distribution.

6.4.1 Stellar mass

In Fig. 6.1 we plot the distribution of stellar masses for the 12 classes (3 scaled velocity bins in each of the 4 scaled radial bins) of galaxies as described above. Due to the flux limit of SDSS, the stellar mass distribution of galaxies in Fig. 6.1 appears to be centred around $M^* = 3{\times}10^{10}\,\mathrm{M}_\odot$ in the local Universe (also see Kauffmann et al. 2003a). The most massive galaxies ($\log M^*/\mathrm{M}_\odot \geq 11$) are mostly confined to the cores of the clusters. However, even in the core there seems to be a correlation between the relative LOS velocity of the galaxy with respect to the cluster and its stellar mass. The Kolmogorov-Smirnov (K-S henceforth) statistic show that the most massive galaxies in clusters have low velocities with respect to the cluster, and the high velocity galaxies show an affinity for the field distribution, which is skewed towards the low mass end. The detailed statistical comparison between different distributions is shown in Table C.3 in Appendix.

When the brightest cluster galaxies (BCGs) are excluded, there is no mass segregation in clusters relative to the field (von der Linden et al. 2010). To explore the inter-dependence of M^*, R_v and LOS velocity of galaxies in clusters, we repeated our analysis by excluding the BCGs from the clusters. Contrary to von der Linden et al. (2010), we find that the different distributions still show similar trends: in the inner regions of clusters the most massive galaxies have lowest absolute LOS velocities (see Table C.4).

To analyse mass segregation in a different way, in Fig. 6.2 we show the fraction of high-stellar mass galaxies as a function of projected radius in three bins of absolute LOS velocity, discarding BCGs. Fig. 6.2 confirms our impression that *mass segregation is present, but only at* $R < 0.5\,R_\mathrm{v}$*, and only for the low- and intermediate* $|v_\mathrm{LOS}|$ *galaxies.*

The difference in low and high mass velocity distributions in the projected cluster core is not simply caused by the BCGs, which are excluded from Fig. 6.2 (see also Table C.4). While

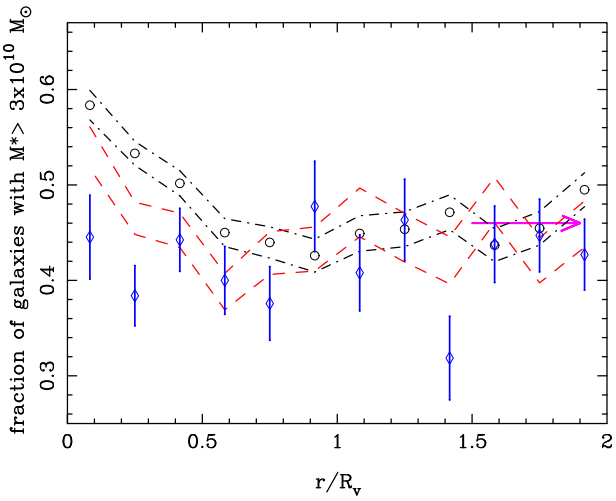

Figure 6.2: The fraction of high stellar mass galaxies ($M^* \geq 3 \times 10^{10}\,\mathrm{M}_\odot$, with brightest cluster galaxies removed), plotted as a function of scaled radius from the cluster centre. The low ($0 - 1\,\sigma_v$) and high ($> 2\,\sigma_v$) absolute velocities shown as *black circles* and *blue diamonds*, respectively, and the $\pm 1\,\sigma$ range (from binomial statistics) are shown as *black dash-dotted lines*, *red dashed lines*, and *blue error bars*, for the low, intermediate (1–2 σ_v) and high LOS absolute velocities, respectively. The *magenta arrow* indicates the field value.

Biviano et al. (1992) also found that high mass non-BCG galaxies had lower absolute LOS velocities, we find that this is limited to galaxies within $0.5R_\mathrm{v}$. In other words, we find that *the high absolute LOS velocity galaxies show no mass segregation*, in contrast with the global luminosity segregation found by others (e.g. Adami, Biviano, & Mazure 1998, von der Linden et al. 2010) when no cuts are made on absolute LOS velocity (which we also find, since the high absolute LOS velocity galaxies are much rarer than their intermediate and low velocity counterparts). Turning things around, the low-mass ($< 3 \times 10^{10}$ M$_\odot$), low absolute LOS velocity galaxies avoid the cluster centre, while their high velocity counterparts do not (Fig. 6.2). We discuss mass segregation amongst cluster galaxies further in §6.6.1.

6.4.2 Galaxy colours

Broadband photometric colours are widely used as proxies for the star formation activity of galaxies. In this chapter we use 'colour offset', which is the difference between $(g-r)^{0.1}$

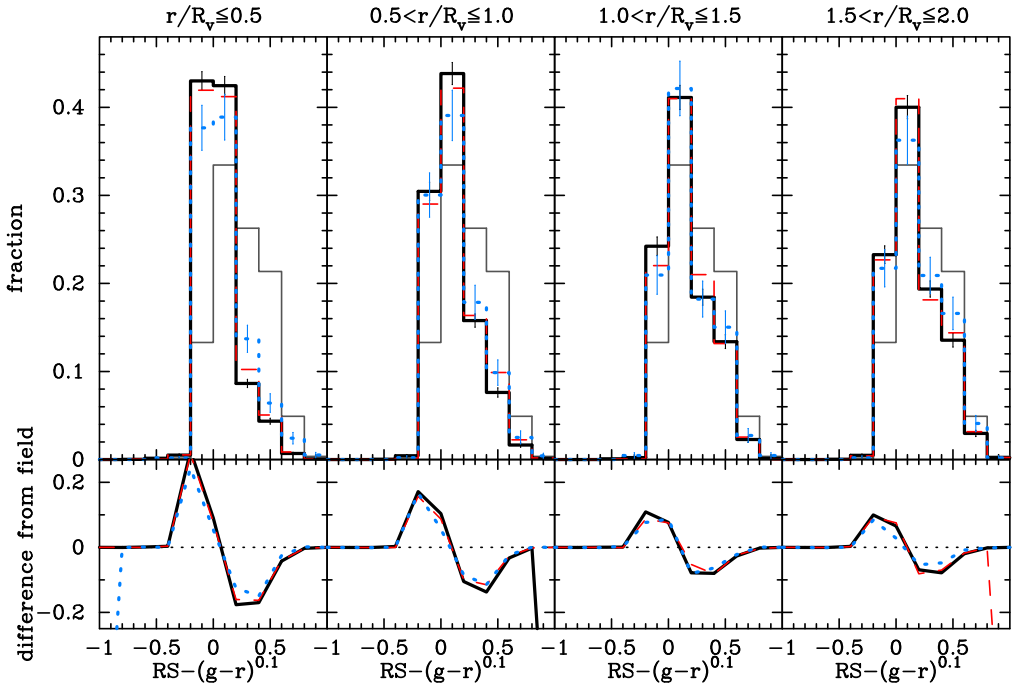

Figure 6.3: Same as Fig. 6.1 but for the "colour offset" of cluster galaxies, i.e., the difference between the $(g-r)^{0.1}$ colour of a galaxy and the Red Sequence colour for a galaxy of the same magnitude. Galaxies bluer than the fitted red sequence (see text) have positive values of the offset on the x-axis. The build-up of the blue tail of the distribution outwards from the cluster core is clearly seen. Interestingly, even in the outermost radial bin (1.5–2$R_{\rm v}$), there are more red sequence galaxies than the field. This shows that physical processes, dependent on environment, efficiently modify properties of galaxies in regions with densities in between the two extremes characterising cluster cores and the field.

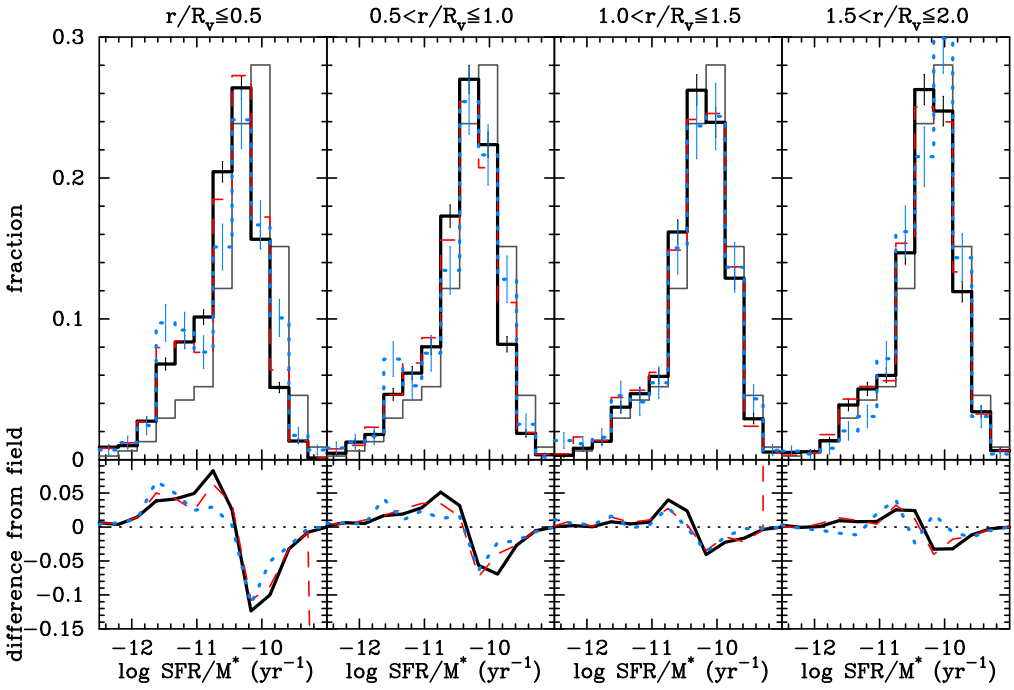

Figure 6.4: Same as Fig. 6.1 but for SFR/M^*. As expected, the cluster distributions are skewed towards the low $\log$ SFR/M^* end in the core region, but only a small tail of galaxies with low $\log$ SFR/M^* is seen in the outer radial bins.

colour of a galaxy and that of the red sequence for a galaxy of the same magnitude, where the red sequence is fitted by stacking all the cluster galaxies together. In Fig. 6.3 we plot the distribution of the colour offset for all 12 classes of galaxies.

The low velocity galaxies in cluster cores are found to have the reddest colours, indicative of their passive evolution. But interestingly, even within the cores the difference between colours of high and low velocity galaxies show statistically significant different distributions (see Table C.5). Out to $2R_{\rm v}$, the distribution of the colour offset for the field galaxies is very different from that of the galaxies residing in and around clusters. As discussed below, on the outskirts of clusters (1–1.5$R_{\rm v}$) the trends seen for broadband colours are consistent with those seen for spectroscopic parameters.

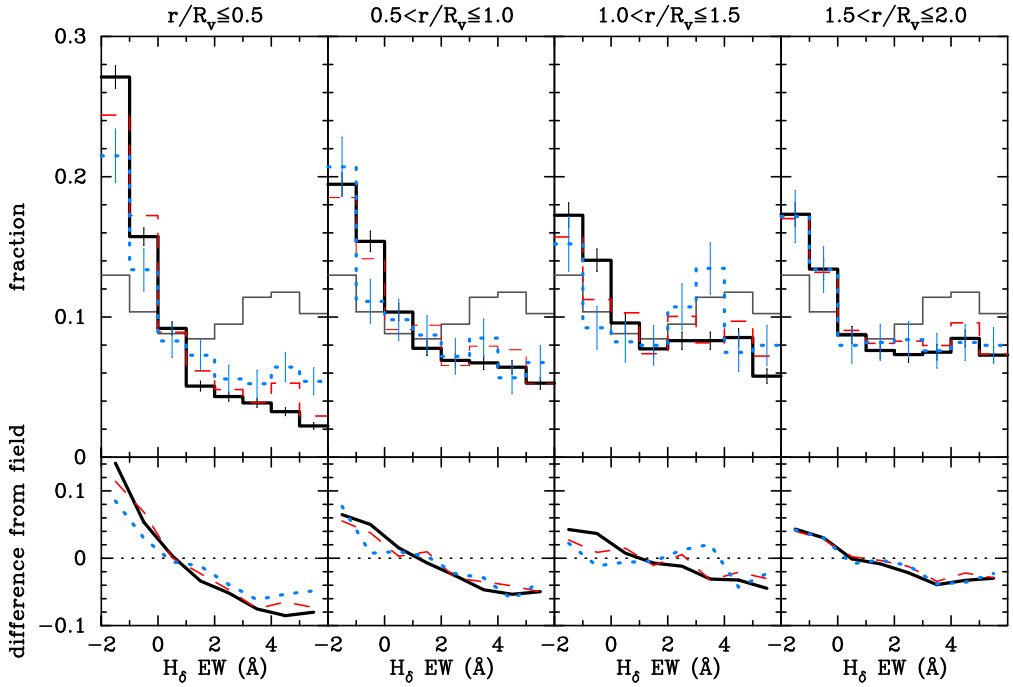

Figure 6.5: Same as Fig. 6.1 but for EW(Hδ). The field distribution shows a clear bimodality around 2 Å. The galaxies in the core of the cluster, most of which are evolving passively, do not show absorption in Hδ. It is interesting to note that the high velocity galaxies in the innermost bins, which are likely to be the newest entrants in the core, are also the ones which are most likely to have experienced a burst of star formation as indicated by relatively high EW(Hδ). This trend in velocity classes continues out to $2R_{\rm v}$ where the difference between the field and the low velocity galaxies is minimum. The difference between the highest (*blue*) and the lowest velocity (*black*) galaxies is statistically significant in all radial bins out to 1.5 $R_{\rm v}$.

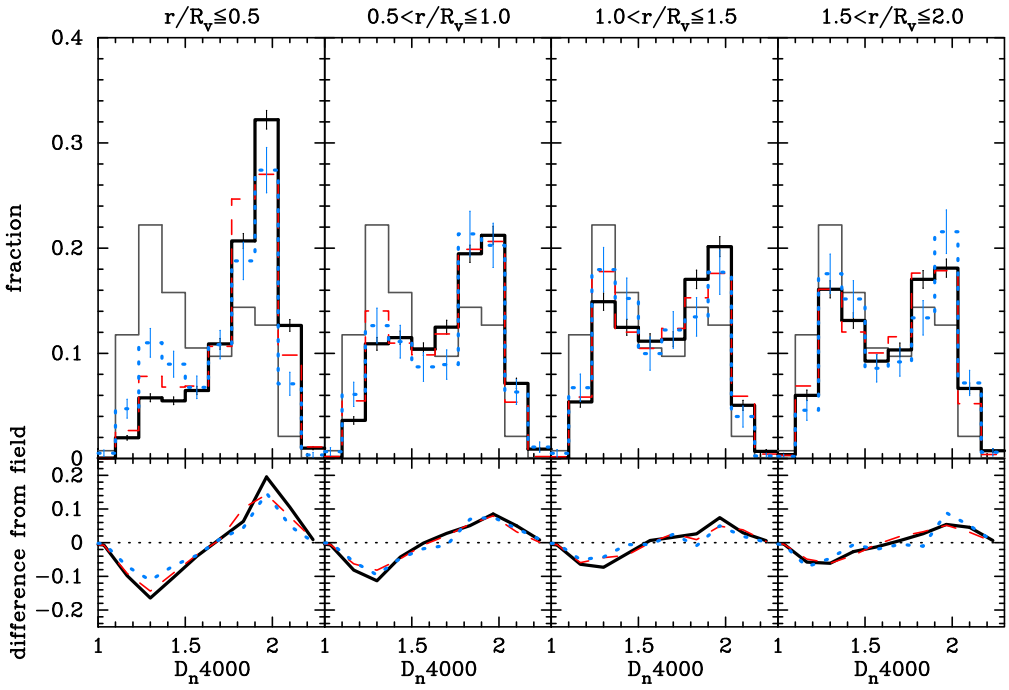

Figure 6.6: Same as Fig. 6.1 but for D_n4000. This figure complements the results in Fig. 6.5. The field distribution is bimodal with a minimum at $D_n4000 \sim 1.5$. The passively evolving galaxies in the cluster core are old and metal-rich, hence their distribution peak at the high end of the D_n4000. However, the high velocity galaxies in the cluster core (dotted blue line) have a distribution similar to that of field galaxies. The trend continues out to $1.5R_{\rm v}$, beyond which the distributions almost merge with the field. The K-S statistics shows the distributions of the high and low velocity galaxies to be statistically different at all distances within $1.5R_{\rm v}$.

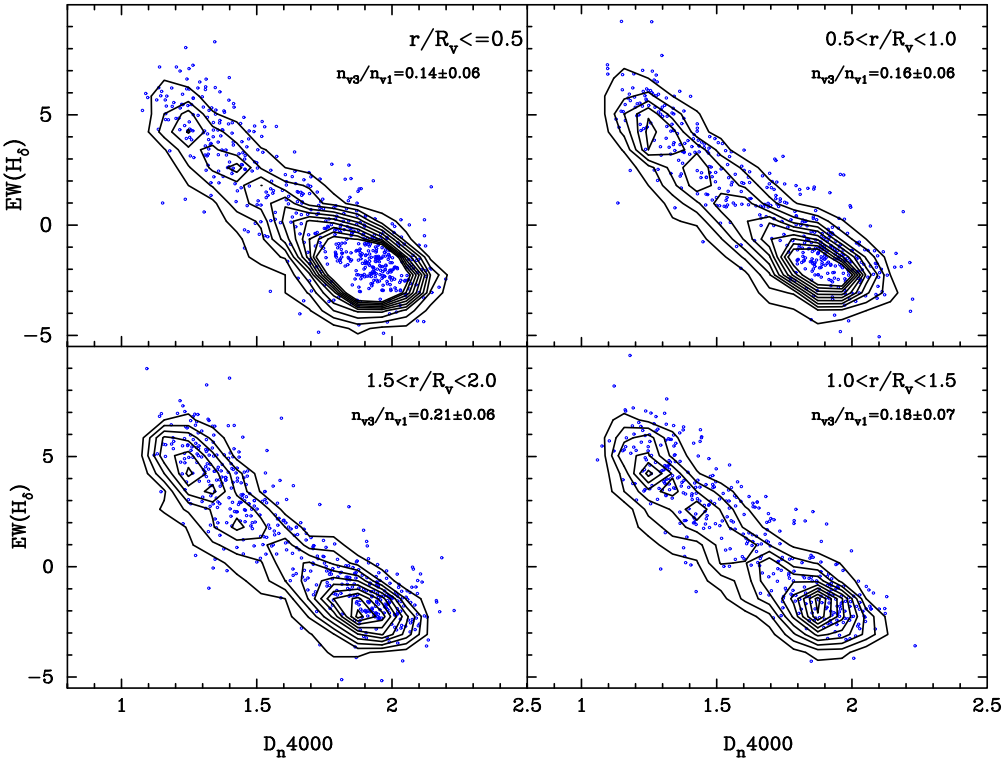

Figure 6.7: The distribution of galaxies having the highest ($|v_{\rm LOS}|/\sigma_v = 2-3$; *blue points*) and the lowest ($|v_{\rm LOS}| < \sigma_v$; *black contours*) absolute LOS velocity relative to the cluster, in bins of increasing (scaled) radius (*clockwise* from top left). The innermost contour represents a density of 100, decreasing by 10 at every subsequent level. The fractions in the top right corner of each panel show the ratio of the numbers in the two classes of galaxies shown, and the scatter in it. Barring the innermost radial bin, the distribution of high velocity galaxies remains the same, although the distribution of the virialized galaxies tends to become bimodal with increasing (scaled) radius.

6.4.3 Diagnostics of specific star formation rate and star formation history

It has been shown that the SFR of galaxies is a function of their stellar mass (e.g. Noeske et al. 2007). So in this work we prefer to use the specific star formation rate (SFR/M^*) to quantify the *current* star formation activity in a galaxy. In Fig. 6.4, we plot the distributions of SFR/M^* as estimated by Brinchmann et al. (2004) for all the galaxies in the spectroscopic galaxy catalogue of the SDSS DR4.

As expected, the cluster galaxies within 0.5 $R_{\rm v}$ have their $\log$ SFR/M^* distributions heavily skewed towards the lower end, indicating passive evolution. Interestingly though, the high end of the values of SFR/M^* in the cluster core, and almost at all radii out to $1.5\,R_{\rm v}$, mostly belongs to galaxies with high velocities. K-S statistic show the difference between the lowest and the highest velocity galaxy distributions (black and blue respectively) to be statistically significant in the core ($< 0.5\,R_{\rm v}$) and on the cluster outskirts ($1-1.5\,R_{\rm v}$; see Table C.6). The field distribution is significantly different from all other classes of galaxies, becoming indistinguishable from the high velocity galaxies only in the outermost radial bin.

Figs. 6.5 and 6.6 show the distributions of EW(Hδ)[3] and D$_n$4000 for the galaxies in 12 different cells of projected phase space (3 scaled absolute LOS velocities times 4 scaled projected radii), and compare them with the distribution of field galaxies. The EW(Hδ) distribution of the cluster galaxies is strikingly different from that of the field galaxies, the latter showing a bimodality at EW(Hδ) ~ 2 Å (also see Table C.7). In the cluster cores, the galaxies with highest velocities, which are most likely to have fallen in recently (Table 1), are the ones that also show Hδ in absorption (EW(Hδ) > 0). This suggests that their likelihood of experiencing a burst of star formation within the last $\sim 1-3$ Gyr is relatively higher than their low velocity counter-

[3]Note that the negative values of EW(Hδ) do not imply Hδ line *emission* in the passive galaxies, because the EW(Hδ) are measured from the pseudo-continuum bands, and so do not always represent the 'true' flux in the Hδ line. The pseudo-continuum bands are required because in the spectra of passive galaxies, the position of several metal lines may coincide with the Hδ line, making it virtually impossible to measure the 'true' flux (G. Kauffmann, priv. comm.; see also Worthey & Ottaviani 1997 and Kauffmann et al. 2003a).

parts. The K-S test shows that the difference between the EW(Hδ) distributions of the highest and the lowest absolute LOS velocity galaxies is statistically significant at all radii within $1.5\,R_{\rm v}$ (Table C.7).

The amplitudes of the 4000 Å break in SDSS galaxy spectra show very different distributions for the highest and lowest classes of $|v_{\rm LOS}|$, both in the core ($< 0.5\,R_{\rm v}$) and on the periphery ($1-1.5\,R_{\rm v}$) of the clusters. However, the distributions of D_n4000 in the $0.5-1\,R_{\rm v}$ bin are only very marginally dissimilar, with $\sim 10\%$ probability of the null hypothesis being satisfied (see Table C.8).

We now take advantage of the fact that together Hδ and D_n4000 yield a good constraint on the SFHs of galaxies (Kauffmann et al. 2003a). In Fig. 6.7 we show the SFHs of galaxies with different absolute LOS velocities in bins of increasing cluster-centric radius. For clarity, we only plot the two extreme absolute LOS velocity classes ($|v_{\rm LOS}| < \sigma_v$ and $|v_{\rm LOS}|/\sigma_v = 2-3$). The distribution of the low $|v_{\rm LOS}|$ galaxies in this plot of EW(Hδ) vs D_n4000, is dominated by the passive sequence (lower right) at low projected radii, and becomes increasingly bimodal with increasing cluster-centric radius. The same evolution occurs for the high $|v_{\rm LOS}|$ galaxies, but is less bimodal at large projected radius. On the other hand, the high absolute LOS velocity galaxies span the entire available parameter space equally at all distances. According to the stellar population study of Kauffmann et al. (2003a) (see their Fig. 3), this is an indication that the SFH is more continuous in the low $|v_{\rm LOS}|$ galaxies and occurs more in bursts in the high velocity galaxies. We discuss these trends in the context of the relative fraction of the infalling and backsplash galaxies, and the fraction of star-forming galaxies as a function of cluster-centric distance in §7.5.

We now refer to galaxies with EW(Hδ) > 2 and $D_n4000 < 1.5$ as *Galaxies with Ongoing or Recent Efficient Star formation* (GORES), following the assumption that a galaxy that experienced "Efficient" star formation $\lesssim 1-3$ Gyr ago is likely to show these features prominently in its spectrum. Our choice of EW(Hδ) and D_n4000 thresholds are based on the bimodality seen

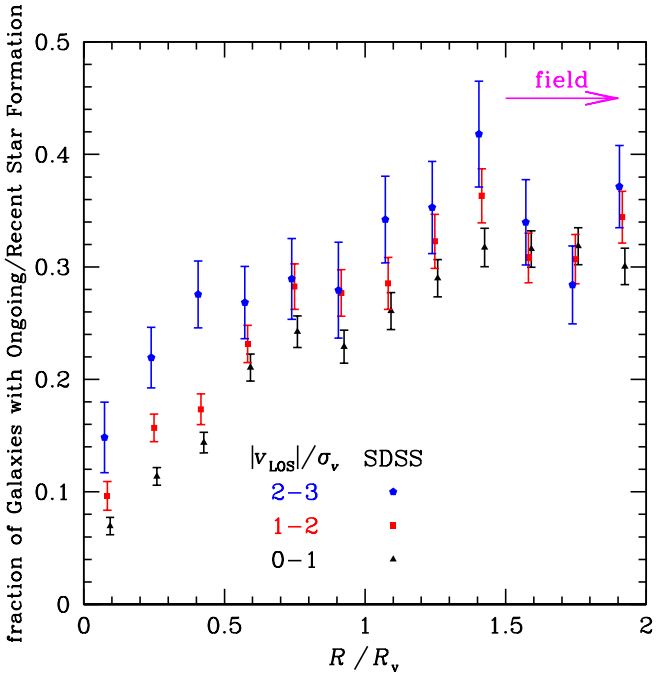

Figure 6.8: The fraction of Galaxies with Ongoing or Recent Efficient Star Formation (GORES, EW(Hδ) > 2 and D$_n$4000 < 1.5) versus projected radius in bins of absolute LOS velocity: $0-1\,\sigma_v$ (*black triangles*), $1-2\,\sigma_v$ (*red squares*), and $> 2\,\sigma_v$ (*blue pentagons*), slightly shifted along the x-axis for clarity. The *magenta arrow* indicates the GORES fraction in the field ($R > 3\,R_{\rm v}$).

in the field distributions (Figs. 6.5 and 6.6).

Fig. 6.8 shows how the fraction of GORES, $f_{\rm GORES}$, varies with projected radius and absolute LOS velocity. The generally increasing radial trend of $f_{\rm GORES}$ is clearly modulated by $|v_{\rm LOS}|$: at all projected radii, the value of $f_{\rm GORES}$ is higher (lower) for high (low) $|v_{\rm LOS}|$.

6.5 Modelling the velocity modulation

In this section, we present simple models to quantify the observed fraction of GORES by combining theoretical predictions (see Appendix C) with the suite of galaxy properties analysed in §6.4.

We build two simple models of the frequency of GORES, one in which their frequency only

depends on the *class* of galaxies, i.e. whether they are part of the virialized, infall or backsplash population, and second, where the frequency of GORES depends upon class *and* the distance from the centre of the cluster. We define the three classes of galaxies in radial phase space (i.e. $[r, v_r]$, where r is the 3D radius and v_r the radial velocity) using the $\mathrm{z} = 0$ output of the cosmological simulation presented in §C.1. We also use this simulation to project onto the observable *projected phase space*, $[R, |v_{\rm LOS}|]$, where R is the projected radius.

The simulations and the classification schemes used to characterise various galaxy populations below are described in Appendix C.

6.5.1 Global deprojection

We first directly deproject the observed fractions of GORES, regardless of the LOS velocity. Writing $f_{\rm GORES}(R) = N_{\rm GORES}(R)/N_{\rm tot}(R)$, we can deduce the surface densities, $\Sigma(R) = N(R)/(\pi R^2)$ of GORES and of all galaxies. Since the projected number profiles $N_{\rm GORES}(R)$ and $N_{\rm tot}(R)$ are fairly noisy, we fit a polynomial to either $\log\Sigma$ vs R or $\log\Sigma$ vs $\log R$ and extrapolate the data beyond the last point by a power-law, whose slope is fit on the last three points. Fig. 6.9 shows the surface density profiles and their polynomial fits. While the fits in $\log R$ diverge dramatically at low R, they match remarkably well at high R, better than the fits in R (but this is masked by the symbols).

One can now perform Abel inversion to deduce the space densities

$$\nu(r) = -1/\pi \int_r^\infty (\mathrm{d}\Sigma/\mathrm{d}R)/\sqrt{R^2 - r^2}\,\mathrm{d}R \tag{6.1}$$

of GORES and all galaxies, and finally obtain the deprojected fraction of GORES by dividing the two space densities. Fig. 6.10 shows the resultant deprojected fraction of GORES. The fits of Σ vs R lead to deprojected GORES fractions (dashed curves) that display larger fluctuations than those obtained from the fits of $\log\Sigma$ vs $\log R$ (thin solid curves). This shows that the

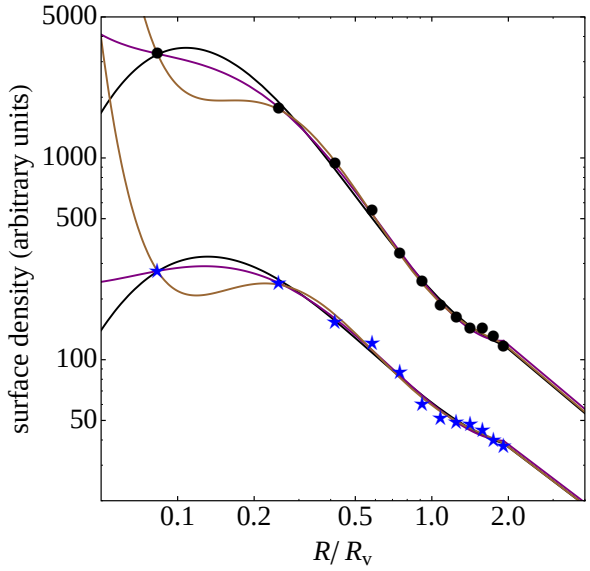

Figure 6.9: Surface density of all galaxies (*top*) and of GORES (*bottom*). The *symbols* are the data (*filled black circles* for all galaxies and *blue stars* for GORES). The *black*, *purple*, and *brown* curves represent the polynomial fits of $\log \Sigma$ vs $\log R$ for orders 3, 4, and 5, respectively. The data were extrapolated beyond $2\,R_{\rm v}$ with power-law fits to the outermost three data points.

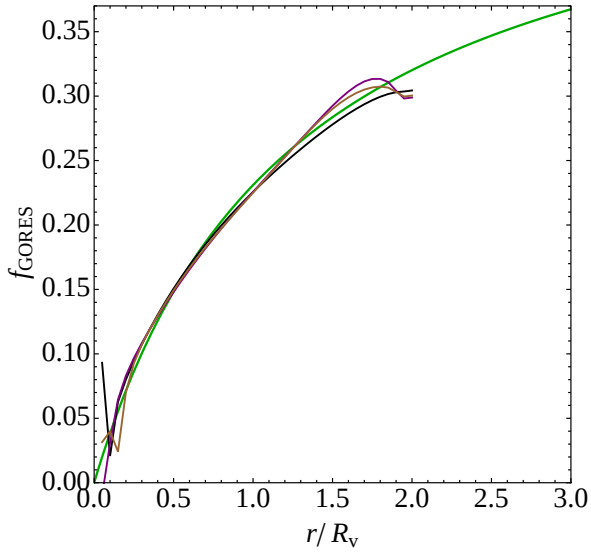

Figure 6.10: Deprojected fractions of GORES (using Eqn. 6.1). *Dashed* and *thin solid curves* respectively show the results obtained by polynomial fits of the log surface density vs $\log R$ (orders 3, 4, and 5 in *black*, *purple* and *brown*, respectively). The *thick green curve* is the fit of Eqn. 6.2 with $f_0 = 0.52$ and $a = 1.26\,R_{\rm v}$, obtained by a χ^2 fit to the order 4 polynomial fit of $\log \Sigma$ vs $\log R$ (*purple solid curve*), with r linearly spaced between 0.05 and $2\,R_{\rm v}$.

quality of the surface density fits is most important at large radii, and this is where the fits in $\log R$ do better. Fig. 6.10 also shows (thick green curve) a fit to the deprojected GORES fraction starting with an order 3 fit to Σ vs R, using

$$f_{\rm GORES}(r) = f_0 \, \frac{r}{r+a} \, . \tag{6.2}$$

We see that the simple, saturated linear model provided in Eqn. 6.2, with asymptotic GORES fraction $f_0 = 0.52$ and *quenching radius for efficient star formation* (hereafter quenching radius) $a = 1.26\,R_{\rm v}$, is a decent representation of the deprojected profile for $f_{\rm GORES}$. While this deprojection leads to an asymptotic value of $f_{\rm GORES} = 0.52$, Eqn. 6.2 yields $f_{\rm GORES} = 0.44$ at our typical minimum projected radius for field galaxies ($6.7\,R_{\rm v}$), very close to their observed fraction of 0.45.

Note that although the constraints from potential SDSS fibre collisions leads to underestimated surface density profiles at low projected radii, this bias in surface density should affect both the total and GORES surface densities in a similar (multiplicative) way (Eqn. 6.1). Hence the effect of fibre collisions on the ratio of GORES to total space densities should be minor.

We now refine the models accounting for the LOS velocity modulation of $f_{\rm GORES}(R)$, using the dynamical classes of the galaxies (virial, infall, and backsplash).

6.5.2 Model 1: Constant recent starburst fraction per class

Suppose that for each of the three classes of galaxies (virial, infall and backsplash), the fraction of galaxies which experienced a recent ($\lesssim 1-3$ Gyr) starburst (GORES) is independent of the 3D radius and radial velocity. Let these three fractions be $f_{\rm v}$, $f_{\rm i}$ and $f_{\rm b}$ respectively.

The fraction of GORES in a cell (R, v_z) of projected phase space can then be written as

$$g_{\rm GORES}(R_i, v_j) = \sum_{\alpha} f_\alpha \, p(\alpha | R_i, v_j) \, , \tag{6.3}$$

Table 6.1: Best-fit parameters for the 3 galaxy classes with the 4 schemes (Appendix C) for the model of constant GORES fraction per class

	$r < R_{\rm v}$ AND					
Scheme	$v_r < v_{r,\rm crit}$	$v_r > -v_{r,\rm crit}$	$f_{\rm v}$	$f_{\rm i}$	$f_{\rm b}$	χ^2_ν
0	virial	virial	0.11	0.33	0.26	4.6
1	infall	virial	0.10	0.34	0.24	3.5
2	infall	backsplash	0.10	0.33	0.28	2.9
3	infall	infall	0.10	0.34	0.23	2.7
4	backsplash	backsplash	0.09	0.32	0.32	3.1
5	backsplash*	backsplash	0.10	0.34	0.31	3.0

Note: χ^2_ν is the χ^2 per degree of freedom. The errors are typically 0.01 on $f_{\rm v}$ and $f_{\rm i}$ and 0.04 on $f_{\rm b}$. In Scheme 5, the extreme negative velocities for $r < R_{\rm v}$ correspond to infall galaxies.

where, $p(\alpha|R_i, v_j)$ is the fraction of particles of class α within the cell (R_i, v_j) of projected phase space (as in Table 1, but with finer radial bins).

One can then perform a χ^2 fit between the observed and predicted fractions of GORES $g_{\rm GORES}(R_i, v_j)$ over all cells (R_i, v_j), using the conditional probabilities for each class, $p(\alpha|R_i, v_j)$, derived from the cosmological simulation (Appendix C). We assume binomial error bars on the observed values of $g_{\rm GORES}(R_i, v_j)$ and that the $p(\alpha|R_i, v_j)$ derived from the cosmological simulation are perfectly known. Furthermore, we use the four Schemes (§C.2) for the three populations, changing the class within the cluster virial sphere for the extreme velocities $|v_r| > |v_{r,\rm crit}(r)|$ (see Fig. C.1). Table 6.1 shows the best fits for each of these four population schemes.

The best-fit predictions for the scheme with the lowest reduced χ^2 (hereafter χ^2_ν), Scheme 3 (where both the very positive and very negative radial velocity objects within the virial sphere are considered to be part of the infall population), provide a reasonable match to the observed fractions of GORES in bins of projected phase space. But $\chi^2_\nu \sim 3$ for this best-fit model, suggests that the model can be improved.

6.5.3 Model 2: Recent starburst fractions increasing with physical radius

In our second model, we suppose that the fraction of GORES is no longer constant per class, but varies with physical radius r as in Eqn. 6.2, varying the normalisation for each class:

$$f_\alpha(r) = f_\alpha \frac{r/R_{\rm v}}{r/R_{\rm v} + a_\alpha} \,, \tag{6.4}$$

i.e. rising roughly linearly with radius for $r < a_\alpha$, and saturating to an asymptotic value f_α at large radii. The predicted fractions of GORES is then

$$g_{\rm GORES}(R_i, v_j) = \sum_\alpha p(\alpha|R_i, v_j) \sum_k f_\alpha(r_k)\, q(r_k|R_i, v_j, \alpha), \tag{6.5}$$

where $q(k|R_i, v_j, \alpha)$ is the fraction of the particles of class α in the cell of projected phase space (R_i, v_j) that are in the kth bin of physical radius. The physical radial bins are expressed as $r_k = R_i \, \cosh u_k$, where u_k is linearly spaced from 0 to $\cosh^{-1} r_{\rm max}/R_i$, using $r_{\rm max} = 50 \, R_{\rm v}$.

Table 6.2 shows the new set of fits. The first set of lines show the fits when we force the same quenching radius for the three classes: $a_{\rm v} = a_{\rm i} = a_{\rm b}$. Again, Scheme 3 provides the lowest χ^2_ν, which is now 1.6 (in comparison with 2.7 for the $f = {\rm cst}$ model). So with the inclusion of an extra parameter, the radially-varying model fits better the data. This is confirmed by the F-test[4] and its significance[5] (Table 6.2). Note that cosmic variance on the finite number of clusters has been incorporated in the errors. The value of quenching radius a is low in Scheme 3, which indicates that it is not that far from the model with constant fraction of GORES per class. The top panel of Fig. 6.11 shows the observed fractions of GORES together with the best fits with Scheme 3 for both the constant per class and radially-varying models with $a_{\rm v} = a_{\rm i} = a_{\rm b}$. Both models capture the initial rise of the GORES fraction with projected radius and subsequent saturation, as well as the velocity modulation, even though the fit is not excellent.

[4]The statistic $F = \sigma_1^2/\sigma_2^2$, where σ_i^2 is the variance.

[5]P is the probability that the F-test rejects the null hypothesis that the two distributions with same means also have the same standard deviations

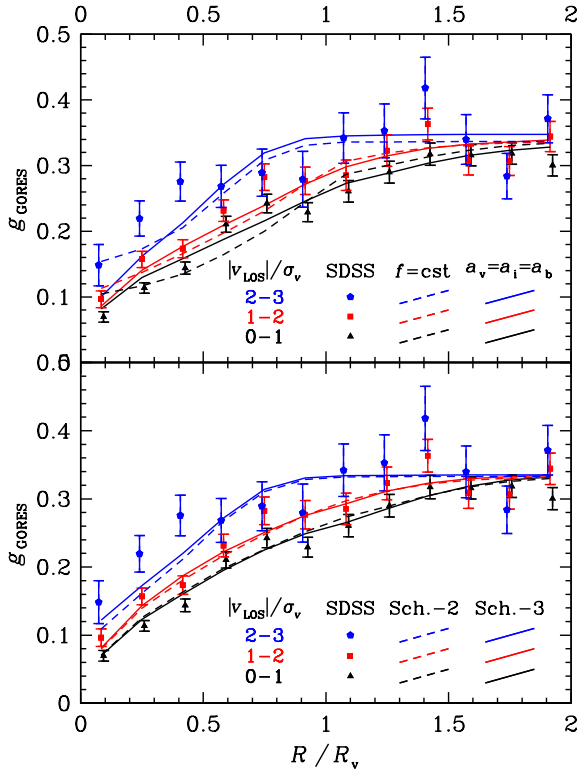

Figure 6.11: Same as Fig. 6.8, with best fit models overplotted: *Top*: the *dashed* and *solid curves* show the best-fit Scheme 3 models (Tables 6.1 and 6.2) assuming no radial dependence (using Eqn. 6.3) and the radially varying one of Eqn.6.4, forcing $a_{\rm v} = a_{\rm i} = a_{\rm b}$, using Eqn. 6.5, respectively. *Bottom*: Best-fit radially varying model (Eqn. 6.4) with free values of $a_{\rm v}$, $a_{\rm i}$, and $a_{\rm b}$, for Schemes 2 (*dashed*) and 3 (*solid*). The schemes are defined in Tables 6.1 and 6.2.

Table 6.2: Best-fit parameters for the three galaxy classes with the four schemes for models of radially-varying GORES fraction

	$r < R_{\rm v}$ AND										
Scheme	$v_r < v_{r,\rm crit}$	$v_r > -v_{r,\rm crit}$	$f_{\rm v}$	$f_{\rm i}$	$f_{\rm b}$	$a_{\rm v}$	$a_{\rm i}$	$a_{\rm b}$	χ^2_ν	F	P
0	virial	virial	0.32	0.38	0.35	0.58	0.58	0.58	1.9	47.3	1.00
1	infall	virial	0.25	0.37	0.29	0.36	0.36	0.36	1.8	32.2	1.00
2	infall	backsplash	0.21	0.36	0.30	0.29	0.29	0.29	1.7	24.2	1.00
3	infall	infall	0.19	0.36	0.26	0.23	0.23	0.23	1.6	23.7	1.00
4	backsplash	backsplash	0.24	0.36	0.38	0.39	0.39	0.39	1.9	22.1	1.00
5	backsplash*	backsplash	0.22	0.36	0.35	0.34	0.34	0.34	1.9	20.5	1.00
0	virial	virial	0.41	0.35	1.00	0.88	0.27	4.83	2.0	0.6	0.44
1	infall	virial	0.34	0.34	0.36	0.72	0.00	0.00	1.5	3.6	0.96
2	infall	backsplash	0.30	0.33	0.20	0.63	0.00	0.00	1.4	3.8	0.97
3	infall	infall	0.29	0.34	0.41	0.64	0.00	1.57	1.2	5.6	0.99
4	backsplash	backsplash	0.24	0.36	0.38	0.39	0.39	0.39	1.9	3.2	1.00
5	backsplash*	backsplash	0.30	0.35	0.27	0.67	0.00	0.00	1.7	3.2	0.95

Notes: The errors are typically 0.01 on $f_{\rm v}$ and $f_{\rm i}$ and 0.04 on $f_{\rm b}$. In Scheme 5, the extreme negative velocities for $r < R_{\rm v}$ are infall.

In the next set of fits, shown in the bottom four rows of Table 6.2, we lift the assumption of $a_{\rm v} = a_{\rm i} = a_{\rm b}$. The best-fit χ^2 values are now ≤ 1.5 for Schemes 1, 2 and 3, much lower than the radially-varying model with the same scale parameters. The F-test indicates that the improvement is significant, even with the inclusion of two extra parameters (three scales instead of a unique one). Using $\mathrm{CDF}(\chi^2, (N-k)\Delta\chi^2_\nu)$ as a statistic, where $N = 33$ is the number of data points in the projected phase space, and $k = 6$ is the number of parameters that were fit, we conclude that Scheme 3, which still leads to the lowest $\chi^2_\nu = 1.2$, is a significantly better fit than Scheme 0 (99.7% confidence) and marginally significantly better fit than Schemes 4 (91% confidence) and 5 (93% confidence). Although a decent fit to the data, this best-fit model still predicts too low values of $f_{\rm GORES}$ for high absolute LOS velocity galaxies within half virial radius of the clusters. Interestingly, the best-fit model (Scheme 3) predicts a constant GORES fraction for the infall class galaxies ($a_{\rm i} = 0$), while the next best-fitting model (Scheme 2)

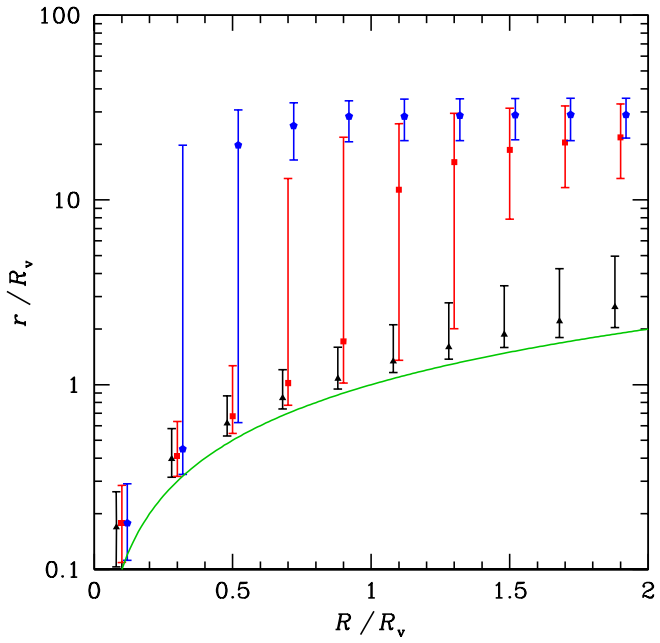

Figure 6.12: Physical radius versus projected radius for particles of stacked mock cluster (medians with error bars for quartiles) in bins of absolute LOS velocity: 0–1 σ_v (*black triangles*), 1–2 σ_v (*red squares*), and 2–3 σ_v (*blue pentagons*). The *green curve* shows $r = R$.

predicts that both infall and backsplash populations have a constant GORES fraction ($a_{\rm i} = a_{\rm b} = 0$).

6.6 Discussion

This chapter is a unique analytical effort to explore the variations in the spectral and physical properties of different dynamical classes of galaxies residing in similar environments projected on the observed sky (projected radius and absolute LOS velocity), and to interpret these differences. We draw a sample of $\sim 20,000$ galaxies ($M_r \leq -20.5$) found within $2R_{\rm v}$ and $|\Delta v_{\rm LOS}| < 3\,\sigma_v$ of 268 galaxy clusters, and a similar sample of field galaxies for this purpose. All the galaxies are taken from the SDSS DR4 spectroscopic galaxy catalogue.

6.6.1 Velocity segregation of stellar mass

Three physical mechanisms might explain the lack of low mass galaxies in the cluster cores amongst the low velocity galaxies (Fig. 6.2): cluster tides, two-body relaxation, and dynamical friction. We examine in turn each one of these.

Tidal effects from the cluster gravitational field (predicted by Merritt 1983; Mamon 1992; Gnedin, Hernquist, & Ostriker 1999, clearly seen in cosmological simulations by Ghigna et al. 1998, and measured through gravitational lensing by Natarajan et al. 2009) will be most effective on slowly moving galaxies, because these have more time to feel the cluster tides. Tides will thus transform massive galaxies into low mass ones, and low mass galaxies into even lower mass ones. So tides cause a decrease in the fraction of high mass galaxies, which goes in the opposite sense of the trend seen in Fig. 6.2.

If two-body relaxation can lead to energy equipartition in the cluster cores, then the high mass galaxies will move slower (in 3D). So the fraction of high mass galaxies among the low 3D velocity ones should increase with decreasing cluster-centric radius. Hence, the fraction of high mass galaxies among the low absolute LOS velocity should also increase with decreasing radius. However, the same argument would lead us to predict that the fraction of high mass galaxies among the high velocity ones should decrease with decreasing radius, and instead Fig. 6.2 shows no such trend. Therefore, the trend in Fig. 6.2 cannot be due to two-body relaxation, unless some other process is increasing the fraction of high mass galaxies among the high velocity ones within the cluster core.

The time required by dynamical friction to make the orbits of galaxies decay towards the cluster centre scales as v^3/m, where v is the 3D velocity of the galaxy of mass m. Therefore the most massive and slowly-moving galaxies should have their orbits decay the most, and be brought to even lower (projected) radius. So dynamical friction should boost the fraction of high-mass slow-moving galaxies in the cluster core. Moreover, the effects of dynamical friction should be weak for the rapidly moving galaxies. This explains the lack of trend in the fraction

of high mass galaxies with projected radius for the galaxies with large absolute LOS velocities.

For high-velocity galaxies, dynamical friction (and tides) act little if one assumes a population in virial equilibrium. Now, the infalling galaxies also tend to have high absolute radial velocities (Fig, C.1), hence high absolute LOS velocities (e.g., Table C.2), in fact even higher than the virialized population. So the same argument applies to the infalling galaxies: their velocities are too high to be seriously affected by dynamical friction or tides.

Is dynamical friction efficient enough to increase the fraction of high mass galaxies towards the centre of the cluster among the slowly moving galaxies? As seen in Table C.2, the virial population should make up over 90% of the low absolute LOS velocity galaxies within $R < 0.5\,R_{\rm v}$, whereas for $|v_{\rm LOS}| > 2\,\sigma_v$, the infall population should account for as much as 24% of the galaxies. Fig. 6.12 shows the distribution of physical radii given the projected radii in our adopted bins of absolute LOS velocity. At $R < 0.5\,R_{\rm v}$, while the low velocities show little contamination by interlopers, at high $|v_{\rm LOS}|$ interlopers account for over 25% of the particles. Note that Fig. 6.12 also indicates that *the physical radii of the low absolute LOS velocity galaxies are close to their projected radii*, so that these low-velocity galaxies can be used to deproject radial trends.

We adopt the dynamical friction timescale that Jiang et al. (2008) carefully calibrated with a cosmological hydrodynamical simulation:

$$t_{\rm df} \simeq 1.4\,\frac{M(r)/m}{\ln[1+M(r)/m]}\,\frac{r}{v_{\rm c}(r)}\,, \tag{6.6}$$

where m is the galaxy mass (with its tidally stripped DM halo) and $v_c(r) = \sqrt{GM(r)/r}$ is the circular velocity at radius r. Eqn. 6.6 incorporates the effects of elongated orbits and tidal stripping. Fig. 6.13 indicates that a galaxy (along with its dark halo) must have a total mass of at least $10^{12.45}{\rm M}_\odot$, for the orbital decay time, at $R = 0.25\,R_{\rm v}$, to be smaller than the age of the Universe. In comparison, Yang, Mo, & van den Bosch (2009) (table 4) find that in the SDSS,

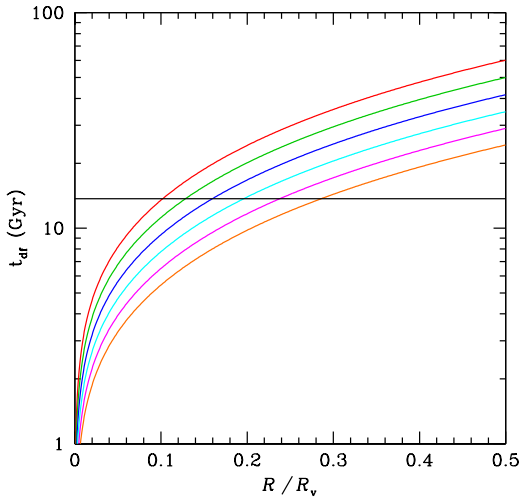

Figure 6.13: Timescale for orbital decay by dynamical friction versus projected radius for galaxies of log total mass (including the tidally stripped dark matter halo) of (from top to bottom) 12 (*red*), 12.1 (*green*), 12.2 (*blue*), 12.3 (*cyan*), 12.4 (*magenta*), and 12.5 (*orange*), orbiting an NFW cluster of scale radius $0.19\,R_{\rm v}$ and mass $M_{\rm V} \equiv M_{100} = 1.9 \times 10^{14} {\rm M}_\odot$ (corresponding to the median mass of $M_{180} = 10^{14.2}\,{\rm M}_\odot$ of the SDSS clusters studied here) within the virial radius $R_{\rm v} \equiv R_{100} = 1.5\,{\rm Mpc}$. The timescale is estimated using Eqn. 6.6 assuming that $r = 1.3\,R$ as inferred from our cosmological simulation (see Fig. 6.12). The age of the Universe is shown as the *horizontal line*.

central group/cluster galaxies of mass $3 \times 10^{10}\mathrm{M}_{\odot}$ reside in halos of mass $10^{12.2}\mathrm{M}_{\odot}$. Also, according to Table 4 of Yang, Mo, & van den Bosch (2009), central haloes of mass $10^{12.45}\mathrm{M}_{\odot}$ have corresponding galaxy masses of $10^{10.66}\mathrm{M}_{\odot}$, i.e. 45% above our galaxy mass threshold. We therefore conclude that dynamical friction might indeed be just sufficiently effective to explain the trend in Fig. 6.2. However, the DM halo of a galaxy extends further out than its stellar component, so halos are tidally stripped more efficiently (e.g., Klimentowski et al. 2009). This means that the ratio of total to stellar mass of cluster galaxies is lower than for field galaxies. One would therefore expect the actual halo masses to be lower than inferred for the central galaxies, from table 4 of Yang, Mo, & van den Bosch 2009, and thus the orbital decay times by dynamical friction to be somewhat longer.

6.6.2 The star-forming galaxies

The distribution of specific star formation rate, broad-band colour, and amplitude of the 4000 Å break show statistical differences with absolute LOS velocity at almost all radii out to $R < 1.5\,R_{\rm v}$ (Figs. 6.3, 6.4, and 6.6; Tables C.5, C.6, and C.8, respectively). However, the field component shows a bimodal distribution in EW(Hδ) (Fig. 6.5) and D$_n$4000 (Fig. 6.6) around 2 Å and 1.5 respectively. This is in agreement with the bimodality of these two diagnostics when plotted in terms of stellar mass, luminosity, or concentration (Kauffmann et al. 2003a). We adopt these thresholds to define a galaxy as a recent starburst galaxy (GORES) if it has EW(Hδ)> 2 Å and D$_n$4000<1.5.

As expected, the fraction of GORES drops within the virial radius $R_{\rm v}$ for all velocity classes (Fig. 6.8). But *the fraction of GORES is modulated by the absolute LOS velocity: at a given projected radius, the galaxies with higher* $|v_{\rm LOS}|$ *have higher fractions of GORES.* For the high absolute LOS velocity galaxies, the fraction of star-forming galaxies declines rapidly but only well within the core region ($\lesssim 0.5\,R_{\rm v}$). This once again strengthens our interpretation that the high-velocity galaxies are the youngest members of the core, having recently fallen in.

A curious feature occurs in the radial variation of both high-mass (Fig. 6.2) and GORES fractions (Fig. 6.8): the galaxies with high absolute LOS velocity show a marginally significant peak (dip) in the fraction of GORES (high mass galaxies) at 1.5 $R_{\rm v}$. If this feature is not a statistical fluke, it may be reflecting the discontinuity seen in SFR of cluster galaxies at the physical radius where infalling and virialized galaxies meet. However, this is expected to occur closer to the virial radius and our simple models involving the virial, infall and backsplash populations do not lead to any discontinuity of $f_{\rm GORES}$ at $1.5\,R_{\rm v}$ (Fig. 6.11). An explanation may require a model going beyond spherical symmetry, e.g., with large-scale filaments feeding clusters (see Porter & Raychaudhury 2007; Porter et al. 2008; Mahajan & Raychaudhury 2009). For the benefit of reader, we emphasise that the enhancement seen in the SFR of galaxies seems to occur in a very narrow region only. This observation is very interesting and still being explored. It might prove useful to distinguish between the backsplash and infall galaxies.

Given the M^*-SSFR anti-correlation (e.g. Mamon, Parker, & Proust 2001; Noeske et al. 2007; Damen et al. 2009), the peak in the fraction of low mass galaxies might be directly linked to the enhancement of SFR in infalling galaxies on the outskirts of clusters before the environmental effects in clusters predominate (Porter & Raychaudhury 2007; Porter et al. 2008).

6.6.3 Identifying backsplash galaxies

The analysis of the $z = 0$ output of DM particles in our cosmological hydrodynamical simulation allows us to distinguish (backsplash) particles that have positions in radial phase space that imply that they previously crossed their parent (mock) clusters from virialized particles (within the virial sphere) and the remaining infall particles (which are actually expanding away from their clusters when they are beyond the turnaround radius of $\simeq 3.5\,R_{\rm v}$). Our analysis in projected phase space indicates that the best place to detect backsplash particles is just beyond the virial radius and at very low velocities (§C.2). With Scheme 3, the backsplash fraction reaches 59% (bottom panel of Fig. C.3) for the lowest absolute LOS velocity bin. With the maximum

backsplash Scheme 5, it reaches 81% for the lowest $|v_{\rm LOS}|$ bin.

Pimbblet (2010) compared the distribution of SSFRs of galaxies with $0.3 < |v_{\rm LOS}|/\sigma_v < 0.5$, attributed to the infall class with the full distribution. This leads him to predict that the fraction of backsplash galaxies decreases as $f_{\rm b} = 0.61 - 0.052\,R/R_{\rm v}$. Such a trend (grey line in the bottom panel of Fig. C.3) appears inconsistent with the backsplash fractions that we predict from our cosmological simulation, even with our maximum backsplash Scheme 5 (upper thick brown curve). It is difficult to understand how could as many as half of all galaxies at 3 virial radii (the maximum projected radius in the analysis of Pimbblet 2010) from clusters be backsplash. Backsplash galaxies typically only bounce out to 1–2 virial radii (Mamon et al. 2004).

Yet, the high fraction of backsplash galaxies found by Pimbblet (2010) agrees with the 54±20% fraction of backsplash particles that Gill, Knebe & Gibson (2005) found in the range of projected radii $1 < R/R_{\rm v} < 2$ from their cosmological simulations. In our Schemes 0–4, we find that only 23%±1%[6] of the particles in this range of projected radius are backsplash particles. However, our backsplash fraction amongst DM particles is marginally consistent with the higher fraction found by Gill, Knebe & Gibson (2005). Even in the maximum backsplash Scheme 5 (partly motivated by Pimbblet (2010)'s high backsplash fraction, but only marginally consistent with the observed fraction of GORES), we find only 40±1% of the particles in the same range of projected radius are backsplash. This is apparently inconsistent with the fraction derived by Pimbblet (2010), although fully consistent with that from Gill, Knebe & Gibson (2005)'s simulations.

Part of our disagreement with Pimbblet (2010) on the fraction of backsplash galaxies in the range $1 < R/R_{\rm v} < 2$ may be caused by too narrow range of $|v_{\rm LOS}|/\sigma_v$ used by him to select the infall galaxies.

[6]The errors in our fractions of backsplash particles are from 50 bootstraps on the 93 halos of the cosmological simulation.

6.6.4 The quenching of star formation in 3D: infalling vs backsplash galaxies

The SDSS spectroscopy provides the means to address the role of the dynamical classes (virial, infall and backsplash) in shaping the properties of galaxies by studying the spectral features as a function of both projected radius *and* absolute LOS velocity.

Beyond the well-known radial dependence of galaxy properties in clusters, our analysis highlights the velocity modulation of these trends for the parameters SFR/M^*, EW(Hδ) and the D$_n$4000. All trends with projected radius are amplified with increasing absolute LOS velocity. As can be seen in Fig. 6.12, the effect of $|v_{\rm LOS}|$ effectively adding to the projected radius is not trivial. Nevertheless, as qualitatively expected from the Hubble flow, in every bin of projected radius the higher absolute LOS velocities leads to higher physical radius.

In §6.4 we find observational evidence to support the statistical differences between the low velocity ($|v_{\rm LOS}| \leq \sigma_v$) and the high velocity ($2 < |v_{\rm LOS}|/\sigma_v \leq 3$) galaxies on the outskirts of clusters (1–1.5 $R_{\rm v}$). K-S tests between different distributions in the clusters and in the field show statistically significant differences between the low and high velocity galaxies between 1–1.5$R_{\rm v}$ in SFR/M^*, EW(Hδ) and the D$_n$4000 (Tables C.3-C.8).

Despite the noisiness of the variations with projected radius of the numbers of galaxies and of GORES, we have been able to deproject the fraction of GORES to show that it is well fit (Fig. 6.10) by a saturated linear model (Eqn. 6.2). Such a model applied in turn to the three different classes of galaxy populations (virialized, infalling and backsplash) with the same quenching radius ($a_{\rm v} = a_{\rm i} = a_{\rm b}$), provides an adequate fit to the variation of GORES with projected radius in three bins of absolute LOS velocity (top four rows of Table 6.2 and upper panel of Fig. 6.11). The model reproduces the rise with projected radius and the higher fractions for higher absolute LOS velocities. Similar models with free star formation quenching radii fit the data even better (bottom four rows of Table 6.2 and lower panel of Fig. 6.11). In particular, the radius-dependent model where galaxies within the virial sphere ($r < R_{\rm v}$) with radial velocity

$|v_r| > |v_{r,\rm crit}|$ are considered to be infalling, provide the best fit to the data (§6.5, Fig. C.1 and Table 6.2).

In contrast, a simpler model, where the fraction of GORES is a constant that only depends on the class of galaxy population, does not provide an adequate fit (Table 6.1), even if it also reproduces these qualitative trends (Fig. 6.11).

The ability of Scheme 3 to better fit the SDSS data than the other three Schemes suggests that the high absolute *radial* velocity galaxies within the virial sphere, both infalling and outflowing, retain their fraction of GORES. However, our best-fit model with Scheme 2 is also an adequate fit, so the model with quenching at pericentre is also consistent with the data.

In the constant GORES fraction model with Scheme 3, the GORES fraction in the backsplash class is half-way between the analogous values for the virial and infalling populations, suggesting that one passage through the cluster environment causes half the quenching of star formation. We now consider the deprojected models to assess how star formation is quenched at the one radius where the three classes can be compared: the virial radius.

Fig. 6.14 shows how the best-fitting models predicts the fraction of GORES as a function of the 3D radius. We first note that for the constant $f_{\rm GORES}$ per class model, the mean variation of $f_{\rm GORES}$ (dashed curve in the top panel of Fig. 6.14) departs more strongly from the global trend (green dash-dotted curve) found by the global deprojection (Sec. 6.5.1) than do the mean variations with the other models. This reinforces the view that the constant $f_{\rm GORES}$ per class model does not reproduce well our data.

With the radially-dependent model of the GORES fraction with equal quenching scale radii, again with Scheme 3, the fraction of GORES in the backsplash population at $r = R_{\rm v}$ is intermediate between those of the infalling and virialized populations, although closer to the virialized one (solid curves in the top panel of Fig. 6.14).

Table 6.3 displays the fractions of GORES at the surface of the virial sphere ($r = R_{\rm v}$) for the better-fitting radially-varying models with free quenching radii. The backsplash quenching

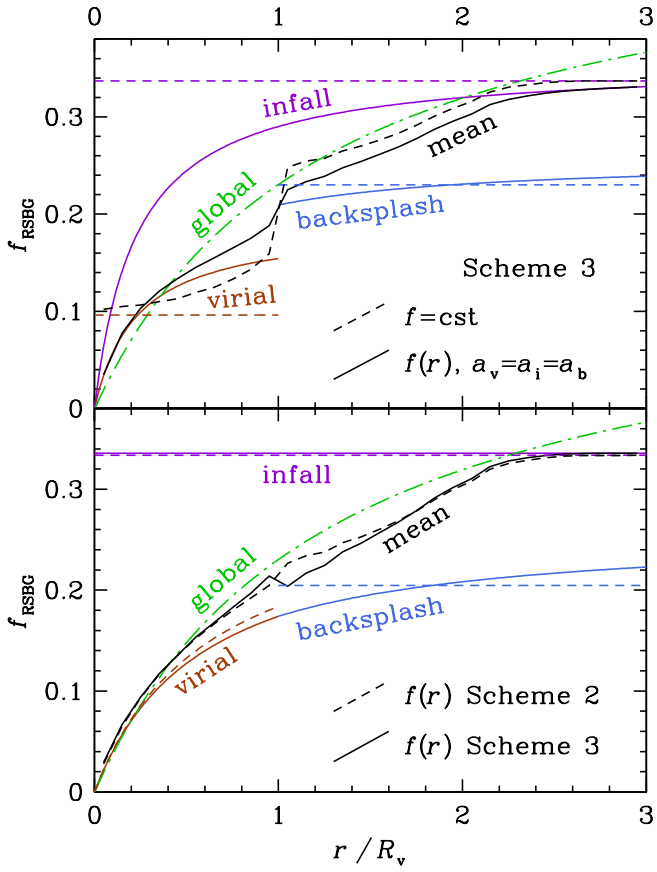

Figure 6.14: Fraction $f(r)$ of GORES versus physical radius, for the virial (*brown*), infall (*purple*) and backsplash (*blue-grey*) populations, their mean (using the cosmological simulation to determine the radial variation of the densities of the three classes, *black*) and the global deprojection (*green dash-dotted curve*). *Top*: best fit constant (*dashed lines*) and radially increasing (Eqn. 6.2) with $a_{\rm v} = a_{\rm i} = a_{\rm b}$ (*solid curves*), both with Scheme 3. *Bottom*: best fit radially increasing (Eqn. 6.2) with free star formation quenching radii for Schemes 2 (*dashed*) and 3 (*solid curves*).

Table 6.3: Quenching at $r = R_{\rm v}$ (models with free quenching radii)

Scheme	$f^{\rm vir}_{\rm GORES}(R_{\rm v})$	$f^{\rm inf}_{\rm GORES}(R_{\rm v})$	$f^{\rm bsp}_{\rm GORES}(R_{\rm v})$	quenching
0	0.22	0.28	0.17	1.7
1	0.20	0.34	0.16	1.3
2	0.18	0.33	0.21	0.9
3	0.18	0.34	0.16	1.1
4	0.17	0.23	0.30	–1.1
5	0.18	0.35	0.27	0.5

Note: the last column lists $Q = (f^{\rm inf}_{\rm GORES} - f^{\rm bsp}_{\rm GORES})/(f^{\rm inf}_{\rm GORES} - f^{\rm vir}_{\rm GORES})$, which measures the effectiveness of quenching of the backsplash population relative to the infall and virial ones.

factor, $Q = (f^{\rm inf}_{\rm GORES} - f^{\rm bsp}_{\rm GORES})/(f^{\rm inf}_{\rm GORES} - f^{\rm vir}_{\rm GORES})$, should lie between 0 (no quenching: backsplash and infall have same GORES fraction at given radius) and 1 (full quenching: backsplash and virial have same GORES fraction at given r). The values above unity imply that the fraction of GORES of the backsplash population lying on the virial sphere are lower than the corresponding fraction of the virial population at the same location, which leads to the unphysical result that on the virial sphere backsplash galaxies are more passive than the virialized ones.

For our best-fitting Scheme 3, $Q = 1.1$ is just above unity, i.e. the backsplash and virialized populations on the virial sphere have very similar fractions of GORES[7], while for the 2nd-best fitting Scheme 2, $Q = 0.9$ (see bottom panel of Fig. 6.14). On the other hand, for Scheme 4 Q is much smaller than 0: the fraction of GORES for galaxies lying on the virial sphere is higher for the backsplash galaxies than for the infall population. This again appears to be an unphysical result, which leads us to disregard Scheme 4 (which also fits the data significantly worse than Scheme 3, see Table 6.2). This suggests that *the backsplash galaxies are strongly quenched relative to the infalling ones*, at least half the way from infalling to virialized galaxies, both at $r = R_{\rm v}$ (for Scheme 5, which is only marginally consistent with the data) to fully nearly quenched to the level of virialized galaxies (Schemes 3 and 2).

[7] Forcing $Q = 1$ in our fit leads to χ^2_ν only 0.003 higher for Scheme 3.

In contrast, using hydrodynamical cosmological simulations of the Local Group, Knebe et al. (2010) find that the luminosities in backsplash galaxies are similar to the infalling galaxies, hence star formation would *not* be quenched as galaxies cross through clusters. This conclusion contradicts our results for the best-fitting Schemes 2 and 3. One major difference between this work and that of Knebe et al. (2010) is that galaxies in the simulations of the latter are orders of magnitude less luminous (all but one with $M_V > -17$) than the luminous galaxies studied here ($M_r < -20.5$). The Fig. 5 of Knebe et al. (2010), which is essentially a Faber-Jackson relation between luminosity and velocity dispersion, indicates that the residuals to the global trend leads to virialized galaxies with significantly *higher* luminosity than the infall galaxies (by typically two magnitudes, with 99.9% confidence using a KS test). The backsplash population on the other hand was in between but not inconsistent with either virial or infall populations. The higher luminosities of the virial population of simulated dwarfs appear to contradict the observed positive luminosity – radius correlation found for luminous virialized galaxies with cluster-centric distances above $\gtrsim 0.1R_{\rm v}$ from their parent rich clusters (Adami, Biviano, & Mazure 1998).

The quest for the physical mechanism responsible for this quenching is beyond the scope of this chapter, be it tidal stripping, ram pressure stripping, harassment, starvation or pre-processing in groups. The lack of dependence of galaxy colour on cluster mass also argues against ram pressure stripping and harassment (van den Bosch et al. 2008).

We note that in our three best-fitting models (Schemes 3, 2, and 5), the fraction of GORES in infalling galaxies is independent of their physical distance to the cluster. Our best-fit model requires a scheme where galaxies within the virial sphere with high outgoing velocities are equivalent to the infalling galaxies within the same volume (those with strong negative velocities). This together with the comparison of GORES fractions at the virial radius suggest that *the star formation in galaxies is quenched on a timescale comparable to the time taken for a galaxy to bounce out of a cluster and reach its virial radius.* This timescale corresponds to about 1 to

2 Gyr, which is very close to the lookback time to which our joint Hδ-D$_n$4000 GORES diagnostic is most sensitive (Sec. 6.3). Correcting for this lookback time, one concludes that *star formation is nearly fully quenched in a single passage through the cluster*.

We find that $18 \pm 1\%$[8] of the galaxies within the *virial cone* (projected radii $R < R_{\rm v}$ and $|v_{\rm LOS}| < 3\,\sigma_v$) are GORES. Yang, Mo, & van den Bosch (2008) find that $\sim$78% of the SDSS cluster galaxies lie on the Red Sequence, hence the remaining $\sim$22% can be called blue. So, *within the virial cone, the fraction of GORES is roughly 80% of the fraction of blue galaxies*, although some blue galaxies are not GORES and some GORES are not blue (Mahajan & Raychaudhury 2009).

However, the Yang, Mo, & van den Bosch (2008) SDSS clusters include galaxies projected along the LOS, except for those that lie in other groups/clusters (which are picked up with the Yang et al. (2007) algorithm in these systems). Using cosmological simulations, Mamon, Biviano, & Murante (2010) recently showed that $23 \pm 1\%$ of galaxies within the virial cone are outside the virial sphere. As discussed by Mamon, Biviano, & Murante (2010), the match between fraction of blue galaxies and fraction of cluster interlopers is probably a coincidence since some galaxies within the cluster sphere must be blue and some interlopers must be Red Sequence galaxies in projected groups.

With our models, we can estimate the fraction of GORES within the *virial sphere*, using the average of the mean fractions $f(r)$ (black curves in Fig. 6.14) weighted by r^2 times the galaxy number density profile, $\nu(r)$ measured in our cosmological simulation. Results given in Table 6.4 indicate that for our three best-fitting models (see Table 6.2), *the fraction of GORES within the virial sphere is* $13 \pm 1\%$. We then predict the fraction of blue galaxies within the virial sphere is $13/0.8 = 16 \pm 2\%$.

Now, while most galaxies within the virial sphere are part of the virial population, some are infalling (Schemes 1 to 3) or backsplash (Scheme 2). Yet, we can proceed even further

[8]The errors here and below on the fractions of GORES are binomial and do not incorporate cosmic variance.

Table 6.4: Fractions of Galaxies with Ongoing or Recent Efficient Star Formation

Model	Scheme	Virial cone	Virial sphere	Virial class	Infall class	Backsplash class
Range		$R<R_{\rm v}$	$r<R_{\rm v}$	($r<R_{\rm v}$)	$R<2\,R_{\rm v}$	$R<2\,R_{\rm v}$
f=cst	3	0.16	0.12	0.10	0.34	0.23
$a_{\rm v}$=$a_{\rm i}$=$a_{\rm b}$	3	0.17	0.13	0.12	0.33	0.22
$f(r)$	1	0.17	0.13	0.12	0.34	0.19
$f(r)$	2	0.17	0.13	0.12	0.33	0.20
$f(r)$	3	0.17	0.13	0.11	0.34	0.19
$f(r)$	5	0.17	0.13	0.11	0.35	0.27
SDSS	NA	0.176	NA	NA	NA	NA

Notes: The last five models are our best-fitting ones ($\chi^2_\nu \leq 1.7$). Note that the fractions of GORES within the virial cone slightly underestimate the observed fraction, but are consistent with it within the 1% errors.

and estimate the fraction of GORES among the virialized class, again using our cosmological simulation to perform the calibration. As seen in Table 6.4, *the fraction of GORES among the virialized class is not zero, but as high as 11 to 12±1%*. We also predict that the fraction of blue galaxies among the virialized population is $11.5/0.8 = 14 \pm 2\%$. Moreover, Table 6.4 indicates that the fraction of GORES among the $R < 2\,R_{\rm v}$ infall galaxies is $34 \pm 1\%$ while among the backsplash galaxies the fraction of GORES is $19 \pm 4\%$ (for Schemes 3, 2 and 1) or perhaps as high as $27 \pm 4\%$ (Scheme 5).

The presence of GORES among the virialized class might be caused by those low metallicity galaxies for which our Hδ-D$_n$4000 estimator of recent efficient star formation has a lookback time as long as 3 Gyr (Sec. 6.3). Alternatively, these GORES might be the consequence of star formation triggered by rapid flybys and rare ongoing direct (satellite-satellite) mergers in clusters.

Finally, our statistics lead us to conclude that a fraction $0.13 \times (1 - 0.23)/0.18 = 0.56$ of the GORES within the virial cone are within the virial sphere, so that *44±2% of GORES within the virial cone are outside the virial sphere*, for all good-fitting Schemes.

Note that the asymptotic behaviour of the best-fit models disagrees with the field value by at least 10%. This may reflect that (i) a different set of environment-dependent phenomena become efficient in modulating galaxy properties at $R > 2\,R_{\rm v}$ from the centres of clusters, and/or (ii) our models are over-simplified and underpredict the fraction of GORES.

6.7 Epilogue

In summary, our work shows that the galaxy properties in and around clusters are not simple functions of stellar mass and local environment (e.g. Haines et al. 2007; von der Linden et al. 2010), but also of absolute LOS velocity. With these velocities, it is then statistically feasible to segregate the infalling and backsplash galaxies at any cluster-centric radius, including cluster outskirts. This velocity modulation will be better seen in the properties of the relatively low-mass galaxies, because they are the first ones to be influenced by any changes in their immediate environment (see Mahajan, Haines & Raychaudhury 2010 for such an effect seen in the nearby Coma cluster). The survival of low-mass galaxies and of star formation in galaxies of all mass, as they pass through the cluster core are important questions that should also be addressed with high-resolution cosmological hydrodynamical simulations.

Chapter 7

The evolution of dwarf galaxies

7.1 Introduction

In hierarchical models of structure formation, dwarf galaxies are the ‘building blocks’ of more massive galaxies. Moreover, the vulnerable nature of these galaxies, which are most abundant in the Universe, makes them an excellent probe for exploring the impact of environment on evolution of galaxies. A reliable census of dwarfs, and detailed knowledge of their properties is required, over a wide range of epochs, to understand the coeval evolution of the large-scale structure and the galaxies therein.

However, unlike their giant counterparts, dwarfs have received little attention in the literature, possibly due to the challenges encountered in observing these faint and low surface brightness galaxies. Nevertheless, studies conducted in the last decade or so have been able to exploit the multiplex gain of wide-field multi-fibre spectrographs (e.g. Poggianti et al. 2001), while others have targeted the low-luminosity (e.g. Lisker et al. 2007; Smith et al. 2008, and references therein) and low surface brightness (e.g. Chiboucas et al. 2010) galaxy population in nearby clusters.

Large samples of dwarf galaxies have now been exploited to show that passive dwarfs are

found only in very dense environments, or accompanying a more massive companion (e.g. Haines et al. 2007). Studies of HI gas content in dwarf galaxies do not find any correlation between the HI gas surface density and star formation rate (Roychowdhury et al. 2009) or star formation efficiency (Bothwell, Kennicutt, & Lee 2009), suggesting that dwarf galaxies are star-forming everywhere. Using HI surface density normalised by stellar mass to quantify star formation efficiency, Bothwell, Kennicutt, & Lee (2009) suggest that mass dependent quenching mechanism(s) are likely to play a dominant role in galaxy evolution. These results imply that transformations in the observable properties of dwarf galaxies may occur only in specific environments, and hence galaxy populations in the process of transformation should be confined to such regions. The post-starburst (or k+A) galaxies are among the best candidates for such transitional populations.

The k+A galaxies show strong Balmer absorption but lack emission lines in their spectra. Such galaxies are mostly found in and around galaxy clusters at $\mathrm{z} \sim 0$ (e.g. Mahajan, Haines & Raychaudhury 2010) and at higher redshifts (e.g. Dressler & Gunn 1982; Poggianti et al. 2004, but see Goto 2005; Yan et al. 2009 for an alternative view). In the Coma and Abell 2199 supercluster ($\mathrm{z} = 0.023$), dwarf galaxies show a stronger relation between star formation rate and local galaxy density than is found in the more massive galaxies (Haines et al. 2006a; Mahajan, Haines & Raychaudhury 2010), while elsewhere (Barazza et al. 2009) a strong colour-density relation is found in Abell 901/902 system ($\mathrm{z} = 0.165$). Clusters and rich groups at intermediate and high redshifts ($\mathrm{z} \sim 0.5$) have more luminous ($M_V \leq -20$) k+A galaxies, which seem to be missing in rich clusters at $\mathrm{z} \sim 0$ (Zabludoff et al. 1996; Poggianti et al. 2004; Nolan et al. 2007).

In Mahajan, Haines & Raychaudhury (2010), we combined the optical photometric and spectroscopic data (from the Sloan Digital Sky survey data release 7, SDSS DR7) with the 24 μm MIPS observations to study the star-formation and active galactic nuclei (AGN) activity in galaxies across one of the nearest ($\sim 100\ h_{70}^{-1}$ Mpc) supercluster, namely Coma. In this chapter we use a subset of data from SDSS DR7 to understand the origin of dwarf k+A galaxies,

and their evolutionary link to the passive red dwarf galaxies that are observed in abundance in the Coma cluster (Jenkins et al. 2007). We briefly describe the dataset and definition of different galaxy populations in the following section. In §7.3 and §7.4 we present our analysis, finally discussing the implications of our analysis in §7.5.

We adopt the concordance cosmology ($\Omega_\Lambda = 0.70; \Omega_M = 0.30; h = 0.7$) for calculating the magnitudes and distances. We note that at the redshift of Coma (z = 0.023), our results are independent of the choice of cosmology. Different techniques give varying estimates for the virial radius of the Coma cluster such that $2 < R_{\rm virial} < 3\,h_{70}^{-1}$Mpc. For this paper the virial radius for the Coma cluster is assumed to be $2\,h_{70}^{-1}$Mpc based on the weak-lensing analysis of Kubo et al. (2007). Any reference to the cluster core in this article imply region $\lesssim 0.2R_{\rm virial}$ of the cluster centre. Throughout this article, we will refer to the pair of clusters Coma and Abell 1367, along with the associated filament of galaxies, as the Coma Supercluster.

7.2 Data

The optical photometric and spectroscopic data acquired by the SDSS DR7 (Abazajian et al. 2009) as described in §2.2 are used to select the galaxies belonging to the Coma supercluster from the SDSS spectroscopic galaxy catalogue only, requiring the member galaxies to be within $170 \leq$RA≤ 200 deg and $17 \leq$Dec≤ 33 deg on the sky, and with a radial velocity within 3,000 km s^{-1} of the mean redshift of the Coma supercluster. All our galaxies are brighter than SDSS magnitude $r = 17.77$ ($\sim$M$^* + 4.7$ for Coma cluster), which is the magnitude limit of the SDSS spectroscopic catalogue. In order to select the dwarf population by stellar mass, we define galaxies with $z \geq 15(M^* + 2)$ as 'dwarfs' throughout this work since it is relatively extinction free compared to other SDSS bands. However, we note that for the sample presented here, the r and z bands are linearly correlated. This gives us a sample of 3,050 dwarf galaxies which is used in this chapter.

The k+A galaxies, defined to have > 3 Å of Hδ in absorption and < 2 Å of Hα in emission, are taken from the catalogue compiled in Mahajan, Haines & Raychaudhury (2010). Hereafter, we consider all galaxies with EW(Hα) > 2 Å as star-forming, and any reference to galaxy colour in context of this work refers to the broadband $(g-r)$ colour (see §7.3).

7.3 Colour and environment

In Fig. 7.1, we plot the radial dependence of $(g-r)$ for all dwarf ($r \leq 17.77; z > 15$) galaxies found in and around the Coma cluster. The mean colour of dwarfs changes from 0.3 around $3R_{\rm virial}$ away from the centre, to 0.7 in the core of the cluster. It is also interesting to note that even with dwarfs alone, the red sequence for the Coma cluster extends beyond the virial radius, suggesting that the potential well of the cluster effectively contributes to the evolution of all galaxies as far as the cluster periphery.

The k+A galaxies in the vicinity of the Coma cluster span a wide range in $(g–r)$ colour, such that most of the blue k+As lie within $R_{\rm virial}$. The blue colour of some k+As suggests that the star formation in these galaxies has been very rapidly quenched no longer than 500 Myr ago (also see Poggianti et al. 2004). In contrast, a Gyr should have elapsed since the termination of the last major episode of star formation in the red k+As, allowing for their observed $(g-r)$ colour. The k+A dwarfs show a relatively scattered distribution compared to red dwarfs. Assuming that some of these galaxies are seen in projection along the line of sight, it is fair to state that the k+As prefer intermediate density regions found in the outer regions and vicinity of rich clusters and groups (Figs. 7.1 & 7.2; also see fig. 12 of Mahajan, Haines & Raychaudhury (2010) for positions of k+A galaxies in the clusters), indicating a possible link between the processes contributing to the k+A phase in dwarf galaxies and the depth of the cluster potential.

We use the $(g-r)-M_r$ colour–magnitude diagram to separate red and blue galaxies in the Coma supercluster, where, the blue galaxies are defined to have $(g-r)$ colour one mean

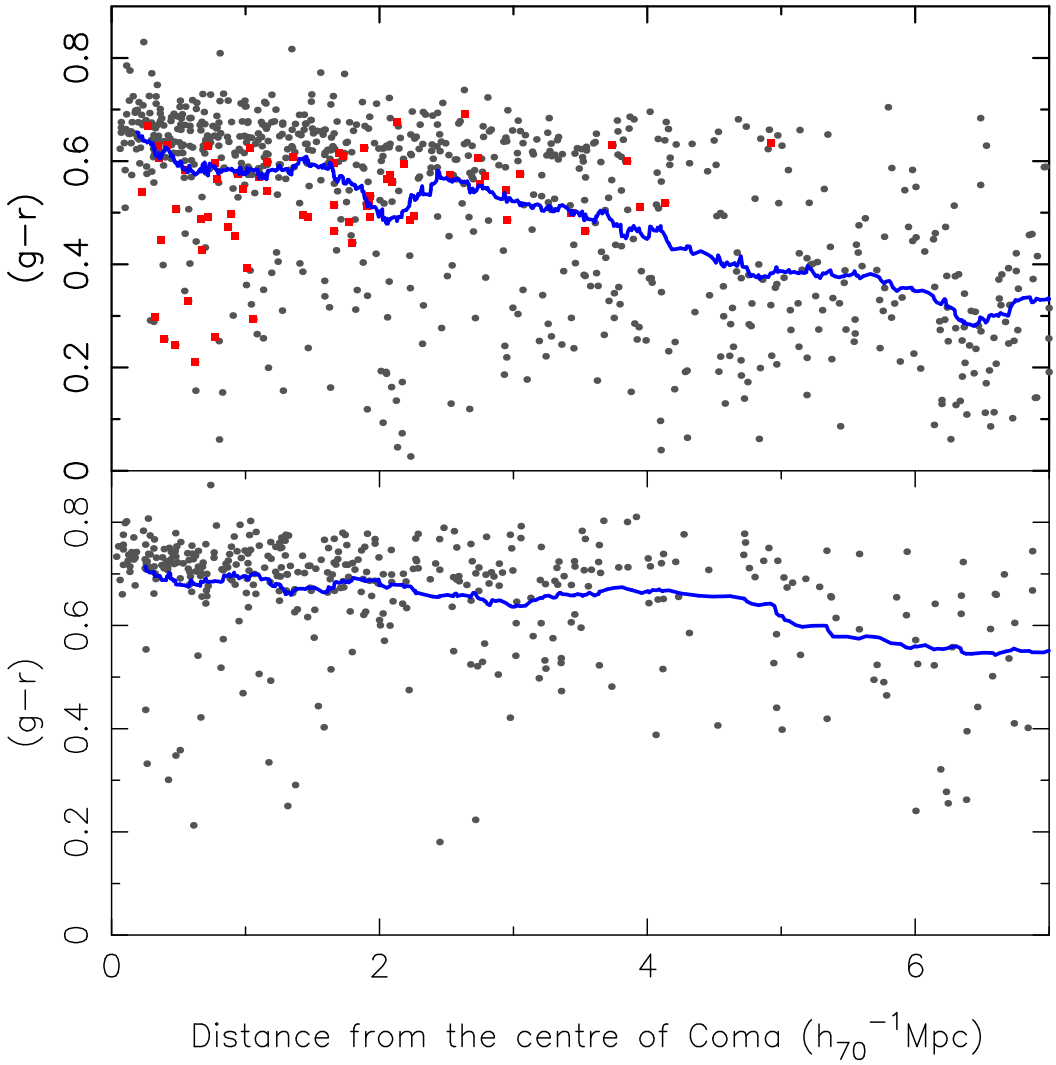

Figure 7.1: The radial dependence of $(g-r)$ colour of *(top)* dwarf (*grey points*; $z>15$) and k+A (*red squares*), and *(bottom)* giant ($z\leq 15$) galaxies within 7 h_{70}^{-1} Mpc of the centre of the Coma cluster. The solid line shows the running mean with 50 galaxies per bin. The red sequence for just the dwarfs in Coma cluster extends out to the virial radius ($2\,h_{70}^{-1}$ Mpc)– same as for the more massive galaxies. Most of the blue k+A dwarfs lie within $R_{\rm virial}$.

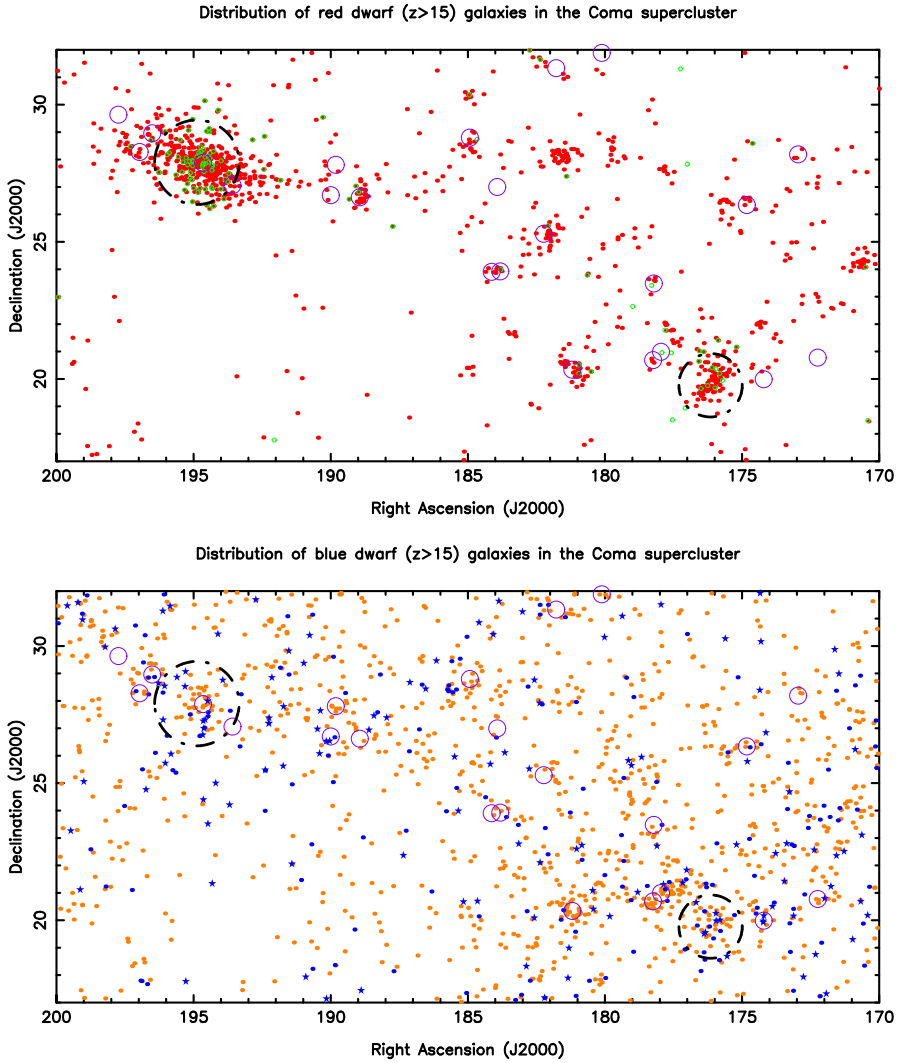

Figure 7.2: *(top)* The distribution of red (*red points*) and k+A (*green points*) dwarf ($r \leq 17.77; z > 15$) galaxies in the Coma supercluster ($cz = 6,973 \pm 3,000$ kms^{-1}). The *purple circles* represent galaxy groups from literature, that lie in the same redshift slice, and the dashed circles are centred on cluster centres with a radius of 3 R_{virial}. *(bottom)* The same for blue galaxies with EW(Hα) < 50Å & EW(Hδ)≤ 0Å *(orange points)*, strabursts ($50 \leq$ EW(Hα)≤ 80Å; *blue points*) and *extreme* starbursts (EW(Hα)> 80Å *(blue stars)*; also see Fig. 7.3). While the blue dwarfs trace the entire supercluster, the red ones are abundant in the high density regions only. The k+A dwarfs are mostly confined to the vicinity of the two clusters, and occasionally the galaxy groups.

absolute deviation (MAD) below the fitted red sequence. For consistency in this work we fitted this red sequence using dwarf galaxies only. This red sequence on an average assigns $(g{-}r) \sim 0.64$ mag to a galaxy of $M_r = -17$ mag. The location of the red and blue dwarf galaxies across the Coma supercluster is shown in Fig. 7.2. The k+A galaxies and galaxy groups found in the NASA Extra-galactic database (NED) (see Mahajan, Haines & Raychaudhury 2010 for the selection criteria) are shown explicitly. The red dwarf galaxies trace the rich structures– clusters, groups and the filament, suggesting a stronger star formation-density relation than their blue counterparts.

7.4 Spectral diagnostics

In the absence of dust, the equivalent width (EW) of Hα is a good indicator of the current star formation rate (SFR) of galaxies. On the other hand, intrinsic Hδ absorption is a characteristic feature of A-type stars, which have a lifetime of 1–1.5 Gyr. Hence, a galaxy that experienced a burst of star formation 1–2 Gyr ago is likely to show strong absorption in Hδ. But star-forming HII regions in galaxies with ongoing starburst can produce enough ionizing radiation to fill-in the Hδ absorption line.

In Fig. 7.3 we show the distribution of dwarfs in the Coma supercluster in the EW(Hα)–EW(Hδ) plane, segregated into four bins of $(g{-}r)$ colour. The four colour bins are such that the both the redder bins contain galaxies belonging to the red sequence. As galaxies become redder towards the cluster core (Figs. 7.1 & 7.2) the narrow ridge formed by blue galaxies having very strong Hα emission but negligible Hδ absorption vanishes. In dealing with the spectral features it is important to check whether the two populations seen in this EW(Hα)–EW(Hδ) plane result from measurement uncertainties. In order to do that, we split the galaxies in each panel into those that have measurement uncertainty according to SDSS, $\leq 15\%$ of the measured EW for both Hα and Hδ (the coloured points in Fig. 7.3) and those that do not (grey points in Fig. 7.3).

As expected, as the emission features become weak for the passively evolving red dwarfs, more galaxies inhabit the uncertain zone.

However among the blue, star-forming class, there exists at least two sub-populations, one that of the starburst dwarfs, which line-up in a narrow ridge on the right hand side of the EW(Hα)–EW(Hδ) plane, and the other of normal star-forming and post-starburst galaxies that have significant absorption in Hδ. The latter class of blue dwarfs overlaps with the red ones, showing relatively low EW(Hα) and some absorption in Hδ. Although most of these galaxies have continuous star formation histories with a low SFR, a sub-population might have been quenched recently ($\lesssim 1$ Gyr old; Poggianti et al. 2004) as they are assembled into clusters via the large-scale structure (e.g. Mahajan, Raychaudhury & Pimbblet 2011c), thus terminating the starburst. From Figs. 7.1 and 7.2 it is also evident that although most of the blue dwarfs within 3R$_{\rm virial}$ of the cluster centres have low Hα emission (<50Å), such galaxies are found elsewhere in the supercluster as well.

The red dwarfs showing Hδ absorption similar to the blue galaxies could be (i) dominated by metal-rich stellar populations (Smith et al. 2008; Mahajan & Raychaudhury 2009), or (ii) transformed large spiral galaxies, whose disks have been removed after they fell into the cluster (Abadi, Moore, & Bower 1999; Barazza et al. 2009), due to the impact of environmental mechanisms such as ram-pressure stripping (Gunn & Gott 1972), or (iii) star-forming dwarf galaxies in the early phases of transformation (Lin & Faber 1983; Boselli et al. 2008 and references therein). We discuss these possibilities further in §7.5.

In the Coma cluster, most ($\sim 71\%$) of the dwarf galaxies are red (Fig. 7.1) and show no Hα emission (Fig. 7.3), while the same fraction is only $\sim 25\%$ in the neighbouring Abell 1367 cluster. Given that a significant fraction of blue galaxies with more than 3 Å of absorption in Hδ, also have < 20 Å of emission in Hα (Fig. 7.3), it is likely that star formation in some of them was abruptly quenched.

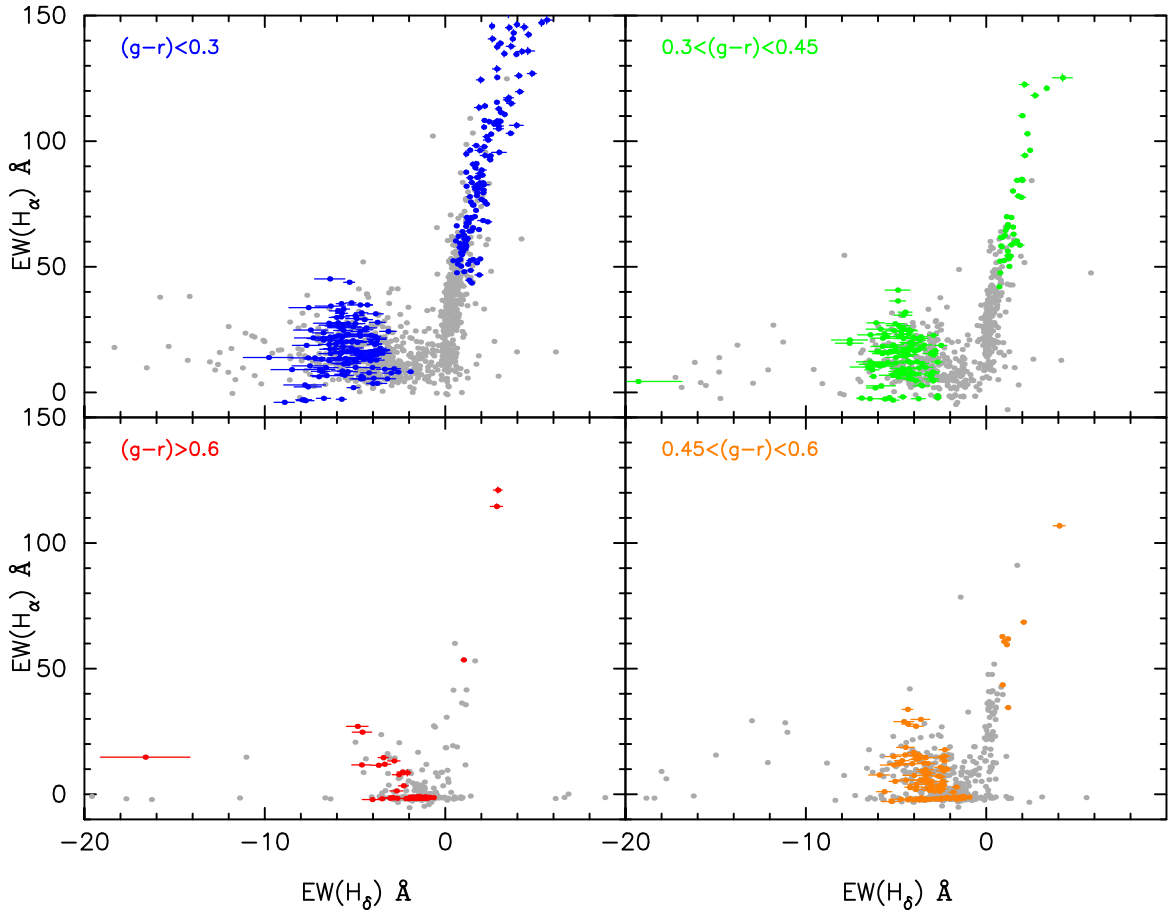

Figure 7.3: The distribution of dwarf galaxies found in the Coma supercluster on the EW(Hα)–EW(Hδ) plane in four bins of $(g-r)$ colour, where colour becomes redder clockwise from the top left panel. The *grey points* show all galaxies belonging to the given panel, while the *coloured points* with error bars are galaxies with $\leq 15\%$ measurement uncertainty in EW(Hα) *and* EW(Hδ). The red dwarfs, which are abundant in the high density regions of the supercluster (see Figs. 7.1 and 7.2), mostly show absorption in Hδ with a few showing some Hα emission, suggesting ongoing star formation. The blue dwarfs on the other hand show at least two sub-populations, one of which show similar spectral features as their red counterparts. The other population of blue dwarf galaxies show very strong emission in Hα and sometimes also in Hδ, indicating a very recent or ongoing burst of star formation.

7.5 Discussion

In this work we attempt to understand the origin of k+A galaxies, and the possible evolutionary link between this transitional population and the red dwarfs found abundantly in the Coma cluster (Jenkins et al. 2007; Chiboucas et al. 2010). We use the publicly available SDSS DR7 data for the entire supercluster, with a view to studying the influence of large-scale structure, if any, on the evolution of the k+A galaxies in the low redshift Universe. In agreement with other studies of cluster dwarfs in the nearby Universe (Poggianti et al. 2004; Boselli et al. 2008), we find that the k+A galaxies prefer the intermediate density regions in the vicinity of rich structures. General studies of k+A galaxies at z ~ 0 also reveal that they preferentially avoid very low and high density regions (Balogh et al. 2005; Goto 2005).

If star formation in a galaxy is truncated by some mechanism affecting the halo gas, star formation is quenched on longer time scales of $\sim 1 - 3$ Gyr (Kodama & Bower 2001; Kawata & Mulchaey 2008). However if the star formation is suddenly quenched, for instance when a galaxy encounters the cluster environment and is stripped not only of the reservoir of gas but also the supply for ongoing star formation, the SFR declines on much shorter timescales of $\sim 100 - 150$ Myr. Thus one is more likely to observe the transient populations, such as the blue passive galaxies (e.g. Mahajan & Raychaudhury 2009) and k+A galaxies in the latter scenario. This is also consistent with the idea that an infalling galaxy can lose most of its gas in a starburst or violent encounters with fellow infalling galaxies on the cluster periphery (Mahajan, Raychaudhury & Pimbblet 2011c and references therein) and subsequently evolve in a passive fashion as it settles into the cluster core, on a timescale equivalent to a few times the cluster crossing time (~ 1 Gyr).

For the dwarf galaxies falling into clusters and groups in the Coma supercluster, the velocity field varies significantly depending upon the depth of the potential well they are approaching. Hence, it is likely that the galaxies falling into deeper potentials undergo a burst of star formation in which they either exhaust all the gas content, and/or lose it through interactions with the

intra-cluster medium (ICM), thus experiencing a sudden and rapid cessation in star formation (e.g. Tzanavaris et al. 2010; also see Fig. 7.5). On the other hand, galaxies falling into relatively shallower potentials are likely to suffer slow quenching. This explains the presence of dwarf k+A galaxies mostly in the vicinity of the two rich clusters, Coma and Abell 1367, and occasionally in galaxy groups embedded in the filament crossing them (Fig. 7.2).

In the Coma supercluster we find that around 86% (78%) of all the k+A dwarfs are found within 10 (5) h_{70}^{-1} Mpc of the centre of the clusters, suggesting a close link between the transitional k+A population and the cluster environment. Consistent with previous results (Poggianti et al. 2004), we find that most of the blue k+A dwarfs in the vicinity of the Coma cluster are found within its virial radius. The blue colour of some k+As suggests that the star formation in these galaxies has been quenched rapidly within the last 500 Myr. These observations are similar to those made for the comparable Virgo cluster. Boselli et al. (2008) studied the evolution of dwarf ($L_H < 10^{9.6}$ $M_\odot$) galaxies in Virgo by comparing their UV to radio spectral energy distributions (SEDs) to multi-zone chemospectrophotometric models. Their results suggest that not only is the star formation in the dwarf galaxies entering the Virgo cluster quenched on short (~ 150 Myr) time-scales, most of the luminous late-type spirals might also be transformed to relatively massive dEs in a similar fashion. The dEs are known to be different from the other dwarf galaxies, and found to be more closely linked to irregular dwarfs (Kormendy 1985). Some also believe that they are defunct versions of late-type dwarfs, and have evolved from them (e.g. Kormendy et al. (2009) and references therein).

In Fig. 7.4 we find evidence to support a similar scenario in the Coma cluster. While the fraction of red dwarfs steadily increases from 4 h_{70}^{-1} Mpc ($2\,R_{\rm virial}$) to the centre of the cluster, the population of blue dwarfs declines steadily within the virial radius. The distribution of k+A dwarf galaxies follows the red dwarfs. Since the k+A phase is relatively short-lived (~ 0.5 Gyr; Balogh et al. 2005) in a galaxy's lifetime, the observation of even a small fraction of such a transitional population suggests that a much larger proportion of all galaxies in the region may

have passed through this stage.

Stellar population synthesis models suggest that galaxies with k+A spectral features (strong Balmer absorption and lack of emission) are best modelled as a post-starburst (Dressler & Gunn 1992; Poggianti et al. 1999 and references therein), i.e. star formation is completely ceased following a burst. Studies of large-scale inter-cluster filaments provide statistical evidence to show that galaxies infalling into clusters are likely to undergo a starburst on the outskirts of clusters, before they are assimilated in their cores (e.g. Porter et al. 2008; Mahajan, Raychaudhury & Pimbblet 2011cand references therein). These results imply that bursts of star formation in galaxies falling into clusters are inevitable consequences of the hierarchical assembly of structures. This is mainly dependent on two factors: (i) the gas content of the infalling galaxies, and (ii) the velocity field around the cluster (e.g. Mahajan, Haines & Raychaudhury 2010). This scenario is further supported by the SDSS based study of k+A galaxies by Balogh et al. (2005), who find that the $(u-g), (r-K)$ colours and the Hδ EW of k+A galaxies are consistent with models where $>5\%$ of the stellar mass of galaxies is formed in a recent starburst.

We find that 7.8% of all dwarf galaxies within $3R_{\rm virial}$ of the Coma cluster are k+As, while in the relatively smaller Abell 1367 this fraction declines to 4.1% within the same aperture. Furthermore, excluding the clusters, the fraction of k+A galaxies in the rest of the supercluster (Fig. 7.2) is only 1.4%. The wide range of ages ($\sim 2-10$ Gyr) and metallicities ($-1 \lesssim [Fe/H] \lesssim 0.0$) in the Coma cluster dwarfs suggests non-unique evolutionary histories for these galaxies (Lisker et al. 2007; Smith et al. 2008 and references therein). While some of the oldest red dwarfs, confined to the cluster core, may belong to the primordial cluster population (Smith et al. 2008), others could have transformed from luminous late-type spirals, after their infall into the cluster (Fig. 7.5; also see Boselli et al. 2008; Barazza et al. 2009). The surface brightness profiles of dwarf ($-18 \leq M_B \leq -16$) galaxies in the Coma cluster also show that while the galaxies fitted with a single Sérsic profile (dEs) could come from star-forming dwarfs, the dwarf lenticulars (fitted with Sérsic + exponential profile) are evolved spirals that

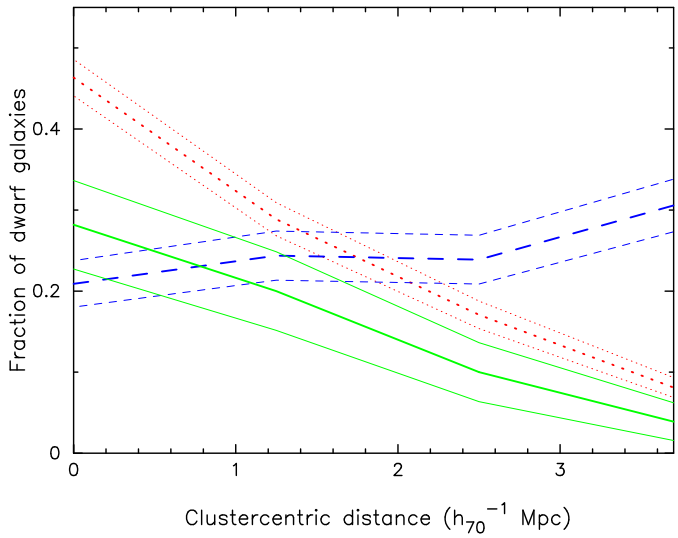

Figure 7.4: The distribution of the red (*red dotted line*), blue (*blue dashed line*) and k+A (*green solid line*) galaxies as a function of clustercentric radius from the centre of the Coma cluster. 525, 157 and 67 galaxies contribute to each of the 3 curves respectively. The *thin lines* corresponding to each distribution represent the $\pm 1\sigma$ scatter, assuming binomial statistics. All curves are individually normalised to unity.

were harassed during infall (Aguerri et al. 2005; also see Porter et al. 2008).

Figs. 7.2 and 7.3 provide further clues to the evolution path adopted by dwarfs. While some blue galaxies show ongoing starburst (right-hand ridge in Fig. 7.3), star formation in others, especially those falling into clusters, must be suddenly quenched (Figs. 7.2 and 7.4). On the other hand, the red galaxies trace the high density regions, suggesting a relatively stronger star formation-density relation throughout the supercluster (Fig. 7.1 & 7.2).

The range of values of various relevant measured parameters, explored in this chapter for the dwarf galaxies in the Coma supercluster do not allow us to sub-divide our sample into galaxies with widely different evolutionary histories. Instead, by considering all dwarfs in Coma as a single ensemble, we have been able to provide some insight into the complex mix of star formation histories among this vulnerable population. It is interesting to note that contrary to the results presented in this chapter, Yan et al. (2009) find that the giant k+A galaxies ($0.1 < z < 0.8$) show an environmental dependence similar to that of blue galaxies. In a study of $0.05 - 0.5\,L^*$ galaxies in a cluster at $z = 0.54$, De Lucia et al. (2009) found only six post-starburst galaxies

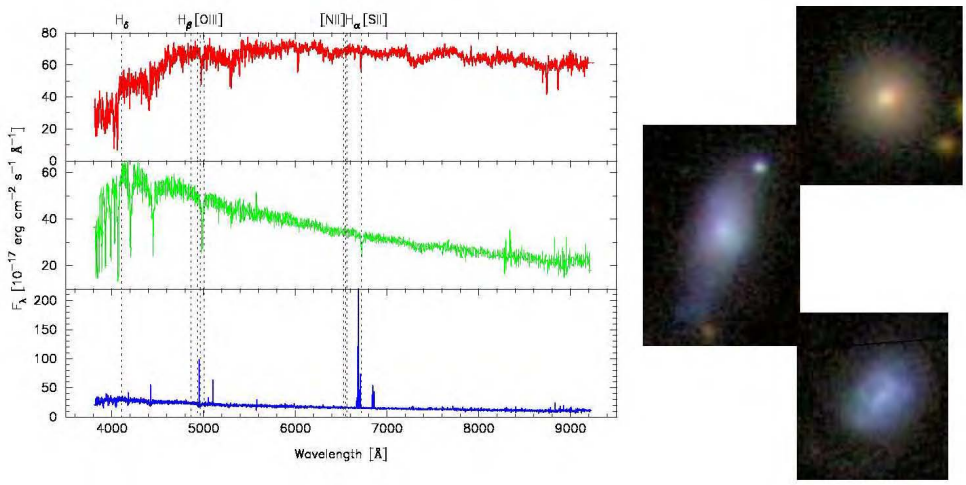

Figure 7.5: Typical SDSS spectra of a red (*top*), k+A (*middle*) and blue star-forming (*bottom*) dwarf galaxy in Coma, and their respective images (*right*). All images are obtained in colour from the SDSS website. In this article we suggest that in the Coma supercluster, transformation of infalling star-forming dwarfs into passive ones occurs via a k+A phase, whereas the dwarf galaxies falling into relatively shallow potential wells of galaxy groups embedded elsewhere in the supercluster are likely to suffer slow quenching.

amongst the spectroscopic cluster members, thus suggesting that the transformation of star-forming infalling galaxies to the faint red ones found in the low redshift clusters must have occurred primarily through physical processes that do not lead to a post-starburst phase. In order to establish and understand the mass dependence in the occurrence and nature of k+A galaxies, a homogeneous analysis of the spectroscopic properties of galaxies spanning a wide range of M^*, environments and different epochs is required. We intend to return to this in future.

7.6 Conclusions

By using the SDSS DR7 data from the spectroscopic galaxy catalogue for the dwarf ($r \leq 17.77; z > 15$) galaxies in the Coma supercluster (z $= 0.023$), we have shown that:

- The mean $(g-r)$ colour of dwarf galaxies in and around the Coma cluster increases from

0.3 at $\sim 3\mathrm{R}_{\mathrm{virial}}$ to 0.7 in the core.

- In the Coma supercluster, the k+A dwarf galaxies are mostly confined to the cluster infall regions, and occasionally galaxy groups, suggesting that most of the dwarf galaxies falling into the Coma and Abell 1367 clusters are likely to experience sudden quenching of star formation and hence are observable in the k+A phase. On the contrary, dwarfs falling into galaxy groups embedded in the filament are likely to suffer slow truncation.

- The blue colour of some k+A dwarfs in the Coma cluster lying within its virial radius, suggests that the star formation in these galaxies was quenched rapidly within the last $500\,$Myr. In contrast, the last major episode of star formation in the red k+A galaxies should have ceased on a timescale of $\sim 1\,$Gyr.

- Assuming the red dwarf galaxies to be passively evolving, they show a stronger star formation-density relation relative to their bluer counterparts.

- A significant fraction of all red galaxies in the Coma supercluster show some absorption in Hδ (0–3 Å), suggesting that star formation in them could have been quenched within the last Gyr.

- The populations of k+A and red dwarfs increases towards the cluster core in Coma from almost twice the virial boundary, while that of the blue ones decreases steadily. The k+A galaxy distribution is flatter relative to red dwarfs, and they are not as concentrated in the core of the cluster as the red dwarfs, suggesting that the k+A galaxies preferentially avoid very dense and underdense regions in equal measures.

Chapter 8

Dust and star formation in nearby galaxies

8.1 Introduction

Star formation is a key driver of galaxy evolution. Stars have created almost all the elements heavier than helium in the Universe and play a key role in recycling dust and metals in the galaxies they form. Hence the rate at which a galaxy forms stars is one of the most important characteristics governing its evolution. Understanding global trends in star formation rate (SFR henceforth) amongst different galaxy populations is a requisite for interpreting the "Hubble sequence" which is a representation of not just the evolutionary trend in galaxy morphology but also gas content, mass, existence of bar, dynamical structure, and environment, all of which influence the SFR (Kennicutt 1998a, and references therein). Precise measurements of SFR and the star formation rate density, are essential for constraining the models of formation of structures in the Universe. However, for a long time accurate measurements of SFR even in the local galaxies were difficult due to the variable dependence of different SFR tracers on the dust content and lack of knowledge about the nature and impact of dust on galaxy observables.

In addition to the standard optical spectral indices (e.g. Hα, [O II]), the indicators most commonly used to quantify star formation in a galaxy are the radio continuum, mid- and far-

infrared (MIR and FIR) and ultraviolet (UV) light. Different wavelengths trace stellar populations at different stages of evolution as well as different components of the galaxy.

Stars more massive than $\sim 8\,M_{\odot}$ produce the Type Ib and Type II supernovae whose remnants (SNRs) accelerate most of the relativistic electrons (Condon 1992). The radio emission from a galaxy has two components, the thermal bremsstrahlung emission and non-thermal synchrotron emission. Non-thermal emission dominates a galaxy's radio luminosity at low ($\leq 5\,$GHz) frequencies while the thermal component with a relatively flatter spectrum dominates at high frequencies ($\nu \gtrsim 10\,$GHz; e.g. Klein & Emerson 1981,Gioia, Gregorini, & Klein 1982). Very massive stars producing radio emission have a lifetime of a few tens of Myr and the relativistic electrons have lifetime of $\lesssim 100\,$Myr (Condon 1992). Radio observations thus probe very recent and current SFR in star-forming and normal galaxies[1].

The FIR luminosity of galaxies originates from dust heated by newly formed stars or by light from older stars (Soifer, Neugebauer, & Houck 1987; Sanders & Mirabel 1996). The former is responsible for the FIR emission of a vast majority of galaxies detected by earlier infrared surveys such as the InfraRed Array Satellite (*IRAS*). However, the origin of FIR luminosity varies for different galaxy types (see Soifer, Neugebauer, & Houck 1987 and references therein). Generally the FIR emission from any galaxy has at least two components, one originating from the interstellar dust heated by the diffuse radiation field and second from the star formation activity in the H 2 regions. Assuming that for nearby galaxies most of the FIR emission is recycled star light, the FIR luminosity can be converted to a SFR measurement (Kennicutt 1998a). However, FIR is also not completely immune to problems because dust can also be heated by old stars, implying non-negligible corrections for star-forming galaxies (Lonsdale Persson & Helou 1987).

UV light is emitted by stars younger than $\sim 200\,$Myr and is thus a good measure of SFR over timescales of few tens of Myr. But the use of this indicator is hampered by the presence

[1]In the context of this paper the term 'normal' is used for galaxies having birth rate parameter around unity, and/or non-AGN galaxies

of dust clouds enshrouding young star-forming regions. Therefore, for dusty galaxies, the UV light absorbed and then re-emitted by dust at longer wavelengths makes the FIR light a more reliable SFR indicator.

Several attempts have been made to utilise the FIR-UV energy budget to quantify dust attenuation in various samples of galaxies selected at different wavelengths (Xu & Buat 1995; Meurer et al. 1999; Buat et al. 2002; Buat et al. 2005; da Cunha et al. 2010). Besides combining UV and FIR measurements with the dust extinction measured using the Balmer decrement (Buat et al. 2002; Lee et al. 2009), several recent attempts have also been made to estimate dust attenuation using UV colour or spectral slope[2] β and the FIR/UV flux ratio (or the infrared excess IRX, as it is more popularly known, e.g. Meurer et al. 1999; Kong et al. 2004; Seibert et al. 2005).

In order to understand the relation between indicators of star formation and dust extinction, various SFR and extinction indicators need to be quantified and compared for a *statistical sample* of galaxies covering a wide range in physical and intrinsic properties and having *known biases*. This idea motivated the Star Formation Reference Survey (SFRS, Paper I henceforth; Ashby et al. 2011), discussed in the following section. Can a single extinction corrected SFR measure be used to estimate the global SFR of a galaxy, or are multi-wavelength data required? How closely does any single SFR indicator measures the 'total' SFR of a galaxy? Is the relation between the individual SFR indicators universal for all types of star-forming galaxies? What are the pros and cons of using different extinction indicators?

This work aims to test empirical formalisms available in the literature to calculate global SFR for galaxies using tracers spanning all possible wavelengths. Such studies have been performed elsewhere (Hopkins, Irwin, & Connolly 2001; Bell et al. 2003; Zhu et al. 2008) but on a smaller or randomly chosen samples, where systematic deviations from the underlying correlations cannot be well explored. The wide range of morphologies, luminosity, sizes, SFR, and

[2] β is defined by a power-law fit of the form $f_\lambda \propto \lambda^\beta$ to a spectrum in the UV wavelength range

stellar mass spanned by the SFRS galaxies, together with well-defined selection criteria makes it an ideal sample to quantify the relation between different SFR measures in nearby galaxies, and hence a benchmark for measuring the SFR in high redshift galaxies. §2 briefly describes the various datasets used in this paper. §8.4 shows the distributions and correlations between various extinction indicators derived from mutually independent data, and §8.5 does the same for various star formation tracers. These results are followed by a discussion of our findings in context of the existing literature, in §7.5, and §7.6 summarises the results. Throughout this paper we use concordance cosmology $\Omega_\Lambda = 0.7$, $\Omega_M = 0.3$, and $h = 0.75$ for evaluating distances and absolute magnitudes.

8.2 The Star Formation Reference Survey (SFRS)

The Star Formation Reference Survey (SFRS; Paper I) is a study of global star formation in a statistically robust, representative sample of star-forming galaxies in the local Universe. We aim to combine SFR tracers at all possible wavelengths to understand the complete picture of global star formation in galaxies. The sample selection criteria are defined objectively to guarantee that the chosen sample spans a full range of properties exhibited by the star-forming galaxies in the nearby Universe. We use all the galaxies at least 20 degrees north of the galactic plane in the IRAS PSCz catalogue (Saunders et al. 2000), an all-sky database of 15,000 galaxies brighter than 0.6 Jy at 60μm, as the parent sample.

The most important characterisation of a star-forming galaxy is its specific star formation rate (SFR per unit stellar mass; SFR/M^* or sSFR henceforth) and the dust temperature. These parameters can provide information such as current star formation, star formation history, the density of star-forming regions and the properties of dust. Combined with some knowledge of other physical attributes of a galaxy such as morphology, these parameters can provide useful hints to the interaction history of the galaxy and hence the influence of immediate and large-

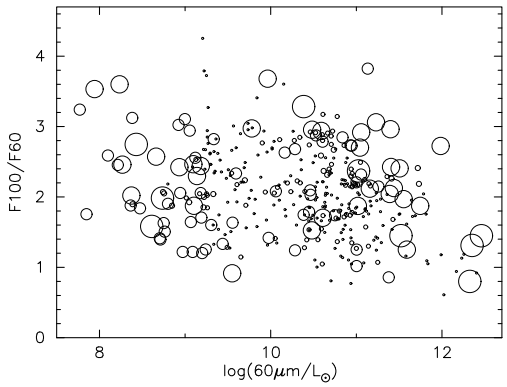

Figure 8.1: This figure shows the F100/F60 colour of all 369 SFRS galaxies as a function of their 60μm luminosity. The sizes of symbols represent the relative weight of the galaxies in the cells of the 3-d selection space in which the sample is selected (see text).

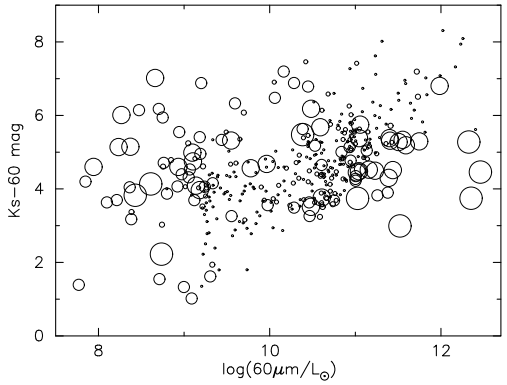

Figure 8.2: Same as Fig. 8.1 but showing the $K_s - 60$ colour as as a function of the 60μm luminosity. It is clear that the weighing the parent sample before selecting the final sample has greatly helped in including the objects on either extreme of the distribution in our sample, thus making it an ideal representation of the star-forming galaxies in the nearby Universe.

scale environment on the SFR.

To define the selection space we use the IRAS 60μm luminosity as an unbiased tracer of star formation and 2MASS Ks-band luminosity as a tracer for stellar mass. The SFRS sample is chosen in a three-dimensional space formed by the 60μm luminosity F_{60}, flux ratio F_{60}/Ks as a proxy for sSFR, and the FIR colour temperature of dust F_{100}/F_{60}. To define our sample we bin this 3d-space and extract the brightest $\sqrt{N}$ galaxies from each cell. This selection sets the sample size to 369 galaxies which span the whole range of properties exhibited by the much larger PSCz catalogue. The sample is thus statistically well-defined and has *known biases*,

which make it ideal for understanding the global star formation properties and the nature of star formation in the nearby star-forming galaxies. Figures 8.1 and 8.2 show all 369 SFRS galaxies in two-dimensional projections of the 3d selection space. The symbol sizes representing the relative weights of the galaxy reflect the key role played by the weighting process in making the sample representative of the entire range of SFR/$M^*$and dust properties exhibited by the star-forming galaxies in the local Universe.

8.3 The data

The 1.4 GHz radio, FIR *IRAS*, *Spitzer* IRAC mid infrared (MIR), SDSS optical and UV data from NASA's *Galex* used in this Chapter are described in Chapter 2. Furthermore, we choose to limit our analysis to galaxies:

(i) within 430.6 h_{75}^{-1} Mpc ($\mathrm{z} \leq 0.1$), and

(ii) having SFR measures available in all wavebands, namely the 1.4 GHz radio, FIR, non-stellar PAH emission, FUV and NUV.

This results in a sub-sample of 314/369 (85%) SFRS galaxies that we use throughout this Chapter unless stated otherwise.

Due to the impact of the nearby Virgo cluster, which is a part of the volume covered by SFRS, and the Great attractor, which lies outside the survey volume but can have profound impact on the velocity field of the nearby galaxies, the recession velocity of the nearby SFRS galaxies can not be directly converted to reliable distance. Hence we use redshift-independent peculiar velocities measured using alternate methods such as the Tully-Fisher relation (Tully & Fisher 1977), Cepheids (Freedman et al. 2001), the luminosity of stars at the tip of the red giant branch (Karachentsev et al. 2004; Karachentsev et al. 2006), and surface brightness fluctuations (Tonry et al. 2001) to quantify distances where necessary. A significant fraction of such distances for the SFRS galaxies are sourced from the catalogue of Tully et al. (2008). A

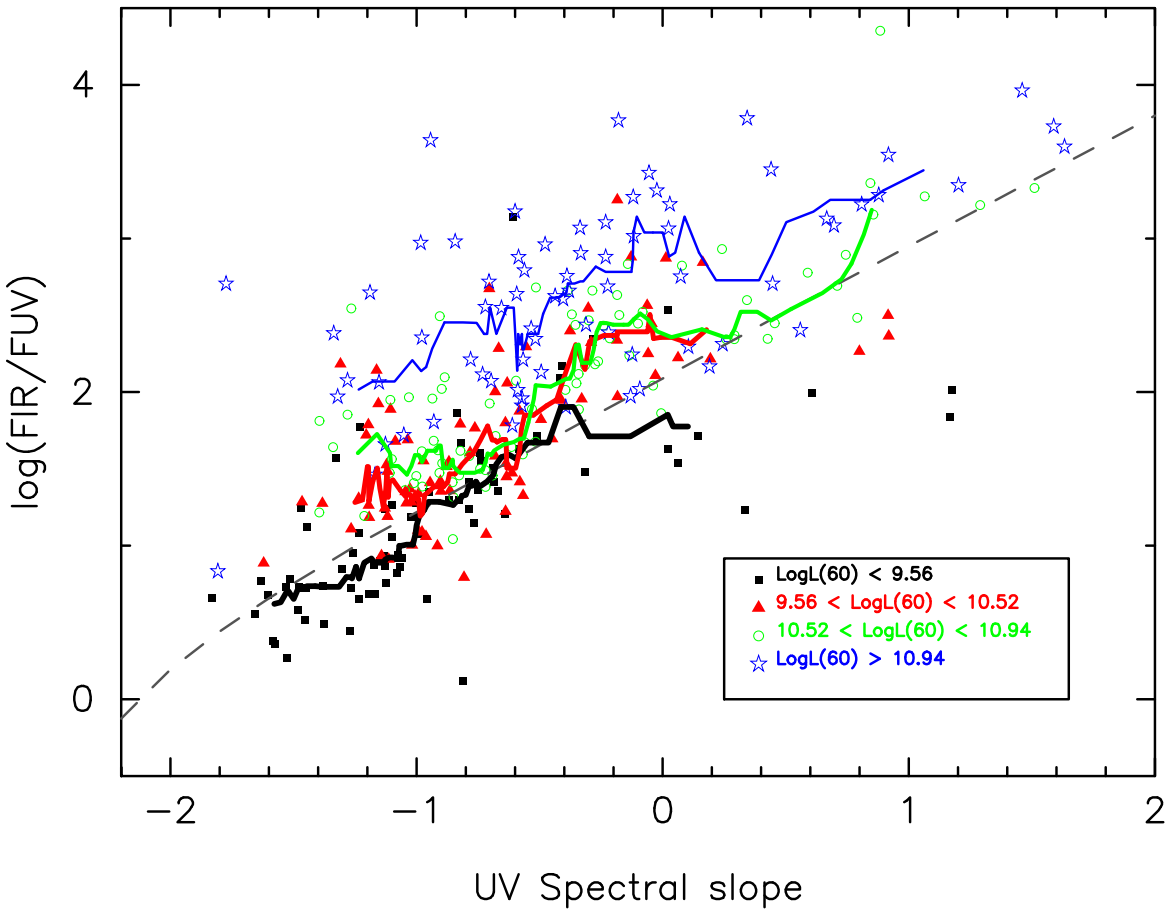

Figure 8.3: IRX as a function of β. The black, red, green, and blue symbols and lines represent the four quartiles of the 60μm luminosity distribution in increasing order respectively. The dashed line is the relation found by Kong et al. (2004) for local starburst galaxies, while the coloured solid lines are the unweighted running median fits computed for 10 galaxies per bin for the four luminosity classes. While almost all the galaxies in the lowest luminosity bin (*black points*; $\log L_{60} < 9.56$) fall below the local starburst relation, their high-luminosity counterparts are mostly above the relation. The low luminosity galaxies deviating away from the relation are nearby early-type galaxies. For any given β, the median IRX for the lowest and highest luminosity (*blue stars*) galaxies vary by at least an order of magnitude. The shift in the median fits along the abscissa also suggests that the more luminous galaxies tend to have higher spectral slopes relative to their low luminosity counterparts.

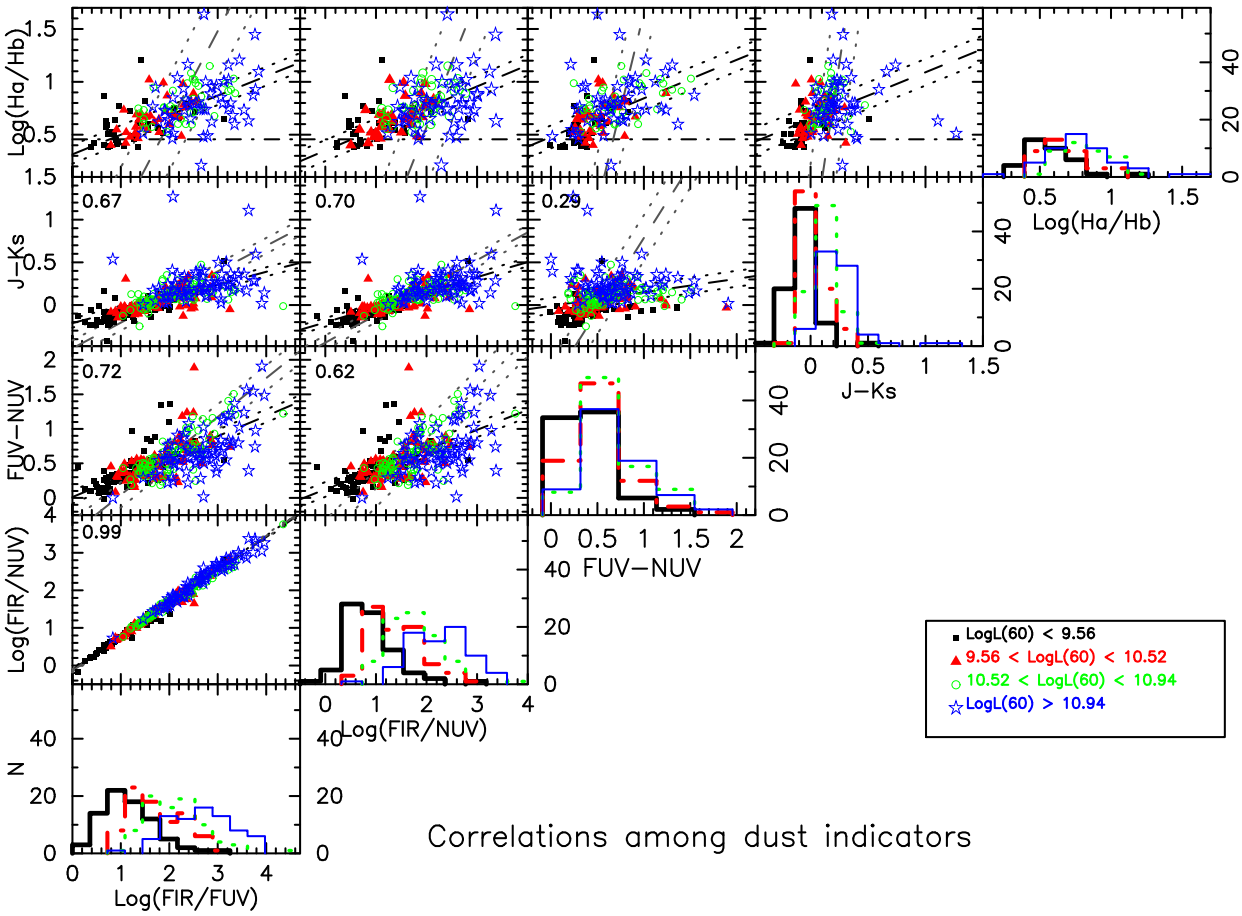

Figure 8.4: The relation between various dust extinction indicators along with their distributions in four bins of luminosity. Points and lines are colour-coded by 60μm luminosity same as in Figure 8.3. The solid and dotted lines in each panel represent the regression lines, y on x (*black*) and x on y (*grey*), and $\pm$ one sigma deviation range in these fits respectively. The product moment correlation coefficient for each dataset is shown in the upper left corner of the panel.

detailed description of methodology and sources for galaxy distances presented in Table A.5 is given in Paper I.

8.4 Extinction indicators

For a young galaxy forming stars at a uniform rate, the SFR is proportional to the UV luminosity, while the amount of dust determines the degree of reddening of the UV continuum. This

simple model results in the empirical relation between total reddening given by the IRX and the UV spectral slope β, otherwise known as the "IRX–β" relation (Meurer et al. 1999). Precise quantification of this correlation becomes particularly critical for estimating internal extinction in galaxies at high redshift for which FIR data are not available (e.g. Meurer et al. 1999,Overzier et al. 2011). Kong et al. (2004) showed that besides dust content, the star formation history of galaxies play an important role in defining the IRX–β correlation. Elsewhere (Charlot & Fall 2000), the IRX–β relation is found to be a sequence in effective optical depth for star-forming galaxies. This relation is obeyed by lower luminosity starbursts, but not the ultraluminous infrared galaxies (ULIRGS) (Meurer et al. 1999; Goldader et al. 2002). Several studies (e.g. Howell et al. 2010) have tried to explore the causes and the luminosity regime where the IRX–β relation breaks down. Gordon et al. (2000) (also see Witt & Gordon 2000) showed that the relation is highly dependent on the dust/star/gas geometry and works for galaxies where dust is close to the source of UV emission and has a shell- or screen-like geometry.

Figure 8.3 shows the SFRS galaxies in the IRX–β space. The low luminosity galaxies which are mostly early-type cluster galaxies at $z \sim 0$ almost always lie below the mean relation found for local starbursts (also see Kong et al. 2004). The most luminous galaxies in our sample on the other hand lie more than an order of magnitude above the median relation found for the low luminosity galaxies, suggesting that *at given β galaxies with higher IRX are likely to have higher SFR*. This trend has previously been noted for other FIR selected samples as well (Takeuchi et al. 2010). Using optical spectroscopic data from the SDSS and UV data from *IUE*, (Kong et al. 2004) have shown that galaxies having higher current SFR relative to their past averaged SFR are likely to deviate above the IRX–β relation. At the high end for β the shift in the median on the abscissa for different luminosity curves suggests that *the high luminosity galaxies are more likely to have relatively higher β values than their low luminosity counterparts*.

With the multitude of data available to us at different wavelengths, it is interesting to explore

how different reddening indicators relate to each other. Figure 8.4 shows the relation between five extinction indicators: the Balmer decrement (Hα/Hβ), 2MASS $J-Ks$ colour, IRX, IRXn, and the *Galex* colour $FUV-NUV$. Except for the low luminosity galaxies, the extinction measures for the rest of the galaxies are correlated with each other. The standard deviation across the entire range of distributions is 0.82, 0.73, 0.35 mag and 0.24 mag for IRX, IRXn, $FUV-NUV$ and $J-Ks$ respectively.

Assuming IRX to be the *perfect* extinction indicator, and barring the handful of extreme outliers, Figure 8.4 suggests that all other indicators analysed here are likely to result in a correction within $10-30\%$ of the extinction correction as determined by the IRX. As can be seen, the magnitude of this uncertainty is independent of the galaxy's 60μm luminosity. In other words, *a galaxy's global SFR is irrelevant to how close to the 'true' correction an indicator predicts the extinction correction*.

(Witt & Gordon 2000) showed that while the relation between attenuation at 1600 Å and IRX$_{1600}$ was almost independent of the dust geometry, the relation between β and IRX$_{1600}$ depended on it (also see Meurer et al. 1999). This lead them to suggest that IRX is a better reddening indicator than β. Thus, it comes as no surprise that despite a statistically significant correlation the scatter in the IRX–$FUV-NUV$ plot is large. An interesting outcome of this analysis is the good correlation between the 2MASS $J-Ks$ colour and the IRX. Given the wide range of galaxies sampled by 2MASS, this correlation is a very versatile tool for correcting the short wavelength fluxes for reddening.

The $FUV-NUV$ colour shows a strong bias for low luminosity galaxies ($\log\ L_{60}/L_{\odot} < 9.56$) only, such that a large fraction of these galaxies are likely to have $FUV-NUV<0.3$. For the more luminous galaxies, the correlation between $FUV-NUV$ and L_{60} seems to be very weak. The dispersion in dust extinction as traced by various indicators, and FIR luminosity is contrary to the expectation but has previously been reported by other authors (Wang & Heckman 1996; Buat et al. 1999; Buat et al. 2002) as well. In particular, (Buat et al. 2002) showed that

the correlation between dust extinction and L_{FIR} is weak but it gets worse for B-band, Hα or UV luminosities.

Traditionally, dust extinction is measured by the Balmer decrement Hα/Hβ flux ratio obtained from the visible spectrum of a galaxy. SDSS fibre spectra are available for 180 SFRS galaxies. Figure 8.4 shows four independent measures of dust extinction, IRX, IRXn, $J-Ks$ and $FUV-NUV$ colour respectively, as a function of the Balmer decrement. Since SFRS galaxies are optically thick, Hα/Hβ for almost all the galaxies is greater than the theoretical limit expected for a dust-free galaxy. As a function of L_{60} the largest scatter in Hα/Hβ is seen for the highest luminosity bin (blue stars in Figure 8.4). The lowest luminosity galaxies on the other hand seem to be much less dusty in other extinction indicators relative to the Balmer decrement when compared to their luminous counterparts having the same Balmer decrement ratio.

Although lines of regression are fitted to Balmer decrement plotted as a function of other photometric reddening indicators, the correlations are biased by the fact that we compared different photometric measures computed for the whole galaxy with the SDSS spectroscopic data which are limited to the center of the galaxy due to the finite fibre size of 3″. This affects the analysis in two ways:
(i) The galaxies for which we are able to measure the Balmer decrement have relatively higher nuclear star formation activity (and hence significant Balmer emission).
(ii) The circumnuclear region of galaxies are dustier than the outer disc (e.g. Popescu et al. 2005, Prescott et al. 2007), and hence for the very nearby galaxies in the SFRS sample the optical and UV luminosity could be very heavily obscured, adding to the scatter in the plots shown in the top row of Figure 8.4. Therefore we suggest the reader to consider these correlations as trends only. With these data we are unable to quantify the correlation between Balmer decrement and other global reddening indicators.

8.5 Star formation rate measures

As noted in §8.1, a wide variety of indicators are used to estimate SFR. Our approach is to adopt a recent or popular calibration of each indicator and compare the resulting SFR for the galaxies in SFRS.

An intriguing estimate for the SFR comes from the Polycyclic Aromatic Hydrocarbon (PAH) molecular features seen by the 8.0μm channel of the IRAC (see Calzetti 2010 for a recent review on the use of PAH features as a SFR tracer). PAHs can form in galaxies from evolved stars, stellar mass loss, merger events or cooling flows. For a sample of star-forming galaxies, Wu et al. (2005) have shown that the 8.0μm dust luminosity, correlates very well with the 1.4 GHz luminosity and the 24μm luminosity, both of which are good star formation tracers. The 8.0μm dust luminosity also correlate almost linearly with the MIPS 160μm luminosity (Zhu et al. 2008). Many authors considered the 8.0μm emission a good measure for diffuse dust emission heated by older stars and hence used it together with optical emission such as extinction corrected Hα to estimate the total SFR for galaxies (e.g. Zhu et al. 2008,Kennicutt et al. 2009).

For majority of galaxies seen by IRAC, the PAH emission dominates the 8.0μm band. However, a stellar continuum is still present especially in the early-type galaxies (Helou et al. 2004; Wu et al. 2005; Huang et al. 2007). In this work the prescription of Wu et al. (2005) (also see Zhu et al. 2008) is used to convert the 8.0μm dust luminosity to SFR:

$$\mathrm{SFR_{PAH}}(M_{\odot}\mathrm{yr}^{-1}) = \frac{\nu L_{\nu}[8.0\mu\mathrm{m};\,\mathrm{dust}]}{1.57\times10^{9}\,\mathrm{L}_{\odot}} \tag{8.1}$$

where, the 8.0μm dust luminosity is calculated by subtracting 0.227 times the 3.6μm stellar continuum luminosity from the observed 8.0μm luminosity (Huang et al. 2007). We note that this factor is close to those used elsewhere (Helou et al. 2004; Wu et al. 2005; Marble et al. 2010). Among others, Boselli, Lequeux & Gavazzi (2004) present a relation between $L(6.75\mu\mathrm{m})$ and

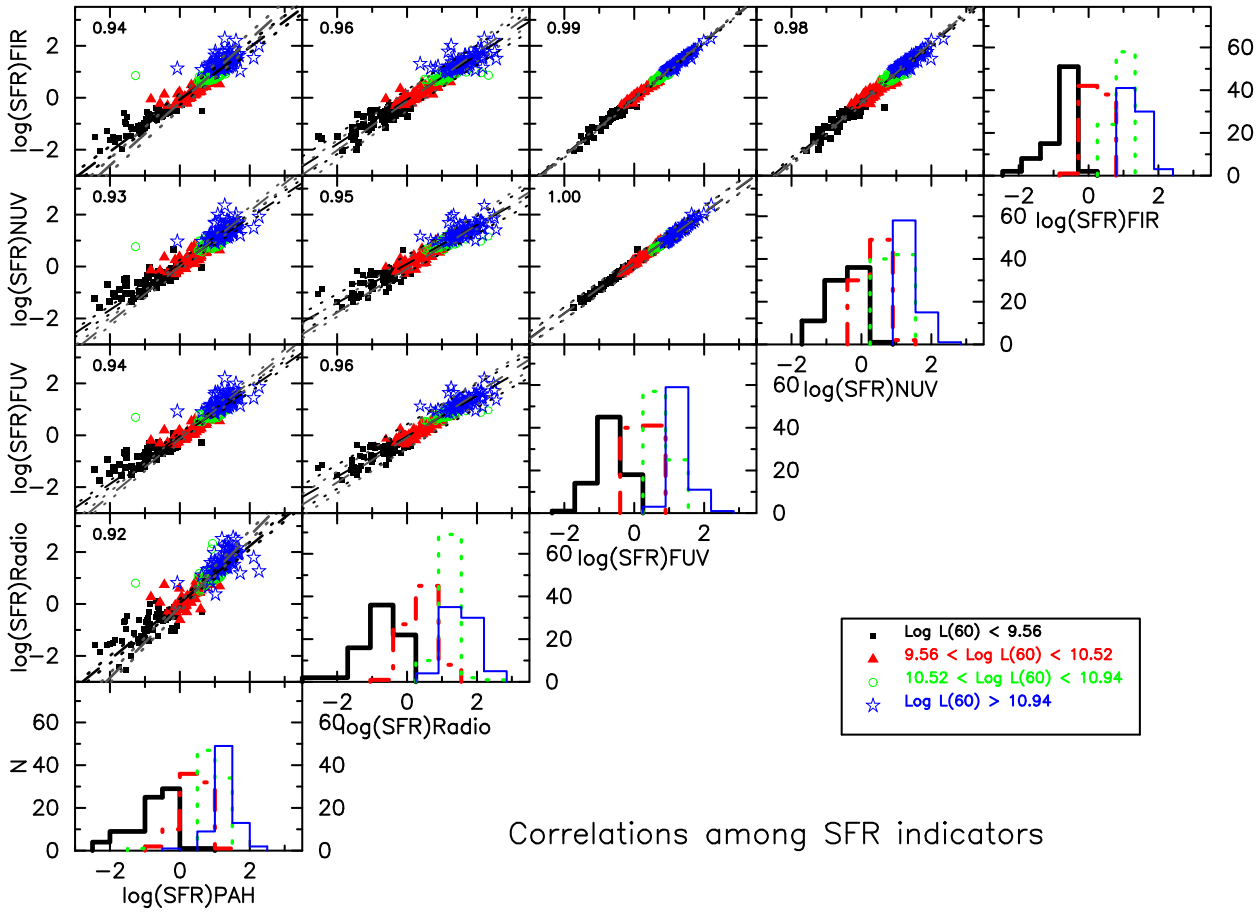

Figure 8.5: Same as Figure 8.4 but for different SFR measures. SFRs measured using different indicators for the SFRS sample are in good agreement with each other. Even though this is a FIR selected sample, the quartiles as described by the 60μm luminosity well represent the four bins at other wavelengths from FUV to radio. An almost perfect correlation between the extinction-corrected FUV SFR and the FIR SFR extending over several orders in luminosity implies that the IRX based correction of Buat et al. (2005) works well in retrieving the light lost due to extinction. This also implies that the total SFR is a strong function of the bolometric luminosity.

the global SFR for late-type galaxies in mid-IR luminosity range $10^{39} \leq L(6.75\mu\mathrm{m}) \leq 10^{43}$ erg s^{-1} and $10^{39} \leq L(15\mu\mathrm{m}) \leq 10^{42.6}$ erg s^{-1}, which can only apply to a subsample of the SFRS galaxies.

The 1.4 GHz radio luminosity in a galaxy originates as (i) thermal bremsstrahlung emission from ionized hydrogen in H2 Regions and (ii) non-thermal synchrotron emission from the relativistic electrons accelerated by the remnants of Type Ib and Type II supernovae and spiralling in the magnetic field of the galaxy (Condon 1992). Assuming the 1.4 GHz luminosity of SFRS galaxies to be entirely thermal (i.e. $\propto$ SFR), we calculate the corresponding SFR using eqn. 13 of Yun, Reddy, & Condon (2001):

$$\mathrm{SFR}_{1.4\,GHz}(M_{\odot}\mathrm{yr}^{-1}) = 5.9 \pm 1.8 \times 10^{-22}\, L_{1.4\,GHz}\,(\mathrm{Watts\,Hz}^{-1}) \tag{8.2}$$

The main uncertainty in this relation comes from the assumed local star formation rate density (SFRD), the best estimates of which are discrepant by a factor of two. In the derivation of this formula Yun, Reddy, & Condon (2001) assumed the local SFRD to be $0.015 \pm 0.005\, M_{\odot}\mathrm{yr}^{-1}$.

Emission line diagnostics are dependent on the photoionization from massive stars. Hence they probe *current* star formation over timescales of $\lesssim$ 10 Myr, beyond which the photoionization declines rapidly (see Marcum et al. 2001 and references therein for a discussion). By contrast, the IR and submillimeter emission from dust grains pose a bigger challenge for determining the star formation history of a galaxy because dust grains can be heated by stars of all ages and the exact nature of dust grains in most galaxy types is yet unknown. The UV continuum emission at $1200-3200$ Å on the other hand probes star formation over timescales of few tens of Myr, thus providing an insight into the *recent* star formation history of the galaxy.

Some of the UV radiation emitted by young massive stars is absorbed by the surrounding dust and re-emitted at longer wavelengths. Hence a linear combination of the SFR measured in these two regimes should provide a good estimate of the 'global' rate at which the galaxy is

Table 8.1: Correlation ($y_i = a + bx_i$) between different SFR distributions

SFR pairs ($x_i - y_i$)	Regression of y_i on x_i					Regression of x_i on y_i				
	a_1	b_1	σ_1[3]	χ^2_1	q_1[4]	a_2	b_2	σ_2[5]	χ^2_2	q_2[6]
PAH–Radio	0.052	1.094	0.146	0.139	0.509	0.078	0.730	0.138	0.093	1.000
PAH–FUV	-0.037	0.919	0.135	0.074	1.000	0.126	0.914	0.143	0.074	1.000
PAH–NUV	0.102	0.888	0.155	0.073	1.000	0.000	0.938	0.144	0.077	1.000
PAH–FIR	-0.066	1.005	0.208	0.096	1.000	0.153	0.826	0.218	0.079	1.000
Radio–FUV	-0.040	0.780	0.464	0.044	1.000	0.110	1.162	0.488	0.065	1.000
Radio–NUV	0.102	0.750	0.341	0.048	1.000	-0.046	1.187	0.339	0.076	1.000
Radio–FIR	-0.073	0.859	0.383	0.052	1.000	0.140	1.057	0.397	0.064	1.000
FUV–NUV	0.138	0.967	0.235	0.003	1.000	-0.138	1.027	0.246	0.003	1.000
FUV–FIR	-0.025	1.092	0.066	0.008	1.000	0.029	0.902	0.056	0.007	1.000
NUV–FIR	-0.170	1.112	0.106	0.021	1.000	0.170	0.866	0.080	0.016	1.000

forming stars. To estimate the SFR in FUV and FIR, we make use of the prescription provided by Iglesias-Páramo et al. (2006):

$$\log SFR_{FUV}(M_{\odot}\mathrm{yr}^{-1}) = \log L_{FUV,corr}(L_{\odot}) - 9.51 \tag{8.3}$$

$$\log SFR_{FIR}(M_{\odot}\mathrm{yr}^{-1}) = \log L_{FIR}(L_{\odot}) - 9.75 \tag{8.4}$$

where $L_{FUV,corr}$ is the FUV luminosity corrected for internal dust extinction using Eqn. 2.1 and $\log L_{FIR}$ is evaluated using the prescription given by Helou et al. (1988):

$$F_{FIR} = 1.26 \times 10^{-14}(2.58 f_{60} + f_{100}) \qquad (\mathrm{Watts/m^2}) \tag{8.5}$$

where f_{60} and f_{100} are flux densities at 60 and 100μm bands in units of Jy. The SFR formulae have been derived from Starburst99 (Leitherer et al. 1999) assuming a solar metallicity and a Salpeter IMF in the range 0.1 to 100 $M_{\odot}$.

Table 8.2: Statistical properties of different SFR distributions

SFR	Mean	Std. deviation	Skewness	Kurtosis	Median
FUV	8.06	14.26	5.55	45.78	4.34
NUV	10.32	18.60	6.11	56.18	5.66
PAH	9.27	15.50	6.42	60.66	5.19
FIR	9.84	18.56	5.35	39.62	4.46
Radio	20.57	43.84	4.55	25.04	7.52

8.5.1 Distributions and correlations of SFR measurements

The correlations between various SFR measures divided into quartiles of 60μm luminosity are shown in Figure 8.5. As is immediately noticeable, despite different prescriptions derived empirically from different samples and very different underlying physics, *the global SFR metrics coming from tracers at different wavelengths correlate remarkably well*. The respective correlations and their standard deviations are listed in Table 8.1. To compute these correlations each galaxy is assigned its weight corresponding to the number of PSCz galaxies it represents given the northern cap area restriction from which the SFRS sample is selected (see Paper I for details). The scatter in the fitted regression lines (Table 8.1) suggests that *it is possible to estimate the SFR expected at any wavelength within a factor of a few by having at least one SFR measurement for a galaxy*. Because the fits are weighted to represent the entire PSCz catalogue, the correlations listed here can be applied to estimate the SFR for any sample of galaxies.

Table 8.2 lists some statistical properties of the different SFR distributions, and Table 8.3 gives results of statistical tests comparing them. The $F-test$ tests the hypothesis that two distributions have significantly different variances by rejecting the null hypothesis that their variances are actually consistent. The statistic F (Table 8.3) is the ratio of the two variances, and hence a value $\ll 1$ or $\gg 1$ indicates significantly different variances. For all SFR dataset pairs except those which include radio, the distributions have similar variances (Table 8.2). The $t-test$ checks against the hypothesis that two distributions with different variances have the

Table 8.3: Results for statistical tests between different SFR distributions

SFR	F		Student's-t		K-S		Pearson's-r	
Distributions	F^a	prob	t^b	prob	D	prob	r^c	prob
PAH-Radio	8.00	0.0	-4.31	0.21E-04	0.15	0.21E-02	0.92	0.0
PAH-FUV	1.18	0.14	1.02	0.31	0.10	0.72E-01	0.94	0.0
PAH-NUV	1.44	0.13E-02	-0.76	0.44	0.06	0.67	0.93	0.0
PAH-FIR	1.43	0.15E-02	-0.42	0.67	0.06	0.60	0.94	0.0
Radio-FUV	9.45	0.0	4.81	0.22E-05	0.21	0.22E-05	0.96	0.0
Radio-NUV	5.56	0.0	3.82	0.16E-03	0.15	0.11E-02	0.95	0.0
Radio-FIR	5.58	0.0	3.99	0.77E-04	0.16	0.59E-03	0.96	0.0
FUV-NUV	1.70	0.31E-05	-1.70	0.89E-01	0.11	0.37E-01	1.00	0.0
FUV-FIR	1.69	0.37E-05	-1.35	0.18	0.06	0.60	0.99	0.0
FUV-NUV	1.00	0.97	0.32	0.75	0.10	0.11	0.98	0.0

[a]The statistic $F = \sigma_1^2/\sigma_2^2$; where σ_i^2 is the variance

[b]The statistic $t = (\overline{x_1} - \overline{x_2})/\sqrt{(\sigma_1^2/n_1) + (\sigma_2^2/n_2)}$; where $\overline{x_i}$ is the mean of a distribution of n_i data points and variance σ_i^2

[c]Unlike all others, this statistic is evaluated in log-log space (also see Figure 8.5)

same mean. As expected from Table 8.2, the mean of the radio SFR distribution is significantly different from all other SFR metrics, which are statistically consistent with each other. Together these results indicate that *the 1.4 GHz emission probes the youngest stellar population that is missed by all other wavelengths studied here.*

Table 8.3 also shows results for the Kolmogorov-Smirnov (K-S) test which checks against the hypothesis that the two distributions in question are drawn from the same parent sample using the D statistic, which is the maximum vertical distance between two cumulative distributions. For the SFR datasets presented here, the K-S statistic suggests that the PAH-FIR, PAH-NUV, FUV-NUV, and the FUV-FIR SFR distributions are likely to be drawn from the same parent sample. While the latter two result from the fact that the FUV and NUV luminosities are corrected using an IRX based recipe (Eqns. 2.1 & 2.2), the similarity between the PAH and FIR SFR distributions imply that they trace the same stellar populations. The last statistic displayed in Table 8.3 is the Pearson's r correlation coefficient that tests the correlation and its statistical significance between the two distributions. Unlike other statistics, the results for r statistic are

Table 8.4: Relation ($\mathrm{SFR}_i = a + b\mathrm{SFR}_{\mathrm{tot}}$) between individual SFR measurements & the total SFR

SFR_i	a	b	σ_{SFR_i}
FUV	0.168	-0.102	0.070
NUV	0.293	-0.136	0.106
PAH	0.238	0.043	0.193
Radio	0.361	0.009	0.191

evaluated in the log space to be in sync with the displayed correlations in Figure 8.5. As can be seen, all the correlations are very tight and very significant.

8.5.2 Individual tracers vs 'Total' SFR

The very tight correlation between the FUV and FIR SFR essentially implies that the global SFR is a very strong function of the bolometric luminosity. With our suite of SFR tracers for a statistical sample of galaxies we can also test if the SFR measured using individual tracers shows any systematic behaviour relative to the measurement corresponding to a galaxy's bolometric luminosity. This exercise is particularly critical for estimating the SFR for high redshift galaxies for which multi-wavelength data are often either not available or observationally expensive. We define the total SFR of a galaxy as the sum of SFRs derived from the FIR and the observed FUV luminosity:

$$\log\ SFR_{Total}(M_{\odot}\mathrm{yr}^{-1}) = \log\ SFR_{FUV,uncorrected} + (1-\eta)\log\ SFR_{FIR} \qquad (8.6)$$

where, $\log SFR_{FUV,uncorrected}$ is calculated using Eqn. 8.3 but using the observed FUV emission, uncorrected for dust extinction. Following Hirashita, Buat, & Inoue (2003), we assume that the old stellar populations contribute $\eta = 30\%$ to the FIR luminosity of our star-forming galaxies. The fractional contribution of other SFR measures namely radio, PAH, NUV, and FUV (latter two corrected for dust extinction) are plotted as a function of the total SFR

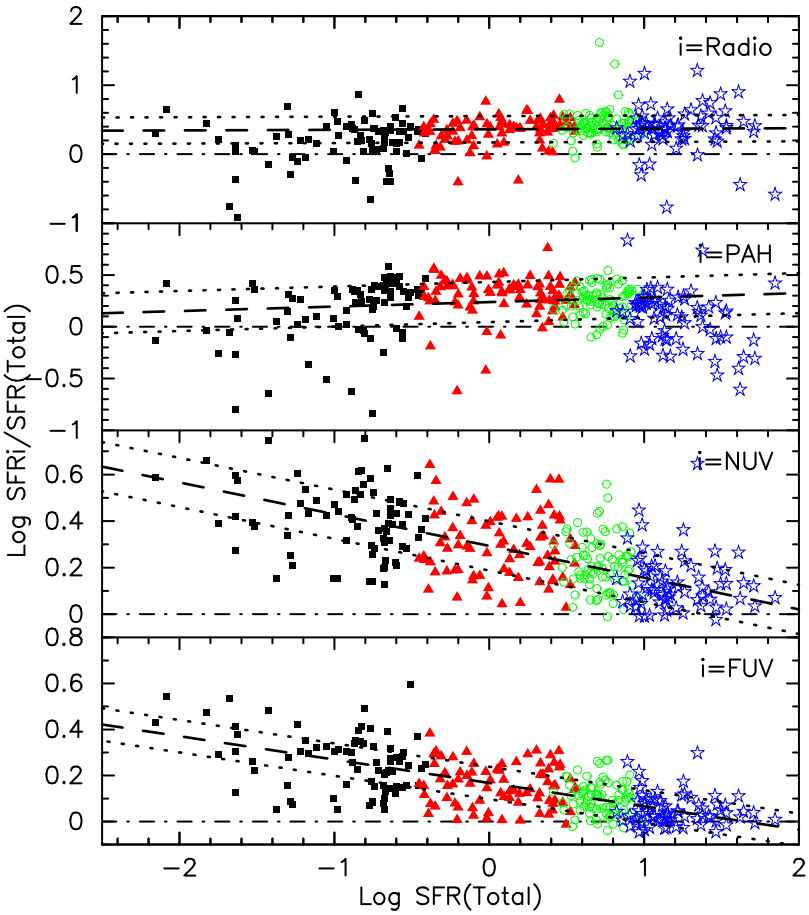

Figure 8.6: The ratio of SFR measured using *(top to bottom)* 1.4 GHz radio, PAH, NUV and FUV to the total SFR (Eqn. 8.6) respectively, as a function of the total SFR. The symbols and colours are the same as in Figure 8.4. The dot-dashed horizontal line in each panel shows the position of equality between the two measures used to evaluate the y-axis. The dashed line is the Median Absolute Deviation (MAD) fit to the data in each panel, and the dotted lines are the $\pm 1-\sigma$ deviation in the MAD fit. The contribution of PAH emission is almost always over-estimated by a factor of 3–4, except for the very underluminous and very FIR bright galaxies. The radio emission increases with galaxy luminosity.

(Eqn. 8.6) in Figure 8.6. The purpose of this analysis is to study the trends in the SFR distributions relative to the 'total' SFR in order to correct the SFR measured for galaxy samples where no more than one tracer is available. Although we have used UV measures where the UV luminosity is dereddened using IRX, the analysis can be used for statistical analysis of samples with UV only data by correcting the UV luminosities for internal extinction by using empirical relations presented elsewhere in literature (e.g. Seibert et al. 2005).

The fraction of SFR measured by UV light is a function of the bolometric luminosity, such that galaxies become more transparent to UV emission with decreasing galaxy luminosity. This is true for both FUV and NUV, although the scatter is slightly larger for NUV. Figure 8.6 suggests that the total SFR can be estimated to within a factor of 1.5(2) by using the $FUV(NUV)$ only data for the luminous ($\log L_{FIR}/L_{\odot} \geq 10.52$) galaxies, while for their fainter counterparts these tracers alone can lead to an overestimation by a factor of 2.5(4).

The PAH SFRs seem to overestimate the global SFR by a factor of 1.5–2 for all but very high and very low luminosity galaxies. For the galaxies at extreme ends of the luminosity distribution, the SFRs could be underestimated by up to an order of magnitude. The lack of PAH emission in low luminosity galaxies has been suggested elsewhere as well (Boselli et al. 1998; Hogg et al. 2005). The less massive galaxies can have less PAHs if they are low in metallicity, i.e. lacking the raw material to form PAHs, or if they are too young to have formed PAH. However, given that the shallow potential wells in these galaxies are unable to retain metals for a prolonged duration, low metallicity seems to be the most likely cause for the underestimated PAH SFR for these galaxies.

Simulations (e.g. Jonsson et al. 2006) and several observational studies (Wang & Heckman 1996; Hopkins, Irwin, & Connolly 2001; Buat et al. 2005) have shown that low luminosity galaxies have less extinction than their more luminous counterparts. An increase in gas density increases the SFR and hence the bolometric luminosity of the galaxy and also increases the dust extinction. This simple toy model presented by Jonsson et al. (2006) accounts for the

observed correlation between galaxy luminosity and dust attenuation and the trends seen in the UV and PAH SFRs as a function of the bolometric luminosity or the total SFR studied in this work (Figure 8.6). The radio bright galaxies occupying the high-luminosity end (top panel of Figure 8.6) may have a relatively harder radiation field due to the presence of an AGN that destroys the PAHs (e.g. Condon 1992; but see Shi et al. 2007 for an alternative view), resulting in the trends seen for the PAH SFRs.

The radio SFRs in this work almost always overestimate the total SFR by a factor of two, showing a very weak trend for higher overestimation for more luminous galaxies. This interesting observation suggests that the implied local star formation rate density (SFRD henceforth) for our sample is twice as much as that used in deriving the conversion relation between 1.4 GHz luminosity and SFR.

Sullivan et al. (2001) suggested that the calibration of $L_{1.4\,GHz}$-SFR may not be perfectly linear, particularly in low luminosity (or low SFR) galaxies, where there is the possibility that a fraction of the SNe remnant accelerated cosmic rays may escape from the galaxy (Condon et al. 1991). This scenario might explain the underestimated 1.4 GHz SFR measures of some low luminosity galaxies in our sample (Figure 8.6).

8.6 The FIR-Radio correlation

Radio and FIR luminosity of galaxies are known to be very well correlated over a large range in luminosity and redshift (e.g. Yun, Reddy, & Condon 2001). However, galaxies at the low luminosity end and very high luminosities deviate from the correlation (Condon et al. 1991; Yun, Reddy, & Condon 2001; Bell et al. 2003). Such nonlinear trends are expected when the radio and FIR luminosity are not directly proportional to the SFR, for instance in the presence of an AGN. For a diverse sample of galaxies Bell et al. (2003) showed that although IR traces most of the star formation in luminous galaxies, only a small fraction is detected in low luminosity

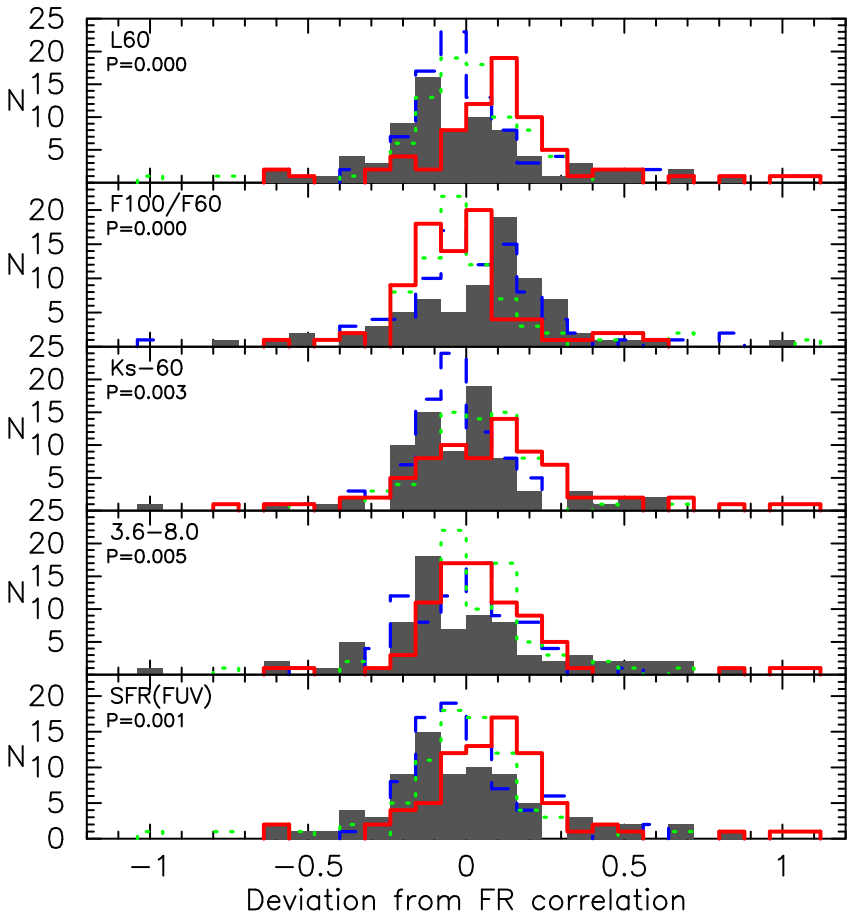

Figure 8.7: *(top to bottom)* The distribution of 60μm luminosity, FIR colour temperature $F100/F60$, $Ks-60$ colour, $3.6-8.0$ colour and the FUV SFR are plotted as a function of the deviation from the FIR-Radio SFR correlation (Fig. 8.5 second panel on the top). Deviation > 0 (rightwards on the x-axis) implies that the galaxy lies above the fitted relation and vice-versa. Each distribution is segregated into quartiles represented in increasing order by *solid grey*, *dotted green*, *dashed blue* and *linear red* histograms respectively. The K-S test probability in favour of the hypothesis that the first and the fourth quartile distributions are drawn from the same parent sample (shown on the left-hand corner of each panel) significantly nullify the hypothesis for all these parameters.

galaxies that have low extinction (also see Figure 8.6). If radio luminosity were a perfect star formation tracer, this effect should lead to a curvature in the FIR-radio (FR henceforth) correlation (also see Sullivan et al. 2001). But because the FR correlation is *linear* over a wide range in galaxy luminosities with less than a factor of two scatter, Bell et al. (2003) suggested that both radio and IR emission underestimate the SFR in low luminosity galaxies, coincidentally in similar ways.

Figure 8.7 explores several parameters as a function of the deviation of galaxies from the FR correlation. The top three panels show the distributions of the deviation of galaxies from the FR correlation, divided into quartiles of the three dimensions of the selection space for the SFRS sample, the 60μm luminosity, F100/F60 colour temperature of dust and the $Ks-60$ colour as a proxy for sSFR respectively. The K-S test statistic applied to the first and the fourth quartile of each of these distributions implies that the two distributions are unlikely to be drawn from the same parent sample. In other words, *galaxies that lie above the correlation are more luminous, much warmer, and have a higher specific star formation rate relative to the ones that lie below the correlation*. The positive deviation of the high-luminosity galaxies can be explained by at least two different phenomenon, presence of an AGN, or overestimated FIR SFR due to dust heated by low mass stars and/or older stellar populations which contribute to FIR emission but not radio continuum. Either of these would also account for higher dust temperature and sSFR as quantified by the $Ks-60$ colour.

Figure 8.7 also shows the deviation of galaxies from the FR correlation divided into quartiles of the $3.6-8.0$ *IRAC* colour. Wu et al. (2007) (also see Engelbracht et al. 2008) have shown that the $3.6-8.0$ colour (a proxy for dust-to-stars ratio) correlates with metallicity. In the optically thick regime, to first order this colour should also correspond to the sSFR. The galaxies with the reddest $3.6-8.0$ colour are almost normally distributed around the mean FR correlation. However, the galaxies in the bluest bin show a bimodal distribution, such that the two sub-populations lie on either side of the correlation.

As hypothesised above, if the old stars contribute to the total FIR emission leading to the deviation of luminous galaxies from the FR correlation, this trend should be reflected in the distribution of the FUV properties of these galaxies. In order to explore this, Figure 8.7 plots the FUV SFR in the same fashion as above mentioned parameters. Counter to expectation, galaxies with highest FUV SFRs are more likely to lie above the FR correlation than below it. However, the observed trend could be illusory because the FUV luminosity for our galaxies is corrected for dust extinction using IRX, thus giving a better correlation between FUV and FIR SFRs than between FUV and radio SFRs (Figure 8.5).

8.7 Optical AGN in SFRS

The nuclear activity and its impact on the host galaxy can mimic star formation activity in a lot of photometric and spectroscopic properties of galaxies. Optical emission lines such as Hα and O II, and FIR luminosity over and above that expected for normal galaxies are seen in AGN as well as star-forming galaxies. In this work we make use of the SDSS fibre spectra available for 180/314 of the SFRS galaxies studied here. 165/180 galaxies have all four emission lines, namely, Hα, [N II], [O III] and Hβ that are required to classify them as AGN or star-forming on the line ratio diagram more commonly known as the BPT diagram (Baldwin, Phillips & Terlevich 1981). We find that 82 of these 165 galaxies are AGN. Since SDSS fibre measures 3$''$ in diameter, for the nearest galaxies the SDSS spectra is dominated by the nuclear emission. However, at $z = 0.1$ this aperture encompasses 40-60% of the total light for a typical galaxy.

In Fig. 8.8 we compare the distributions of $J-Ks$ colour, 60μm luminosity, IRX and the $FUV-NUV$ *Galex* colour for the optically selected AGN and all the SFRS galaxies studied here. Except IRX, we do not find any differences between optical AGN and the ensemble of all the SFRS galaxies in the multi-wavelength space explored here, suggesting that the optical AGN are only likely to be more dusty than other SFRS galaxies. Given that the *Galex* colour

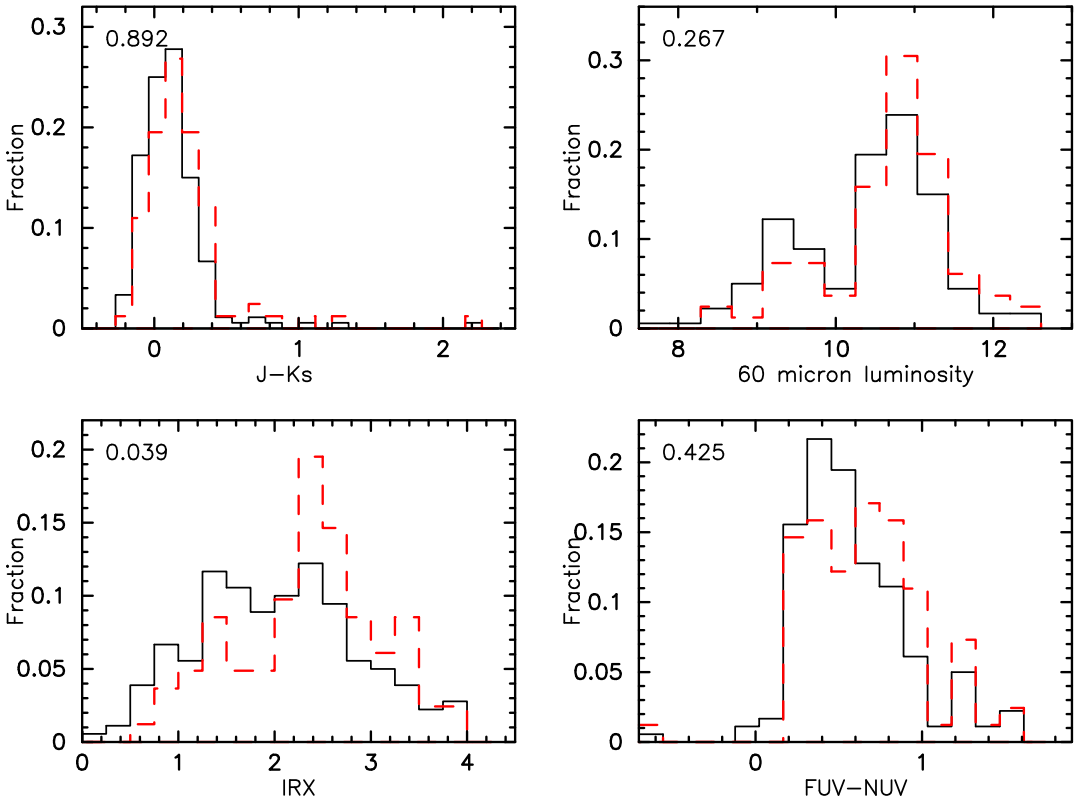

Figure 8.8: The distribution of *(clockwise from top left)* $J-Ks$ colour, 60μm luminosity, IRX and the $FUV-NUV$ *Galex* colour for optical AGN *(red dashed histogram)* and all other SFRS galaxies *(black solid histogram)*. The K-S statistics probability that the two distributions are derived from the same parent distribution are shown in the top left of each panel. K-S test suggests that only the distribution of IRX ratio for BPT selected AGN is different from other FIR selected galaxies such that the AGN are more dusty on average.

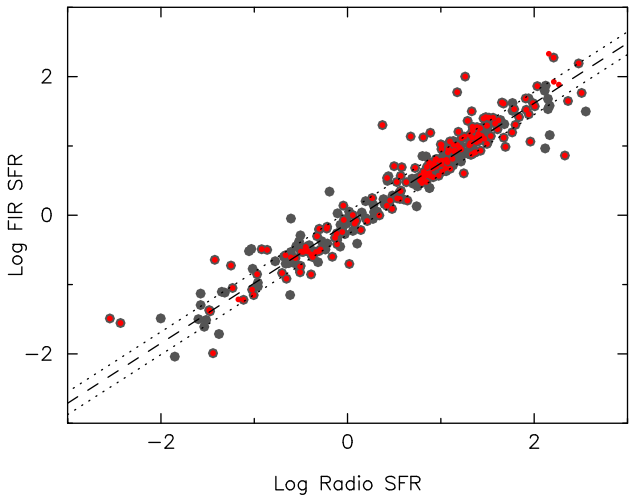

Figure 8.9: The correlation between the SFR measures derived from the FIR and 1.4 GHz radio luminosity for all *grey points* and optically selected AGN *red points* in our sample are shown, with the correlation from Fig. 8.5 over-plotted. The AGN hosts show similar FIR-Radio ratio as expected for other star-forming galaxies.

for AGN shows no difference with other star-forming galaxies, while IRX does, these galaxies will lie above the star-forming galaxies in the IRX-β relation (Meurer et al. 1999; Fig. 8.3).

Morić et al. (2010) have recently studied the FIR-radio correlation (§8.6) for different types of galaxies in the local Universe. One of their main results is that even though (radio-detected) AGN add an excess of FIR and radio power to the bolometric luminosity, relative to a star-forming galaxy of the same luminosity, their FIR/Radio ratio (often called the q-parameter) on an average are consistent with those expected for star-forming galaxies. In Fig. 8.9 we find the same for the SFRS galaxies. The optically selected AGNs (which are almost all LINERS[7]) follow the same Radio-SFR relation as all the other SFRS galaxies. This is expected when the contribution of AGN to the total luminosity of the galaxy (and hence the corresponding SFR) is comparable in FIR and radio emission. Hence, unlike the radio-loud AGN, the optically selected AGN can not be distinguished from the star-forming galaxies using a q-discriminator value.

[7]Low-Ionisation Nuclear Emission-line Region

8.8 Summary and conclusions

In this chapter we have utilised the arsenal of data from UV to radio wavebands made available for 330/369 SFRS galaxies found within $z \leq 0.1$ to build a suite of global SFR metrics. For UV emission, we make use of the empirical correction (Eqns. 2.1 & 2.2) based on the IRX(n) ratio to account for the radiation lost due to absorption by dust. We explore the correlations between different extinction (Fig. 8.4) and SFR (Fig. 8.5) measures and their distributions in quartiles of 60μm luminosity. Our main results are summarised below:

- SFR measures obtained independently from 1.4 GHz radio continuum, FIR, non-stellar PAH emission and *Galex* UV imaging correlate well with each other.
- All SFR measures (FUV, NUV, non-stellar PAH, FIR & radio) can estimate the SFR of a galaxy to within a factor of 1.5–4 of the 'total' SFR ($\mathrm{FIR}+\mathrm{FUV}$) expected from the bolometric luminosity of the galaxy.
- Barring radio, the distribution of different SFR measures show similar statistical properties, such that the median of all distributions are within 25% of each other. This suggests that the datasets are statistically consistent but have slightly different sampling properties.
- The SFR values estimated from the non-stellar 8.0μm PAH emission are within a factor of two for all but the very low luminosity and very high luminosity galaxies. For the galaxies occupying the extreme ends of the luminosity distribution, the SFRs can be under estimated by as much as a factor of two of the total SFR expected from the bolometric luminosity of the galaxy.
- The contribution of FUV SFR to the total SFR ($\mathrm{FIR}+\mathrm{FUV}$) corresponding to the bolometric luminosity of the galaxy decreases with increasing SFR for the FIR selected SFRS sample.

- The radio SFRs are overestimated by a factor of two relative to the 'total' SFR for all galaxies.

- Galaxies lying above the FIR-Radio correlation statistically have redder 3.6–$8.0\,\mu$m IRAC and $J-Ks$ colours, higher $F100/F60$ FIR dust temperature, higher 60μm luminosity and higher FUV SFR relative to the galaxies that lie below the fitted correlation. For the high-luminosity galaxies, this suggests the presence of an AGN and/or overestimated FIR luminosity due to dust heated by the older stellar populations.

- The optically-selected (BPT) AGN exhibit similar 60μm luminosities, $FUV-NUV$ and $J-Ks$ colour as the rest of the star-forming galaxies in the SFRS sample. However, the IRX ratio in AGN is higher than other galaxies, suggesting that they are relatively more dusty than a randomly FIR selected galaxy.

- Optically-selected AGN obey the same FIR-Radio correlation as the other galaxies and hence can not be selected using the FIR/Radio flux ratio.

Chapter 9

Conclusions and future aspects

The theme of this thesis is extra-galactic star formation- a critical driver of galaxy evolution- and how it responds to factors such as environment, extinction and AGN activity. We have used photometric and spectroscopic data obtained by the Sloan digital sky survey (SDSS) to explore the effects of the local and global environment on the star formation rate (SFR) of galaxies in nearby clusters ($z \sim 0.1$), and utilised *Spitzer* (IRAC & MIPS), *Galex* and 1.4 GHz radio (VLA/NVSS) imaging to understand the nature of star formation and dust properties in nearby star-forming galaxies. In the following, we summarise the results obtained in this work along with the future prospects for the exciting avenues opened by it. To do so, we broadly classify the research presented in this work into two subsections below.

9.1 The Large-scale structure and galaxy evolution

We have exploited the various photometric and spectroscopic observables obtained by SDSS to show that the classical correspondence between photometric colours and spectroscopically derived SFR/indicators fails for a non-negligible fraction of cluster galaxies under special circumstances (chapter 3). An interesting finding of this work is that not all optically red galaxies are dusty. In fact, our results suggest that almost 50% of the dusty (optically)red galaxies found

in chapter 3 seem to obtain their colours from metal-rich stellar populations. Better metallicity indicators and well-fit SED modelling is required to confirm this result for a statistical sample of galaxies.

By combining SDSS data covering 500 sq. degrees with the 24μm MIPS data for the Coma and Abell 1367 clusters, we have analysed the progressive evolution of SFR with environment in the Coma supercluster. We show that the SFR of massive galaxies are relatively lower than their low mass counterparts irrespective of their position in the supercluster (chapter 4). We also show that among the dwarf population, those showing a k+A or post-starburst phase (EW(Hα) < 2 Å in emission & EW(Hδ) > 3 Å in absorption) are likely seen near the larger structures such as the galaxy groups and clusters in the supercluster. Moreover, we find that these k+A dwarfs are likely to be the progenitors of the dEs, found in abundance in the cluster cores in the nearby Universe (chapter 7).

This thesis focuses on the variation of SFR in galaxies with environment– both local, defined by the immediate galaxy density and global, which is the position of a galaxy in the cosmic web (chapter 5). In particular, we were interested in exploring how the star formation in galaxies respond to the gravitational influence of large-scale filaments. At z ~ 0, Porter & Raychaudhury (2005), Porter et al. (2008) and Mahajan, Raychaudhury & Pimbblet (2011c) have shown that the SFR in galaxies falling into clusters is enhanced at the cluster periphery. Using the 24μm data for a filament of galaxies feeding Abell 1763 (z $= 0.23$) Fadda, Biviano & Durret (2008) find more starburst galaxies in the filament relative to the cluster and the field.

In the near future, we intend to take this work further by utilising the multi-wavelength data made available by the Herschel Multi-tiered Extragalactic Survey (HERMES[1]). HERMES is the largest guaranteed time program for ESA's *Herschel* space observatory designed to study evolution of galaxies at high redshift. The first data release for the survey was made in July 2010. HERMES is designed to image well-studied fields with panchromatic multi-band imaging with

[1]http://hedam.oamp.fr/HerMES/

Herschel's PACS & SPIRE instruments. These fields are selected so as to have a dataset exhibiting whole range of environments from dense clusters to sparse field, thus facilitating the study of galaxy evolution as a function of environment at intermediate and high redshift.

With our experience and existing knowledge of variation in galaxy observables with environment for nearby Universe, we are well equipped to interpret the observations at higher redshift as well as draw conclusions on how, if at all, does the relation between various galaxy observables and their environment evolve over time.

9.2 The Star Formation Reference Survey

In chapter 8 of this thesis we have presented the first results from the Star Formation Reference Survey (SFRS). SFRS is the first systematic attempt to assess the SFR metric for a wide range of galaxies, encompassing all possible conditions under which stars form in the local Universe. The key science driver for this project is to compile and compare SFR indicators, both global and resolved (for the nearby galaxies) in order to understand better the physical process of star formation and its effects on other galaxy observables.

We have estimated and compared the global SFRs obtained using empirical recipes available in the literature from the far ultra-violet (FUV), far infrared (FIR), non-stellar polycyclic aromatic hydrocarbon (PAH) emission and 1.4 GHz radio continuum imaging. Now with most of the multi-wavelength data for all the SFRS galaxies either available or in the process of acquisition (Table 9.2), we are capable of taking this analysis to the next level of analysis. The key questions that we will try to answer at the end of this analysis are:

- Are dust masses and temperatures in passive, normal and star-forming galaxies different?
- How does the presence of dust influence various measures of SFR– globally and in individual star-forming regions?

Bandpass	Observatory	Sample Coverage
1.4 GHz	VLA/NVSS	100%
12,25,60,100 μm	*IRAS*	100%
65,90,140,160 μm	*Akari* FIR All-Sky Survey	95%
12, 23 μm	*WISE*	100% (survey under way)
24 μm	*Spitzer*/MIPS	70%
3.6, 4.5, 5.8, 8.0 μm	*Spitzer*/IRAC	100%
JHK_s	2MASS	100%
JHK_s	PAIRITEL	70% (campaign ongoing)
Y	Pan-STARRS	100% (campaign ongoing)
$ugriz$	SDSS	100%
Optical Spectra	SDSS (fiber)	210/369
Optical Spectra	FAST (longslit)	100/369 (campaign ongoing)
Hα	NAOC	30% (campaign ongoing)
0.13–0.28 μm	*GALEX*	90% to date
0.5-8.0 keV (X-ray)	*Chandra, XMM*	$> 50\%$

Table 9.1: Summary of available data for SFRS galaxies

- How does the star formation metric change globally, and on smaller scales for different galaxy populations?

- How does the SED of star-forming galaxies evolve over time?

In order to answer the first three questions we would like to carry out this research as two parallel projects.

Project 1: The first follow-on step in building the SFRS legacy is to fit the spectral energy distribution (SED) for all the SFRS galaxies. This suite of SEDs will not only provide useful clues to the nature of star formation in the local star-forming galaxies, but will also act as an ideal sample for a comparison with star-forming galaxies observed at higher redshift, thus providing an insight into the evolution of star formation rate density over the age of the Universe.

The extensive SFRS dataset comprises imaging from UV (for 90% of the sample; see Table 9.2) to radio, which not only allows us to see the energy distribution, for almost all possible conditions under which the stars form in the local Universe, but also to explore causes for a

deviation from the normal behaviour, such as the presence of an AGN.

We intend to carry out this work in three steps:

(i) Develop a set of model SEDs ranging from a pure early-type, passively evolving galaxy to a late-type star-forming galaxy. These models can then be convolved with the filter functions of individual IR instruments (e.g; MIPS) to give unique K-corrections for each of the wavebands (3.6-160μm) at different redshifts (idea based on Huang et al. 2007). For the UV and NIR 2MASS data, K-corrections can be applied using the KCORRECT software (Blanton & Roweis 2007).

(ii) Once K-corrected, these photometric data can be used to constrain rest frame SEDs for the bulk of the SFRS galaxies using simple stellar population (SSP) models such as GALAXEV (Bruzual & Charlot 2003), which are now capable of fitting the entire spectral range from UV to FIR (private communication, S. Charlot).

(iii) Since our sample comprises passively evolving galaxies such as those found in local clusters, as well as normal star-forming and extreme starburst galaxies, we are curious to know if the peak of emission due to star formation and SFR metrics varies systematically in different populations of galaxies. For instance, if the hard radiation field in radio galaxies destroys dust grains, their dust emissivity should be very different from (say) normal star-forming galaxies. Well fit SEDs for a variety of galaxies across a wide range in wavelength will help us in addressing several such issues with SFRS (as an example see the recent work by Morić et al. 2010, where they analyse the FIR-Radio correlation in context of other galaxy properties obtained from empirical SED fits for different types of galaxies). The results of this analysis can then be compared to those obtained for other high redshift studies, in order to better understand the evolution of star formation density in the Universe and the SED of star-forming galaxies as a function of time and luminosity, thus answering point 4 mentioned above.

Project 2: Since $\sim 60\%(90\%)$ of the SFRS galaxies are within 100(180) h_{73}^{-1}Mpc, the *Spitzer* data from IRAC and MIPS (3.6-160μm) and UV data from *Galex* (1350-3000 Å) can be resolved into individual HII regions for the nearby galaxies. These data, together with FAST long-slit spectra, that are being acquired for a substantial fraction of SFRS, and narrow-band Hα imaging for the entire sample (Table 9.2), will provide an insight into the evolutionary link between the individual star-forming regions and the global SFR and extinction metrics which have been evaluated using the arsenal of multi-band data available to us already.

In the near future, we also intend to apply for integral field unit (IFU) spectroscopy, for a few ($\sim$5–10) of the nearby SFRS galaxies, in addition to the existing UV and IR imaging. Such observations can be carried out on instruments like GMOS on *Gemini*. Together with the narrow-band Hα imaging, these data are likely to provide unprecedented information about the nature of star formation in local galaxies. In particular, we will be able to understand the influence of dust geometry on the measures of SFR, both locally and globally. By including some interacting pairs of galaxies in this small sample, one can compare the properties of star-forming regions in these systems to those in unperturbed galaxies. This will help us in understanding the effects of gravitational interactions on the nature of star formation on large scales.

To conclude, we remark that in this thesis we have reduced and analysed multi-wavelength imaging and optical spectroscopic data for nearby galaxies, and in doing so dealt with large datasets as well as individual galaxies. This work mainly contributes to our current understanding of how global star formation measures vary with the use of different SFR indicators, and how star formation in a galaxy responds to a change in its environment– due to change in local galaxy density, global environment defined by the large-scale cosmic web and the velocity fields generated by deep potential wells of galaxy clusters.

In future we would like to take this research to a new level, by exploring the nature of star formation and dust properties of individual star-forming regions in the nearby galaxies, for which data already exist or are in the process of acquisition. We intend to apply for observing

time at ground-based observatories to compliment the existing suite of space-based observations for SFRS. We would like to explore the variation in star formation properties of galaxies with environment at higher redshift using data from HERMES. This work will enhance our current knowledge of evolution of galaxies as a function of environment over cosmic time, and the relationship between dust and the rate of star formation in galaxies, thus leading to a better understanding of the formation and evolution of galaxies and of large-scale structures such as clusters and intra-cluster filaments in the Universe.

Appendix A

Catalogues

Table A.1: Catalogue of Coma galaxies detected at 24μm

RA (J2000)	Dec (J2000)	z	g mag	r mag	z mag	24μm flux (mJy)	flag[1]
194.4574	28.6243	0.0250	17.80091	17.35266	17.24303	0.3091	1
195.1548	28.6641	0.0236	17.47583	16.89538	16.49190	1.2472	1
194.5385	28.7086	0.0255	15.21324	14.56441	14.08494	36.0163	1
194.9172	28.6308	0.0179	15.67984	15.47081	15.30021	7.8987	1
194.3645	28.4397	0.0260	17.16748	16.57682	16.19059	0.7535	1
194.5628	28.5218	0.0231	17.00793	16.56577	16.32964	1.8391	1
194.3912	28.4823	0.0209	14.35161	13.54058	13.00418	1.8628	3
194.4747	28.4998	0.0244	15.94461	15.18044	14.56075	0.0425	0
195.2170	28.3661	0.0255	14.51777	13.73402	13.10617	1.3893	0
195.3123	28.5217	0.0281	17.48560	17.11399	16.98313	1.0568	1
194.8986	28.5514	0.0253	15.79564	15.02592	14.40227	0.4444	0
195.6700	28.3713	0.0248	15.15665	14.39596	13.83882	2.8855	0
195.5361	28.3871	0.0253	15.02371	14.19748	13.52015	7.7050	0
195.9768	28.3105	0.0268	17.32578	16.92387	17.08466	0.4582	1
196.1306	28.3019	0.0263	17.74597	17.50979	17.26107	0.6907	1
194.6261	28.8588	0.0267	15.94322	15.11644	14.57277	0.4682	0
194.5555	28.9481	0.0256	14.88157	14.12878	13.51413	1.5400	0
194.6801	28.9100	0.0278	15.57888	14.97807	14.58375	5.3501	1
195.0147	26.8981	0.0198	14.17546	13.42696	12.83778	1.5172	0
194.9764	26.8200	0.0268	16.34796	15.78004	15.33257	0.7258	2
194.0175	27.2855	0.0224	17.93143	17.39572	17.11758	0.7348	1
193.9221	27.2508	0.0237	14.54856	13.75319	13.07945	0.7467	0
193.7299	27.4127	0.0262	13.82080	12.98482	12.37692	9.6323	3
194.1975	27.2923	0.0262	16.90458	16.23294	15.76256	0.7358	0
194.1191	27.2913	0.0251	15.28508	14.82707	14.54622	17.1425	1
194.1443	27.2276	0.0240	15.96509	15.39901	14.99258	5.7342	1
194.5776	27.3108	0.0247	16.39763	15.97154	15.50994	24.6126	1
194.6553	27.1766	0.0256	15.34060	15.01515	14.76351	39.0962	1
194.6054	27.2000	0.0269	17.02492	16.38847	15.90987	1.2912	1
194.6381	27.3644	0.0232	15.73970	14.98249	14.40896	0.4546	0
194.6472	27.2647	0.0246	15.56636	15.28582	15.01500	24.3478	1
194.8184	27.1581	0.0223	16.08671	15.36038	14.77889	0.4061	0
194.0254	27.6781	0.0165	15.39373	15.05404	14.80908	67.7281	1
194.0825	27.7510	0.0230	15.23852	14.42984	13.76227	0.5760	0

Continued on next page

[1]Classification on the basis of BPT diagram,where
0: unclassified
1: star-forming
2: AGN
3: AGN according to Miller et al. (2003)'s criteria (see text)

Table A.1 – continued from previous page

RA (J2000)	Dec (J2000)	z	g mag	r mag	z mag	24μm flux (mJy)	flag
194.2690	27.7730	0.0252	16.32501	15.66651	15.07298	6.5628	1
194.2677	27.7300	0.0297	16.61880	15.94118	15.45292	1.4767	1
193.8544	27.7980	0.0246	14.73661	13.90918	13.29552	1.2009	0
194.1109	27.8306	0.0209	15.15755	14.38029	13.76368	0.8152	0
194.3199	27.6185	0.0242	16.21049	15.41362	14.75481	0.4243	0
194.7171	27.7850	0.0189	15.40765	14.64100	14.00507	0.7567	0
194.6975	27.6747	0.0280	14.68235	13.86892	13.30637	0.4696	0
194.3242	27.8109	0.0239	15.98041	15.44634	15.03971	0.3093	0
194.7421	27.5947	0.0201	15.76913	14.98863	14.33799	0.2002	0
194.7812	27.7678	0.0212	15.47125	14.69546	14.06058	0.7887	0
194.7842	27.7841	0.0235	14.92247	14.10093	13.42276	2.2066	0
194.7721	27.6444	0.0181	14.87768	14.46940	14.24197	28.0886	1
193.8372	27.6691	0.0237	17.86424	17.07880	16.51597	0.6946	0
194.6466	27.5964	0.0257	14.07095	13.47282	12.95085	42.9670	3
194.7929	27.6199	0.0192	16.05716	15.30879	14.69412	0.7714	0
194.9464	27.7103	0.0280	14.61854	13.88087	13.27900	1.7857	0
194.9159	27.5765	0.0167	16.03037	15.64959	15.36893	7.9639	1
195.3012	27.6045	0.0252	16.16354	15.41326	14.83540	0.6352	0
195.1403	27.6378	0.0250	15.44649	15.17704	14.88305	15.0254	1
195.4739	27.6244	0.0262	13.79127	12.93928	12.34770	2.7049	0
195.5328	27.6483	0.0230	14.93765	14.38136	13.93213	63.7086	1
195.1486	27.5742	0.0170	15.74702	15.02376	14.44816	25.2645	1
194.8062	27.7746	0.0228	15.34113	14.56991	13.95732	0.7119	0
194.4528	28.1804	0.0241	15.45448	14.68872	14.05055	0.3124	0
194.3750	28.1881	0.0232	14.94220	14.16724	13.54112	2.9573	3
194.1681	28.2178	0.0277	17.48277	17.00570	16.61437	0.8961	1
194.1619	28.0811	0.0271	16.56031	15.80329	15.19356	0.2678	0
194.2702	28.2097	0.0172	17.91273	17.59471	17.58008	0.4229	1
194.6064	28.1289	0.0274	16.54907	16.09058	15.71724	3.6988	1
194.4905	28.0618	0.0272	15.64717	15.16274	14.77069	20.2265	1
194.5575	28.1826	0.0240	15.50403	14.80390	14.26388	8.4389	0
194.7663	28.1237	0.0265	14.22019	13.40088	12.73469	4.7499	0
194.5904	28.1488	0.0263	15.46361	14.67064	14.01652	0.8997	0
194.6515	28.1137	0.0227	15.06789	14.25201	13.57534	1.4517	0
194.8810	28.0466	0.0231	15.44123	14.67593	14.09292	0.8565	0
194.9322	27.9947	0.0223	15.89121	15.10485	14.43568	0.4357	0
194.9834	28.0347	0.0272	14.97157	14.14716	13.44777	1.8129	0
194.8608	27.9985	0.0222	16.48579	15.73821	15.11057	0.5111	0
194.7115	28.0840	0.0203	16.09372	15.33235	14.69072	0.2701	0
194.8328	28.0843	0.0153	14.34264	13.55494	12.88491	5.1958	0
194.9657	28.0985	0.0255	17.40591	16.66592	16.05626	0.9514	0
195.0185	27.9876	0.0213	14.90291	14.12746	13.40177	1.5330	0
195.0333	28.0786	0.0242	15.46070	14.65478	13.95144	2.0328	0
195.0266	28.0041	0.0243	15.73390	14.97444	14.33570	0.9211	0
195.0536	28.0755	0.0250	15.82425	15.04208	14.40300	0.5704	0
195.0709	28.0639	0.0205	16.13618	15.36019	14.69497	0.7157	0
195.0922	28.0470	0.0273	15.26168	14.49118	13.83529	0.7286	0
195.1578	28.0581	0.0255	15.44332	15.02546	14.55610	95.0291	1
195.1860	28.1006	0.0220	16.16693	15.41045	14.79128	0.4079	0
195.2027	28.0907	0.0233	14.76154	13.94601	13.26109	2.2823	3
195.0380	28.1704	0.0225	15.62700	14.84597	14.20179	0.7811	0
195.2269	28.0076	0.0166	14.13522	13.33965	12.69467	2.9028	0
195.0614	28.0413	0.0192	15.51282	14.73852	14.06774	1.9528	0
195.1702	27.9966	0.0236	15.40250	14.61031	13.93665	0.4518	0
195.2034	28.1583	0.0194	14.07834	13.35604	12.89258	2.9724	3
195.3631	27.9992	0.0255	16.44680	15.65585	14.95814	0.5109	0
195.4459	28.0950	0.0194	15.01314	14.22293	13.56537	1.1373	0
195.4899	28.0058	0.0258	14.37721	13.53147	12.78415	5.6928	0
195.7536	28.0325	0.0180	13.90280	13.17408	12.59664	2.1144	0
195.7357	28.0704	0.0259	15.47304	14.75912	14.21280	0.2444	0
195.8177	28.0304	0.0203	14.71906	14.03575	13.45075	9.4016	3
195.9373	28.0842	0.0188	15.12308	14.34683	13.71208	6.8212	3
195.8449	27.9360	0.0201	15.86241	15.13201	14.54587	0.8216	0

Continued on next page

Table A.1 – continued from previous page

RA (J2000)	Dec (J2000)	z	g mag	r mag	z mag	24μm flux (mJy)	flag
194.2069	27.0939	0.0232	15.40390	14.59548	13.91649	3.3019	3
194.4023	27.0314	0.0246	15.65812	14.85474	14.24633	0.7735	0
194.2998	27.1033	0.0246	16.85365	16.14658	15.59263	0.3251	3
194.1813	27.1788	0.0253	13.84386	13.02796	12.39427	4.7470	0
194.6285	26.9949	0.0249	17.78315	17.56542	18.05516	0.2678	1
194.6612	27.0132	0.0234	17.37781	16.95312	16.72545	1.9289	1
194.4861	27.0375	0.0248	16.09861	15.35353	14.73896	4.4676	3
194.6129	27.0235	0.0252	17.67763	17.28261	17.03164	2.1430	1
194.8195	27.1061	0.0280	16.74682	16.03175	15.32730	19.7361	2
194.9552	26.9743	0.0235	17.15859	16.78551	16.61056	2.0836	1
194.2892	27.4664	0.0249	14.99065	14.17044	13.47709	1.3793	0
194.1766	27.5483	0.0253	17.37177	16.74824	16.20049	0.2429	0
194.3994	27.4932	0.0244	14.81708	13.98657	13.26944	1.2978	0
194.4006	27.4848	0.0241	15.89907	15.09599	14.41773	0.5762	0
194.2948	27.4049	0.0207	15.64411	14.93878	14.36571	5.0386	3
194.0695	27.4460	0.0214	15.86288	15.09272	14.46627	0.2359	0
194.3455	27.4930	0.0275	17.38874	16.63356	15.94578	0.8985	0
194.3577	27.5461	0.0186	15.45795	14.68514	14.02069	0.7461	0
194.3552	27.4046	0.0160	15.81493	15.25920	14.81355	14.3435	2
194.4615	27.4909	0.0246	18.28703	17.52258	16.87655	0.4397	0
194.4843	27.5814	0.0165	16.27615	16.07672	15.81883	1.8512	1
194.3515	27.4978	0.0245	13.41864	12.58183	12.13002	2.7522	0
194.1425	27.5390	0.0237	15.41677	14.58385	13.87773	0.7427	0
194.5253	27.4189	0.0192	16.84729	16.15375	15.55515	0.5133	0
194.6576	27.4640	0.0210	16.55176	15.90585	15.28488	5.5069	1
194.6184	27.5594	0.0254	16.05664	15.50840	15.04940	3.5995	3
194.5855	27.4294	0.0252	17.36975	16.78251	16.27332	1.7136	1
194.6336	27.4563	0.0234	15.87415	15.10327	14.46973	0.4966	0
193.8776	27.5443	0.0235	16.11431	15.39089	14.87932	0.2901	0
194.4765	27.4906	0.0167	15.84596	15.18564	14.65198	4.1085	2
194.4863	27.4426	0.0257	17.73988	17.32263	16.72349	1.1538	1
195.1398	27.5041	0.0186	16.29861	15.99774	15.74321	5.4464	1
195.0796	27.5537	0.0196	15.61589	14.84437	14.19983	0.5829	0
194.8071	27.4026	0.0189	15.14973	14.36789	13.71326	1.6499	0
193.9894	27.9049	0.0219	16.68529	15.95988	15.41401	0.5531	0
193.9542	27.9059	0.0232	15.82088	15.03217	14.39868	0.7339	0
194.0413	27.8442	0.0253	15.36234	14.54430	13.93022	0.2730	0
194.1786	28.0204	0.0209	14.72390	13.92732	13.29665	1.7641	0
194.1242	27.9400	0.0222	15.23310	14.45436	13.84450	0.7067	0
194.5119	27.9783	0.0220	17.73338	17.00301	16.47225	0.5446	0
194.3406	27.8804	0.0249	16.09577	15.46183	14.91877	0.4547	0
194.4503	27.8831	0.0196	15.17633	14.41580	13.79195	1.6652	0
194.4471	27.8333	0.0202	15.68265	14.90932	14.27083	0.6096	0
194.4866	27.9918	0.0153	17.08829	16.87379	17.10896	1.6798	1
194.5146	27.8149	0.0238	15.56672	14.80265	14.15936	0.5750	0
194.6894	27.8799	0.0283	18.33102	17.58195	17.07590	0.3871	0
194.5910	27.9678	0.0201	14.96606	14.16329	13.51749	5.1148	3
194.7030	27.8104	0.0198	14.83844	14.05399	13.38524	1.5863	0
194.8135	27.9707	0.0161	15.11443	14.32648	13.67031	2.5894	0
194.7831	27.8550	0.0220	15.29355	14.48387	13.76770	2.7792	3
194.7359	27.8220	0.0292	17.28110	16.62817	16.16483	1.2606	2
194.7693	27.9110	0.0214	16.07529	15.32364	14.70003	0.2547	0
194.8341	27.8860	0.0216	15.94896	15.22243	14.65589	0.5831	0
194.7503	27.9675	0.0278	16.48549	15.71399	15.08829	0.2181	0
194.7751	27.9967	0.0256	15.10456	14.26289	13.69356	1.7393	0
194.7332	27.8334	0.0252	14.69920	14.06716	13.44553	16.2896	3
194.8555	27.9679	0.0257	16.25248	15.46052	14.85575	0.2170	0
194.8922	27.9468	0.0240	15.25769	14.42903	13.71631	3.0171	0
194.9080	27.9073	0.0267	15.44143	14.63132	13.95457	2.1395	0
194.8748	27.9564	0.0227	14.96188	14.10954	13.52506	2.8316	0
194.8866	27.9836	0.0194	15.00175	14.21154	13.56408	1.3949	0
194.9350	27.9125	0.0224	15.08558	14.28395	13.62290	1.1290	0
194.9422	27.8572	0.0270	15.73695	14.95616	14.33338	0.1523	0

Continued on next page

Table A.1 – continued from previous page

RA (J2000)	Dec (J2000)	z	g mag	r mag	z mag	24μm flux (mJy)	flag
194.9152	27.9539	0.0268	16.42066	15.58561	15.05022	0.6510	0
194.8988	27.9593	0.0239	13.26043	12.40858	11.82636	25.8840	0
194.8725	27.8501	0.0227	15.35503	14.53862	13.82677	3.0662	0
194.8784	27.8842	0.0157	15.06871	14.27393	13.58319	3.0573	0
194.8970	27.8636	0.0210	17.09708	16.36186	15.80202	0.2099	0
194.9861	27.9300	0.0257	16.07116	15.28813	14.64116	0.2283	0
195.1657	27.9239	0.0250	14.89413	14.09755	13.45031	0.5046	0
195.0262	27.7758	0.0206	15.71107	14.91861	14.26113	0.4637	0
195.0229	27.8076	0.0219	15.59987	14.81515	14.15590	0.7060	0
195.1355	27.7661	0.0223	16.36462	15.58434	14.95910	0.5382	0
195.0339	27.9769	0.0215	12.93777	12.07790	11.37875	6.2005	0
195.0381	27.8665	0.0177	15.89448	15.40541	14.97026	47.6964	2
195.1782	27.9713	0.0213	14.86372	14.02732	13.41474	4.8487	3
195.1785	27.9631	0.0281	15.65637	14.85555	14.30190	0.4164	0
195.1975	27.9222	0.0286	16.03495	15.26045	14.64232	1.0860	0
195.2336	27.7909	0.0267	13.68739	12.96331	12.48091	95.2491	3
195.3233	27.8091	0.0244	14.62144	13.81769	13.15253	1.4737	0
195.3589	27.8860	0.0183	13.81247	12.88702	12.88754	7.6067	3
195.3825	27.8475	0.0182	14.43348	13.58975	13.01080	0.6377	0
195.6328	27.9356	0.0221	16.78349	16.07216	15.49408	0.8777	0
195.4593	27.8936	0.0252	15.39442	14.59219	13.92830	1.4464	0
195.5006	27.7827	0.0239	15.43027	14.91210	14.48631	1.0138	0
195.7197	27.8666	0.0274	15.09485	14.31627	13.68465	0.8161	0
194.5233	28.2426	0.0240	14.30958	13.73345	13.30407	141.8147	2
194.6230	28.3012	0.0197	16.57898	15.93913	15.50143	2.1801	0
195.0747	28.2024	0.0285	13.96555	13.17093	12.52373	3.1112	0
194.5243	28.3710	0.0255	16.68273	16.06996	15.59586	0.6006	0
195.1282	28.3464	0.0199	14.49264	13.71028	13.06436	2.7597	0
195.1843	28.3373	0.0264	15.33792	14.59640	13.94859	0.7094	0
194.7575	28.2253	0.0268	14.92556	14.12497	13.41369	6.6399	3
194.6829	28.2827	0.0255	16.77540	16.08118	15.47446	0.0520	0
195.5429	28.1918	0.0191	16.29786	15.53170	15.02577	1.3116	0
195.5533	28.2148	0.0273	15.40340	15.01469	14.72994	21.9659	1
195.5897	28.2308	0.0186	15.13262	14.38511	13.76172	0.9486	0
195.5902	28.2560	0.0228	15.51392	14.71360	14.07477	3.4633	3
195.9581	28.1857	0.0233	13.53963	12.82170	12.23971	4.1427	0
196.0423	28.2479	0.0198	15.12529	14.32663	13.65586	2.3778	0

Table A.2: Catalogue of dwarf ($z > 15$), k+A (EW(Hα)< 2 Å & EW(Hδ)< -3 Å) galaxies in the Coma supercluster

RA (J2000)	Dec (J2000)	z	z mag	EW(Hα) Å	EW(Hδ) Å
177.2428	31.3049	0.0218	16.1572	0.2227	-4.7659
182.7488	31.9867	0.0222	16.6544	1.4347	-3.3410
182.3647	31.6434	0.0229	16.0288	0.5219	-3.5259
195.4972	28.7095	0.0203	16.8559	-1.9535	-20.5023
197.3014	28.4677	0.0256	17.3388	-2.2295	-28.4729
194.5285	29.0346	0.0243	15.9273	-2.3700	-4.0093
194.4403	29.1300	0.0251	17.1745	-3.0015	-4.7125
195.1982	29.0672	0.0251	16.6926	-2.9974	-4.0958
196.0426	29.0154	0.0220	15.1248	-1.5807	-3.0571
195.0447	29.4665	0.0230	17.2948	-1.7479	-3.6940
194.7338	28.4636	0.0198	15.1591	-2.6499	-5.6373
194.4338	29.0204	0.0265	15.7484	1.0245	-5.6618
196.5631	28.7123	0.0195	16.7749	-1.9496	-3.4598
190.2894	29.5387	0.0235	15.8032	-1.7191	-4.2396
194.1019	29.8049	0.0261	17.0757	-2.0568	-3.6341
194.5968	30.1430	0.0259	16.0933	-2.0399	-3.4398
174.6209	28.5871	0.0236	15.3615	1.8792	-3.9275

Continued on next page

Table A.2 – continued from previous page

RA (J2000)	Dec (J2000)	z	z mag	EW(Hα) Å	EW(Hδ) Å
192.4220	28.8448	0.0218	17.1838	-1.3320	-30.0913
192.8569	28.7203	0.0241	17.0417	-1.1904	-3.1975
184.9469	30.3540	0.0279	17.5233	-1.5275	-18.4185
193.9028	26.5644	0.0211	16.9923	-1.8170	-6.2012
194.5201	26.3706	0.0232	15.7774	-1.8387	-6.3831
195.0435	26.4612	0.0221	16.6272	-2.0973	-3.2747
189.0882	27.0333	0.0251	16.6488	-1.9006	-3.0789
194.0083	26.9208	0.0191	16.5278	-1.4534	-4.9134
194.8421	26.7971	0.0216	16.3322	-1.8160	-3.4187
194.5845	26.9206	0.0231	16.7371	-2.2506	-4.0615
194.3291	26.9376	0.0255	17.0953	-1.7735	-17.6970
195.3337	26.8867	0.0270	16.6565	-1.6988	-3.6881
193.8519	27.2805	0.0218	17.2508	-1.5588	-4.9116
195.0651	27.2567	0.0238	17.2064	-1.5646	-4.2207
195.1217	27.3332	0.0285	16.1242	-3.9583	-8.9234
177.0027	27.8295	0.0294	17.2770	1.8830	-5.1079
194.3261	27.7474	0.0229	16.2116	-3.1924	-4.0341
194.3317	27.6138	0.0259	16.4081	-2.3109	-3.7263
194.3242	27.8109	0.0239	15.0397	-1.9183	-3.7562
194.6775	27.7605	0.0292	16.4920	-2.0745	-8.0808
195.4189	27.5489	0.0218	17.2388	-1.0178	-4.1032
196.2638	27.5371	0.0217	16.0286	-1.6276	-3.9339
194.4050	28.0404	0.0214	16.2932	-1.5346	-18.8713
194.4011	28.2334	0.0227	16.5172	-1.5096	-4.3530
194.5822	28.0948	0.0240	17.3822	-2.4560	-14.7593
194.7913	28.1645	0.0287	16.9180	-1.8845	-3.3484
194.8817	28.1005	0.0249	17.0590	-2.1038	-16.2841
195.2736	28.0620	0.0249	16.9871	-1.9288	-3.5458
195.5597	28.1016	0.0198	15.5436	-1.8929	-3.0570
181.4093	27.3884	0.0260	16.2933	-0.0126	-3.0881
189.3277	26.5529	0.0223	17.2642	1.2530	-3.7039
194.2701	26.3025	0.0219	17.1058	-2.1523	-3.1414
194.4194	26.2053	0.0203	16.6462	-1.4743	-3.3308
188.9783	26.8187	0.0239	16.4599	-1.4958	-3.0209
191.8350	27.2468	0.0259	16.4833	-2.0984	-4.0560
193.7519	27.1938	0.0248	17.1631	-1.6498	-3.4329
194.3455	26.9878	0.0279	16.9238	-1.0602	-3.0967
195.0049	26.9561	0.0239	16.5168	-2.8617	-5.2764
194.7693	26.9582	0.0271	16.6031	-1.9618	-4.7561
195.2300	27.1216	0.0217	17.2178	-1.2565	-6.4533
192.4454	27.6407	0.0237	16.6023	-0.8859	-19.6060
193.7139	27.4945	0.0234	17.1928	-2.3049	-3.3775
194.6184	27.5594	0.0254	15.0494	0.1507	-4.4772
195.1218	27.5148	0.0248	15.2935	-2.9847	-7.9423
195.6466	27.4394	0.0181	15.5251	-2.2929	-3.4347
193.9990	27.9551	0.0271	15.4055	-1.7715	-3.5246
194.4388	27.9060	0.0272	17.2064	0.2690	-5.1346
194.5759	27.8485	0.0255	16.7560	-2.3638	-6.7499
194.6590	27.8226	0.0181	17.1756	-2.5596	-6.4691
194.6503	27.8729	0.0238	17.1200	-1.4219	-6.6766
195.0431	27.9591	0.0211	17.2378	-1.3996	-3.1626
195.0237	27.9265	0.0265	17.5079	-2.8396	-5.2153
195.2188	27.8050	0.0228	17.2281	-1.0408	-21.8067
195.0336	27.7733	0.0291	16.7548	-2.7428	-5.7567
195.1434	27.9347	0.0293	16.7987	-1.4564	-11.4004
195.3910	27.9111	0.0218	16.7305	-1.5997	-4.3740
184.6648	28.7379	0.0244	16.7971	0.4404	-3.4990
194.2773	28.2966	0.0225	16.3383	-0.9956	-23.9825
194.6345	28.3780	0.0199	17.2156	-2.4019	-8.3938
194.8124	28.2510	0.0250	16.2288	-3.3317	-7.7611
194.7232	28.2890	0.0262	16.6274	-1.1677	-3.4578
195.8904	28.2394	0.0275	16.5538	-1.8815	-3.8909

Continued on next page

Table A.2 – continued from previous page

RA (J2000)	Dec (J2000)	z	z mag	EW(Hα) Å	EW(Hδ) Å
195.9602	28.1786	0.0213	16.5434	-1.4389	-3.0689
183.7986	23.9856	0.0236	17.5737	-0.4491	-11.8214
175.2078	21.1617	0.0215	16.6653	0.3180	-3.6103
177.8146	21.7783	0.0262	17.2836	1.9790	-16.9142
178.9917	22.6390	0.0219	16.3417	1.5887	-4.0393
199.9460	22.9811	0.0229	17.0785	-2.3896	-3.4854
175.8773	21.4125	0.0230	16.4789	-1.6002	-3.1014
178.2979	23.4103	0.0240	18.2052	-0.4672	-8.1233
180.6513	23.7831	0.0220	17.1961	-1.6950	-5.8163
170.5020	24.0794	0.0280	17.1569	-1.9613	-6.5907
182.0746	25.5937	0.0223	16.3284	-0.5176	-7.2917
187.7478	25.5618	0.0223	15.0069	-0.6586	-16.2399
175.7164	19.9492	0.0195	16.1078	1.7614	-6.1743
175.8159	20.1951	0.0184	17.0474	-1.0149	-3.9421
175.9490	20.3633	0.0225	15.1049	-2.2800	-6.9285
180.9449	20.5111	0.0247	17.1795	-1.7672	-3.6389
177.5397	18.5089	0.0214	17.9746	-0.9310	-7.9179
192.0635	17.7740	0.0206	15.1408	-2.0766	-5.3952
170.4149	18.4849	0.0185	17.0916	-1.6648	-23.4080
177.0765	18.9379	0.0198	16.7157	-1.4219	-23.9976
175.9861	19.6706	0.0220	17.0041	-2.5407	-3.7697
176.2576	19.7637	0.0275	16.1546	-1.8242	-4.6518
176.4929	19.6498	0.0214	16.0301	-3.1085	-5.1961
180.5077	20.2651	0.0227	15.6367	1.5226	-3.1669
180.9543	20.2023	0.0226	15.7898	-1.3539	-3.6284
176.0950	20.4094	0.0246	17.1032	-1.3121	-3.0118
176.5801	20.6404	0.0219	16.4091	-18.0133	-3.5510
176.4010	20.9896	0.0233	17.5688	-0.8533	-3.6643
176.5630	21.0241	0.0224	17.6586	-0.4119	-5.8503
177.9206	20.9589	0.0236	16.4579	1.9720	-4.2062
177.5828	20.9525	0.0259	16.8810	1.9607	-4.0131

Table A.3: Abell clusters with starburst galaxies on outskirts (the SB clusters)

Abell	RA (J2000)	Dec (J2000)	Richness	z	σ_v (kms^{-1})
152	01 09 50.0	+13 58 45	0	0.0581	756
175	01 19 33.0	+14 52 29	2	0.1288	705
628	08 10 09.5	+35 12 28	0	0.0838	741
646	08 22 12.0	+47 05 44	0	0.1303	849
655	08 25 23.1	+47 06 32	3	0.1267	858
714	08 54 50.2	+41 54 00	1	0.1397	609
724	08 58 20.4	+38 33 48	1	0.0934	492
856	09 45 30.1	+56 32 43	0	0.1393	450[2]
874	09 50 43.8	+58 01 29	1	0.1480	1551
941	10 09 42.7	+03 40 56	1	0.1049	195
971	10 19 49.6	+40 57 34	1	0.0929	873
975	10 22 47.3	+64 37 29	2	0.1182	273
1004	10 25 36.5	+51 03 23	1	0.1414	963
1021	10 28 45.2	+37 39 21	1	0.1114	828
1076	10 45 09.5	+58 09 55	1	0.1164	507
1132	10 58 25.5	+56 47 41	1	0.1363	792
1190	11 11 49.2	+40 50 30	2	0.0752	693
1227	11 21 38.4	+48 02 22	2	0.1120	813
1238	11 22 58.6	+01 06 21	1	0.0733	552
1341	11 40 35.8	+10 23 18	1	0.1050	834
1342	11 40 41.8	+10 04 18	1	0.1061	390
1346	11 41 10.9	+ 5 41 18	1	0.0976	711
1354	11 42 11.7	+10 09 14	1	0.1178	456
1373	11 45 27.8	-02 24 40	2	0.1314	627

Continued on next page

Table A.3 – continued from previous page

Abell	RA (J2000)	Dec (J2000)	Richness	z	σ_v (kms^{-1})
1377	11 47 02.4	+55 44 16	1	0.0511	684
1424	11 57 34.1	+05 02 14	1	0.0774	699
1446	12 01 55.9	+58 01 14	2	0.1031	747
1496	12 13 26.2	+59 16 19	1	0.0937	396
1518	12 19 03.9	+63 30 24	0	0.1080	783
1534	12 24 07.5	+61 30 26	0	0.0698	321
1544	12 27 46.3	+63 25 25	1	0.1454	597
1713	13 19 11.8	+58 05 22	1	0.1406	1095
1738	13 25 09.7	+57 36 35	2	0.1155	597
1750	13 30 52.4	-01 51 06	0	0.0855	795
1896	14 18 40.9	+37 48 27	0	0.1329	534
1999	14 54 05.6	+54 20 05	1	0.0994	333
2026	15 08 33.8	-00 15 51	1	0.0875	753[2]
2051	15 16 46.4	-00 56 28	2	0.1155	600
2053	15 17 15.8	-00 40 23	1	0.1127	831
2142	15 58 16.3	+27 13 53	2	0.0894	942
2149	16 01 37.9	+53 52 57	0	0.1068	723
2183	16 21 31.6	+42 43 20	1	0.1366	495
2197	16 28 10.3	+40 54 47	1	0.0301	564
2199	16 28 36.8	+39 31 48	2	0.0299	759
2244	17 02 44.2	+34 04 13	2	0.0970	1164
2255	17 12 30.5	+64 05 33	2	0.0809	1116

Table A.4: Abell clusters without starburst galaxies on outskirts (the CN clusters)

Abell	RA (J2000)	Dec (J2000)	Richness	z	σ_v (kms^{-1})
190	01 23 41.9	-09 51 30	0	0.1015	354
612	08 01 04.0	+34 48 02	1	0.0774	186
667	08 28 06.0	+44 42 23	0	0.1450	792
671	08 28 31.0	+30 24 26	0	0.0503	801
690	08 39 16.0	+28 49 50	1	0.0788	516
695	08 41 26.1	+32 16 40	1	0.0687	375
775	09 16 21.2	+05 52 02	1	0.1340	975
819	09 32 17.9	+09 39 18	0	0.0764	561
858	09 43 26.6	+05 52 52	0	0.0881	918
990	10 23 33.8	+49 09 30	1	0.1440	1041
1024	10 28 18.5	+03 45 21	1	0.0743	690
1038	10 32 59.4	+02 15 17	1	0.1246	297
1064	10 38 46.9	+01 16 04	1	0.1320	594
1068	10 40 50.2	+39 57 01	1	0.1386	1317
1080	10 43 58.8	+01 05 00	0	0.1205	432
1139	10 58 04.9	+01 30 45	0	0.0395	249
1169	11 08 10.0	+43 56 34	1	0.0587	591
1171	11 07 29.2	+02 56 31	0	0.0757	159[2]
1173	11 09 14.4	+41 34 33	1	0.0759	570
1205	11 13 23.0	+02 30 29	1	0.0759	810
1225	11 21 24.5	+53 46 22	0	0.1040	732
1270	11 29 33.3	+54 04 20	0	0.0686	600
1302	11 33 30.4	+66 25 18	2	0.1160	834
1318	11 36 30.6	+54 58 16	1	0.0564	366
1361	11 43 48.3	+46 21 17	1	0.1167	453
1364	11 43 39.8	-01 46 36	1	0.1063	558
1368	11 45 01.7	+51 15 13	1	0.1291	762
1372	11 45 29.3	+11 31 13	1	0.1126	435
1383	11 48 13.5	+54 37 12	1	0.0600	426
1385	11 48 05.5	+11 33 16	1	0.0831	531

Continued on next page

[2]Popesso et al. (2007)

Table A.4 – continued from previous page

Abell	RA (J2000)	Dec (J2000)	Richness	z	σ_v (kms^{-1})
1387	11 48 54.1	+51 37 12	1	0.1320	753
1390	11 49 35.1	+12 15 15	0	0.0829	342
1402	11 52 37.4	+60 25 15	0	0.1058	219
1452	12 03 42.6	+51 44 14	0	0.0628	513[3]
1552	12 29 50.6	+11 44 29	1	0.0859	711
1559	12 33 10.0	+67 07 31	1	0.1066	693
1564	12 34 57.3	+01 51 32	0	0.0792	687
1566	12 35 05.1	+64 23 32	2	0.1000	561
1577	12 37 52.0	-00 16 22	1	0.1405	366
1621	12 48 45.9	+62 41 46	1	0.1029	534
1630	12 51 44.8	+04 34 49	1	0.0648	426
1637	12 53 59.3	+50 49 51	1	0.1270	564
1646	12 55 48.6	+62 09 53	0	0.1063	468
1650	12 58 46.1	-01 45 57	2	0.0845	513
1663	13 02 46.4	-02 31 49	1	0.0847	891
1764	13 34 43.2	+59 55 51	0	0.1167	585
1773	13 42 08.5	+02 15 07	1	0.0766	1098
1780	13 44 38.1	+02 53 12	1	0.0786	426
1882	14 14 39.8	-00 20 33	3	0.1367	612
1885	14 13 47.6	+43 40 15	1	0.0890	1038
1918	14 25 09.2	+63 09 41	3	0.1394	1008
1920	14 27 17.5	+55 46 46	2	0.1310	570
1936	14 34 28.8	+54 50 05	1	0.1386	498
2018	15 01 12.8	+47 16 26	1	0.0872	1029
2046	15 12 41.4	+34 51 09	1	0.1489	948
2062	15 21 19.8	+32 05 38	1	0.1155	537
2110	15 39 43.5	+30 42 45	1	0.0980	654
2175	16 20 23.1	+29 55 18	1	0.0972	876
2196	16 27 21.6	+41 29 43	0	0.1332	687
2211	16 34 04.0	+40 57 09	1	0.1355	537
2245	17 02 45.0	+33 33 13	1	0.0852	984

Table A.5: *Galex* data for SFRS galaxies

Galaxy	IRAS Id	RA(J2000)	Dec(J2000)	Dist (Mpc)	FUV[5]	NUV[5]	A(FUV)[5]	A(NUV)[5]	E($B-V$)[5]
IC486	Q07572+2645	120.0874	26.6135	114.37	18.175	17.618	3.762	2.563	0.040
IC2217	Q07577+2738	120.2072	27.5005	76.07	16.430	15.983	3.212	2.143	0.041
NGC2500	O07581+5052	120.4716	50.7371	15.00	13.921	13.829	1.463	0.836	0.040
MCG6-18-009	Q08002+3336	120.8706	33.4624	164.35	17.886	17.108	4.073	2.670	0.052
NGC2532	Q08070+3406	122.5632	33.9566	77.58	15.413	14.906	2.883	1.803	0.054
UGC4261	Q08076+3658	122.7342	36.8282	93.18	16.481	16.203	2.503	1.624	0.055
NGC2535	Q08082+2521	122.8045	25.2043	61.56	15.704	15.334	2.650	1.692	0.043
NGC2543	Q08096+3624	123.2413	36.2546	26.30	15.982	15.560	3.002	1.971	0.069
NGC2537	O08097+4608	123.3114	45.9894	15.00	14.960	14.796	2.237	1.463	0.054
IC2233	O08104+4553	123.4951	45.7455	13.70	14.996	14.849	1.309	0.681	0.052
IC2239	Q08111+2401	123.5283	23.8664	88.51	19.173	18.085	5.822	4.040	0.053
UGC4286	Q08112+1835	123.5457	18.4393	75.11	17.368	16.989	3.079	2.073	0.047
UGC4306	Q08143+3536	124.4025	35.4474	36.00	18.675	18.175	5.575	4.339	0.069
NGC2552	O08156+5009	124.8316	50.0058	11.40	14.732	14.631	0.998	0.458	0.047
IC2339	Q08206+2130	125.8925	21.3476	79.28	17.096	16.746	3.363	2.357	0.047
IRAS08234+1054	Q08234+1054	126.5329	10.7476	272.62	19.649	19.005	5.767	4.394	0.050
IRAS08269+1514	Q08269+1514	127.4383	15.0776	134.48	20.732	19.802	6.189	4.537	0.033
NGC2604	Q08303+2942	128.3464	29.5388	36.30	15.004	14.550	1.652	0.794	0.041
NGC2608	Q08322+2838	128.8211	28.4752	36.30	16.000	15.458	2.918	1.808	0.039

Continued on next page

[3] Struble & Rood (1999)

[5] AB magnitude

Table A.5 – continued from previous page

Galaxy	IRAS Id	RA(J2000)	Dec(J2000)	Dist (Mpc)	FUV	NUV	A(FUV)	A(NUV)	E($B-V$)
NGC2623	Q08354+2555	129.6000	25.7545	81.57	17.508	16.905	6.261	4.912	0.041
CGCG120-018	Q08368+2319	129.9615	23.1434	107.88	20.645	19.441	7.229	5.289	0.034
Q08512+2727	Q08512+2727	133.5699	27.2665	265.30	18.409	17.849	3.835	2.628	0.034
Q08519+2017	Q08519+2017	133.7036	20.1085	1258.85	19.096	18.326	4.329	2.913	0.028
IRAS08538+4256	Q08538+4256	134.2930	42.7564	121.16	19.894	18.705	6.891	4.975	0.024
IRAS08550+3908	Q08550+3908	134.5573	38.9422	367.76	19.939	19.659	5.513	4.482	0.029
NGC2718	Q08561+0629	134.7103	6.2930	57.38	15.768	15.342	3.065	2.025	0.071
NGC2712	O08561+4506	134.8770	44.9139	30.90	15.368	15.089	2.352	1.489	0.020
NGC2719	Q08571+3555	135.0655	35.7276	51.09	16.231	15.803	2.689	1.686	0.033
IRAS08572+3915NW	Q08572+3915	135.1057	39.0649	244.31	20.649	20.256	7.906	6.730	0.027
IRAS08579+3447	Q08579+3447	135.2741	34.5913	273.54	19.023	18.304	5.606	4.169	0.028
NGC2731	Q08594+0829	135.5350	8.3017	35.00	16.617	16.143	3.525	2.409	0.065
NGC2730	Q08594+1702	135.5659	16.8383	58.93	15.749	15.434	1.854	1.038	0.027
IC2431	Q09018+1447	136.1433	14.5943	208.97	18.783	18.217	5.855	4.552	0.050
NGC2750	Q09028+2538	136.4497	25.4375	37.00	14.989	14.681	2.467	1.572	0.036
IC2434	Q09041+3725	136.8169	37.2154	104.51	17.586	17.085	3.869	2.707	0.020
NGC2761	Q09047+1838	136.8785	18.4348	125.03	18.749	17.896	5.761	4.195	0.036
NGC2773	Q09070+0722	137.4340	7.1738	80.41	18.349	17.690	5.023	3.663	0.048
NGC2776	O09089+4509	138.0605	44.9548	36.00	14.516	14.133	2.120	1.221	0.014
NGC2789	Q09120+2956	138.7486	29.7302	93.60	18.277	17.262	4.813	3.156	0.026
NGC2824	Q09121+3908	138.8423	38.9431	42.50	19.232	17.994	4.854	3.005	0.032
IRAS09184+4356	Q09184+4356	140.4114	43.7261	170.06	20.277	19.608	6.124	4.717	0.015
CGCG238-041	Q09190+4727	140.6054	47.2444	131.47	18.118	17.671	3.579	2.480	0.015
UGC4985	Q09197+2210	140.6558	21.9574	143.36	19.731	19.486	5.272	4.277	0.036
NGC2854	Q09206+4925	141.0118	49.2038	25.00	16.738	16.254	3.178	2.084	0.018
UGC5046	Q09253+1724	142.0277	17.1965	64.88	17.858	17.064	4.592	3.139	0.034
UGC5055	Q09266+5604	142.5490	55.8524	110.59	16.564	16.156	2.919	1.905	0.034
NGC2893	Q09273+2945	142.5707	29.5400	24.00	16.225	15.718	2.980	1.889	0.023
MCG3-24-062	Q09275+1941	142.5958	19.4692	66.25	18.400	18.174	4.440	3.485	0.045
CGCG238-066	Q09277+4917	142.7782	49.0798	147.04	19.004	18.325	5.021	3.644	0.012
UGC5097	Q09316+0027	143.5443	0.2422	72.46	16.206	15.885	3.101	2.137	0.039
CGCG289-012	Q09328+5937	144.1328	59.3984	172.45	17.390	16.992	3.606	2.545	0.020
MCG8-18-013	Q09333+4841	144.1549	48.4744	110.93	18.167	17.616	5.489	4.209	0.024
CGCG181-068	Q09343+3402	144.3301	33.8238	100.61	20.202	19.440	6.068	4.576	0.014
NGC2936	Q09351+0259	144.4339	2.7608	100.47	16.651	16.254	3.348	2.306	0.034
NGC2955	Q09382+3606	145.3192	35.8823	103.50	16.391	15.897	2.955	1.876	0.011
CGCG182-010	Q09422+3456	146.3134	34.7123	175.05	18.723	18.146	4.964	3.679	0.012
UGC5228	Q09434+0153	146.5150	1.6684	28.20	16.933	16.484	3.318	2.239	0.164
NGC3015	Q09468+0122	147.3455	1.1454	108.78	17.954	17.276	4.417	3.074	0.084
MCG2-25-039	Q09469+0914	147.4041	9.0052	77.56	18.046	17.512	4.163	2.956	0.031
NGC3020	O09474+1302	147.5277	12.8136	18.30	14.488	14.244	1.532	0.810	0.038
NGC3049	Q09521+0930	148.7065	9.2711	18.30	15.473	15.166	2.461	1.567	0.038
NGC3055	Q09526+0430	148.8253	4.2700	25.00	15.199	14.788	2.681	1.691	0.052
IC2520	Q09534+2727	149.0838	27.2276	26.40	16.492	16.215	3.570	2.609	0.021
UGC5403	Q09598+1925	150.6481	19.1769	33.00	18.114	17.546	4.696	3.431	0.031
UGC5459	O10049+5319	152.0420	53.0837	25.80	15.525	14.552	2.445	1.125	0.007
MCG5-24-022	Q10071+3219	152.5141	32.0702	92.06	19.484	18.247	5.166	3.293	0.022
IC2551	Q10078+2439	152.6680	24.4142	94.91	17.986	17.048	4.805	3.214	0.036
Q10106+2745	Q10106+2745	153.3729	27.5111	215.63	21.132	19.996	6.559	4.702	0.054
NGC3162	O10107+2259	153.3816	22.7376	26.40	14.475	14.173	1.896	1.081	0.023
Q10120+1653	Q10120+1653	153.6996	16.6472	517.20	23.084	21.851	8.408	6.419	0.036
NGC3190	O10153+2205	154.5236	21.8323	26.40	17.504	16.321	4.626	2.843	0.025
IC602	Q10157+0717	154.5822	7.0493	57.61	15.488	15.228	2.590	1.716	0.026
NGC3191	Q10160+4642	154.7714	46.4541	134.03	16.239	15.878	2.785	1.819	0.012
NGC3206	O10185+5710	155.4483	56.9304	25.80	14.387	14.142	1.093	0.466	0.014
UGC5613	Q10203+5235	155.8856	52.3420	139.78	17.581	16.649	4.732	3.152	0.014
UGC5644	R10231+1358	156.4427	13.7169	137.59	17.324	16.933	2.792	1.804	0.042
NGC3245	O10244+2845	156.8267	28.5074	20.90	17.741	16.387	4.059	2.204	0.025
MCG7-22-012	Q10272+4336	157.5476	43.3606	65.98	18.823	18.174	4.934	3.587	0.011
Q10276+1119	Q10276+1119	157.5615	11.0711	271.28	18.170	17.949	3.965	3.031	0.033
NGC3265	Q10282+2903	157.7782	28.7967	21.80	17.269	16.828	3.736	2.631	0.024
UGC5713	Q10288+2614	157.9121	25.9839	95.02	18.371	18.053	3.786	2.779	0.019
NGC3274	Q10294+2755	158.0718	27.6688	10.00	14.683	14.523	1.203	0.590	0.024

Continued on next page

Table A.5 – continued from previous page

Galaxy	IRAS Id	RA(J2000)	Dec(J2000)	Dist (Mpc)	FUV	NUV	A(FUV)	A(NUV)	E($B-V$)
UGC5720	Q10293+5439	158.1328	54.4010	20.00	15.067	14.875	2.528	1.707	0.012
NGC3306	Q10345+1254	159.2926	12.6526	46.60	16.444	16.117	3.342	2.355	0.025
NGC3323	Q10368+2535	159.9126	25.3227	79.45	16.077	15.721	2.543	1.607	0.024
IC2598	Q10369+2659	159.9266	26.7274	89.09	18.404	17.663	5.170	3.732	0.029
NGC3338	O10394+1400	160.5314	13.7470	21.40	14.296	13.891	2.010	1.114	0.031
NGC3353	Q10422+5613	161.3419	55.9611	16.00	14.864	14.711	2.467	1.679	0.007
UGC5881	P10439+2611	161.6772	25.9315	92.99	18.491	17.732	4.566	3.144	0.030
NGC3370	O10443+1732	161.7669	17.2736	20.90	14.841	14.485	2.361	1.446	0.031
NGC3381	Q10456+3458	162.1034	34.7114	25.70	15.112	14.772	1.872	1.038	0.020
UGC5941	Q10474+4143	162.5900	41.4640	106.97	19.105	17.962	5.619	3.798	0.012
NGC3413	Q10485+3301	162.8364	32.7664	16.20	15.489	15.153	1.761	0.948	0.023
NGC3430	Q10501+1715	163.0475	32.9504	28.41	20.142	19.405	6.965	5.475	0.024
NGC3408	Q10490+5842	163.0487	58.4381	138.03	16.985	16.492	2.736	1.682	0.012
CGCG95-055	Q10494+3312	163.2114	16.9854	25.70	14.598	14.212	1.422	0.649	0.031
IRAS10565+2448W	Q10565+2448	164.8255	24.5430	185.24	******	19.019	*****	6.214	0.015
UGC6074	Q10570+5110	164.9927	50.9030	38.00	18.285	17.485	5.045	3.560	0.015
NGC3495	O10586+0353	165.3176	3.6280	17.50	15.287	14.770	2.682	1.618	0.046
UGC6103	Q10591+4529	165.4958	45.2280	91.72	16.204	15.720	2.972	1.899	0.009
MCG7-23-019	Q11010+4107	165.9763	40.8500	150.56	17.340	16.964	4.829	3.728	0.009
UGC6135	Q11017+4523	166.1540	45.1252	90.88	16.547	15.985	3.165	2.014	0.008
CGCG241-078	Q11037+4618	166.6557	46.0388	110.94	20.436	19.227	6.732	4.801	0.009
IRAS11069+2711	Q11069+2711	167.4140	26.9150	296.38	19.300	19.285	5.649	4.864	0.021
IC676	Q11100+0919	168.1659	9.0558	26.90	17.792	16.883	4.515	2.970	0.025
IRAS11102+3026	Q11102+3026	168.2390	30.1746	129.61	22.423	20.939	8.695	6.462	0.021
IC2637	Q11112+0951	168.4573	9.5863	128.22	17.405	16.739	3.784	2.496	0.022
MCG9-19-013	Q11120+5035	168.7057	50.3229	201.77	19.954	19.309	5.542	4.174	0.016
7ZW384	Q11139+5948	169.2267	59.5308	340.35	18.645	18.048	4.317	3.048	0.008
IRAS11167+5351	Q11167+5351	169.8917	53.5885	447.29	20.353	20.047	6.161	5.095	0.014
NGC3633	Q11178+0351	170.1092	3.5856	30.00	18.615	17.823	5.319	3.828	0.062
NGC3656	Q11208+5406	170.9110	53.8421	37.00	17.268	16.531	3.966	2.606	0.015
NGC3664	Q11218+0336	171.1011	3.3253	26.90	14.681	14.485	1.164	0.543	0.045
NGC3666	Q11218+1137	171.1086	11.3422	16.30	15.528	15.064	2.803	1.762	0.033
IC691	Q11238+5925	171.6846	59.1554	16.00	16.556	16.295	3.532	2.585	0.014
NGC3686	O11251+1729	171.9332	17.2242	21.00	14.428	13.934	2.146	1.174	0.024
UGC6469	Q11257+0255	172.0738	2.6540	102.57	16.330	15.953	2.741	1.768	0.037
NGC3690	Q11257+5850	172.1313	58.5643	52.56	15.992	15.555	6.306	5.113	0.017
IC698	Q11264+0923	172.2660	9.1121	96.84	18.441	17.465	5.399	3.739	0.043
Q11267+1558	Q11267+1558	172.3529	15.6948	736.56	22.042	21.709	7.375	6.265	0.045
NGC3705	O11275+0933	172.5293	9.2780	16.30	15.005	14.561	2.573	1.573	0.046
MCG3-29-061	Q11284+2030	172.7654	20.2356	67.49	18.781	18.098	5.276	3.884	0.022
NGC3720	Q11297+0104	173.0900	0.8040	89.77	23.126	21.904	9.627	7.637	0.029
NGC3729	O11310+5324	173.4555	53.1255	17.10	15.622	15.112	2.804	1.731	0.011
NGC3758	Q11338+2152	174.1206	21.5963	131.56	17.696	16.878	3.732	2.330	0.025
UGC6583	Q11342+2015	174.2265	19.9717	93.24	16.847	16.335	3.415	2.279	0.026
NGC3769	O11350+4810	174.4338	47.8931	17.10	15.159	14.796	2.353	1.435	0.023
NGC3773	Q11356+1223	174.5544	12.1123	16.30	15.236	15.007	1.749	1.000	0.027
NGC3781	R11364+2638	174.7657	26.3617	103.45	20.370	18.808	7.805	5.510	0.026
UGC6625	Q11371+2012	174.9481	19.9334	158.17	16.256	15.822	2.604	1.607	0.026
NGC3808	Q11381+2243	175.1860	22.4469	107.21	18.372	17.688	5.091	3.707	0.026
NGC3822	Q11395+1033	175.5455	10.2809	94.58	17.911	16.958	4.807	3.203	0.056
UGC6665	Q11396+0036	175.5509	0.3345	85.00	15.731	15.366	2.877	1.899	0.025
MCG3-30-051	Q11398+2023	175.6021	20.1193	90.38	17.570	17.217	3.957	2.913	0.020
UGC6732	Q11428+5915	176.3881	58.9781	53.57	19.411	17.523	5.199	2.775	0.020
IC730	Q11430+0330	176.3969	3.2318	93.06	18.774	18.083	5.544	4.135	0.021
NGC3912	Q11474+2645	177.5186	26.4792	22.50	16.282	15.665	3.376	2.163	0.021
NGC3928	Q11491+4857	177.9484	48.6831	16.90	15.654	15.264	2.674	1.699	0.020
NGC3934	Q11496+1707	178.0527	16.8519	61.61	19.684	18.789	5.983	4.371	0.055
UGC6865	R11510+4344	178.4165	43.4609	91.19	18.338	17.384	4.868	3.260	0.020
UGC6901	Q11530+4319	178.9098	43.0459	107.59	18.680	17.500	5.130	3.308	0.015
CGCG013-010	Q11545+0124	179.2747	1.1256	172.34	19.814	18.690	6.665	4.817	0.016
NGC3991	Q11549+3237	179.3790	32.3370	55.59	14.577	14.493	1.812	1.140	0.022
NGC4004	Q11555+2809	179.5218	27.8789	57.94	15.809	15.498	3.027	2.076	0.025
NGC4014	Q11560+1627	179.6493	16.1772	62.61	17.125	16.492	3.916	2.643	0.065

Continued on next page

Table A.5 – continued from previous page

Galaxy	IRAS Id	RA(J2000)	Dec(J2000)	Dist (Mpc)	FUV	NUV	A(FUV)	A(NUV)	E($B-V$)
NGC4010	O11560+4732	179.6579	47.2615	17.10	16.138	15.652	3.081	1.995	0.025
NGC4018	Q11561+2535	179.6699	25.3164	72.64	18.071	17.334	4.793	3.377	0.021
NGC4020	Q11563+3041	179.7362	30.4119	14.30	15.454	15.166	1.789	0.998	0.017
Q11571+3003	Q11571+3003	179.9275	29.7868	218.64	21.132	20.301	6.509	4.940	0.018
UGC7017	Q11598+3008	180.5938	29.8618	55.25	16.727	16.431	3.866	2.873	0.019
UGC7016	Q11598+1507	180.5999	14.8436	110.30	18.978	17.950	5.047	3.363	0.038
MCG3-31-030	Q12010+1620	180.8998	16.0555	13.11	16.816	16.450	2.529	1.588	0.030
NGC4062	O12015+3210	181.0160	31.8958	16.30	14.933	14.404	2.389	1.357	0.025
NGC4064	O12016+1843	181.0475	18.4407	8.47	17.030	15.933	4.020	2.368	0.021
CGCG098-059	Q12045+1716	181.7898	16.9956	102.29	19.222	18.064	6.101	4.242	0.049
NGC4116	Q12050+0258	181.9034	2.6923	16.00	14.274	14.112	1.539	0.861	0.022
NGC4136	O12067+3012	182.3238	29.9276	16.30	14.045	13.785	1.419	0.711	0.018
NGC4150	Q12080+3040	182.6403	30.4016	13.70	17.722	16.370	3.682	1.884	0.018
Q12086+1441	Q12086+1441	182.8099	14.4098	13.11	21.096	20.551	6.689	5.387	0.036
NGC4162	Q12093+2423	182.9710	24.1185	42.50	15.545	14.982	2.628	1.540	0.035
NGC4178	O12102+1108	183.1955	10.8691	16.80	14.111	13.778	1.904	1.069	0.028
NGC4189	Q12112+1342	183.4469	13.4248	16.80	15.321	14.842	2.694	1.655	0.033
NGC4204	O12127+2056	183.8102	20.6586	10.00	15.184	14.990	1.559	0.861	0.034
NGC4207	Q12129+0951	183.8771	9.5849	16.80	17.280	16.648	4.240	2.946	0.017
UGC7286	Q12134+2743	183.9969	27.4422	115.44	19.077	18.228	4.531	3.036	0.020
NGC4234	Q12146+0357	184.2899	3.6848	30.00	15.422	15.055	2.155	1.261	0.018
NGC4237	Q12146+1536	184.2976	15.3240	16.80	16.245	15.360	3.410	1.992	0.030
NGC4244	O12149+3805	184.3727	37.8074	4.29	13.041	12.590	0.640	0.086	0.021
NGC4253	Q12159+3005	184.6105	29.8129	64.88	17.585	16.883	4.478	3.110	0.020
MCG3-32-005	Q12182+1717	185.1968	17.0161	13.11	18.594	17.764	5.246	3.723	0.028
NGC4290	Q12183+5822	185.1980	58.0925	37.00	15.855	15.390	3.192	2.111	0.014
NGC4294	O12187+1147	185.3242	11.5075	16.80	14.540	14.209	1.863	1.035	0.034
NGC4314	O12200+3010	185.6334	29.8955	16.30	15.844	14.995	3.046	1.703	0.025
NGC4385	Q12231+0050	186.4283	0.5726	29.00	15.570	15.257	2.940	1.995	0.025
NGC4396	Q12234+1556	186.4965	15.6710	16.80	15.133	14.834	1.840	1.036	0.026
NGC4412	Q12240+0414	186.6503	3.9647	30.60	15.363	15.015	2.531	1.602	0.018
NGC4420	Q12244+0246	186.7437	2.4943	17.60	15.001	14.528	2.280	1.300	0.018
NGC4424	O12246+0941	186.7984	9.4207	6.00	16.292	15.462	3.231	1.876	0.021
NGC4435	O12251+1321	186.9186	13.0790	16.70	18.511	16.807	4.605	2.405	0.030
NGC4438	O12252+1317	186.9401	13.0088	16.80	15.840	15.285	3.239	2.087	0.028
NGC4448	Q12257+2853	187.0644	28.6203	16.30	16.306	15.629	2.929	1.722	0.024
3C273	Q12265+0219	187.2779	2.0524	657.77	13.809	13.771	1.116	0.579	0.021
NGC4470	Q12270+0806	187.4074	7.8242	16.80	15.234	14.912	2.117	1.257	0.024
NGC4491	Q12284+1145	187.7380	11.4835	16.80	17.592	16.947	4.120	2.823	0.042
NGC4500	Q12290+5814	187.8423	57.9646	52.00	******	15.281	*****	1.958	0.012
NGC4495	Q12289+2924	187.8454	29.1365	74.23	17.240	16.690	4.196	2.974	0.021
IC3476	Q12301+1419	188.1745	14.0504	16.80	15.073	14.541	1.731	0.815	0.036
NGC4509	Q12306+3222	188.2780	32.0929	11.07	15.408	15.282	1.545	0.887	0.012
NGC4519	O12309+0855	188.3761	8.6547	16.80	14.305	13.999	1.889	1.072	0.020
NGC4548	O12329+1446	188.8602	14.4963	16.20	14.969	14.506	2.452	1.455	0.038
IRAS12337+5044	Q12337+5044	189.0279	50.4719	172.48	18.226	17.737	4.285	3.110	0.012
NGC4592	Q12367-0015	189.8281	-0.5319	11.10	14.173	13.884	1.468	0.736	0.022
NGC4607	Q12386+1209	190.3009	11.8866	16.80	17.939	17.246	4.815	3.436	0.032
NGC4625	Q12395+4132	190.4697	41.2740	9.20	15.279	15.030	1.926	1.138	0.018
NGC4630	Q12399+0414	190.6297	3.9602	15.60	15.489	15.167	2.507	1.598	0.030
MCG5-30-069	Q12422+2641	191.1719	26.4196	74.03	20.273	18.866	6.882	4.761	0.015
IC3721	Q12423+1901	191.2213	18.7553	98.54	17.719	17.058	4.156	2.844	0.019
NGC4670	Q12428+2724	191.3219	27.1256	14.30	14.309	14.159	1.552	0.879	0.015
MCG7-26-051	Q12445+4232	191.7368	42.2664	146.88	19.700	18.933	6.390	4.884	0.022
NGC4688	O12452+0436	191.9438	4.3360	15.60	14.736	14.669	1.268	0.688	0.031
NGC4704	Q12464+4211	192.1935	41.9212	122.79	16.975	16.599	3.206	2.191	0.017
Q12468+3436	Q12468+3436	192.3215	34.3286	498.26	24.886	22.842	*****	7.459	0.014
MCG8-23-097	Q12483+4812	192.6660	47.9334	131.18	19.744	18.910	6.893	5.313	0.013
NGC4747	O12493+2602	192.9400	25.7750	14.30	16.440	16.223	3.110	2.224	0.010
UGC8017	Q12504+2838	193.2233	28.3713	107.07	17.544	17.131	4.077	2.976	0.010
NGC4765	Q12507+0444	193.3107	4.4633	15.60	15.195	14.820	2.144	1.247	0.040
VCC2096	Q12508+1158	193.3533	11.7101	13.11	18.507	17.872	4.412	3.106	0.051
UGC8041	O12526+0023	193.8027	0.1167	23.00	14.958	14.680	1.476	0.748	0.022

Continued on next page

Table A.5 – continued from previous page

Galaxy	IRAS Id	RA(J2000)	Dec(J2000)	Dist (Mpc)	FUV	NUV	A(FUV)	A(NUV)	E($B-V$)
NGC4837	Q12545+4834	194.2013	48.2969	132.52	16.654	16.248	3.220	2.181	0.014
UM530	R12555+0207	194.5348	1.8623	282.67	18.847	18.550	4.169	3.162	0.021
IC3961	O12566+3507	194.7580	34.8559	18.50	14.624	14.474	1.531	0.862	0.010
NGC4922	Q12590+2934	195.3553	29.3137	107.23	19.221	18.553	6.522	5.107	0.011
UGC8179	Q13028+3216	196.3090	31.9997	222.14	17.505	17.196	3.297	2.328	0.013
NGC5001	Q13074+5345	197.3880	53.4943	134.78	18.219	17.144	4.941	3.223	0.016
IC856	Q13082+2048	197.6722	20.5363	64.31	17.791	17.279	4.038	2.857	0.035
UGC8269	Q13090+4657	197.8130	46.7006	124.13	20.810	19.789	7.442	5.672	0.012
NGC5014	Q13092+3632	197.8801	36.2821	18.50	16.775	16.187	3.410	2.216	0.008
NGC5012	O13092+2311	197.9043	22.9155	40.20	15.086	14.556	2.426	1.388	0.014
Q13116+4508	Q13116+4508	198.4495	44.8829	258.26	22.281	21.044	7.675	5.693	0.016
IC860	Q13126+2452	198.7646	24.6188	54.45	20.268	18.360	8.572	5.934	0.013
IRAS13144+4508	Q13144+4508	199.1656	44.8764	381.78	18.888	18.649	4.198	3.240	0.018
NGC5060	Q13147+0618	199.3176	6.0374	97.42	17.118	16.477	4.063	2.774	0.034
UGC8357	Q13154-0002	199.4950	-0.3117	146.90	17.285	16.724	3.939	2.724	0.026
UGC8361	Q13157+0635	199.5774	6.3354	106.29	18.917	18.181	5.476	4.028	0.038
IC883	Q13183+3423	200.1475	34.1393	104.66	17.699	16.983	6.065	4.617	0.013
NGC5100	Q13184+0914	200.2483	8.9783	142.18	18.097	17.333	4.576	3.149	0.029
NGC5104	Q13188+0036	200.3462	0.3424	87.79	18.078	17.578	5.679	4.441	0.023
NGC5107	Q13191+3847	200.3529	38.5376	18.50	15.416	15.107	1.591	0.824	0.011
NGC5123	Q13209+4320	200.7938	43.0863	123.43	16.081	15.648	2.796	1.778	0.013
IRAS13218+0552	Q13218+0552	201.0829	5.6180	850.44	20.560	21.208	5.991	5.833	0.031
IRAS13232+1731	Q13232+1731	201.4328	17.2647	331.77	18.030	17.487	3.556	2.384	0.021
NGC5147	Q13237+0221	201.5822	2.1009	18.00	14.289	13.982	1.774	0.975	0.027
NGC5204	O13277+5840	202.4024	58.4204	3.25	13.163	13.058	0.967	0.432	0.013
UGC8502	Q13283+3132	202.6640	31.2841	149.92	15.939	15.753	2.412	1.606	0.011
UGC8561	Q13326+3417	203.7386	34.0441	107.54	15.815	15.499	2.917	1.971	0.011
NGC5230	Q13330+1355	203.8828	13.6762	105.64	15.231	14.797	2.090	1.165	0.025
IRAS13349+2438	Q13349+2438	204.3280	24.3843	453.52	18.656	17.388	3.822	2.065	0.012
NGC5256	Q13362+4831	204.5713	48.2767	125.22	16.802	16.336	4.503	3.336	0.013
UGC8626	Q13358+0708	204.5978	6.8877	108.84	17.816	17.237	3.789	2.570	0.028
NGC5263	Q13376+2839	204.9819	28.4008	77.47	16.834	16.438	3.937	2.858	0.013
MCG1-35-028	Q13379+0501	205.1133	4.7738	105.13	18.502	17.727	5.043	3.580	0.030
IC910	Q13387+2331	205.2827	23.2820	120.34	18.350	17.728	5.458	4.114	0.017
MK268	Q13388+3037	205.2964	30.3782	173.73	19.020	18.434	4.808	3.523	0.016
NGC5278	Q13397+5555	205.4135	55.6706	114.39	16.353	15.908	2.885	1.849	0.009
NGC5273	O13399+3554	205.5349	35.6543	16.50	17.492	16.664	2.976	1.658	0.010
UGC8685	Q13408+3035	205.7868	30.3377	152.63	16.689	16.346	3.424	2.419	0.014
UGC8686	Q13411+0408	205.9172	3.8965	105.40	17.115	16.928	3.624	2.732	0.026
UGC8696	Q13428+5608	206.1757	55.8871	163.03	18.373	17.606	7.006	5.487	0.008
NGC5297	O13443+4407	206.5986	43.8723	30.90	14.888	14.512	2.174	1.271	0.014
MK796	Q13443+1439	206.7061	14.4005	98.46	18.249	17.538	5.009	3.604	0.026
IRAS13446+1121	Q13446+1121	206.7682	11.1063	104.55	20.633	19.266	7.194	5.100	0.035
NGC5303	Q13455+3833	206.9375	38.3046	23.00	15.482	15.136	2.674	1.730	0.014
NGC5313	Q13475+4013	207.4348	39.9848	30.90	15.795	15.284	3.141	2.031	0.008
MCG3-35-034	Q13507+1454	208.2903	14.6558	178.63	19.048	18.327	4.907	3.499	0.023
NGC5347	Q13510+3344	208.3241	33.4908	39.00	16.291	15.927	2.617	1.667	0.021
NGC5350	O13512+4036	208.3401	40.3639	30.90	14.830	14.585	2.212	1.389	0.011
UGC8827	Q13520+1517	208.6299	15.0441	85.38	17.455	16.759	4.435	3.075	0.023
UGC8856	Q13538+3019	209.0329	30.0814	137.91	18.935	18.442	5.291	4.070	0.016
NGC5374	Q13549+0620	209.3735	6.0970	68.94	15.669	15.258	2.808	1.805	0.027
UGC8902	Q13566+1548	209.7617	15.5657	114.44	16.931	16.467	3.143	2.067	0.022
NGC5403	Q13577+3825	209.9615	38.1823	37.00	17.577	17.059	4.671	3.451	0.009
MCG7-29-036	Q13589+4305	210.2410	42.8557	144.55	19.866	19.493	6.285	5.153	0.011
MCG5-33-046	Q14026+3058	211.2000	30.7437	116.36	20.708	19.201	7.152	4.927	0.014
NGC5474	O14032+5354	211.2559	53.6623	5.62	14.314	14.235	1.615	0.972	0.011
MCG6-31-070	Q14046+3400	211.7045	33.7718	155.82	18.297	18.084	4.894	3.938	0.016
CGCG074-129	Q14082+1347	212.6723	13.5580	76.50	20.449	19.145	7.020	4.991	0.024
NGC5520	Q14105+5034	213.0950	50.3484	30.50	15.872	15.316	2.801	1.695	0.018
NGC5515	Q14105+3932	213.1590	39.3102	114.09	17.677	16.874	4.124	2.697	0.008
NGC5526	Q14122+5800	213.4740	57.7713	27.90	17.712	16.905	4.273	2.831	0.012
NGC5522	Q14124+1522	213.7099	15.1469	72.08	17.438	16.767	3.933	2.629	0.024
NGC5541	Q14144+3949	214.1325	39.5891	115.37	16.544	15.958	3.335	2.150	0.011

Continued on next page

Table A.5 – continued from previous page

Galaxy	IRAS Id	RA(J2000)	Dec(J2000)	Dist (Mpc)	FUV	NUV	A(FUV)	A(NUV)	E($B-V$)
IC4395	Q14151+2705	214.3378	26.8574	160.45	17.636	16.728	4.401	2.867	0.017
UGC9165	Q14165+2510	214.6991	24.9405	81.33	18.754	18.167	5.593	4.277	0.017
MK1490	Q14178+4927	214.9301	49.2366	116.16	20.858	19.315	8.127	5.845	0.018
NGC5585	O14182+5657	214.9508	56.7293	5.62	13.314	13.186	0.841	0.330	0.016
IC4408	Q14190+3013	215.3046	29.9935	134.93	18.447	17.725	4.820	3.414	0.021
NGC5584	O14198-0009	215.5990	-0.3877	23.10	14.300	13.970	1.700	0.901	0.039
NGC5633	Q14255+4622	216.8683	46.1465	36.50	15.707	15.174	2.868	1.771	0.017
NGC5660	O14280+4950	217.4576	49.6227	38.90	14.270	13.912	2.018	1.150	0.021
NGC5656	Q14283+3532	217.6063	35.3210	53.73	15.912	15.381	3.044	1.928	0.015
NGC5657	Q14285+2924	217.6798	29.1805	64.44	17.252	16.979	3.428	2.477	0.018
CGCG133-083	Q14296+2209	217.9754	21.9384	190.64	19.035	18.398	5.414	4.058	0.048
MCG7-30-028	Q14318+4018	218.4515	40.0942	116.13	17.792	17.374	4.245	3.131	0.012
MCG6-32-070	Q14332+3520	218.8266	35.1187	127.05	17.137	16.376	3.972	2.592	0.010
UGC9412	Q14349+5900	219.0920	58.7943	138.66	14.821	14.822	1.718	1.108	0.007
NGC5691	Q14353-0011	219.4722	-0.3989	19.80	15.268	14.841	2.562	1.575	0.037
MCG9-24-035	Q14441+5147	221.4380	51.5808	137.38	19.055	18.032	5.649	3.934	0.022
MCG9-24-038	Q14451+5626	221.6545	56.2330	166.58	19.250	18.466	5.219	3.740	0.016
UGC9560	Q14489+3546	222.7357	35.5721	23.00	15.356	15.367	1.427	0.862	0.012
IC1076	Q14526+1814	223.7484	18.0373	92.55	16.875	16.333	3.264	2.119	0.031
Q14538+1730	Q14538+1730	224.0356	17.3096	432.87	21.039	19.733	6.892	4.865	0.027
NGC5795	Q14546+4935	224.0855	49.4005	38.20	17.961	17.273	4.759	3.386	0.019
UGC9618	Q14547+2448	224.2533	24.6173	145.79	19.174	18.626	6.779	5.472	0.042
UGC9639	Q14568+4504	224.6500	44.8836	157.66	18.078	17.210	4.692	3.169	0.018
MCG6-33-022	Q15060+3434	227.0249	34.3909	194.51	18.681	18.158	5.275	4.028	0.016
NGC5879	O15084+5711	227.4449	57.0002	15.50	14.594	14.333	2.160	1.333	0.012
MCG9-25-036	Q15113+5134	228.2180	51.3986	160.13	20.676	19.820	5.931	4.357	0.018
NGC5899	Q15132+4214	228.7634	42.0499	43.50	16.319	15.723	3.644	2.423	0.034
NGC5905	O15140+5542	228.8472	55.5173	58.68	15.354	15.199	2.546	1.750	0.015
MK848	Q15163+4255	229.5256	42.7458	173.92	17.806	17.159	5.539	4.170	0.026
IC4553	Q15327+2340	233.7384	23.5037	83.52	17.958	17.219	8.223	6.710	0.051
UGC9922	Q15340+3850	233.9745	38.6755	86.68	16.581	16.369	3.262	2.370	0.017
IC4567	Q15354+4327	234.3053	43.2983	88.64	16.498	15.932	3.328	2.158	0.029
MCG4-37-016	Q15373+2506	234.8646	24.9476	102.93	17.948	17.282	4.294	2.969	0.047
NGC5975	Q15377+2137	234.9915	21.4706	69.26	19.001	18.245	5.956	4.473	0.063
NGC5980	Q15391+1556	235.3768	15.7877	65.21	16.418	15.888	3.597	2.432	0.035
NGC5992	Q15425+4114	236.0896	41.0864	140.24	16.570	16.156	3.045	2.016	0.020
NGC5996	Q15447+1802	236.7453	17.8842	53.98	14.832	14.519	2.363	1.477	0.034
Q15519+3537	Q15519+3537	238.4536	35.4673	354.11	20.625	20.070	6.061	4.763	0.025
UGC10099	Q15548+4201	239.1517	41.8807	152.22	16.367	16.078	2.893	1.969	0.018
MCG5-38-006	Q15566+2657	239.6821	26.8181	69.60	18.670	18.017	5.182	3.821	0.051
UGC10120	Q15572+3510	239.7901	35.0299	138.92	16.566	16.197	2.195	1.294	0.025
NGC6027A	Q15570+2053	239.8041	20.7592	70.60	20.471	19.644	6.050	4.499	0.055
NGC6040	Q16021+1753	241.1105	17.7420	177.01	17.104	16.759	2.694	1.749	0.044
UGC10200	Q16040+4128	241.4412	41.3447	31.20	15.082	14.950	1.630	0.955	0.010
Q16052+5334	Q16052+5334	241.6375	53.4423	366.14	22.842	21.865	8.255	6.514	0.012
IRAS16053+1836	Q16053+1836	241.9105	18.4801	161.42	20.853	19.633	7.038	5.088	0.043
NGC6090	Q16104+5235	242.9180	52.4564	131.16	16.468	15.915	4.058	2.841	0.020
UGC10273	Q16107+2824	243.1862	28.2861	111.32	17.261	17.022	3.710	2.772	0.051
P16150+2233	P16150+2233	244.2873	22.4411	278.13	21.364	20.554	7.109	5.547	0.112
UGC10322	P16160+2220	244.5327	22.2257	69.06	17.794	17.501	4.348	3.338	0.090
NGC6120	Q16180+3753	244.9505	37.7744	134.89	17.356	16.793	4.501	3.250	0.018
MCG3-42-004	Q16220+2017	246.0632	20.1835	171.90	18.167	17.663	4.188	3.005	0.066
UGC10407	Q16268+4119	247.1162	41.2176	124.74	15.785	15.515	2.370	1.512	0.008
IRAS16320+3922	Q16320+3922	248.4568	39.2632	139.42	17.008	16.654	2.711	1.758	0.010
NGC6186	Q16322+2138	248.6062	21.5409	162.81	16.908	16.267	3.815	2.544	0.047
UGC10514	Q16403+2510	250.5986	25.0865	100.54	17.244	16.926	3.919	2.905	0.051
IRAS16435+2154	Q16435+2154	251.4195	21.8219	142.34	20.363	19.648	6.609	5.146	0.047
IC4623	Q16489+2236	252.7722	22.5274	138.49	19.022	18.612	5.153	4.013	0.064
Q16516+3030	Q16516+3030	253.4049	30.4360	306.12	21.393	20.598	7.388	5.834	0.034

Table A.6: SFR measures for SFRS galaxies

Galaxy	SFR_{FUV}	SFR_{NUV}	SFR_{PAH}	SFR_{FIR}	$SFR_{1.4\,GHz}$
IC486	3.709	5.364	4.648	3.712	9.464
IC2217	4.968	7.377	6.634	4.508	7.717
NGC2500	0.386	0.617	0.261	0.204	0.235
MCG6-18-009	14.568	23.432	15.593	13.858	34.296
NGC2532	10.758	18.397	20.375	8.261	19.852
UGC4261	4.117	6.920	2.674	2.854	5.050
NGC2535	3.841	5.973	4.531	3.034	4.892
NGC2543	0.915	1.693	0.987	0.643	0.599
NGC2537	0.336	0.557	0.143	0.217	0.168
IC2233	0.114	0.209	0.008	0.051	0.027
IC2239	6.520	9.906	4.132	7.049	6.946
UGC4286	1.891	2.922	2.823	1.597	1.561
UGC4306	1.535	2.528	2.167	1.451	2.491
NGC2552	0.073	0.133	0.018	0.028	0.004
IC2339	3.516	5.289	2.133	3.133	2.675
IRAS08234+1054	37.092	53.329	13.155	40.927	46.920
IRAS08269+1514	4.310	5.500	4.987	5.511	8.338
NGC2604	1.000	1.816	0.731	0.573	0.879
NGC2608	1.262	1.942	1.859	1.095	1.421
NGC2623	35.059	46.470	10.032	42.288	45.167
CGCG120-018	7.894	10.015	6.271	10.333	10.154
Q08512+2727	16.429	22.629	29.114	17.393	40.440
Q08519+2017	295.700	390.220	1119.729	347.755	169939.422
IRAS08538+4256	13.495	16.018	6.946	18.900	21.867
IRAS08550+3908	34.814	41.994	24.658	44.517	230.246
NGC2718	5.709	10.672	5.646	4.002	6.913
NGC2712	0.841	1.107	1.448	0.729	0.840
NGC2719	1.563	2.284	0.360	1.346	5.499
IRAS08572+3915NW	71.339	82.264	183.693	100.109	18.206
IRAS08579+3447	48.394	59.714	22.424	62.663	129.504
NGC2731	1.418	2.471	1.647	1.131	2.077
NGC2730	1.436	2.147	2.008	0.997	2.192
IC2431	52.464	74.857	16.011	58.122	322.455
NGC2750	2.147	3.172	2.627	1.704	2.428
IC2434	5.044	6.183	5.622	5.969	16.425
NGC2761	15.957	21.009	21.443	19.587	31.048
NGC2773	5.299	7.710	8.691	5.683	10.365
NGC2776	1.930	2.585	3.729	1.628	2.859
NGC2789	5.347	6.973	9.379	6.677	11.372
NGC2824	0.497	0.698	0.270	0.595	1.140
IRAS09184+4356	8.605	9.465	14.950	12.593	20.104
CGCG238-041	3.602	4.292	3.671	4.246	10.299
UGC4985	5.412	6.890	7.937	6.469	8.893
NGC2854	0.329	0.416	0.751	0.353	0.833
UGC5046	3.279	4.464	4.672	3.779	6.599
UGC5055	6.714	9.615	7.731	6.053	9.890
NGC2893	0.420	0.565	0.465	0.418	0.302
MCG3-24-062	1.963	2.718	3.622	2.050	3.580
CGCG238-066	7.353	8.204	10.083	10.380	13.649
UGC5097	4.925	7.064	5.048	4.441	10.316
CGCG289-012	12.910	15.792	17.221	14.712	28.689
MCG8-18-013	15.250	18.089	20.991	20.233	29.765
CGCG181-068	3.041	3.345	5.586	4.475	9.047
NGC2936	7.597	10.487	10.717	7.456	20.908
NGC2955	5.983	7.354	13.089	6.481	9.802
CGCG182-010	12.808	14.172	20.381	18.007	26.300
UGC5228	1.212	4.454	0.663	0.438	0.773
NGC3015	10.521	20.651	13.556	8.142	17.207
MCG2-25-039	2.595	3.411	4.970	2.928	6.273
NGC3020	0.357	0.593	0.136	0.199	1.045
NGC3049	0.340	0.510	0.335	0.265	0.216

Continued on next page

Table A.6 – continued from previous page

Galaxy	SFR_{FUV}	SFR_{NUV}	SFR_{PAH}	SFR_{FIR}	$SFR_{1.4\,GHz}$
NGC3055	1.112	1.863	1.440	0.826	1.623
IC2520	0.675	0.815	1.466	0.759	1.191
UGC5403	0.720	0.927	1.038	0.857	0.912
UGC5459	0.501	0.744	0.705	0.493	0.784
MCG5-24-022	2.286	2.908	3.317	3.020	3.367
IC2551	7.698	10.707	11.072	8.899	16.485
Q10106+2745	12.655	18.904	18.841	13.961	26.715
NGC3162	0.940	1.349	1.528	0.683	0.890
Q10120+1653	57.701	72.959	15.170	76.566	184.052
NGC3190	0.724	0.975	1.011	0.897	0.247
IC602	3.412	4.561	3.885	3.022	6.992
NGC3191	9.940	12.090	14.199	10.282	16.310
NGC3206	0.434	0.657	0.131	0.228	0.038
UGC5613	19.177	22.735	33.555	26.069	68.742
UGC5644	4.881	7.473	7.248	4.023	17.591
NGC3245	0.216	0.319	0.026	0.253	0.208
MCG7-22-012	1.602	1.775	3.599	2.265	3.736
Q10276+1119	23.953	30.800	19.759	25.995	30.277
NGC3265	0.268	0.338	0.367	0.302	0.340
UGC5713	1.860	2.205	3.930	2.193	0.640
UGC5720	0.514	0.612	0.442	0.499	0.471
NGC3274	0.059	0.091	0.012	0.031	0.031
NGC3306	1.836	2.338	3.059	1.928	3.589
NGC3323	3.559	4.839	4.226	3.161	6.000
IC2598	6.128	7.758	10.246	7.676	15.314
NGC3338	0.859	1.337	1.592	0.613	1.387
NGC3353	0.361	0.412	0.246	0.358	0.281
UGC5881	3.561	4.691	4.286	4.221	6.563
NGC3370	0.686	1.002	1.141	0.548	0.772
NGC3381	0.473	0.676	0.651	0.349	0.356
UGC5941	6.146	6.988	7.952	8.999	10.146
NGC3413	0.123	0.182	0.111	0.085	0.095
NGC3408	5.072	6.424	10.155	5.186	8.244
NGC3430	0.632	0.732	0.148	0.886	1.872
CGCG95-055	0.546	0.935	4.199	0.303	0.492
IRAS10565+2448W	....	76.718	47.976	109.602	138.738
UGC6074	0.996	1.151	0.861	1.377	0.901
NGC3495	0.480	0.793	0.642	0.374	0.560
UGC6103	5.584	6.734	8.659	6.164	8.712
MCG7-23-019	29.240	31.135	22.316	41.625	58.529
UGC6135	4.737	5.676	9.393	5.481	10.194
CGCG241-078	5.290	5.649	6.062	8.271	14.230
IRAS11069+2711	43.470	48.516	10.285	59.510	14.954
IC676	0.521	0.677	0.799	0.638	0.498
IRAS11102+3026	7.737	8.810	4.226	11.610	12.512
IC2637	8.422	10.857	17.613	9.703	49.213
MCG9-19-013	9.612	10.807	17.730	13.595	17.904
7ZW384	27.816	30.850	24.975	38.062	146.259
IRAS11167+5351	57.008	60.969	63.696	84.195	228.484
NGC3633	0.844	1.364	1.480	0.830	1.239
NGC3656	0.892	1.090	1.119	1.111	1.923
NGC3664	0.487	0.892	0.135	0.211	0.482
NGC3666	0.338	0.493	0.472	0.299	0.317
IC691	0.214	0.245	0.257	0.252	0.686
NGC3686	0.787	1.177	1.570	0.621	0.494
UGC6469	6.223	9.189	6.653	5.262	13.507
NGC3690	51.073	56.098	25.480	74.112	132.683
IC698	9.613	13.687	16.170	10.976	20.688
Q11267+1558	126.437	167.653	32.542	152.711	119.297
NGC3705	0.489	0.800	0.796	0.370	0.388
MCG3-29-061	2.597	3.091	2.697	3.455	2.649
NGC3720	4.875	5.787	0.054	7.141	6.345
NGC3729	0.289	0.362	0.511	0.302	0.436

Continued on next page

Table A.6 – continued from previous page

Galaxy	SFR_{FUV}	SFR_{NUV}	SFR_{PAH}	SFR_{FIR}	$SFR_{1.4\,GHz}$
NGC3758	6.617	9.027	14.888	7.396	12.277
UGC6583	5.464	7.243	7.816	5.767	11.470
NGC3769	0.320	0.442	0.468	0.271	0.409
NGC3773	0.160	0.235	0.097	0.106	0.109
NGC3781	14.956	17.940	7.607	21.098	38.032
UGC6625	12.842	18.009	18.621	11.414	30.878
NGC3808	8.306	10.259	8.688	10.589	20.790
NGC3822	9.567	15.468	19.268	9.495	21.574
UGC6665	7.671	10.204	4.886	7.339	16.707
MCG3-30-051	4.153	4.946	8.421	4.972	7.069
UGC6732	0.840	1.154	1.395	1.130	1.038
IC730	6.316	7.396	11.005	8.599	14.006
NGC3912	0.498	0.652	0.743	0.542	0.765
NGC3928	0.260	0.342	0.402	0.246	0.247
NGC3934	2.325	3.509	2.866	2.493	7.539
UGC6865	4.821	5.942	12.444	6.330	11.443
UGC6901	5.998	7.209	15.087	8.339	13.877
CGCG013-010	22.459	25.192	29.705	33.224	82.165
NGC3991	3.483	4.632	4.463	2.470	7.541
NGC4004	3.813	4.944	4.136	3.769	6.953
NGC4014	4.073	7.116	7.475	3.440	5.561
NGC4010	0.258	0.347	0.449	0.258	0.421
NGC4018	3.680	4.465	6.838	4.766	11.191
NGC4020	0.097	0.134	0.103	0.071	0.099
Q11571+3003	9.437	10.615	6.584	13.683	4.747
UGC7016	5.294	7.447	7.767	6.140	10.270
UGC7017	3.078	3.622	5.724	3.669	7.708
MCG3-31-030	0.051	0.072	0.069	0.043	0.033
NGC4062	0.375	0.552	0.849	0.317	0.138
NGC4064	0.064	0.087	0.101	0.077	0.048
CGCG098-059	10.435	15.294	13.252	11.770	13.582
NGC4116	0.296	0.422	0.300	0.187	0.314
NGC4136	0.330	0.485	0.300	0.202	0.275
NGC4150	0.063	0.093	0.041	0.074	0.027
Q12086+1441	0.048	0.060	0.048	0.060	0.077
NGC4162	1.954	3.033	3.071	1.631	4.382
NGC4178	0.557	0.838	0.614	0.391	0.607
NGC4189	0.393	0.582	0.694	0.339	0.356
NGC4204	0.056	0.088	0.029	0.032	0.003
NGC4207	0.238	0.285	0.530	0.301	0.374
UGC7286	2.869	3.561	3.631	3.659	2.741
NGC4234	0.620	0.846	0.835	0.513	0.313
NGC4237	0.317	0.471	0.595	0.324	0.120
NGC4244	0.029	0.059	0.021	0.010	0.036
NGC4253	3.411	4.160	3.353	4.328	11.376
MCG3-32-005	0.118	0.150	0.207	0.150	0.310
NGC4290	1.594	1.948	2.072	1.771	1.835
NGC4294	0.378	0.598	0.280	0.249	0.422
NGC4314	0.297	0.441	0.117	0.295	0.247
NGC4385	1.099	1.435	1.156	1.066	0.781
NGC4396	0.202	0.298	0.227	0.140	0.406
NGC4412	0.962	1.250	1.298	0.892	0.970
NGC4420	0.353	0.491	0.569	0.304	0.088
NGC4424	0.031	0.043	0.041	0.033	0.010
NGC4435	0.117	0.179	-0.011	0.139	0.030
NGC4438	0.387	0.534	0.211	0.390	1.267
NGC4448	0.173	0.247	0.171	0.169	0.096
3C273	516.680	741.286	661.629	260.979	1687694.750
NGC4470	0.234	0.330	0.300	0.183	0.310
NGC4491	0.193	0.281	....	0.199	0.090
NGC4495	4.768	5.824	9.072	5.831	11.765
NGC4500	....	3.586	4.531	3.201	5.409
IC3476	0.208	0.371	....	0.128	0.150

Continued on next page

Table A.6 – continued from previous page

Galaxy	SFR_{FUV}	SFR_{NUV}	SFR_{PAH}	SFR_{FIR}	$SFR_{1.4\,GHz}$
NGC4509	0.047	0.060	0.004	0.032	0.025
NGC4519	0.432	0.608	0.437	0.320	0.513
NGC4548	0.420	0.661	0.703	0.327	0.093
IRAS12337+5044	10.520	11.856	14.944	13.915	27.433
NGC4592	0.147	0.223	0.076	0.089	0.059
NGC4607	0.247	0.323	0.514	0.294	0.458
NGC4625	0.054	0.073	0.077	0.041	0.034
NGC4630	0.239	0.337	0.320	0.201	0.218
MCG5-30-069	3.290	3.698	4.294	4.934	3.810
IC3721	5.130	6.296	8.137	6.341	16.186
NGC4670	0.220	0.295	0.106	0.147	0.199
MCG7-26-051	14.719	17.045	25.806	20.619	47.898
NGC4688	0.154	0.234	0.062	0.079	0.045
NGC4704	6.485	7.935	7.700	7.061	10.481
Q12468+3436	45.743	50.853	24.518	77.878	89.812
MCG8-23-097	16.728	17.979	10.718	25.484	36.253
NGC4747	0.125	0.141	0.119	0.141	0.107
UGC8017	6.178	6.854	14.300	8.103	23.501
NGC4765	0.242	0.391	0.127	0.169	0.304
VCC2096	0.071	0.109	0.070	0.071	0.243
UGC8041	0.308	0.465	0.236	0.188	0.056
NGC4837	10.052	12.093	16.430	11.226	31.765
UM530	15.351	18.107	10.739	18.714	24.371
IC3961	0.260	0.337	0.030	0.179	0.350
NGC4922	12.664	13.405	12.351	19.379	31.646
UGC8179	13.745	15.993	25.962	15.692	58.105
NGC5001	12.188	14.746	21.790	16.591	31.698
IC856	2.072	2.817	3.009	2.235	3.696
UGC8269	9.237	9.830	6.081	14.376	20.438
NGC5012	1.887	2.546	4.099	1.751	3.405
NGC5014	0.199	0.235	0.313	0.241	0.277
Q13116+4508	13.170	14.506	10.401	19.991	2.366
IC860	8.353	9.115	0.842	13.273	6.477
IRAS13144+4508	27.065	30.948	129.649	33.870	61.000
NGC5060	8.976	12.347	10.351	9.786	10.906
UGC8357	14.689	18.937	20.431	16.760	31.227
UGC8361	7.720	10.322	9.177	9.198	13.864
IC883	32.678	35.571	26.725	48.450	81.117
NGC5100	11.982	15.673	19.625	14.328	146.692
NGC5104	12.267	14.317	13.913	16.563	21.813
NGC5107	0.134	0.185	0.029	0.094	0.109
NGC5123	9.937	12.394	20.166	10.229	20.208
IRAS13218+0552	165.633	192.979	943.370	213.392	143.647
IRAS13232+1731	25.501	32.423	44.155	28.616	87.447
NGC5147	0.477	0.720	0.503	0.321	0.579
NGC5204	0.019	0.027	0.005	0.009	0.014
UGC8502	11.541	13.741	9.915	10.915	12.276
UGC8561	10.595	12.505	17.462	11.381	24.036
NGC5230	9.107	13.527	14.608	6.994	11.478
IRAS13349+2438	31.944	43.217	185.401	39.933	285.956
UGC8626	4.371	5.795	5.340	4.813	5.294
NGC5256	25.342	28.412	23.670	34.009	140.476
NGC5263	5.595	6.374	10.075	7.048	16.177
MCG1-35-028	6.990	9.000	7.385	8.615	12.387
IC910	13.977	15.843	10.297	19.527	39.754
MK268	8.572	9.841	9.600	11.549	90.989
NGC5278	6.991	8.417	8.805	7.571	21.441
NGC5273	0.056	0.074	-0.005	0.061	0.068
UGC8685	15.593	18.256	15.554	18.064	25.448
UGC8686	6.610	8.139	8.450	7.215	11.584
UGC8696	97.580	100.531	40.157	154.902	299.391
MK796	7.274	9.042	8.054	9.220	131.067
NGC5297	1.061	1.407	1.888	0.911	1.558

Continued on next page

Table A.6 – continued from previous page

Galaxy	SFR_{FUV}	SFR_{NUV}	SFR_{PAH}	SFR_{FIR}	$SFR_{1.4\,GHz}$
IRAS13446+1121	7.316	9.433	9.426	9.495	15.817
NGC5303	0.539	0.670	0.919	0.535	0.934
NGC5313	1.071	1.271	2.679	1.234	3.000
MCG3-35-034	10.207	12.480	15.553	13.138	47.079
NGC5347	0.737	0.974	1.167	0.682	0.604
NGC5350	1.133	1.402	2.127	1.009	1.138
UGC8827	6.546	8.178	7.481	8.085	11.893
UGC8856	9.109	10.190	14.159	12.699	29.275
NGC5374	5.096	7.003	8.056	4.726	8.159
UGC8902	5.752	7.487	8.443	5.955	11.519
NGC5403	1.227	1.334	2.556	1.724	3.632
MCG7-29-036	10.211	10.696	7.317	15.500	7.707
MCG5-33-046	6.928	7.707	6.857	10.544	9.988
NGC5474	0.035	0.044	0.010	0.025	0.029
MCG6-31-070	14.530	16.019	17.884	19.709	31.173
CGCG074-129	3.635	4.326	3.795	5.109	3.155
NGC5515	6.379	7.400	14.204	8.543	26.591
NGC5520	0.767	1.026	1.322	0.761	0.977
NGC5526	0.437	0.517	0.766	0.577	0.878
NGC5522	3.007	3.895	4.399	3.481	6.486
NGC5541	9.163	11.114	14.934	10.695	31.157
IC4395	18.129	22.405	21.232	23.362	41.270
UGC9165	4.982	5.608	10.431	7.011	14.357
MK1490	15.221	17.094	12.254	23.003	19.334
NGC5585	0.044	0.068	0.014	0.019	0.042
IC4408	9.199	11.131	18.575	11.940	25.958
NGC5584	0.797	1.343	0.784	0.474	0.734
NGC5633	1.350	1.768	2.957	1.370	2.637
NGC5660	2.715	3.851	3.617	2.097	3.585
NGC5656	2.803	3.553	5.439	3.001	4.259
NGC5657	1.711	2.036	3.140	1.924	3.034
CGCG133-083	22.694	32.476	21.578	24.961	28.616
MCG7-30-028	6.848	7.658	10.192	9.018	12.053
MCG6-32-070	11.483	13.580	23.739	14.867	25.190
UGC9412	14.151	16.499	53.226	10.821	15.275
NGC5691	0.523	0.798	0.568	0.423	0.528
MCG9-24-035	11.783	14.247	8.558	16.007	15.396
MCG9-24-038	9.309	10.725	20.828	12.920	27.163
UGC9560	0.189	0.236	0.028	0.122	0.221
IC1076	4.743	6.650	7.406	4.691	12.577
Q14538+1730	61.427	75.036	52.784	84.088	162.153
NGC5795	1.074	1.279	2.239	1.409	1.894
UGC9618	39.226	51.746	45.024	47.736	140.365
UGC9639	15.327	18.607	32.207	20.140	62.945
MCG6-33-022	22.587	25.343	33.502	31.458	357.201
NGC5879	0.340	0.429	0.630	0.296	0.332
MCG9-25-036	4.526	5.183	7.320	6.423	9.094
NGC5899	2.538	3.568	5.697	2.615	5.624
NGC5905	3.537	4.251	13.728	3.368	4.909
MK848	55.599	67.349	37.822	72.846	107.925
IC4553	159.797	222.181	19.177	188.168	161.454
UGC9922	4.893	5.763	6.016	5.383	11.725
IC4567	6.435	8.887	12.315	6.537	13.320
MCG4-37-016	6.378	9.560	3.597	6.464	15.105
NGC5975	5.714	9.072	5.533	5.758	7.520
NGC5980	5.030	7.057	9.501	5.105	7.631
NGC5992	10.846	13.861	17.600	11.180	22.321
NGC5996	4.729	6.970	4.882	3.699	6.118
Q15519+3537	27.581	32.506	40.294	37.307	101.399
UGC10099	13.177	16.307	14.735	13.347	24.325
MCG5-38-006	3.500	5.171	3.840	3.709	3.711
NGC6027A	1.572	2.357	0.976	1.691	3.995
UGC10120	5.069	7.259	8.684	4.031	7.529

Continued on next page

Table A.6 – continued from previous page

Galaxy	SFR_{FUV}	SFR_{NUV}	SFR_{PAH}	SFR_{FIR}	$SFR_{1.4\,GHz}$
NGC6040	9.184	14.226	8.650	7.279	213.141
UGC10200	0.532	0.674	0.242	0.383	0.773
Q16052+5334	26.151	27.448	49.434	41.510	96.994
IRAS16053+1836	13.112	17.883	18.585	15.947	25.876
NGC6090	26.480	32.371	31.323	32.105	58.573
UGC10273	8.456	12.596	5.461	7.725	19.514
P16150+2233	43.955	98.098	12.076	31.623	21.400
UGC10322	4.827	9.441	6.046	3.543	8.255
NGC6120	18.307	21.567	31.759	23.641	43.495
MCG3-42-004	15.235	25.834	15.070	13.201	21.589
UGC10407	8.661	10.378	8.815	8.279	20.309
IRAS16320+3922	4.878	5.874	5.758	5.034	8.962
NGC6186	26.728	41.207	35.219	25.552	32.716
UGC10514	8.489	12.685	9.045	7.982	22.873
IRAS16435+2154	11.108	15.374	10.101	12.947	16.671
IC4623	10.781	17.172	11.202	10.326	14.965
Q16516+3030	36.930	45.913	47.730	48.527	87.078

Appendix B

Catalogues used in this work

B.1 Derived data products from the SDSS: Catalogues by the Garching group

In this thesis, we use various quantities derived from the SDSS optical spectra by Brinchmann et al. (2004) (B04 henceforth), based on SDSS DR4 catalogue[1]. From this and related work (Kauffmann et al. 2003b), we use specific spectral indices (emission corrected Hδ equivalent width (EW) and [Ne III] contamination corrected D_n4000)[2].

Two of the galaxy parameters we use, namely the specific star formation rate (SSFR, or SFR/M^*) and stellar mass (M^*), are derived using the SDSS galaxy spectra by B04 and Kauffmann et al. (2003b) respectively. B04 construct a grid of $\sim 2 \times 10^5$ spectral synthesis models (Bruzual A. & Charlot 1993; Charlot & Longhetti 2001) over four relevant parameters spanning a range in metallicity (Z) of $-1 < \log Z/Z_\odot < 0.6$, ionisation parameter ($U$) $-4.0 < \log U < -2.0$, total dust attenuation (τ_V) $0.01 < \tau_V < 4.0$ and dust-to-metal-ratio (ξ) $0.1 < \xi < 0.5$. The attenuation by dust is treated using a physically motivated model of Charlot & Fall (2000), which provides a consistent model for UV to IR emission.

B04 compared the modelled line-ratios for each model in their grid directly with those in the observed spectrum, and, for each galaxy, constructed a log-likelihood function for each point on the model grid, summed over all lines observed in the spectrum of that galaxy. It is worth mentioning here that since they studied relative line fluxes only, their analysis was insensitive to stellar ages, star formation history and the relative attenuation by dust in the molecular gas clouds and the interstellar medium.

B04 derived their values for SFR and sSFR using a Bayesian technique, involving the likelihood functions mentioned above, using the entire spectrum of each galaxy (it is worth noting that the spectrum came from a fibre of diameter 3″). It is shown that their work yields better estimates of the SFR and SFR/M^* than any single spectroscopic SFR indicator, such as EW of the Hα or O II lines, which are used extensively in literature. Furthermore, the combination

[1] http://www.mpa-garching.mpg.de/SDSS/DR4/Data/sfr_catalogue.html

[2] The EW(Hδ) values used in Chapter 7 are taken directly from the sixth data release of the SDSS and are uncorrected for [Ne III] contamination

of several line indices enabled them to separate the galaxies with a significant AGN component from those with emission entirely due to star formation. The derived parameters (SFR and SFR/M^*) were then corrected for aperture biases using broadband photometric colours. Out of the three statistical estimates (mean, median and mode) for the probability distribution function (PDF) of SFR and SFR/M^* derived for each galaxy, we used the median of the distribution in this work for each quantity, since it is independent of binning.

Star-forming galaxies can be separated from the AGN-dominated ones on the basis of the so-called BPT diagram (Baldwin, Phillips & Terlevich 1981), namely a plot of the line ratio [O III]/Hβ against Hα/[N II] (e.g. Fig. 3.2), for galaxies with all four emission lines. B04 divided all galaxies into four classes (star forming, AGN, composite and unclassified) using the BPT diagram. For those galaxies whose spectra did not showed all the above mentioned emission lines, (called 'unclassified' galaxies; see §5.2.3), and those that were classified as AGN-dominated, B04 adopted an indirect method for estimating the SFRs. They used the relationship between D_n4000 and SFR derived for the high S/N (≥ 3) star-forming galaxies (SFR_e) to estimate the SFR of AGN and low S/N galaxies (SFR_a; see section 4.1 of B04 for details).

To check the reliability of the integrated SFRs derived for galaxies in our sample, in Fig. B.1 we plot the 68% confidence intervals (C.I.) for the log SFR estimate for each galaxy, and then calculate the scatter in this value in bins of log SFR and log SFR/M^* respectively. The trends are similar to those seen in fig. 14 of B04 (they analysed all the galaxies in SDSS spectroscopic galaxy catalogue in DR4). For the low S/N and non-emission line galaxies, most of which are passively evolving, the indirectly measured SFR results in higher uncertainty in the estimated SFR and SFR/M^* while for the star-forming galaxies with high S/N in the emission lines, the uncertainties are low. However, we chose not to select galaxies based on the confidence interval values derived from the PDF of individual galaxies, because excluding galaxies with higher uncertainties in SFR/M^* (or SFR) distribution would preferentially exclude a significant number of passive galaxies and thus bias our samples.

Using the entire spectrum also made it possible to obtain an independent estimate of stellar mass M^*, which further constraints the estimated SFR/M^*, making it a more reliable parameter for evaluating star formation properties of galaxies, compared to other luminosity based parameters employed elsewhere (e.g. Lewis et al. 2002; Gómez et al. 2003). Kauffmann et al. (2003a) adopted similar methodology as B04 for estimating the stellar mass M^*. Their models were characterised by star-to-light ratio, dust attenuation and fraction of mass formed in a major burst of star formation (the burst mass fraction). They then computed the total mass in stars by multiplying the dust-corrected and k-corrected z-band luminosity of the galaxy, by the estimated z-band mass-to-light ratio of the best-fitting model, found using the Bayesian technique described above.

B.2 The cluster catalogue

We selected our galaxy clusters from the 'group' catalogue compiled by Yang et al. (2007) from the DR4 of the SDSS. Their iterative algorithm identifies first order groups using a Friends-of-

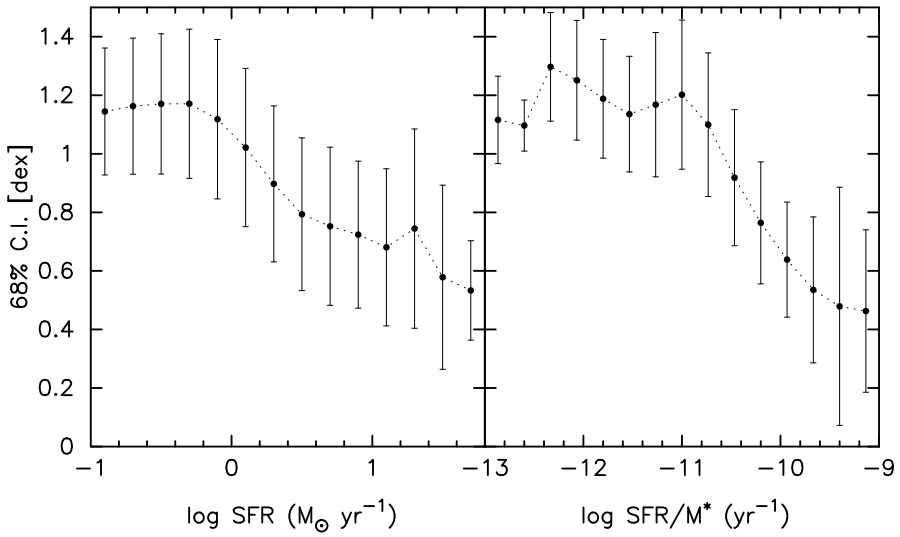

Figure B.1: The distribution of errors on the SFRs of galaxies in our sample. The solid points denote the mean 68% confidence interval (C.I.) of the likelihood distributions for SFR in bins of log SFR (*left*) and log SFR/M^* (*right*). The error bars show the 2σ scatter in each bin. Galaxies with high SFR have higher S/N ratio in the emission lines, and hence tighter constraints on the estimated SFR and SFR/M^* relative to the galaxies with low or no optical emission. It is also noticeable that the scatter in the C.I. in all the bins of SFR (and log SFR/M^*) is comparable.

Friends (FoF) algorithm in redshift space, with a small linking length in projected space and a large one along the direction of the LOS. This algorithm thus selects potential groups at a high surface density threshold, so that groups embedded within the virial radii of more massive ones will be extracted as two (or more) separate entities. All galaxies left out by this grouping method are treated as additional potential groups (of single galaxies).

The raw luminosities and (luminosity-weighted) centres are measured and then the luminosities (corrected for incompleteness), masses (assuming a given mass-to-light ratio) and velocity dispersions (from a mass / velocity dispersion relation) are derived. The radii R_{180}, i.e. of spheres that are 180 times denser than the critical density of the Universe are derived from the masses. The distribution of galaxies around each group centre in projected phase space are examined to determine group membership, based upon the assumption of a projected NFW (Navarro, Frenk, & White 1996, hereafter NFW) surface density profile and a Gaussian distribution of LOS velocities with dispersion independent of projected radius. The algorithm is iterated with these new group assignments, where the mass-to-light ratio used for estimating the new mass is a function of luminosity derived from the previous iteration. The iteration continues until the membership converges. Yang et al. (2007) have tested their algorithm on mock galaxy catalogues constructed in real space and converted to redshift space.

In the present work, we define the galaxy clusters with the following criteria:

1. redshift range: $0.02 \leq z \leq 0.12$;

2. membership: at least 15 galaxies;

3. minimum halo mass (within R_{180}): $10^{14}\mathrm{M}_{\odot}$.

All of our chosen clusters have at least 12 galaxies ($M_r \leq -20.5$) with SDSS spectra within R_{180} of each cluster centre. For our chosen cosmology, the virial radius, within which the cluster may be thought to be in dynamical equilibrium, is commonly believed to be very close to R_{100} where the density is 100 times critical. In this chapter, we adopt R_{100} for the virial radius, and more precisely

$$R_v = 1.3\, R_{180}\ , \tag{B.1}$$

which, for NFW models with concentrations between 3 and 10, matches R_{100} to an accuracy of 2%. This gives us a sample of 268 clusters in the SDSS DR4 footprint with median $M_{180} \sim 10^{14.2}\mathrm{M}_{\odot}$, corresponding to a median virial radius $R_{100} = 1.5\,\mathrm{Mpc}$ (using Eqn. B.1).

The range of 1.5 dex in cluster masses should not be a concern given that the properties of non-central (satellite) galaxies depend little on the mass of the group or cluster they live in (van den Bosch et al. 2008).

Appendix C

Simulations

C.1 Cosmological simulation

We use the high-resolution cosmological hydrodynamical simulation run by (Borgani et al. 2004). To summarise, the simulation assumes a cosmological model with $\Omega_0 = 0.3$, $\Omega_\Lambda = 0.7$, $\Omega_\mathrm{b} = 0.039$, $h = 0.7$, and $\sigma_8 = 0.8$. The box size is $L = 192\,h^{-1}$ Mpc. The simulation uses 480^3 DM particles and (initially) as many gas particles, for a DM particle mass of $4.62 \times 10^9\,h^{-1}\mathrm{M}_\odot$. The softening length was set to $22.5\,h^{-1}\,\mathrm{comoving\ kpc}$ until redshift $z = 2$ and fixed for subsequent epochs (i.e., at $7.5\,h^{-1}$ kpc). DM halos were identified by Borgani et al. (2004) at redshift $z = 0$ by applying a standard FoF analysis to the DM particle set, with linking length 0.15 times the mean inter-particle distance. After the FoF identification, the centre of the halo was set to the position of its most bound particle. A spherical overdensity criterion was then applied to determine the virial radius, R_{200} of each halo. In this manner, 117 halos were identified within the simulated volume, among which 105 form a complete subsample with virial mass M_{200} larger than $10^{14}\,h^{-1}\mathrm{M}_\odot$. To save computing time, the subsequent analysis was performed on a random subsample of roughly 2 million particles selected from the whole sample of 480^3 particles. We deliberately chose to analyse DM particles rather than galaxies in the simulations, as we do not trust the galaxy distribution, with a homogeneous core found in these and other hydrodynamic cosmological simulations, as they conflict with the observations (Saro et al. 2006). Moreover, the particle data provide us with much better statistics.

A sample of 93 non-bimodal mock clusters were extracted from these simulations by Mamon, Biviano, & Murante (2010). This yields fairly regular clusters that should resemble those of (Yang et al. 2007) (in the latter case, their high threshold causes multimodal clusters to be fragmented into several).

C.2 Classification schemes

Ideally, one should define the virial, infall and backsplash classes by following the orbits of the particles (Gill, Knebe & Gibson 2005), but this task is beyond the scope of the present article. Instead, we define the classes using the present-day radial phase space distribution of particles.

Particles that are outside the virial radius, and travelling at velocities lower than the critical velocity, are falling into the cluster for the first time, while particles outside the virial radius with higher velocities must have crossed the cluster at least once.

Sanchis, Łokas, & Mamon (2004) have analysed the distribution of DM particles in the radial phase space (r, v_r) at $z = 0$, for a cluster-mass halo in a dissipationless cosmological n-body simulation (256^3 particles in a box of $150\,h^{-1}\,\mathrm{Mpc}$ width). Their Fig. 1 (see also Mamon et al. 2004) suggests that the separation of particles belonging to the infall, backsplash and virialized populations can be written with a critical radial velocity delimiting the infall regime from the other two classes:

$$\frac{v_{r,\mathrm{crit}}}{V_\mathrm{v}} = -1.8 + 1.06 \left(\frac{r}{R_\mathrm{v}}\right) . \tag{C.1}$$

Fig. C.1 shows the distribution of DM particles in the stack of 93 clusters in radial phase space (r, v_r). Overplotted (red lines) are the cuts of (Sanchis, Łokas, & Mamon 2004) designed to separate the virialized, infall, and backsplash classes of particles (Eq. C.1). The particles within the virial radius with large absolute radial velocities have uncertain classes.

We devise several *Schemes* to identify the three classes of particles (we refer to Fig. 6 in Bertschinger 1985 for a schematic view of the trajectories of particles in radial phase space). The rapidly infalling particles with $r < r_\mathrm{v}$ might represent the low-end tail of the radial velocity distribution of the virial class, which we denote by Scheme 0, or might indeed be part of the infall class (Schemes 1 to 3), or may even be mainly populated by particles on their second infall, i.e. backsplash class (Scheme 4). The rapidly expanding particles with $r < r_\mathrm{v}$ might again represent the high-end tail of the radial velocity distribution of the virial class (Schemes 0 and 1), or the backsplash class (Schemes 2 and 4), or the infall class (if the star forming properties of galaxies in this region of radial phase space reflect those of the rapidly infalling class within the virial radius, Scheme 3). Scheme 0 corresponds to maximum virialization while Scheme 3 corresponds to maximum infall.

Although Fig. C.1 is based upon a very different simulation (hydrodynamical instead of dissipationless and with three times better mass resolution) and on a stacked halo instead of a single one, it shows that the critical radial velocity of Eq. C.1 is fully adequate to distinguish between infalling and backsplash particles in the stacked mock cluster obtained from the cosmological hydrodynamical simulation analysed here.

One may argue that the red solid line separating the infall and backsplash classes is too high and that we may be missing an important fraction of backsplash particles at high r and low v_r. We thus created a *maximum backsplash* Scheme 5, where we consider the critical velocity

$$\frac{v^{(2)}_{r,\mathrm{crit}}}{V_\mathrm{v}} = -2.2 + 0.83 \left(\frac{r}{R_\mathrm{v}}\right) . \tag{C.2}$$

This is shown as the magenta dashed line in Fig. C.1: particles with $v_r < v^{(2)}_{r,\mathrm{crit}}$ are infalling, other particles are backsplash or virial according to Scheme 4 applied with $v_{r,\mathrm{crit}}$. These Scheme definitions are shown in Table C.1.

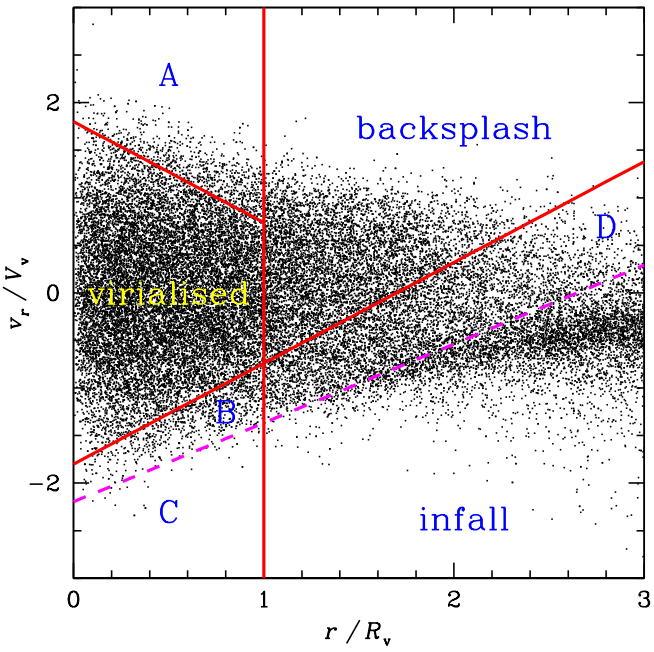

Figure C.1: Radial phase space distribution of dark matter particles of the stack of 93 regular mock clusters from the cosmological hydrodynamical simulation of Borgani et al. (2004). The units of radius and radial velocity are the virial radius r_{100} and the circular velocity at that radius, respectively. The critical velocity separating infall from backsplash population (*long diagonal red line*) is given in Eq. C.1. The *short diagonal line* represents the negative critical velocity threshold (see §6.5). For clarity, only 1 out of 550 particles of the original simulation is plotted. The question marks denote uncertain populations. The negative velocity question mark region is virialized in our Scheme 0, backsplash in Scheme 4, and infall otherwise. The positive velocity question mark region is virialized in Schemes 0 and 1, backsplash in Schemes 2 and 4 and infall in Scheme 3. The *dashed magenta line* delimits the infall and backsplash particles in Scheme 5.

Table C.1: Schemes of particle classes from positions in radial phase space

Scheme	A	B	C	D
$r/R_{\rm v}$	< 1	< 1	< 1	> 1
v_r	$> -v_{r,\rm crit}$	$v^{(2)}_{r,\rm crit} \leftrightarrow v_{r,\rm crit}$	$< v^{(2)}_{r,\rm crit}$	$v^{(2)}_{r,\rm crit} \leftrightarrow v_{r,\rm crit}$
0	virial	virial	virial	infall
1	virial	infall	infall	infall
2	backsplash	infall	infall	infall
3	infall	infall	infall	infall
4	backsplash	backsplash	backsplash	infall
5	backsplash	backsplash	infall	backsplash

Note: The letters A to D correspond to the regions in Fig. C.1.

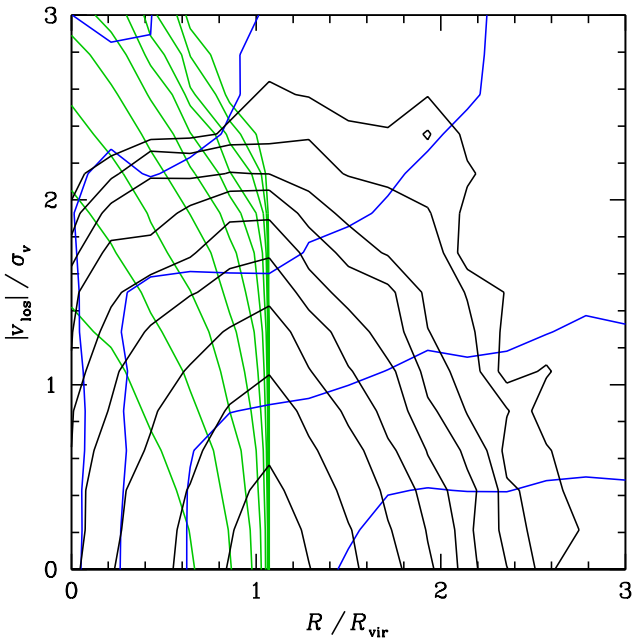

Figure C.2: Density in projected phase space of virial (*green*), infall (*blue*) and backsplash (*black contours*) particles of the stacked mock cluster with our preferred model (Scheme 3, see Fig. C.1). The *contours* are logarithmically spaced by a factor of 2.3, and the same set of contours is used for all three classes: the highest contours are on the lower left (virial), lower right (infall) and bottom (backsplash), where the latter two classes only reach the 2nd highest contour of the virial class.

The cosmological simulation provides us with a unique way of measuring the frequency of the three classes of particles (galaxies) in projected phase space. We translate velocities from $V_{\rm v} = V_{100}$ to the observable cluster velocity dispersion, σ_v, noting that the stacked cluster has a velocity dispersion (limited to the aperture $r < R_{\rm v}$) of $0.65\,V_{\rm v}$, as measured in the hydrodynamical simulation by (Mamon, Biviano, & Murante 2010), and within 5% of what is expected for isotropic NFW models of clusters (Appendix A of Mauduit & Mamon 2007).

Fig. C.2 shows the fractions of the three classes in projected phase space. The virialized particles are necessarily at radii $r < R_{\rm v}$, the infalling particles prefer large projected distances and high velocities, while the backsplash particles are mostly found just around the virial radius and have *low absolute LOS velocities*. This preference of backsplash galaxies for low $|v_{\rm LOS}|$ is an immediate consequence of their lower radial velocities and has also been noted by Gill, Knebe & Gibson (2005).

In the top panel of Fig. C.3, we show the contours for the fraction of particles that are backsplash, while the bottom panel provides the fraction of backsplash particles versus projected radius in wide bins of absolute LOS velocity. The two plots of Fig. C.3 indicate that the fraction of backsplash particles reaches a maximum of 59% just outside the virial radius at very low $|v_{\rm LOS}|$ for Scheme 3 (81% for Scheme 5). At high $|v_{\rm LOS}|$ the fraction of backsplash particles is

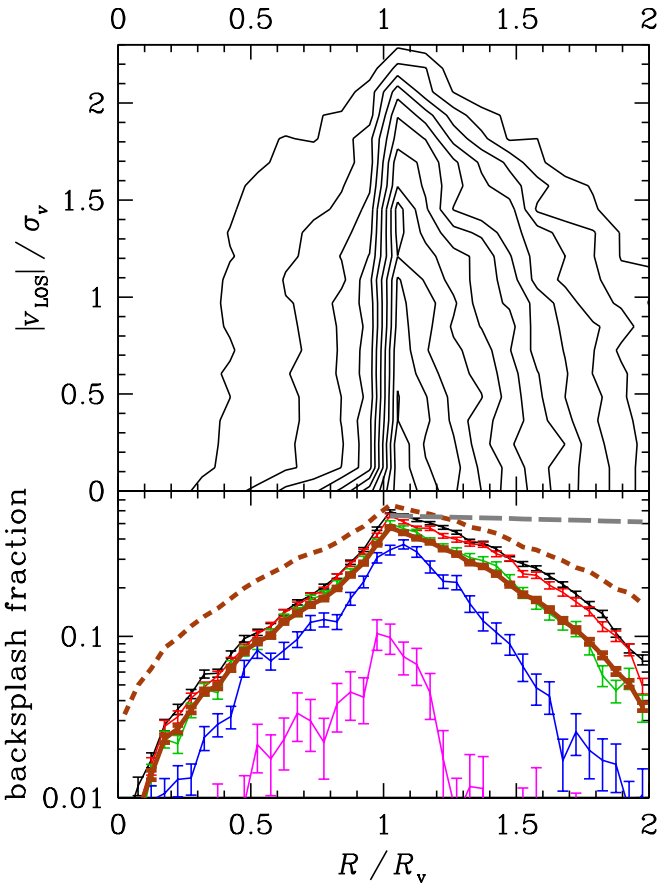

Figure C.3: *Upper panel*: contours in projected phase space of the fraction of particles of the stacked mock cluster that contribute to the backsplash class (Scheme 3; see Fig. C.1). *Contours* are linearly spaced from 0.05 to 0.55 going downwards. *Lower panel*: fraction of backsplash particles in bins of absolute LOS velocity: 0–0.5 (*top*, *black*), 0.5–1.0 (*red*), 1.0–1.5 (*green*), 1.5–2.0 (*blue*), and $> 2.0\,\sigma_v$ (*bottom*, *magenta*), and summed over all LOS velocities $< 3\,\sigma$ (*thick brown*). The *dashed thick brown curve* shows the maximum backsplash fraction from Scheme 5 while the *long-dashed thick grey line* is the relation deduced from observations by Pimbblet (2010) (see Sec. 6.6.3).

Table C.2: The fraction of virialized (v) infall (i) and backsplash (b) particles of the stacked mock cluster in cells of projected phase space with Scheme 3

$r/R_{\rm v}$	0–0.5			0.5–1			1–1.5			1.5–2		
$\lvert v_{\rm LOS}\rvert/\sigma_v$	v	i	b	v	i	b	v	i	b	v	i	b
0–1	0.89	0.07	0.04	0.50	0.29	0.21	0.00	0.56	0.44	0.00	0.83	0.17
1–2	0.81	0.16	0.03	0.41	0.42	0.17	0.00	0.67	0.33	0.00	0.92	0.08
2–3	0.68	0.32	0.00	0.27	0.71	0.02	0.00	0.98	0.02	0.00	1.00	0.00

Note: 'v', 'i' and 'b' stand for the virial, infall and backsplash classes, respectively.

Table C.3: K-S test probabilities for the null hypothesis that pairs of subsamples have distributions of M^* arising from the same parent distribution. Columns $v1$, $v2$, and $v3$ correspond to $|v_{\rm LOS}|/\sigma_v = 0$–1, 1–2, and 2–3, respectively. Statistically significant differences between subsample pairs are highlighted in bold.

	$R/R_{\rm v}\leq$0.5			0.5$<R/R_{\rm v}\leq$1.0			1.0$<R/R_{\rm v}\leq$1.5			1.5$<R/R_{\rm v}\leq$2.0			field
	$v1$	$v2$	$v3$	$v1$	$v2$	$v3$	$v1$	$v2$	$v3$	$v1$	$v2$	$v3$	
	1	2	3	4	5	6	7	8	9	10	11	12	
1	1.0E+00	**7.3E-08**	**2.5E-09**	**4.2E-20**	**2.9E-20**	**1.6E-09**	**1.2E-12**	**1.8E-09**	**4.1E-08**	**2.7E-11**	**1.4E-10**	**8.5E-06**	**0.0E+00**
2		1.0E+00	**1.7E-02**	**3.1E-03**	**6.2E-06**	**9.9E-04**	**5.9E-03**	6.1E-02	**1.2E-03**	**2.1E-02**	5.5E-02	6.5E-02	**2.6E-13**
3			1.0E+00	1.7E-01	3.6E-01	3.6E-01	**4.3E-02**	1.2E-01	2.6E-01	**3.6E-02**	3.2E-01	7.3E-01	2.6E-01
4				1.0E+00	**2.8E-02**	1.3E-01	2.1E-01	7.6E-01	2.3E-01	1.4E-01	8.8E-01	6.7E-01	**5.6E-07**
5					1.0E+00	6.5E-01	**2.5E-02**	8.8E-02	8.9E-01	**3.3E-03**	**3.2E-02**	6.4E-01	1.3E-01
6						1.0E+00	**3.8E-02**	9.9E-02	7.8E-01	**2.0E-02**	7.9E-02	2.6E-01	1.8E-01
7							1.0E+00	7.9E-01	1.0E-01	9.7E-01	5.8E-01	6.7E-01	**2.6E-04**
8								1.0E+00	1.5E-01	8.4E-01	7.9E-01	8.3E-01	**5.4E-03**
9									1.0E+00	**4.3E-02**	9.9E-02	5.2E-01	4.3E-01
10										1.0E+00	4.9E-01	7.0E-01	**5.4E-06**
11											1.0E+00	9.1E-01	**3.7E-03**
12												1.0E+00	3.8E-01

symmetric relative to the virial radius. However, at low $|v_{\rm LOS}|$ the fraction is skewed towards higher values beyond the virial radius (see, e.g. thick brown curve of bottom panel representing all particles with $|v_{\rm LOS}| < 3\,\sigma_v$). Indeed, at projected radii smaller than the virial radius, the backsplash particles must be in the foreground or background of the virial sphere, and geometric effects typically cause their 3D velocities to be aligned with the line of sight, making it difficult to obtain small absolute LOS velocities. These trends are confirmed in Table C.2, which lists the fractions of the three classes of particles in cells of projected phase space.

C.3 Kolmogorov-Smirnov Statistics

In this section, we present tables of probabilities, from the Kolmogorov-Smirnov test, that various sub-samples of different physical quantities arise from the same parent distributions (§ 6.4).

Table C.4: Same as Table C.3, but with BCGs excluded.

	$R/R_{\rm v} \leq 0.5$			$0.5 < R/R_{\rm v} \leq 1.0$			$1.0 < R/R_{\rm v} \leq 1.5$			$1.5 < R/R_{\rm v} \leq 2.0$			field
	$v1$	$v2$	$v3$	$v1$	$v2$	$v3$	$v1$	$v2$	$v3$	$v1$	$v2$	$v3$	
	1	2	3	4	5	6	7	8	9	10	11	12	
1	1.0E+00	**5.2E-08**	**6.6E-10**	**1.5E-20**	**1.2E-21**	**1.2E-09**	**6.9E-15**	**9.0E-10**	**6.5E-09**	**2.0E-12**	**9.5E-11**	**3.9E-06**	**0.0E+00**
2		1.0E+00	**9.2E-03**	**1.5E-03**	**1.7E-06**	**2.3E-04**	**8.9E-04**	**3.6E-02**	**5.1E-04**	**4.0E-03**	**3.8E-02**	**3.8E-02**	**3.9E-13**
3			1.0E+00	2.0E-01	4.3E-01	2.7E-01	9.8E-02	1.3E-01	2.5E-01	**4.4E-02**	2.2E-01	7.4E-01	3.4E-01
4				1.0E+00	**2.3E-02**	6.3E-02	5.5E-01	7.6E-01	1.7E-01	3.0E-01	8.5E-01	6.5E-01	**2.6E-06**
5					1.0E+00	6.9E-01	**4.6E-02**	1.0E-01	8.4E-01	**5.4E-03**	**2.5E-02**	6.7E-01	5.8E-01
6						1.0E+00	6.7E-02	7.7E-02	7.3E-01	**3.4E-02**	**4.1E-02**	2.6E-01	1.5E-01
7							1.0E+00	9.8E-01	1.0E-01	8.9E-01	8.1E-01	7.8E-01	**4.5E-03**
8								1.0E+00	1.3E-01	8.9E-01	7.3E-01	8.7E-01	**1.7E-02**
9									1.0E+00	5.2E-02	6.9E-02	4.5E-01	1.9E-01
10										1.0E+00	4.9E-01	6.8E-01	**5.8E-05**
11											1.0E+00	9.0E-01	**8.2E-03**
12												1.0E+00	5.3E-01

Table C.5: Same as Table C.3, but for the difference between the $(g-r)^{0.1}$ colour and the best-fitted red sequence (RS).

	$R/R_{\rm v} \leq 0.5$			$0.5 < R/R_{\rm v} \leq 1.0$			$1.0 < R/R_{\rm v} \leq 1.5$			$1.5 < R/R_{\rm v} \leq 2.0$			field
	$v1$	$v2$	$v3$	$v1$	$v2$	$v3$	$v1$	$v2$	$v3$	$v1$	$v2$	$v3$	
	1	2	3	4	5	6	7	8	9	10	11	12	
1	1.0E+00	1.2E-01	**1.0E-04**	**5.9E-30**	**3.4E-29**	**1.3E-10**	**0.0E+00**	**0.0E+00**	**2.0E-29**	**0.0E+00**	**0.0E+00**	**9.0E-27**	**0.0E+00**
2		1.0E+00	**1.7E-02**	**1.5E-16**	**6.1E-17**	**1.8E-07**	**1.0E-41**	**7.3E-41**	**6.2E-23**	**1.4E-45**	**8.4E-36**	**7.6E-20**	**0.0E+00**
3			1.0E+00	**5.8E-05**	**4.6E-06**	**1.6E-02**	**1.2E-13**	**4.5E-16**	**1.8E-12**	**3.9E-15**	**2.5E-13**	**2.4E-08**	**0.0E+00**
4				1.0E+00	5.6E-02	3.3E-01	**1.3E-11**	**1.2E-14**	**3.8E-10**	**2.2E-15**	**2.2E-11**	**1.1E-07**	**0.0E+00**
5					1.0E+00	8.1E-01	**1.1E-04**	**1.6E-07**	**1.3E-06**	**5.4E-06**	**1.8E-05**	**1.0E-04**	**0.0E+00**
6						1.0E+00	**2.4E-03**	**4.1E-05**	**6.1E-05**	**8.0E-04**	**9.9E-04**	**5.5E-03**	**4.9E-29**
7							1.0E+00	1.1E-01	**1.8E-02**	6.1E-01	2.7E-01	1.0E-01	**0.0E+00**
8								1.0E+00	3.3E-01	1.3E-01	6.5E-01	3.6E-01	**1.7E-23**
9									1.0E+00	**5.0E-02**	1.5E-01	1.5E-01	**3.0E-06**
10										1.0E+00	8.1E-01	4.8E-01	**0.0E+00**
11											1.0E+00	5.6E-01	**1.4E-31**
12												1.0E+00	**1.9E-16**

Table C.6: Same as Table C.3, but for SFR/M^*.

	$R/R_{\rm v} \leq 0.5$			$0.5 < R/R_{\rm v} \leq 1.0$			$1.0 < R/R_{\rm v} \leq 1.5$			$1.5 < R/R_{\rm v} \leq 2.0$			field
	$v1$	$v2$	$v3$	$v1$	$v2$	$v3$	$v1$	$v2$	$v3$	$v1$	$v2$	$v3$	
	1	2	3	4	5	6	7	8	9	10	11	12	
1	1.0E+00	**5.8E-04**	**1.0E-04**	**1.0E-26**	**8.1E-28**	**4.7E-12**	**0.0E+00**	**5.6E-45**	**1.1E-22**	**0.0E+00**	**1.8E-40**	**1.5E-21**	**0.0E+00**
2		1.0E+00	**1.7E-02**	**1.0E-08**	**6.2E-13**	**1.3E-06**	**4.1E-25**	**1.1E-25**	**1.2E-16**	**2.1E-33**	**1.7E-21**	**1.2E-14**	**0.0E+00**
3			1.0E+00	**3.4E-03**	**1.4E-02**	**3.1E-02**	**1.5E-06**	**1.1E-07**	**7.5E-08**	**1.0E-07**	**2.5E-06**	**3.4E-06**	**1.6E-21**
4				1.0E+00	6.1E-02	8.4E-02	**4.1E-07**	**1.6E-09**	**4.5E-09**	**2.3E-11**	**3.2E-08**	**7.9E-07**	**0.0E+00**
5					1.0E+00	4.7E-01	**6.2E-04**	**1.1E-04**	**6.1E-06**	**3.0E-05**	**3.4E-04**	**1.8E-04**	**1.4E-26**
6						1.0E+00	**9.1E-03**	**2.3E-02**	**6.3E-03**	**4.1E-03**	**1.6E-02**	**1.1E-02**	**5.5E-07**
7							1.0E+00	1.5E-01	**2.5E-03**	3.0E-01	**7.3E-02**	**2.9E-02**	**1.9E-17**
8								1.0E+00	**9.7E-02**	4.6E-01	5.2E-01	4.5E-01	**2.9E-05**
9									1.0E+00	**1.7E-02**	8.9E-02	7.5E-01	1.1E-01
10										1.0E+00	4.3E-01	1.9E-01	**2.7E-14**
11											1.0E+00	6.0E-01	**1.8E-08**
12												1.0E+00	**2.9E-03**

Table C.7: Same as Table C.3, but for Hδ.

	$R/R_{\rm v}$ ≤0.5			0.5<$R/R_{\rm v}$ ≤1.0			1.0<$R/R_{\rm v}$ ≤1.5			1.5<$R/R_{\rm v}$ ≤2.0			field
	$v1$	$v2$	$v3$	$v1$	$v2$	$v3$	$v1$	$v2$	$v3$	$v1$	$v2$	$v3$	
	1	2	3	4	5	6	7	8	9	10	11	12	
1	1.0E+00	**1.7E-06**	**7.0E-09**	**0.0E+00**	**0.0E+00**	**6.1E-22**	**0.0E+00**	**0.0E+00**	**8.9E-37**	**0.0E+00**	**0.0E+00**	**1.1E-27**	**0.0E+00**
2		1.0E+00	**6.6E-04**	**1.4E-18**	**2.6E-24**	**9.6E-14**	**3.7E-38**	**7.7E-39**	**4.4E-25**	**1.5E-39**	**6.2E-35**	**1.6E-17**	**0.0E+00**
3			1.0E+00	**6.0E-03**	**8.5E-05**	**2.8E-03**	**7.3E-07**	**2.8E-10**	**2.0E-09**	**2.7E-06**	**9.4E-08**	**1.2E-04**	**4.4E-36**
4				1.0E+00	**2.4E-03**	**5.8E-03**	**7.2E-07**	**1.9E-11**	**4.4E-11**	**1.3E-08**	**3.6E-09**	**1.4E-04**	**0.0E+00**
5					1.0E+00	7.8E-01	2.0E-01	**2.4E-04**	**2.7E-06**	5.5E-02	**1.3E-02**	7.8E-02	**1.6E-42**
6						1.0E+00	2.1E-01	**1.6E-02**	**6.4E-04**	2.2E-01	7.7E-02	1.7E-01	**1.0E-12**
7							1.0E+00	**3.6E-02**	**3.6E-04**	1.0E-01	3.1E-01	5.7E-01	**6.1E-42**
8								1.0E+00	1.6E-01	**1.8E-02**	3.2E-01	4.3E-01	**5.4E-13**
9									1.0E+00	**9.9E-04**	**1.0E-02**	6.6E-02	**1.3E-02**
10										1.0E+00	4.1E-01	8.6E-01	**1.0E-43**
11											1.0E+00	9.8E-01	**9.1E-19**
12												1.0E+00	**7.3E-09**

Table C.8: Same as Table C.3, but for D_n4000.

	$R/R_{\rm v}$ ≤0.5			0.5<$R/R_{\rm v}$ ≤1.0			1.0<$R/R_{\rm v}$ ≤1.5			1.5<$R/R_{\rm v}$ ≤2.0			field
	$v1$	$v2$	$v3$	$v1$	$v2$	$v3$	$v1$	$v2$	$v3$	$v1$	$v2$	$v3$	
	1	2	3	4	5	6	7	8	9	10	11	12	
1	1.0E+00	**3.5E-09**	**5.1E-09**	**0.0E+00**	**0.0E+00**	**9.8E-15**	**0.0E+00**	**0.0E+00**	**8.8E-35**	**0.0E+00**	**0.0E+00**	**1.2E-27**	**0.0E+00**
2		1.0E+00	**1.1E-04**	**3.1E-23**	**1.9E-23**	**8.4E-09**	**4.7E-40**	**6.2E-38**	**1.9E-24**	**1.4E-45**	**1.3E-35**	**5.2E-18**	**0.0E+00**
3			1.0E+00	**8.1E-03**	**7.2E-05**	**4.7E-02**	**7.4E-07**	**9.2E-09**	**5.7E-09**	**9.0E-07**	**3.7E-08**	**8.2E-05**	**1.2E-34**
4				1.0E+00	**2.2E-02**	1.0E-01	**1.2E-06**	**4.8E-09**	**2.5E-07**	**1.6E-11**	**5.6E-09**	**1.9E-05**	**0.0E+00**
5					1.0E+00	2.8E-01	6.3E-02	**8.2E-04**	**9.8E-05**	**1.0E-03**	**5.8E-03**	**1.7E-02**	**0.0E+00**
6						1.0E+00	**1.4E-02**	**5.6E-04**	**5.1E-05**	**1.7E-02**	**5.2E-03**	9.5E-02	**1.1E-17**
7							1.0E+00	7.1E-02	**7.5E-03**	1.1E-01	6.9E-02	1.8E-01	**0.0E+00**
8								1.0E+00	2.1E-01	1.2E-01	9.4E-01	1.0E-01	**7.4E-17**
9									1.0E+00	**2.1E-02**	1.1E-01	**4.9E-02**	**1.3E-03**
10										1.0E+00	3.5E-01	5.9E-01	**2.5E-38**
11											1.0E+00	1.2E-01	**1.5E-21**
12												1.0E+00	**4.1E-10**

Bibliography

Abadi M. G., Moore B., Bower R. G., 1999, MNRAS, 308, 947

Abazajian K. N., et al., 2009, ApJS, 182, 543

Abell, G. O., Corwin, H. G., Jr., Olowin, R. P., 1989, ApJS, 70, 1

Abraham, R. G., van den Bergh, S., Glazebrook, K., Ellis, R. S., Santiago, B. X., Suva, P., Griffiths, R. E., 1996, ApJS, 107, 1

Adami C., Biviano A., Mazure A., 1998, A&A, 331, 439

Adami C., Biviano A., Durret F., Mazure A., 2005, A&A, 443, 17

Adelman-McCarthy et al., J. K., 2006, AJS, 162, 38

Aguerri J. A. L., Iglesias-Páramo J., Vílchez J. M., Muñoz-Tuñón C., Sánchez-Janssen R., 2005, AJ, 130, 475

Ann H. B., Park C., Choi Y.-Y., 2008, MNRAS, 389, 86

Arnold T. J., Martini P., Mulchaey J. S., Berti A., Jeltema T. E., 2009, ApJ, 707, 1691

Ashby, M.L.N., & the SFRS team

Ashman, K.M., Bird, C.M. & Zepf, S.E., 1994, AJ, 108, 2348

Bai L., Rieke G. H., Rieke M. J., Hinz J. L., Kelly D. M., Blaylock M., 2006, ApJ, 639, 827

Bai, L., Rasmussen, J., Mulchaey, J. S., Dariush, A., Raychaudhury, S., Ponman, T. J., 2010, ApJ, 713, 637

Baldwin, J. A., Phillips, M. M., Terlevich, R., 1981, PASP, 93, 5

Balogh, M. L., Morris, S. L., Yee, H. K. C., Carlberg, R. G., Ellingson, E., 1999, ApJ, 527, 54

Balogh, M.L., Navarro, J. F., Morris, S. L., 2000, ApJ, 540, 113

Balogh, M. L., Baldry, I K., Nichol, R., Miller, C., Bower, R., Glazebrook, K., 2004, ApJ, 615L, 101

Balogh, M. L., et al., 2004, MNRAS, 348, 1355

Balogh M. L., Miller C., Nichol R., Zabludoff A., Goto T., 2005, MNRAS, 360, 587

Balogh M. L., Navarro J. F., Morris S. L., 2000, ApJ, 540, 113

Barazza F. D., et al., 2009, A&A, 508, 665

Barkana, R., & Loeb, A., 1999, ApJ, 523, 54

Beers, T. C., Flynn, K., & Gebhardt, K., 1990, ApJ, 100, 32

Bekki, K., 1999, ApJ, 510, L15

Bekki, K., Couch, W. J., Shioya, Y., 2001, PASJ, 53, 395

Bell E. F., McIntosh D. H., Katz N., Weinberg M. D., 2003, ApJS, 149, 289

Bergvall, N., Laurikainen, E., Aalto, S., 2003, astro-ph/0304384

Bernstein G. M., Guhathakurta P., Raychaudhury S., Giovanelli R., Haynes M. P., Herter T., Vogt N. P., 1994, AJ, 107, 1962

Berrier J. C., Stewart K. R., Bullock J. S., Purcell C. W., Barton E. J., Wechsler R. H., 2009, ApJ, 690, 1292

Bertin E., Arnouts S., A&AS, 117, 393

Bertin, E., Mellier, Y., Radovich, M., Missonnier, G., Didelon, P., & Morin, B., 2002, Astronomical Data Analysis Software and Systems XI, 281, 228

Bertschinger E., 1985, ApJS, 58, 39

Best, P. N., Kauffmann, G., Heckman, T. M., Brinchmann, J., Charlot, S., Ivezic', $\check{Z}$., White, S. D. M., 2005, MNRAS, 362, 25

Bharadwaj, S., Sahni, V., Sathyaprakash, B. S., Shandarin, S. F., Yess, C., 2000, ApJ, 528, 21

Bharadawaj, S. & Pandey, B., 2004, ApJ, 615, 1

Bigiel, F., Leroy, A., Walter, F., Brinks, E., de Blok, W. J. G., Madore, B., Thornley, M. D., 2008, AJ, 138, 2846B

Bildfell, C., Hoekstra, H., Babul, A., Mahdavi, A., 2008, MNRAS, 389, 1637

Biviano A., Girardi M., Giuricin G., Mardirossian F., Mezzetti M., 1992, ApJ, 396, 35

Biviano, A., Katgert, P., Mazure, A., Moles, M., den Hartog, R., Perea, J., Focardi, P., 1997, A&A, 321, 84

Blanton M. R., et al., 2001, AJ, 121, 2358

Blanton M. R., et al., 2003, ApJ, 592, 819

Blanton, M. R., et al., ApJ, 129, 2562

Blanton M. R., Eisenstein D., Hogg D. W., Zehavi I., 2006, ApJ, 645, 977

Blanton M. R., Roweis S., 2007, AJ, 133, 734

Bond, J. R., Kofman, L. & Pogosyan, D., 1996, Nature, 380, 603

Bond N. A., Strauss M. A., Cen R., 2010, MNRAS, 409, 156

Boquien, M., et al. 2009, ApJ, 706, 553

Borgani S., et al., 2004, MNRAS, 348, 1078

Boselli A., Gavazzi G., Lequeux J., Buat V., Casoli F., Dickey J., Donas J., 1997, A&A, 327, 522

Boselli A., et al., 1997, A&A, 324, L13

Boselli, A., et al. 1998, A&A, 335, 53

Boselli, A., Gavazzi, G., Donas, J., Scodeggio, M., 2001, AJ, 121, 753

Boselli A., Lequeux J., Gavazzi G., 2004, A&A, 428, 409

Boselli, A. & Gavazzi, G., 2006, PASP, 118, 517

Boselli A., Boissier S., Cortese L., Gavazzi G., 2008, ApJ, 674, 742

Bothun G. D., Schombert J. M., 1990, ApJ, 360, 436

Bothun G. D., Schommer R. A., Sullivan W. T., III, 1984, AJ, 89, 466

Boúe, G., Durret, F., Adami, C., Mamon, G. A., Ilbert, O., Cayatte, V., 2008, A&A, 489, 11

Bothwell M. S., Kennicutt R. C., Lee J. C., 2009, MNRAS, 400, 154

Boquien, M., et al., 2009, ApJ, 706, 553

Bournaud, F., Combes, F., & Jog, C. J., 2004, A&A, 418L, 27

Bouwens R. J., Illingworth G. D., Blakeslee J. P., Broadhurst T. J., Franx M., 2004, ApJ, 611, L1

Bouwens R. J., et al., 2010, arXiv, arXiv:1006.4360

Bowen, I. S., 1927, Nat, 120, 473

Bowen, I. S., 1928, ApJ, 67, 1

Bressan A., et al., 2006, ApJ, 639, L55

Briel U. G., Henry J. P., Böhringer H., 1992, A&A, 259, L31

Brinchmann, J., Charlot, S., White, S. D. M., Tremonti, C., Kauffmann, G., Heckman, T., & Brinkmann, J., 2004, MNRAS, 351, 1151

Bruzual, A. G., 1983, ApJ, 273, 105

Bruzual A. G., Charlot S., 1993, ApJ, 405, 538

Bruzual G., Charlot S., 2003, MNRAS, 344, 1000

Buat, V., Donas, J., Milliard, B., & Xu, C. 1999, A&A, 352, 371

Buat, V., Boselli, A., Gavazzi, G., & Bonfanti, C. 2002, A&A, 383, 801

Buat, V., et al., 2005, ApJ, 619, L59

Burns J. O., Roettiger K., Ledlow M., Klypin A., 1994, ApJ, 427 L87

Butcher H., Oemler A., Jr., 1978, ApJ, 226, 559

Butcher, H., & Oemler, A., Jr., 1984, ApJ, 285, 426

Caldwell N., Rose J. A., Sharples R. M., Ellis R. S., Bower R. G., 1993, AJ, 106, 473

Caldwell N., Rose J. A., 1997, AJ, 113, 492

Calzetti, D. 2010, arXiv:1010.4996

Caldwell, N., Rose, J.A., & Dendy, K., 1999, AJ, 117, 140

Calzetti, D., 1994, ApJ, 429, 582

Calzetti, D., 1997, AJ, 113, 162

Calzetti D., et al., 2005, ApJ, 633, 871

Calzetti, D., et al., 2007, ApJ, 666, 870

Cao, C., Wu, H., Wang, J., Hao, C., Deng, Z., Xia, X., Zou, Z., 2006, ChJAA, 6, 197

Capak P., et al., 2007, ApJS, 172, 99

Carlberg, R. G., Yee, H. K. C., Ellingson, E., 1997, ApJ, 478, 462

Cen, R., Ostriker, J. P., 1999, ApJ, 514, 1

Chen, Y.-M., Wang, J.-M., Yan, C.-S., Hu, C., Zhang, S., 2009, ApJ, 695L, 130

Charlot S., Fall S.M., 2000, ApJ, 539, 718

Charlot S., Longhetti, M., 2001, MNRAS, 323, 887

Chiboucas K., Tully R. B., Marzke R. O., Trentham N., Ferguson H. C., Hammer D., Carter D., Khosroshahi H., 2010, ApJ, 723, 251

Chincarini G., Rood H. J., 1976, ApJ, 206, 30

Chincarini G., Rood H. J., 1977, ApJ, 214, 351

Choi E., Bond N. A., Strauss M. A., Coil A. L., Davis M., Willmer C. N. A., 2010, MNRAS, 406, 320

Clemens M. S., Bressan A., Panuzzo P., Rampazzo R., Silva L., Buson L., Granato G. L., 2009, MNRAS, 392, 982

Colberg, J. M., White, S. D. M., Jenkins, A., & Pearce, F. R., 1999, MNRAS, 308, 593

Colberg, J. M., et al., MNRAS, 319, 209

Colberg, J. M., Krughoff, K. S., Connolly, A. J., 2004, MNRAS, 359, 272

Colberg J. M., 2007, MNRAS, 375, 337

Colless M., Dunn A. M., 1996, ApJ, 458, 435

Colless, M. M., et al., 2001, MNRAS, 328, 1239

Combes, F., Young, L.M., & Bureau, M., 2007, MNRAS, 377, 1795

Condon, J. J., Anderson, M. L., & Helou, G. 1991, ApJ, 376, 95

Condon J. J., 1992, ARA&A, 30, 575

Condon J. J., Cotton W. D., Greisen E. W., Yin Q. F., Perley R. A., Taylor G. B., Broderick J. J., 1998, AJ, 115, 1693

Condon J. J., Cotton W. D., Greisen E. W., Yin Q. F., Perley R. A., Taylor G. B., Broderick J. J., 2002, yCat, 8065, 0

Conselice, C. J., 2003, ApJS, 147, 1

Cooper, M. C., et al., 2007, MNRAS, 376, 1445

Cortese L., Gavazzi G., Boselli A., Iglesias-Páramo J., Carrasco L., 2004, A&A, 425, 429

Cortese, L., et al., 2007, MNRAS, 376, 157

Cortese L., Gavazzi G., Boselli A., 2008, MNRAS, 390, 1282

Cowie L. L. & Songaila A., 1977, Nature, 266, 501

Croft, R. A. C., Di Matteo, T., Davè, R., Hernquist, L., Katz, N., Fardal, M. A., Weinberg, D. H., 2001, ApJ, 557, 67

Crocker, A. F., Jeong, H., Komugi, S., Combes, F., Bureau, M., Young, L. M., Yi, S., 2009, MNRAS, 393, 1255

da Cunha E., Eminian C., Charlot S., Blaizot J., 2010, MNRAS, 403, 1894

Dale D. A., Helou G., 2002, ApJ, 576, 159

Dale, D. A., et al., 2007, ApJ, 655, 863

Maaike, D., Labbé, I., Franx, M., van Dokkum, P. G., Taylor, E. N., Gawiser, E. J., 2009, ApJ, 690, 937

Davies, R. I., Sternberg, A., Lehnert, M. D., Tacconi-Garman, L. E., 2005, ApJ, 633, 105

Davies, R. I., Sànchez, F. M., Genzel, R., Tacconi, L. J., Hicks, E. K. S., Friedrich, S., Sternberg, A., 2007, ApJ, 671, 1388

Davis D. S., Mushotzky R. F., 1993, AJ, 105, 409

Del Pozzo W., Raychaudhury S., Babul A., 2011, in preparation

De Lucia G., Poggianti B. M., Halliday C., Milvang-Jensen B., Noll S., Smail I., Zaritsky D., 2009, MNRAS, 1379

De Propris R., Stanford S. A., Eisenhardt P. R., Dickinson M., 2003, ApJ, 598, 20

De Propris, R., et al., MNRAS, 2004, 351, 125

de Vaucouleurs G., 1961, ApJS, 6, 213

de Zeeuw, P.T., et al., 2002, MNRAS, 329, 513

Diaferio, A., Geller, M. J., 1997, ApJ, 481, 633

Dolag, K., Meneghetti, M., Moscardini, L., Rasia, E., Bonaldi, A., 2006, MNRAS, 2006, 370, 656

Dolag K., Borgani S., Murante G., Springel V., 2009, MNRAS, 399, 497

Dressler, A., 1980, ApJ, 236, 531

Dressler A., Gunn J. E., 1982, ApJ, 263, 533

Dressler A., Gunn J. E., 1992, ApJS, 78, 1

Dressler A., Shectman S. A., 1988, AJ, 95, 985

Dressler, A., Oemler, A., Jr., Poggianti, B. M., Smail, I., Trager, S., Shectman, S. A., Couch, W.J., & Ellis, R.S., 2004, ApJ, 617, 867

Dünner R., Reisenegger A., Meza A., Araya P. A., Quintana H., 2007, MNRAS, 376, 1577

Ebeling, H., Barrett, E., Donovan, D., 2004, ApJ, 609L, 49

Edwards L. O. V., Fadda D., Frayer D. T., Lima Neto G. B., Durret F., 2010, AJ, 140, 1891

Edwards L. O. V., Fadda D., Frayer D. T., 2010, ApJ, 724, L143

Ellingson, E., Lin, H., Yee, H. K. C., Carlberg, R. G., 2001, ApJ, 547, 609

Ellison, S. L., Patton, D. R., Simard, L. & McConnachie, A. W., 2008, ApJ, 672, L107

Rev. Mexicana Astron. Astrofis. Conf. Ser. 6, 165

Elmegreen, B. G., & Efremov, Y. N., 1997, ApJ, 480, 235

Engelbracht, C. W., Rieke, G. H., Gordon, K. D., Smith, J.-D. T., Werner, M. W., Moustakas, J., Willmer, C. N. A., & Vanzi, L. 2008, ApJ, 678, 804

Faber, S. M., 1973, ApJ, 179, 731

Fadda, D., Biviano, A., & Durret, F., 2008, ApJ, 672, L9

Feulner, G., Gabasch, A., Salvato, M., Drory, N., Hopp, U., & Bender, R. 2005, ApJ, 633, L9

Finoguenov A., Briel U. G., Henry J. P., 2003, A&A, 410, 777

Fontanelli P., 1984, A&A, 138, 85

Freedman, W. L., et al. 2001, ApJ, 553, 47

Fujita, Y., 1998, ApJ, 509, 587

Fujita, Y., & Nagashima, M., 1999, ApJ, 516, 619

Fujita, Y., 2004, PASJ, 56, 29F

Gao, Y. & Solomon, P. M., 2004, ApJ, 606, 271

Gallazzi, A., Charlot, S., Brinchmann, J., White, S. D. M., Tremonti, C. A., 2005, MNRAS, 362, 41

Gallazzi, A., et al., 2009, ApJ, 690, 1883

Gavazzi, G., Cortese, L., Boselli, A., Iglesias-Paramo, J., Vìlchez, J. M., Carrasco, L., 2003, ApJ, 597, 210

Gay C., Pichon C., Le Borgne D., Teyssier R., Sousbie T., Devriendt J., 2010, MNRAS, 404, 1801

Geller M. J., Huchra J. P., 1989, Sci, 246, 897

Ghigna S., Moore B., Governato F., Lake G., Quinn T., Stadel J., 1998, MNRAS, 300, 146

Gil de Paz, A., et al., 2007, ApJS, 173, 185

Gill, S. P. D., Knebe, A., & Gibson, B. K., 2005, MNRAS, 356, 1327

Gioia I. M., Gregorini L., Klein U., 1982, A&A, 116, 164

Giovanelli R., Haynes M. P., 1985, ApJ, 292, 404

Girardi M., Rigoni E., Mardirossian F., Mezzetti M., 2003, A&A, 406, 403

Goldader J. D., Meurer G., Heckman T. M., Seibert M., Sanders D. B., Calzetti D., Steidel C. C., 2002, ApJ, 568, 651

Gnedin O. Y., Hernquist L., Ostriker J. P., 1999, ApJ, 514, 109

Gnedin, O. Y., 2003a, ApJ, 589, 752

Gnedin, O. Y., 2003b, ApJ, 582, 141

Gómez, P. L., et al., 2003, ApJ, 584, 210

González R. E., Padilla N. D., 2009, MNRAS, 397, 1498

González R. E., Padilla N. D., 2010, MNRAS, 407, 1449

Gordon K. D., Clayton G. C., Witt A. N., Misselt K. A., 2000, ApJ, 533, 236

Goto, T., et al., 2003, PASJ, 55, 771

Goto, T., et al., 2003, PASJ, 55, 739

Goto, T., et al.,2003c, PASJ, 55, 757

Goto, T., Yagi, M., Tanaka, M., Okamura, S., 2004, MNRAS, 348, 515

Goto T., 2005, MNRAS, 357, 937

Goto, T., 2006, MNRAS, 369, 1765

Goulding A. D., Alexander D. M., 2009, MNRAS, 398, 1165

Graci-Carpio, J., Garcìa-Burillo, S., Planesas, P., 2008, Ap&SS, 313, 331G

Graves, G.J., Faber, S.M., Schiavon, R.P. & Yan, R., 2007, ApJ, 671, 243

Graves G. J., Faber S. M., Schiavon R. P., 2009, ApJ, 693, 486

Gray M. E., Wolf C., Meisenheimer K., Taylor A., Dye S., Borch A., Kleinheinrich M., 2004, MNRAS, 347, L73

Gregory S. A., Thompson L. A., 1978, ApJ, 222, 784

Gunn, J. E., & Gott, J. R., III, 1972, ApJ, 176, 1

Haarsma D. B., Partridge R. B., Windhorst R. A., Richards E. A., 2000, ApJ, 544, 641

Haines, C. P., La Barbera, F., Mercurio, A., Merluzzi, P., Busarello, G., 2006, ApJ, 647L, 21

Haines, C. P., Merluzzi, P., Mercurio, A., Gargiulo, A., Krusanova, N., Busarello, G., La Barbera, F., Capaccioli, M., 2006, MNRAS, 371, 55

Haines, C. P., Gargiulo, A., La Barbera, F., Mercurio, A., Merluzzi, P., Busarello, G., 2007, MNRAS, 381, 7

Haines, C. P., Gargiulo, A. & Merluzzi, P., 2008, MNRAS, 385, 1201

Haines C. P., et al., 2009, ApJ, 704, 126

Hartwick, F. D. A., 1971, ApJ, 163, 431

Helou G., Salpeter E. E., Krumm N., 1979, ApJ, 228, L1

Helou, G., Khan, I. R., Malek, L., & Boehmer, L. 1988, ApJS, 68, 151

Helou, G., et al. 2004, ApJS, 154, 253

Hickox R. C., et al., 2009, ApJ, 696, 891

Hirashita H., Buat V., Inoue A. K., 2003, A&A, 410, 83

Hogg, D. W., Tremonti, C. A., Blanton, M. R., Finkbeiner, D. P., Padmanabhan, N., Quintero, A. D., Schlegel, D. J., & Wherry, N. 2005, ApJ, 624, 162

Hopkins A. M., Irwin M. J., Connolly A. J., 2001, ApJ, 558, L31

Hopkins, A. M., 2004, ApJ, 615, 209

Hopkins, P. F., Hernquist, L., Cox, T. J., Kereš, D., 2008, ApJS, 175, 356

Howell J. H., et al., 2010, ApJ, 715, 572

Huang, J.-S., et al. 2007, ApJ, 664, 840

Huchra, J. P. & Geller, M. J., 1982, ApJ, 257, 423

Huggins, W., Miller, W. A., 1864, RSPT, 154, 437

Iglesias-Páramo J., Boselli A., Gavazzi G., Cortese L., Vílchez J. M., 2003, A&A, 397, 421

Iglesias-Páramo, J., et al. 2006, ApJS, 164, 38

Ishigaki, M., Goto, T., & Matsuhara, H., 2007, MNRAS, 382, 270

Jenkins L. P., Hornschemeier A. E., Mobasher B., Alexander D. M., Bauer F. E., 2007, ApJ, 666, 846

Jiang C. Y., Jing Y. P., Faltenbacher A., Lin W. P., Li C., 2008, ApJ, 675, 1095

Jogee, S., Scoville, N., Kenney, J. D. P., ApJ, 630, 837

Jonsson P., Cox T. J., Primack J. R., Somerville R. S., 2006, ApJ, 637, 255

Kaastra, J. S., Lieu, R., Tamura, T., Paerels, F. B. S., den Herder, J. W., 2003, A&A, 397, 445

Kannappan S.J., Guie J.M., Baker A.J., 2009, AJ, 138, 579

Kapferer, W., Sluka, C., Schindler, S., Ferrari, C., Ziegler, B., 2009, A&A, 499, 87

Karachentsev, I. D., Karachentseva, V. E., Huchtmeier, W. K., & Makarov, D. I. 2004, AJ, 127, 2031

Karachentsev, I. D., Kudrya, Y. N., Karachentseva, V. E., & Mitronova, S. N. 2006, Astrophysics, 49, 450

Kartaltepe, J.S., Ebeling, H., Ma, C.J., & Donovan, D., 2008, MNRAS, 389, 1240

Kauffmann, G., Colberg, J. M., Diaferio, A., White, S. D. M., 1999, MNRAS, 303, 188

Kauffmann, G., et al., 2003a, MNRAS, 341, 33

Kauffmann, G., et al., 2003b, MNRAS, 346, 1055

Kauffmann, G., White, S. D. M., Heckman, T. M., Menàrd, B., Brinchmann, J., Charlot, S., Tremonti, C., Brinkmann, J., 2004, MNRAS, 353, 713

Kawata, D., & Mulchaey, J. S., 2008, ApJ, 672L, 103

Keel, W. C., 2005, AJ, 129, 1863

Kennicutt, R. C., Jr., ARA&A, 36, 189

Kennicutt, R. C., Jr., ApJ, 498, 541

Kennicutt, R. C., Jr., et al., 2003, PASP, 115, 928

Kennicutt R. C., et al., 2009, ApJ, 703, 1672

Kewley, L. J. & Dopita, M. A., 2002, ApJS, 142, 35

Khosroshahi H. G., Raychaudhury S., Ponman T. J., Miles T. A., Forbes D. A., 2004, MNRAS, 349, 527

Kim, K.-T., Kronberg, P. P., Giovannini, G., & Venturi, T., 1989, Nature, 341, 720

Klein U., Emerson D. T., 1981, A&A, 94, 29

Klimentowski J., Łokas E. L., Kazantzidis S., Mayer L., Mamon G. A., 2009, MNRAS, 397, 2015

Knapp G. R., Guhathakurta P., Kim D., Jura M. A., 1989, ApJS, 70, 329

Knebe A., Libeskind N. I, Knollmann S. R., Martinez-Vaquero L. A., Yepes G., Gottloeber S., Hoffman Y., 2010, arXiv, arXiv:1010.5670

Kodama T., Bower R. G., 2001, MNRAS, 321, 18

Kong, X., Charlot, S., Brinchmann, J., & Fall, S. M. 2004, MNRAS, 349, 769

Kormendy J., 1985, ApJ, 295, 73

Kormendy J., Fisher D. B., Cornell M. E., Bender R., 2009, ApJS, 182, 216

Koulouridis, E., Chavushyan, V., Plionis, M., Krongold, Y., Dultzin-Hacyan, D., 2006, ApJ, 651, 93

Koyama Y., et al., 2008, MNRAS, 391, 1758

Kubo J. M., Stebbins A., Annis J., Dell'Antonio I. P., Lin H., Khiabanian H., Frieman J. A., 2007, ApJ, 671, 1466

Laine, S., van der Marel, R. P., Rossa, J., Hibbard, J. E., Mihos, J. C., B*ö*ker, T., Zabludoff, A. I., 2003, AJ, 126, 2717

Larson, R. B., Tinsley, B. M., Caldwell, C. N., 1980, ApJ, 237, 692

Laurikainen, E., &, Moles, M., 1989, ApJ, 345, 176

Lee J. C., Kennicutt R. C., José G. Funes S. J., Sakai S., Akiyama S., 2009, ApJ, 692, 1305

Le Floc'h E., et al., 2005, ApJ, 632, 169

Leitherer C., et al., 1999, ApJS, 123, 3

Leroy, A. K., Walter, F., Brinks, E., Bigiel, F., de Blok, W. J. G., Madore, B., Thornley, M. D., 2008, AJ, 136, 2782

Lewis, I., et al., 2002, MNRAS, 334, 673

Li, C., Kauffmann, G., Heckman, T. M., White, S. D. M., Jing, Y. P., 2008, MNRAS, 385, 1915

Lilly, S. J., Le Fevre, O., Hammer, F., Crampton, D., 1996, ApJ, 460, L1

Lin D. N. C., Faber S. M., 1983, ApJ, 266, L21

Lisker T., Grebel E. K., Binggeli B., Glatt K., 2007, ApJ, 660, 1186

Lonsdale Persson, C. J., & Helou, G. 1987, ApJ, 314, 513

Lupton, R., Gunn, J. E., Ivezic, Z., et al. 2001, in Astronomical Data Analysis Software and Systems X, ed. F. R. Harnden, Jr., F. A. Primini, & H. E. Payne (San Francisco: ASP), ASP Conf. Ser., 238, 269

Mac Low M.-M., Ferrara A., 1999, ApJ, 513, 142

Madau, P., Ferguson, H. C., Dickinson, M. E., Giavalisco, M., Steidel, C. C.; Fruchter, A., 1996, MNRAS, 283, 1388

Madgwick, D. S., et al.(the 2dFGRS team), 2002, MNRAS, 333, 133

Madore, B. F., 1977, MNRAS, 178, 1

Mahajan, S., Raychaudhury, S., 2009, MNRAS, 400, 687

Mahajan, S., Haines, C. P., Raychaudhury, S., 2010, MNRAS, 404, 1745

Mahajan S., Haines C. P., Raychaudhury S., 2011a, MNRAS, 412, 1098

Mahajan, S., Mamon, G. A., Raychaudhury, S., 2011b, submitted to MNRAS

Mahajan, S., Raychaudhury, S. & Pimbblet, K. B., 2011c, in preparation

Mahajan, S., Ashby M. L. N., Willner S. P., G. G. Fazio, Raychaudhury, S., 2011d, in preparation

Mamon G. A., 1992, ApJ, 401, L3

Mamon G. A., Parker Q. A., Proust D., 2001, PASA, 18, 232

Mamaon, G. A., Sanchis, T., Salvador-Solé, E., Solanes, J.M., 2004, A&A, 414, 445

Mamon G. A., Biviano A., Murante G., 2010, A&A, 520, A30

Manning C. V., 2002, ApJ, 574, 599

Marble A. R., et al., 2010, ApJ, 715, 506

Marcillac, D., Rigby, J. R., Rieke, G. H., Kelly, D. M., 2006, ApJ, 654, 825

Marcolini A., D'Ercole A., Brighenti F., Recchi S., 2006, MNRAS, 371, 643

Marcum, P. M., et al. 2001, ApJS, 132, 129

Margoniner, V. E., de Carvalho, R. R., 2000, AJ, 119, 1562

Margoniner, V. E., de Carvalho, R. R., Gal, R. R., & Djorgovski, S. G., 2001, ApJ, 548, L143

Markevitch, M., et al., 2003, ApJ, 583, 70

Martin, D. C., et al., 2005, ApJL, 619, L1

Martini P., Kelson D. D., Kim E., Mulchaey J. S., Athey A. A., 2006, ApJ, 644, 116

Masters, K. L., et al. 2010, MNRAS, 404, 792

Mauduit J.-C., Mamon G. A., 2007, A&A, 475, 169

McCarthy, I. G., Frenk, C. S., Font, A. S., Lacey, C. G., Bower, R. G., Mitchell, N. L., Balogh, M. L., Theuns, T., 2008, MNRAS, 383, 593

McDermid R. M., et al., 2006, MNRAS, 373, 906

McLin K. M., Stocke J. T., Weymann R. J., Penton S. V., Shull J. M., 2002, ApJ, 574, L115

Melnick, J., Sargent, W.L.W., 1977, ApJ, 215, 401

Mercurio, A., Busarello, G., Merluzzi, P., Barbera, F. La, Giradi, M., Haines, C. P., 2004, A&A, 424, 79

Merritt D., 1983, ApJ, 264, 24

Meurer, G. R., Heckman, T. M., & Calzetti, D. 1999, ApJ, 521, 64

Miles T. A., Raychaudhury S., Russell P. A., 2006, MNRAS, 373, 1461

Miller C. J., Nichol R. C., Gómez P. L., Hopkins A. M., Bernardi M., 2003, ApJ, 597,142

Mohr J. J., Geller M. J., Fabricant D. G., Wegner G., Thorstensen J., Richstone D. O., 1996, ApJ, 470, 724

Moore, B., Katz, N., Lake G., Quinn, Dressler, A., Oemler, A., Jr., 1996, Nature, 379, 613

Moran, S. M., Ellis, R. S., Treu, T., Smail, I., Dressler, A., Coil, A. L., Smith, G. P., 2005, ApJ, 634, 977

Morić I., Smolčić V., Kimball A., Riechers D. A., Ivezić Ž., Scoville N., 2010, ApJ, 724, 779

Morrissey, P., et al., 2005, ApJL, 619, L7

Morrissey, P., et al., 2007, ApJS, 173, 682

Moss C., Dickens R. J., 1977, MNRAS, 178, 701

Moss, C., 2006, MNRAS, 373, 167

Mould, J. R., et al. 2000, ApJ, 529, 786

Natarajan P., Kneib J.-P., Smail I., Treu T., Ellis R., Moran S., Limousin M., Czoske O., 2009, ApJ, 693, 970

Navarro J. F., Frenk C. S., White S. D. M., 1996, ApJ, 462, 563

Neumann D. M., et al., 2003, A&A, 406, 789

Noeske, K. G., Faber, S. M., Weiner, B. J., Koo, D. C., Primack, J. R., Dekel, A., Papovich, C., Conselice, C. J., Le Floc'h, E., Rieke, G. H., Coil, A. L., Lotz, J. M., Somerville, R. S., Bundy, K., 2007, ApJ, 660L, 47

Nolan, L., Raychaudhury, S., Kabàn, A., 2007, MNRAS, 375, 381

Oemler A. J., 1974, ApJ, 194, 1

Oemler, A., Dressler, A., Kelson, D., Rigby, J., Poggianti, B. M., Fritz, J., Morrison, G., Smail, I., 2009, ApJ, 693, 152O

Osterbrock D. E. & Ferland G. J., Astrophysics of Planetary Nebulae and Active Galactic Nuclei, University Science Books, First edition, 1989

Overzier R. A., et al., 2011, ApJ, 726, L7

Pandey, B. & Bharadawaj, S., 2005, MNRAS, 357, 1068

Pandey, B. & Bharadawaj, S., 2006, MNRAS, 372, 827

Phillips, L. A., Ostriker, J. P., & Cen, R., 2001, ApJ, 554, L9

Pimbblet, K. A., Drinkwater, M. J., & Hawkrigg, M. C., 2004, MNRAS, 354, L61

Pimbblet, K. A., Smail, A., Edge, A. C., O'Hely, E., Couch, W. J., Zabludoff, A. I., 2006, MNRAS 366, 645

Pimbblet K. A., 2010, arXiv, arXiv:1010.3468

Piovan L., Tantalo R., Chiosi C., 2003, A&A, 408, 559

Pisani A.,1993, MNRAS, 265, 706

Pisani, A., MNRAS, 278, 697

Pivato M. C., Padilla N. D., Lambas D. G., 2006, MNRAS, 373, 1409

Poggianti, B. M., Smail, I., Dressler, A., Couch, W. J., Barger, A. J., Butcher, H., Ellis, R. S., Oemler, A., Jr., 1999, ApJ, 518, 576

Poggianti B. M., et al., 2001, ApJ, 562, 689

Poggianti B. M., Bridges T. J., Komiyama Y., Yagi M., Carter D., Mobasher B., Okamura S., Kashikawa N., 2004, ApJ, 601, 197

Poggianti, B. M., et al., 2006, ApJ, 642, 188

Poggianti, B. M., et al., 2008, ApJ, 684, 888

Poggianti B. M., et al., 2009, ApJ, 693, 112

Popescu C. C., et al., 2005, ApJ, 619, L75

Popesso, P., Biviano, A., Bohringer, H., Romaniello, M., 2007, A&A, 461, 397

Porter, S. C., Raychaudhury, S., 2005,

Porter, S. C., Raychaudhury, S., 2007, MNRAS, 375, 1409

Porter, S. C., Raychaudhury, S., Pimbblet, K. A., Drinkwater, M. J., 2008, MNRAS, 388, 1152

Postman M., et al., 2005, ApJ, 623, 721

Prescott M. K. M., et al., 2007, ApJ, 668, 182

Prochaska, L. C., Rose, J. A., Caldwell, N., Castilho, B. V., Concannon, K., Harding, P., Morrison, H., & Schiavon, R. P., 2007, AJ, 134, 321

Quilis, V., Moore, B., & Bower, R., 2000, Science, 288, 1617

Rasmussen, J., Sommer-Larsen, J., Pedersen, K., Sune, T., Benson, A., Bower, R. G., Olsen, L.F., 2006, astro, arXiv:astro-ph/0610893

Raychaudhury S., 1989, Nature, 342, 251

Raychaudhury S., von Braun K., Bernstein G. M., Guhathakurta P., 1997, AJ, 113, 2046

Reverte, D., V*ì*lchez, J. M., Hern*à*ndez-Fern*à*ndez, J. D., Iglesias-P*à*ramo, J, 2007, AJ, 133, 705

Reichard, T. A., Heckman, T. M., Rudnick, G., Brinchmann, J., Kauffmann, G., 2008, ApJ, 677, 186

Reichard, T. A., Heckman, T. M., Rudnick, G., Brinchmann, J., Kauffmann, G., 2009, ApJ, 691, 1005

Rieke G. H., et al., 2004, ApJS, 154, 25

Rieke G. H., Alonso-Herrero A., Weiner B. J., Pérez-González P. G., Blaylock M., Donley J. L., Marcillac D., 2009, ApJ, 692, 556

Rines K., Geller M. J., Kurtz M. J., Diaferio A., 2003, AJ, 126, 2152

Rines, K., Geller, M. J., Kurtz, M. J., Diaferio, A., 2005, AJ, 130, 1482

Rines, K., Diaferio, A., 2006, AJ, 132, 1275

Rix, H., & Zaritsky, D., 1995, ApJ, 447, 82

Rogers B., Ferreras I., Kaviraj S., Pasquali A., Sarzi M., 2009, MNRAS, 399, 2172

Rossa, J, Laine, S., van der Marel, R. P., Mihos, J. C., Hibbard, J. E., B*ö*ker, T., Zabludoff, A. I., 2007, AJ, 134, 2124

Roychowdhury S., Chengalur J. N., Begum A., Karachentsev I. D., 2009, MNRAS, 397, 1435

Saintonge, A., Tran, K. H. & Holden, B. P., 2008, ApJ, 685, L113

Salim, S., et al., 2005, ApJ, 619L, 39

Sanchis T., Łokas E. L., Mamon G. A., 2004, MNRAS, 347, 1198

Sandage A., Tammann G. A., 1976, ApJ, 210, 7

Sanders, D. B., & Mirabel, I. F. 1996, ARA&A, 34, 749

Sanduleak, N., 1969, AJ, 74, 47

Saro A., Borgani S., Tornatore L., Dolag K., Murante G., Biviano A., Calura F., Charlot S., 2006, MNRAS, 373, 397

Sato, T. & Martin, C. L., 2006, ApJ, 647, 946

Sato K., Kelley R. L., Takei Y., Tamura T., Yamasaki N. Y., Ohashi T., Gupta A., Galeazzi M., 2010, arXiv, arXiv:1009.2968

Saunders W., et al., 2000, MNRAS, 317, 55

Schawinski, K., Virani, S., Simmons, B., Urry, C. M., Treister, E., Kaviraj, S., Kushkuley, B., 2009, ApJ, 692L, 19

Schlegel, D. J., Finkbeiner, D. P., & Davis, M., 1998, ApJ, 500, 525

Schmidt, M., ApJ, 129, 243

Schuster M. T., Marengo M., Patten B. M., 2006, SPIE, 6270

Seibert, M., et al., 2005, ApJL, 619, L55

Shen Y., Mulchaey J. S., Raychaudhury S., Rasmussen J., Ponman T. J., 2007, ApJ, 654, L115

Silk, J., ApJ, 481, 702

Silverman B. W., 1986, Density Estimation for Statistics and Data Analysis, Chapman and Hall, London

Smith R. J., Hudson M. J., Lucey J. R., Nelan J. E., Wegner G. A., 2006, MNRAS, 369, 1419

Smith, R. J., et al., 2008, MNRAS, 386, L96

Smith R. J., Lucey J. R., Hudson M. J., Allanson S. P., Bridges T. J., Hornschemeier A. E., Marzke R. O., Miller N. A., 2009, MNRAS, 392, 1265

Smith R. J., et al., 2010, MNRAS, 408, 1417

Sodre L., Jr., Capelato H. V., Steiner J. E., Mazure A., 1989, AJ, 97, 1279

Soifer B. T., Neugebauer G., Houck J. R., 1987, ARA&A, 25, 187

Sol Alonso, M., Lambas, D. G., Tissera, P., Coldwell, G., 2006, MNRAS, 367, 1038

Solomon, P. M., Downes, D., Radford, S. J. E. & Barrett, J. W., 1997, ApJ, 478, 144

Sousbie T., 2010, arXiv, arXiv:1009.4015

Springel, V., et al., 2005, Nature, 435, 629

Steidel, C. C. & Hamilton, D., 1992, AJ, 104, 941

Steidel, C. C., Adelberger, K. L., Giavalisco, M., Dickinson, M., Pettini, M., 1999, ApJ, 519, 1

Stocke J. T., Danforth C. W., Shull J. M., Penton S. V., Giroux M. L., 2007, ApJ, 671, 146

Stoughton, C., et al., 2002, AJ, 123, 485

Strateva, I., et al., 2001, AJ, 122, 1861

Strauss, M. A., et al., 2002, AJ, 124, 1810

Struble M. F., 1979, AJ, 84, 50

Struble, M. F., Rood, H. J., 1999, ApJS, 125, 35

Struck, C., 2006, in Astrophysics Update 2, ed. J. W. Mason (Heidelberg: Springer), 115

Sullivan W. T., III, Johnson P. E., 1978, ApJ, 225, 751

Sullivan M., Mobasher B., Chan B., Cram L., Ellis R., Treyer M., Hopkins A., 2001, ApJ, 558, 72

Sun, M., Murray, S. S., 2002, AJ, 577, 139

Sun, M., Jones, C., Forman, W., Nulsen, P. E. J., Donahue, M., Voit, G. M., 2006, ApJ, 637L, 81

Takeuchi T. T., Buat V., Heinis S., Giovannoli E., Yuan F.-T., Iglesias-Páramo J., Murata K. L., Burgarella D., 2010, A&A, 514, A4

Tasca L. A. M., et al., 2009, A&A, 503, 379

Tanaka, M., Goto, T., Okamura, S., Shimasaku, K., Brinkmann, J., 2004, ApJ, 128, 2677

Thilker, D. A., et al., 2007, ApJS, 173, 538

Tonnesen, S., 2007, New Astronomy Reviews, 51, 80

Tonry, J. L., Dressler, A., Blakeslee, J. P., Ajhar, E. A., Fletcher, A. B., Luppino, G. A., Metzger, M. R., & Moore, C. B. 2001, ApJ, 546, 681

Toomre, A., Toomre, J., 1972, ApJ, 178, 623

Trager, S. C., Faber, S. M., Worthey, G., & Gonzalez, J. J., 2000, AJ, 119, 1645

Tremonti, C., et al., 2004, ApJ, 613, 898

Trentham, N., Blain, A. W., Goldader, J., 1999, MNRAS, 305, 61

Tully, R. B., & Fisher, J. R. 1977, A&A, 54, 661

Tully, R. B., ApJ, 321, 280

Tully, R. B., Shaya, E. J., Karachentsev, I. D., Courtois, H. M., Kocevski, D. D., Rizzi, L., & Peel, A. 2008, ApJ, 676, 184

Tzanavaris P., et al., 2010, ApJ, 716, 556

Valluri, M., & Jog, C. J., 1991, ApJ, 374, 103

van den Bosch F. C., Aquino D., Yang X., Mo H. J., Pasquali A., McIntosh D. H., Weinmann S. M., Kang X., 2008, MNRAS, 387, 79

van Zee, L., 2001, AJ, 121, 2003

Verdugo, M., Ziegler, B. L., Gerken, B., A&A, 486, 9

Vollmer B., 2009, A&A, 502, 427

von der Linden A., Wild V., Kauffmann G., White S. D. M., Weinmann S., 2010, MNRAS, 404, 1231

Vulcani B., et al., 2011, MNRAS, 412, 246

Wang, B., & Heckman, T. M. 1996, ApJ, 457, 645

Weinmann, S. M., van den Bosch, F. C., Yang, X., Mo, H. J., 2006, MNRAS, 366, 2

West M. J., 1998, ucb..proc, 36

Wild V., Walcher C. J., Johansson P. H., Tresse L., Charlot S., Pollo A., Le Fèvre O., de Ravel L., 2009, MNRAS, 395, 144

Witt A. N., Gordon K. D., 2000, ApJ, 528, 799

Worthey, G., Faber S. M., Gonzàlez, J., Burstein D., 1994, ApJS, 94, 687

Worthey, G., & Ottaviani, D.L., 1997, ApJS, 111, 377

Wolf, C., Gray, M.E. & Meisenheimer, K., 2005, A&A, 443, 435

Wolf, C., et al., 2009, MNRAS, 393, 1302

Wu H., Cao C., Hao C.-N., Liu F.-S., Wang J.-L., Xia X.-Y., Deng Z.-G., Young C. K.-S., 2005, ApJ, 632, L79

Wu, H., Zhu, Y.-N., Cao, C., & Qin, B. 2007, ApJ, 668, 87

Xu, C., & Buat, V. 1995, A&A, 293, L65

Yan R., et al., 2009, MNRAS, 398, 735

Yang X., Mo H. J., van den Bosch F. C., Weinmann S. M., Li C., Jing Y. P., 2005, MNRAS, 362, 711

Yang, X., Mo, H. J., Van den Bosch, F. C., Pasquali, A., Li, C., Barden, M., 2007, ApJ, 671, 153

Yang X., Mo H. J., van den Bosch F. C., 2008, ApJ, 676, 248

Yang X., Mo H. J., van den Bosch F. C., 2009, ApJ, 695, 900

Yi, S. K., et al., 2005, ApJ, 619, L111

York, D. G., et al., 2000, AJ, 120, 1579

Yun M. S., Reddy N. A., Condon J. J., 2001, ApJ, 554, 803

Zabludoff A. I., Zaritsky D., Lin H., Tucker D., Hashimoto Y., Shectman S. A., Oemler A., Kirshner R. P., 1996, ApJ, 466, 104

Zeldovich, I. B., Einasto, J. & Shandarin, S. F., 1982, Nature, 300, 407

Zheng X. Z., Bell E. F., Papovich C., Wolf C., Meisenheimer K., Rix H.-W., Rieke G. H., Somerville R., 2007, ApJ, 661, L41

Zhu Y.-N., Wu H., Cao C., Li H.-N., 2008, ApJ, 686, 155